Université du Québec

INRS Institut national de la recherche scientifique

Centre Énergie, Matériaux et Télécommunications

DEVELOPMENT OF HIERARCHICALLY ORGANIZED NANOSTRUCTURED TITANIUM DIOXIDE NANORODS FOR FUEL CELL APPLICATIONS

Par

Naser Mohammadi

Thèse présentée pour l'obtention du grade de

Philosophiae Doctor (Ph.D.)

en sciences de l'énergie et des matériaux

Jury d'évaluation

Président du jury et Examinateur interne	Prof. François Vidal INRS-ÉMT
Examinateur externe	Prof. Samaneh Shahgaldi UQTR
Examinateur externe	Prof. Sasha Omanovic Université McGill
Directeur de recherche	Prof. Mohamed Mohamedi INRS-ÉMT

REMERCIEMENTS

I am writing this letter with profound gratitude and deep appreciation for Professor Mohamed Mohamedi's invaluable guidance and mentorship throughout my Ph.D. journey. Your wisdom, encouragement, and unwavering support have been instrumental in shaping both the academic and personal dimensions of this monumental undertaking. Your belief in my potential has been a driving force, and I am truly thankful for the opportunities to learn and grow under your tutelage.

To my esteemed team members, Dr. Alonso Moreno Zuria, Juan Carlos Abrego Martínez, Haixia Wang, Youling Wang, Ahmed Khawtar Hasan, Soraya Bouachma, Mohamed Fatahine, I extend my heartfelt thanks for your collaborative spirit, insightful contributions, and the camaraderie that made this research journey both fulfilling and enjoyable. Each one of you played a crucial role in the success of this thesis, and I am grateful for the collective effort and shared passion for our work.

I extend my heartfelt appreciation to the esteemed members of the jury Prof. Samaneh Shahgaldi, Prof. Sasha Omanovic, and Prof. François Vidal for their time, expertise, and constructive feedback. Your insights have contributed significantly to the refinement of my research, and I am honored to have had the opportunity to present my work before such a distinguished panel.

I would also like to express my sincere gratitude to Mr. Christophe Chabanier, Mr. Étienne Charette, Mr. Catalin Harnagea and Mr. Sylvain Gingras for their valuable suggestions and professional technical support.

To my dear family, your unwavering support, understanding, and patience have been my anchor throughout this challenging but rewarding pursuit. Your sacrifices and encouragement have been my source of strength, and I want to express my deepest gratitude for being my pillars of support.

Completing this Ph.D. would not have been possible without the collective support of my supervisor, team members, and family. This achievement is a reflection of the collaborative spirit, resilience, and dedication of each individual involved.

As I embark on the next chapter of my journey, I carry with me the lessons learned, the memories created, and the bonds formed during this Ph.D. experience. I am proud to have been part of such an inspiring and supportive community.

Thank you once again for being an exceptional supervisor, amazing team members, and a loving family. Your contributions are deeply appreciated, and I look forward to carrying the values instilled in me into future endeavors.

With sincere gratitude,

Naser Mohammadi

RÉSUMÉ

À l'aide d'une combinaison de méthodes de dépôt hydrothermal et laser pulsé, des catalyseurs tridimensionnels en Pt sur des structures de TiO_2 ont été synthétisés pour l'électro-oxydation de l'éthanol en milieu acide. La microscopie électronique à balayage (MEB) a révélé que le TiO_2 préparé avec 0,6 M de HCl était composé d'un mélange de nanofils et de nanotiges. En revanche, des concentrations plus élevées en HCl ont entraîné la formation de structures de TiO_2 sous forme de barres verticales alignées ou de larges cristaux ramifiés ressemblant à des fleurs. Malgré une charge équivalente en Pt, seules les structures tridimensionnelles Pt/TiO_2/Ti avec du TiO_2 préparé avec 0,6 M de HCl ont montré une activité spécifique de zone et des activités massiques actuelles significativement supérieures, dépassant de plus de 50 fois les catalyseurs Pt/Ti non supportés. Cela suggère des applications prometteuses dans les piles à combustible à l'éthanol. L'étude présente la synthèse d'une structure tridimensionnelle en forme de pomme de pin sans liant ni gabarit, composée de Pt/TiO_2/Ti. Le TiO_2 synthétisé hydrothermiquement sur le treillis de Ti était composé de nanotiges ressemblant à des fleurs et de structures en forme de barres alignées verticalement, tandis que le film de Pt fabriqué par dépôt laser pulsé affichait une surface lisse. Les analyses de diffraction des rayons X ont révélé des tailles moyennes de cristallites de 41,4 nm et 68,5 nm pour les nanotiges de TiO_2 et le Pt, respectivement. En solution acide sulfurique, la formation d'oxyde de Pt sur l'électrode Pt/TiO_2/Ti s'est produite 180 mV plus négativement que sur l'électrode Pt/Ti, indiquant que le TiO_2 facilite la présence d'espèces oxygénées à des potentiels plus bas. Cela a facilité l'élimination des intermédiaires de type CO et accéléré les réactions d'oxydation de l'éthanol (ROE). Le catalyseur Pt/TiO_2/Ti a présenté une activité actuelle de 1,19 mA envers la ROE, remarquablement supérieure de 4,4 fois par rapport à l'électrode Pt/Ti (0,27 mA). De plus, la présence de TiO_2 en support du Pt a fourni un courant à l'état stable de 2,1 mA, montrant une augmentation de durabilité de 6,6 fois par rapport à l'électrode Pt/Ti (0,32 mA). Pt a été choisi comme catalyseur de référence, et ces structures en forme de pomme de pin tridimensionnelles pourraient trouver des applications dans diverses réactions catalytiques ou photoélectrochimiques, surtout avec des catalyseurs surpassant le Pt.

La recherche détaille la synthèse hydrothermale de nanotiges hiérarchiques en TiO_2 pour la première fois, cultivés à partir d'une couche de semence en Ti déposée par laser pulsé sur un substrat de papier carbone (CP) sans l'utilisation de gabarits ou de liants. La diffraction des rayons X a révélé que les nanotiges en TiO_2 cristallisaient dans la phase rutile. Ces nanotiges en TiO_2

ont considérablement amélioré l'électroactivité et la stabilité du Pt vis-à-vis des réactions d'oxydation de l'éthanol. Des études de durabilité par chronoampérométrie ont montré que l'activité massique spécifique du catalyseur Pt/TiO_2-NRs/CP était de 47,92 mA mg^{-1}, sept fois supérieure à celle du Pt commercial (6,72 mA mg^{-1}). Lorsqu'il était utilisé comme anode dans une pile à combustible à l'éthanol microfluidique sans membrane, le catalyseur Pt/TiO_2-NRs/CP a fourni une densité de courant maximale de 56,4 mA cm^{-2} et 5,1 mW cm^{-2}, avec une durabilité comparable à une anode de Pt commercial ayant 16,7 fois plus de charge en Pt que le catalyseur Pt/TiO_2-NRs/CP. Cette performance était attribuée à l'interface tridimensionnelle poreuse ouverte des nanotiges hiérarchiques en TiO_2, offrant une accessibilité électrolytique favorable, une meilleure stabilité et des voies directes pour le mouvement des électrons vers l'électrode. De plus, la nature autoportante, la faible charge de platine et la grande stabilité font de TiO_2-NRs/CP un support de catalyseur prometteur pour les technologies de piles à combustible.

Mots-clés: synthèse hydrothermale, dépôt laser pulsé, dioxyde de titane ; maille en titane; méthode hydrothermale; électrooxydation à l'éthanol; couche de graine de titane; des nanotiges de dioxyde de titane recouvertes de papier carbone; électrocatalyseur au platine; pile à combustible microfluidique sans membrane

ABSTRACT

Through a combination of hydrothermal and pulsed laser deposition methods, three-dimensional Pt catalysts on TiO_2 structures were synthesized for ethanol electro-oxidation in an acidic medium. Scanning electron microscopy (SEM) revealed that TiO_2 prepared with 0.6 M HCl consisted of a mixture of nanowires and nanorods. In contrast, higher HCl concentrations resulted in TiO_2 structures forming vertically aligned bars or large branched crystals resembling flowers. Despite equal Pt loading, only the 3D Pt/ TiO_2/Ti structures with TiO_2 prepared with 0.6 M HCl exhibited significantly higher area-specific activity and current mass activities, surpassing unsupported Pt/Ti catalysts by over 50 times. This suggests promising applications in ethanol fuel cells.

The study introduces the synthesis of a binderless and template-less three-dimensional pinecone-shaped Pt/ TiO_2/Ti mesh structure. The TiO_2 hydrothermally synthesized onto the Ti mesh comprised flowers-like nanorods and vertically aligned bar-shaped structures, while the Pt film grown by pulsed laser deposition displayed a smooth surface. X-ray diffraction analyses revealed average crystallite sizes of 41.4 nm and 68.5 nm for TiO_2 nanorods and Pt, respectively. In sulfuric acid solution, the Pt oxide formation on the Pt/ TiO_2/Ti mesh electrode occurred 180 mV more negatively than on the Pt/Ti mesh electrode, indicating TiO_2's facilitation of oxygen species at lower potentials. This facilitated the removal of CO-like intermediates and accelerated ethanol oxidation reactions (EOR). The Pt/ TiO_2/Ti mesh catalyst exhibited a current activity of 1.19 mA towards EOR, remarkably superior by 4.4 times compared to the Pt/Ti mesh electrode (0.27 mA). Moreover, the presence of TiO_2 as a support for Pt delivered a steady-state current of 2.1 mA, showing a durability increment of 6.6 times compared to Pt/Ti mesh (0.32 mA). Pt was chosen as a benchmark catalyst, and the authors anticipate that these 3D pinecone structures could find utility in various catalytic or photoelectrochemical reactions, especially with catalysts outperforming Pt.

The research details the hydrothermal synthesis of hierarchical TiO_2 nanorods (NRs) for the first time, grown from a pulsed laser-deposited Ti seed layer on a carbon paper (CP) substrate without the need for templates or binders. X-ray diffraction revealed that TiO_2-NRs crystallized in the rutile phase. These TiO_2-NRs significantly enhanced the electroactivity and stability of Pt towards ethanol oxidation reactions. Durability studies through chronoamperometry demonstrated that the specific mass activity of the Pt/ TiO_2-NRs/CP catalyst was 47.92 mA mg^{-1}, seven times superior to that of commercial Pt (6.72 mA mg^{-1}). When employed as an anode in a

membraneless microfluidic ethanol fuel cell, the Pt/ TiO_2-NRs/CP catalyst delivered a maximum current density of 56.4 mA cm^{-2} and 5.1 mW cm^{-2}, with durability comparable to a commercial Pt anode that had 16.7 times higher Pt loading than the Pt/ TiO_2-NRs/CP catalyst. This performance was attributed to the 3D open porous interface of hierarchical TiO_2-NRs, offering favorable electrolyte accessibility, better stability, and direct pathways for electron movement to the electrode. Additionally, the free-standing nature, low platinum loading, and high stability make TiO_2-NRs/CP a promising catalyst support for fuel cell technologies.

Keywords: hydrothermal synthesis, pulsed laser deposition, titanium dioxide; titanium mesh; hydrothermal method; ethanol electrooxidation; titanium seed layer; carbon paper-coated titanium dioxide nanorods; platinum electrocatalyst; membrane less microfluidic fuel cell

SOMMAIRE RÉCAPITULATIF

1.1 Introduction

L'énergie constitue l'un des piliers les plus significatifs de notre mode de vie contemporain, alimentant nos voitures, cuisinant nos aliments, nous réchauffant, nous rafraîchissant, éclairant nos nuits, et nous connectant aux personnes proches et lointaines. Notre consommation d'énergie provient principalement de la combustion de combustibles fossiles, tels que le pétrole, le charbon et le gaz naturel, qui sont considérés comme des ressources non renouvelables en raison de leur épuisement inévitable. Les impacts environnementaux de la combustion de ces combustibles fossiles, tels que le réchauffement climatique et la pollution de l'air, sont préoccupants. Les émissions de dioxyde de carbone liées à l'énergie ont été projetées pour augmenter, aggravant les problèmes environnementaux.

Face à la demande croissante en énergie, à l'épuisement des combustibles fossiles et à la détérioration accélérée de l'environnement, une transition vers des sources d'énergie propres et renouvelables est nécessaire. Les énergies renouvelables, telles que l'énergie solaire, éolienne, hydraulique, géothermique et la biomasse, sont en croissance rapide et offrent une alternative plus durable. Parmi les sources d'énergie renouvelable, les sources électrochimiques telles que les piles à combustible (FC), les batteries et les condensateurs électrochimiques, montrent un grand potentiel pour diverses applications.

1.2 Contexte

Cette section examine les changements dans le domaine des piles à combustible (FC) et les défis auxquels elles sont actuellement confrontées. Elle commence par définir ce qu'est une pile à combustible et se penche sur les facteurs qui ont conduit à ces évolutions. Une attention particulière est portée sur les piles à combustible à hydrogène et oxygène comme exemple, décrivant leur réaction globale et soulignant les inefficacités énergétiques associées aux méthodes traditionnelles de production d'électricité.

En outre, la section souligne l'importance croissante des piles à combustible, non seulement en tant que source d'énergie stationnaire, mais aussi dans des applications mobiles et portables. L'émergence des voitures électriques à pile à combustible (FCEV) est mise en avant, mettant en

lumière leur commercialisation croissante et leur rôle potentiel dans la réduction des émissions de CO_2. Enfin, l'accent est mis sur les micro-FC en tant que source d'énergie portable, offrant une vision à long terme de l'autonomie par rapport aux prises électriques traditionnelles. Cependant, l'auteur souligne que le marché des micro-FC est encore à ses débuts et nécessitera des améliorations progressives et révolutionnaires pour atteindre son plein potentiel.

En somme, cette section trace le paysage énergétique contemporain, soulignant la nécessité d'une transition vers des sources d'énergie plus propres et présentant les piles à combustible comme une solution prometteuse dans cette évolution énergétique. Les piles à combustible (FC), en revanche, offrent une autre méthode pour utiliser les électrons pendant les processus de reconfiguration des liaisons entre le réactif à haute énergie et le produit à basse énergie, permettant une conversion plus efficace de l'énergie chimique du carburant en électricité. En utilisant une membrane pour séparer deux gaz, les FC divisent la réaction globale susmentionnée en deux parties, nécessitant un transport d'électrons pour terminer la reconfiguration des liaisons sur une échelle de longueur significativement prolongée. En résumé, les molécules de H_2 perdent des électrons d'un côté (l'anode), comme le montre l'équation 1.2, pour créer des protons qui traversent la membrane. Comme le montre l'équation 1.3, ces protons forment de l'eau du côté opposé (cathode) où ils interagissent avec les molécules de O_2 et gagnent des électrons de la cathode.

Réaction à l'anode :

$$2H_2 \rightarrow 4H^+ + 4e^- \qquad (1.2)$$

Réaction à la cathode :

$$O_2 + 4H^+ + 4e^- \rightarrow 2H_2O \qquad (1.3).$$

En essence, les deux réactions sur les deux électrodes se produisent sur des surfaces de catalyseurs, abaissant la barrière énergétique des réactions et améliorant la cinétique globale du processus. En utilisant les électrons lorsqu'ils se déplacent à travers un circuit externe de l'anode à la cathode, de l'électricité peut être générée. Dans les FC, l'ensemble de la procédure n'inclut pas la conversion de chaleur en énergie mécanique, ce qui entraîne un rendement de conversion élevé pouvant atteindre 60%. Comparé à la réaction de combustion, cette valeur est deux à trois fois plus élevée.

Comme le montre le graphique de Ragone (Figure 1.3), les FC ont une capacité énergétique substantiellement plus élevée par rapport à d'autres sources d'énergie électrochimiques. Parce que les FC et les batteries produisent de l'électricité par des réactions électrochimiques, leur

fonctionnement est similaire. Cependant, lorsqu'elles produisent de l'électricité, ce qui peut être vu comme les coques extérieures des usines qui utilisent les carburants comme matières premières et produisent de l'électricité comme produit, les FC ne sont pas consommées. Contrairement aux batteries, qui nécessitent plus de temps pour se recharger, elles peuvent produire de l'énergie de manière continue et rapide tant que le carburant est continuellement fourni.

1.3 Types de piles

De nombreux types de piles à combustible sont actuellement en développement. L'électrolyte utilisé dans les cellules individuelles est la manière la plus courante de catégoriser les piles à combustible, et il existe cinq types principaux : les piles à combustible à oxyde solide (SOFC), piles à combustible à membrane échangeuse de protons(PEMFC), les piles à combustible à carbonate fondu (MCFC), les piles à combustible à acide phosphorique (PAFC) et les piles à combustible alcalines (AFC). Le type d'électrolyte influence tous les aspects des piles à combustible, tels que les processus électrochimiques, les catalyseurs appropriés, le carburant nécessaire, la plage de température de fonctionnement, et d'autres paramètres. Chaque type de pile à combustible est adapté à des applications spécifiques, comme le montre le tableau 1.1.

Les PEMFC (piles à combustible à membrane échangeuse de protons) sont l'un de ces cinq grands groupes de piles à combustible, et en raison de leur basse température de fonctionnement et de leurs caractéristiques de démarrage rapide, elles sont considérées comme l'une des sources d'énergie les plus prometteuses pour les applications portables et de transport. L'assemblée d'électrodes à membrane (MEA), qui comprend deux électrodes (anode et cathode) et une membrane échangeuse de protons (comme l'ionomère Nafion), est un composant crucial des PEMFC. Une pile à combustible peut être créée en combinant de nombreuses MEA pour produire la sortie électrique nécessaire. Les carburants peuvent être de différentes natures, notamment l'hydrogène gazeux ou des composés organiques riches en hydrogène tels que le méthanol, l'éthanol, l'acide formique et le glycol éthylénique, entre autres. En conséquence, les PEMFC peuvent être subdivisées en PEMFC à hydrogène, PEMFC au méthanol direct (DMFC), PEMFC à éthanol direct (DEFC), PEMFC à acide formique direct (DFAFC), PEMFC à glycol éthylénique direct (DEGFC), et ainsi de suite, en fonction du type de carburant utilisé dans la cellule.

1.4 Introduction des DEFC (Direct Ethanol Fuel Cells)

En raison des propriétés attrayantes de l'éthanol, les piles à combustible à éthanol direct (DEFC) ont suscité beaucoup d'intérêt ces dernières années. À la température ambiante normale et à la pression atmosphérique, l'éthanol est liquide et, contrairement à l'hydrogène, il est facile à manipuler, stocker et transporter. Dans les DEFC, l'éthanol est immédiatement oxydé au lieu d'être transformé en gaz d'hydrogène. Comme le montre le tableau 1.2, les carburants liquides tels que l'éthanol ont une densité d'énergie volumétrique beaucoup plus élevée que les carburants gazeux tels que l'hydrogène, ce qui rend le système plus compact et prometteur en tant que source d'énergie pour des dispositifs électroniques portables tels que les téléphones mobiles, les ordinateurs portables et les blocs d'alimentation portables. De plus, l'utilisation d'éthanol liquide permet d'utiliser les infrastructures existantes du gazole au lieu de dépenser des coûts importants pour construire une infrastructure d'hydrogène.

L'éthanol présente de nombreux avantages par rapport à l'alcool liquide le plus largement utilisé (méthanol), notamment une toxicité plus faible, une densité d'énergie théoriquement plus élevée, une biocompatibilité et une disponibilité répandue à partir de biomasses renouvelables telles que la canne à sucre, le blé, le maïs, la paille ou même les algues. Le Brésil, qui possède la première économie de biocarburants durable au monde, est également considéré comme un modèle de politique pour d'autres nations et un leader de l'industrie du bioéthanol. Le Canada cultive chaque année des millions de tonnes de cultures pouvant être utilisées pour produire du bioéthanol, un carburant propre et renouvelable, sans nuire à l'approvisionnement alimentaire du pays. Cela fait du Canada un pays de possibilités renouvelables. Cette énorme source d'énergie équivaut à une offre annuelle de 436 millions de gallons de carburants renouvelables actuellement sous-utilisés. Par conséquent, le développement des DEFC repose sur des bases solides grâce à la croissance explosive de l'industrie du bioéthanol.

En ce qui concerne les performances de l'éthanol dans les FC, sa cinétique d'oxydation à basse température est comparable à celle du méthanol. Cependant, l'éthanol présente une perméabilité inférieure à travers la membrane Nafion par rapport au méthanol. Par conséquent, l'éthanol présente un taux de passage inférieur au méthanol et a un impact moins significatif sur l'efficacité de la conversion d'énergie. La MEA (assemblée d'électrodes à membrane) en forme de sandwich est le composant clé des DEFC (piles à combustible à éthanol direct), tout comme

pour d'autres FC (piles à combustible) basées sur PEM (membrane échangeuse de protons). Une seule MEA est constituée d'une membrane échangeuse de protons en contact avec une électrode d'anode et une électrode de cathode de chaque côté, comme illustré dans la Figure 1.4. La membrane Nafion®, fabriquée par DuPont, est actuellement la membrane la plus développée, commercialement accessible et performante utilisée pour les FC basées sur PEM. Cette membrane est responsable du transfert des protons générés de l'anode à la cathode et de la séparation spatiale des deux électrodes. Des catalyseurs sont nécessaires pour les électrodes d'anode et de cathode afin que ces réactions puissent aller plus vite. Jusqu'à présent, les catalyseurs à base de Pt sont considérés comme les plus efficaces et durables pour les réactions de cathode et d'anode, respectivement.

La réaction d'oxydation de l'éthanol (ROE) à l'anode est un mécanisme plus complexe à plusieurs électrons que l'oxydation de l'hydrogène, comme indiqué dans l'équation 1.4. L'oxydation complète de l'éthanol entraîne la rupture des liaisons C-H, C-O et C-C et produit 12 électrons, dépassant les 6 électrons dans les DMFC (piles à combustible au méthanol direct) et les 4 électrons dans les PEMFC à hydrogène. L'O_2 gazeux est fourni à la cathode des DEFC de manière similaire aux PEMFC à hydrogène, et la réaction de réduction de l'oxygène (RRO) a lieu en mélangeant l'O_2 avec les électrons et les protons produits à l'anode (équation 1.5). La réaction complète des DEFC est donc représentée par l'équation 1.6, avec le changement d'enthalpie (ΔH^0), l'énergie libre de Gibbs (ΔG^0), et la force électromotrice standard équilibre (emf) de -1367.9 kJ mol^{-1}, -1326.7 kJ mol^{-1} et 1.145 V, respectivement.

Sous des conditions normales réversibles, le rapport entre l'efficacité énergétique théorique et l'énergie utilisable ΔG^0 et l'énergie totale de la réaction chimique, ΔH^0, peut être déterminé avec l'équation $\eta_{théo} = \Delta G^0/\Delta H^0 \times 100\% = 1326.7/1367.9 \times 100\% = 97\%$ (1.7). Cependant, la cinétique de l'oxydation de l'éthanol est plus complexe, entraînant une surtension élevée et une faible densité de courant malgré les données thermodynamiques prometteuses des DEFC. En raison de trois pertes potentielles principales, la tension de la pile mesurée à une densité de courant j pendant le fonctionnement diminue en dessous du potentiel d'équilibre E_0. La définition de la tension réelle de la pile E_{cell} est : $E_{cell} = E_0 - \Delta E_{acti} - \Delta E_{ohmic} - \Delta E_{conc}$ (1.8) où E_{acti} est la perte d'activation ou la surtension d'activation due au besoin de déplacer les électrons et de rompre/former des liaisons chimiques à la fois dans ROE et RRO; E_{ohmic} est la perte ohmique principalement due aux résistances de matériau et d'interface; et E_{conc} est la perte de concentration ou la polarisation de concentration due à la diminution de la concentration des réactifs à la fois à l'anode et à la cathode lorsqu'ils sont consommés dans les réactions. La Figure

1.5 est une courbe de polarisation typique des DEFC qui met en évidence les pertes de potentiel mentionnées précédemment. En raison des vitesses cinétiques lentes de ROE et RRO, la perte d'activation est la principale source de la chute abrupte de potentiel qui se produit à faibles densités de courant. Des catalyseurs plus actifs sont nécessaires sur les deux électrodes pour réduire les pertes d'activation. Les pertes ohmiques s'intensifient à mesure que la densité de courant augmente jusqu'à des niveaux intermédiaires. En raison de la limite de transport de masse des réactifs accessibles aux sites réactifs dans les couches de catalyseurs, à mesure que l'intensité du courant augmente, la tension de la pile diminue de manière significative.

1.5 Revue de la littérature

1.5.1 Introduction aux catalyseurs d'anode pour les DEFCs

Les catalyseurs ont un impact considérable sur le coût, les performances et la durabilité des DEFCs. Le Pt et les alliages à base de Pt sont les catalyseurs d'anode et de cathode les plus souvent utilisés et les plus largement étudiés pour les DEFCs fonctionnant en milieu acide, en termes de performances catalytiques et de durabilité. En raison du coût élevé et des réserves limitées de Pt, la réduction de la charge en Pt dans la couche catalytique est d'une importance cruciale pour surmonter la barrière des coûts pour la commercialisation des DEFCs. Ainsi, la méthode la plus populaire pour maximiser l'utilisation du Pt consiste à disperser des catalyseurs Pt nanostructurés sur des matériaux supports à grande surface comme le noir de carbone (par exemple, Vulcan XC-72). Jusqu'à présent, le Pt supporté par Vulcan XC-72 est couramment utilisé comme catalyseur d'anode et de cathode dans les DEFCs. En effet, le support de Vulcan XC-72 augmente considérablement l'activité catalytique des catalyseurs. Cependant, au cours d'une utilisation à long terme des FCs, il subit une corrosion sévère, entraînant l'agglomération, la dissolution et l'isolement des nanoparticules de Pt, compromettant ainsi considérablement les performances et la durabilité des DEFCs.

Il est largement connu que le Pt en tant que catalyseur d'anode est particulièrement actif pour la rupture des liaisons C-H et l'adsorption dissociative de l'éthanol, mais il ne peut pas accomplir l'oxydation complète de l'éthanol en CO_2 libérant 12 électrons en rompant efficacement les liaisons C-O et C-C à basses températures. Par une oxydation partielle de l'éthanol (oxydation à 2 électrons et à 4 électrons), des sous-produits indésirables tels que l'acétaldéhyde (CH_3CHO, AAL) et l'acide acétique (CH_3COOH) sont générés, respectivement. L'oxydation incomplète de l'éthanol abaisse non seulement l'efficacité énergétique en raison d'un échange moins important

d'électrons par rapport à la réaction d'oxydation complète, mais elle génère également de l'acétate ou du (bi)sulfate qui s'adsorbe fortement sur la surface des catalyseurs et affecte significativement la réactivité des catalyseurs. De plus, le Pt lui-même a peu de résistance à l'empoisonnement, car des espèces intermédiaires telles que le CO_{ads} peuvent être largement adsorbées sur sa surface, empoisonnant les catalyseurs et entraînant ainsi un taux de réaction lent et potentiellement une détérioration irréversible des performances catalytiques.

Pour résoudre les problèmes susmentionnés dans les DEFCs, beaucoup de travaux ont été concentrés sur la recherche de catalyseurs multi-composants par rapport au Pt pur, visant à développer des catalyseurs très actifs, sélectifs et durables. Ces dernières années, diverses tentatives ont été faites, telles que le mélange du Pt avec des métaux de transition non nobles pour générer des catalyseurs binaires/ternaires, l'ajout d'oxydes de métaux de transition au Pt pour former des catalyseurs nanocomposites. Une revue complète de la littérature portant sur les travaux sur les catalyseurs Pt-métaux de transition (Pt-M) et Pt-oxydes de métaux de transition est élaborée dans la section suivante. Selon la portée de cette thèse, seuls les catalyseurs utilisés en milieu acide seront présentés et abordés.

1.5.2 Oxydation de l'éthanol sur des catalyseurs à base d'oxyde métallique fonctionnel

En plus des études approfondies sur les catalyseurs, beaucoup d'efforts ont été déployés pour explorer de nouveaux catalyseurs à base de Pt en introduisant divers oxydes métalliques fonctionnels (FMOs) tels que CeO_2, SnO_2, MnO_2, TiO_2, WO_3, etc. Comme on le sait, ces FMOs sont bon marché et abondants par rapport au Pt, et donc l'incorporation de FMOs à grande surface spécifique pourrait largement réduire le coût des catalyseurs. De plus, ces FMOs présentent également les qualités significatives suivantes pour des utilisations futures dans les DEFCs:

Stabilité chimique et électrochimique élevée dans les conditions de fonctionnement des piles à combustible, réduisant l'agglomération ou la coalescence des nanoparticules de catalyseur et augmentant ainsi leur durabilité. L'interaction forte des nanoparticules de catalyseur avec les supports d'oxyde (interaction métal-support, SMSI) pourrait immobiliser les nanoparticules de catalyseur sur les surfaces des matériaux supports, empêchant la croissance et la frittage des nanoparticules de catalyseur, et pourrait également modifier la distribution électronique des catalyseurs pour diminuer l'effet d'empoisonnement par le CO. Production facile de nombreux

groupes hydroxyle (OH) sur leurs surfaces, ce qui pourrait augmenter les performances catalytiques sur la base du mécanisme bifonctionnel. Il a été rapporté que Les FMO dans les DEFC fonctionnent comme des catalyseurs (promoteurs) pour assister des processus catalytiques spécifiques. Cependant, la plupart des FMOs ont une faible conductivité électronique qui pourrait être augmentée en les nanostructurant ou en les mélangeant avec des matériaux carbonés plus conducteurs pour produire des composites ou en dopant des éléments étrangers. Les carbones nanostructurés, tels que les nanotubes de carbone, le graphène, le carbone mésoporeux, et autres, sont considérés comme les principaux supports dans les matériaux composites. Les FMOs sont considérés comme des supports secondaires qui sont généralement utilisés pour promouvoir et modifier les supports primaires. Bien que de nombreux FMOs ont été considérés et décrits en détail dans la littérature, pour l'application dans des DEFCs, dans cette thèse, notre accent est mis sur le TiO_2.

1.5.3 Catalyseurs à base de TiO_2

Le dioxyde de titane, également connu sous le nom d'oxyde de titane (IV), est l'oxyde naturel du titane. Le dioxyde de titane se trouve naturellement sous trois phases principales : rutile, anatase et brookite. Les cellules unitaires des trois phases de TiO_2 sont présentées dans la Figure 1.6. La phase rutile est la forme naturelle la plus fréquente de TiO_2 et possède une cellule unitaire tétragonale centrée, avec des paramètres de cellule unitaire a=b=4,584 Å, et c=2,953 Å. Six atomes d'oxygène forment un octaèdre autour de chaque cation de titane. Les anions oxygène ont un nombre de coordination de 3, résultant en une coordination planaire trigonale. La phase rutile montre également un axe hélicoïdal lorsque les octaèdres sont vus séquentiellement. L'anatase cristallise dans le système tétragonal. La pyramide commune de l'anatase, parallèle aux faces desquelles il y a des clivages parfaits, a un angle sur le bord polaire de 82°9', l'angle comparable du rutile étant de 56°52½'. La brookite appartient à la classe de cristal orthorhombique 2/m 2/m 2/m. Les paramètres de la cellule unitaire sont : a=5,4558 Å, b=9,1819 Å et c=5,1429 Å. La formule est TiO_2, avec 8 unités de formule par cellule unitaire (Z=8). La structure brookite est construite à partir d'octaèdres déformés avec un ion de titane au centre et des ions d'oxygène à chacun des six sommets. Chaque octaèdre forme une forme orthorhombique lorsqu'il partage trois arêtes avec des octaèdres voisins. Les bandes interdites de rutile et d'anatase TiO_2 sont généralement estimées à 3,03 et 3,20 eV, respectivement. Dans le contexte des piles à combustible, des oxydes de Ti nanostructurés ont été introduits pour améliorer les performances en tant que membrane, support de catalyseur ou catalyseur lui-

même. Ont passé en revue les été démontré comme un photocatalyseur efficace pour la dégradation de polluants organiques présents dans différents environnements tels que l'eau ou l'air, en raison de son activité redox puissante. Les électrodes Pt-TiO_2 ont été principalement discutées dans la littérature en tant que photocatalyseurs pour les cellules photoélectrochimiques. ont démontré une performance considérablement améliorée de l'oxydation du méthanol (ROE) avec une électrode Pt-TiO_2 nanostructurée sous irradiation UV par rapport à celle sans illumination UV. Les auteurs ont attribué la performance nettement améliorée sous l'illumination UV à la photocatalyse de l'oxydation du méthanol par des trous photo-générés dans le TiO_2. Ils ont démontré les caractéristiques photocatalytiques et d'auto-nettoyage UV de nanotubes de titane décorés de nanoparticules de Pt (Pt-NPs/TNT) pour le processus d'électro-oxydation du méthanol. L'électrode Pt-NPs/TNT a été balayée dans une solution aqueuse de H_2SO_4 à 0,1 M + 0,1 M de méthanol pendant 250 cycles dans la plage de potentiel de 0,0 à 1,0 V par rapport à SCE. Inévitablement, la densité de courant a diminué avec l'augmentation du nombre de cycles, principalement en raison de l'impact d'empoisonnement par le CO. Après avoir exposé l'électrode à l'UV pendant 5 minutes, curieusement, les auteurs ont constaté que les voltammogrammes cycliques de Pt-NPs/TNT pouvaient revenir à leur forme et magnitude d'origine, ce qui était attribué aux propriétés d'auto-nettoyage du TiO_2. De plus, il a été noté que la densité de courant de crête de MOR sous illumination UV était presque 2,1 fois plus grande qu'en l'absence d'irradiation UV. Sur la base des expériences et de la littérature pertinente, les auteurs ont conclu que l'électrooxydation du méthanol sur Pt-NPs et l'électrooxydation photochimique du méthanol sur le TiO_2 se déroulaient simultanément sous l'illumination UV et contribuaient à la densité de courant de crête améliorée dans les tests CV. Comme le TiO_2 est plus durable que les supports carbonés traditionnels pour l'ORR, il a également été suggéré comme une cathode potentielle. Divers mécanismes ont été discutés pour le rôle du TiO_2 et l'activité électrocatalytique du Pt-TiO_2 vers l'ORR. Le TiO_2 réduit l'agrégation des particules de Pt pour les électrodes cathodiques et protège la membrane Nafion des radicaux peroxyde produits pendant l'ORR.

D'autre part, certaines recherches ont rapporté que le TiO_2 peut augmenter l'activité électrocatalytique du Pt vers l'oxydation du méthanol et l'oxydation de l'éthanol dans l'obscurité en minimisant l'impact de l'empoisonnement par le CO. Ont observé que le TiO_2 pouvait améliorer les performances du catalyseur Pt–Ru pour l'oxydation du méthanol sans irradiation UV en minimisant les effets d'empoisonnement par le CO. Ont synthétisé un catalyseur ultrasoniquement du Pt/C commercial et des nanoparticules de TiO_2, et ont examiné l'influence de la taille et de la quantité de TiO_2. Le catalyseur Pt/C+TiO_2 avec 20 % en poids de particules de TiO_2 (de 10 nm de diamètre) a démontré la plus grande performance catalytique pour

l'oxydation de l'éthanol, bien supérieure au Pt/C d'origine. La performance catalytique améliorée de Pt/C+TiO_2 a été attribuée à la présence de TiO_2 qui pourrait favoriser l'élimination oxydative du CO, vérifiée par le test de stripping au CO, et à la teneur et à la taille optimales de TiO_2 qui pourraient garantir des interfaces TiO_2-Pt-C optimisées et une bonne conductivité électronique pour les catalyseurs composites. L'effet synergique des catalyseurs Pt avec un support en sphères de TiO_2 de taille submicrométrique a été rapporté, qui a abaissé le potentiel de début vers ROE et EOR par rapport au Pt supporté par du noir de carbone, démontrant une cinétique de réaction améliorée. Par le biais de la décomposition thermique de précurseurs chlorés H_2PtCl_6 et $TiCl_3$ à haute température, ont préparé des électrocatalyseurs binaires Pt-TiO_2 avec différents rapports molaires Pt: TiO_2 pour l'EOR et le ROE. Il a été constaté que Pt (50 %)-TiO_2 (50 %) était la composition optimale, présentant une activité EOR et MOR considérablement améliorée par rapport au Pt pur. La formation de nanoparticules de Pt plus petites et leur dispersion uniforme ont été attribuées à l'ajout de TiO_2, cité comme la principale cause de l'amélioration des performances électrocatalytiques des électrodes binaires Pt-TiO_2 plutôt que l'effet bifonctionnel.

1.5.4 Mécanisme de réaction de l'oxydation de l'éthanol

Il est bien connu que l'oxydation complète de l'éthanol conduit à la rupture de la liaison C-C et génère des espèces CO adsorbées qui sont finalement oxydées en CO_2. Tout le processus implique un transfert d'électrons de 12 par molécule d'éthanol, donnant une densité d'énergie de 8,0 kWh kg-1. Cependant, à basse température, il a été constaté que la rupture de la liaison C-C n'est pas facilement réalisée sur les catalyseurs Pt actuellement disponibles. Divers intermédiaires (par exemple, $CH_{x,ads}$, COads, CH_3COH_{ads}) et produits (par exemple, CO_2 et méthane) sont formés par de nombreuses réactions parallèles, ce qui diminue considérablement la densité d'énergie exploitable (8,0 kWh kg^{-1}) de l'éthanol. Par conséquent, une compréhension approfondie du mécanisme de réaction de l'oxydation de l'éthanol est précieuse et cruciale pour la conception de nouveaux catalyseurs avec une activité, une sélectivité et une stabilité élevées.

Dans ce contexte, de nombreuses études ont été consacrées à élucider le mécanisme de réaction de l'oxydation de l'éthanol en identifiant les intermédiaires adsorbés et en quantifiant les produits et sous-produits de réaction. Pour ce faire, certaines méthodes électrochimiques combinées avec d'autres techniques physicochimiques, notamment la FTIR (Transformée de Fourier infrarouge) in situ, la spectrométrie électrochimique de masse différentielle (DEMS) en ligne, la chromatographie liquide à haute performance (HPLC), la chromatographie en phase

gazeuse (GC), la spectroscopie de résonance magnétique nucléaire in situ (NMR) et la spectroscopie Raman amplifiée en surface (SERS). De plus, des études théoriques avec des calculs DFT (la théorie fonctionnelle de la densité) ont été réalisées pour fournir une base fondamentale à la compréhension des observations expérimentales et pour donner des orientations expérimentales supplémentaires.

1.6 Problématiques du catalyseur électrochimique pour l'oxydation de l'éthanol (EOR)

Au cours des dernières décennies, de nombreux progrès ont été réalisés pour améliorer les performances des DEFCs. Cependant, il reste encore des problèmes critiques liés aux catalyseurs électrochimiques à résoudre, en particulier des difficultés liées au développement des catalyseurs d'anode, qui sont résumées comme suit : (i) Le coût élevé des catalyseurs électrochimiques. Le platine est un métal noble rare et coûteux, et la charge élevée de Pt dans la MEA constitue un obstacle critique limitant la commercialisation des DEFCs. (ii) Cinétique de réaction lente à l'anode ; (iii) Les difficultés liées à l'oxydation complète de l'éthanol en CO_2 et à la rupture de la liaison C-C. L'oxydation partielle de l'éthanol abaisse non seulement l'efficacité de la pile à combustible entière, mais détériore également la durabilité des catalyseurs en raison des nombreux intermédiaires empoisonnants ; (iv) La faible durabilité des catalyseurs est un autre problème significatif pour l'application pratique des DEFCs. Au cours du fonctionnement à long terme des DEFCs, la corrosion électrochimique des matériaux de support (par exemple, Vulcan XC-72 et nanotubes de carbone) entraîne l'agrégation, la dissolution et l'isolement des catalyseurs, entraînant ainsi la dégradation des performances de l'ensemble de la DEFC.

1.7 Objectifs de la thèse

Comme discuté dans la section sur les problématiques, les supports de catalyseurs tels que les matériaux à base de carbone utilisés dans les dispositifs de piles à combustible sont coûteux et sujets à la corrosion, ce qui provoque le détachement et/ou l'agrégation du catalyseur. Le TiO_2 est bon marché, non toxique, présente une haute résistance mécanique et est très stable dans des environnements acides et oxydatifs. Notre objectif ultime est de développer des nanotiges de TiO_2 comme support de catalyseur alternatif aux carbones conventionnels dans les DEFCs à

basse température pour améliorer la dispersion et la durabilité du catalyseur. Dans cette optique, nous suivrons les sous-objectifs suivants :

Développer la technique hydrothermale acide et optimiser les paramètres de traitement pour synthétiser des nanotiges de TiO_2 sur substrat à l'aide de feuilles de Ti et de treillis de Ti comme substrats et une source de Ti. Plusieurs paramètres de synthèse seront modifiés, notamment la concentration de HCl, le temps, la température et le volume de la solution. Le papier carbone (CP), constitué d'un réseau de fibres de carbone, reste le principal produit du substrat macroporeux pour la couche de diffusion gazeuse (GDL) des piles à combustible à membrane échangeuse de protons (PEMFCs). Le deuxième objectif de ce travail est de synthétiser des nanotiges de TiO_2 sur un substrat CP sans recourir à l'utilisation de gabarits ou de liants. Nous proposons donc une nouvelle approche qui consiste d'abord à synthétiser, via le dépôt pulsé au laser (PLD), une couche de semence de Ti sur CP. Au-dessus de cette couche de semence de Ti, des nanotiges de TiO_2 orientées de manière hiérarchique sont cultivées en une étape via la technique hydrothermale en utilisant les paramètres de traitement optimisés découverts dans l'objectif 1).

Optimiser les paramètres du dépôt pulsé au laser pour faire croître des nanoparticules de Pt (catalyseur de référence) sur des nanotiges/substrats de TiO_2 (feuille de Ti, treillis de Ti, papier carbone). L'objectif ici est de fabriquer des nanotiges/substrats de Pt/TiO_2 hiérarchiques en tant que catalyseurs électrochimiques hybrides avancés. Ainsi, les catalyseurs cultivés seront soumis à une étude de réaction d'électrooxydation de l'éthanol (EOR) afin d'investiguer les propriétés de support des nanotiges/substrats de TiO_2 sur les performances électrocatalytiques du Pt.

Performances de la pile à combustible. Les structures de nanotiges de TiO_2 supportant le Pt qui présentent les meilleures performances électrochimiques envers l'EOR (objectif 3) seront intégrées dans un dispositif de micro pile à combustible à éthanol direct à respiration d'air pour obtenir des profils courant-tension, densité de puissance et durabilité. Enfin, dans le but de comparer la compétitivité de nos catalyseurs électrochimiques hybrides, une comparaison des performances de la pile à combustible avec le catalyseur Pt composite (commercial) de pointe sera réalisée.

1.8. Organisation de la thèse

Cette thèse se compose de 7 chapitres comprenant le résumé et les références. L'organisation de la thèse est listée ci-dessous:

Le chapitre 1 présente tout d'abord dans les grandes lignes le contexte et la motivation de la recherche sur les DEFC acides. Une revue de la littérature sur l'état de la recherche sur les DEFC. Ensuite les problématiques et les objectifs sont résumés.

Le chapitre 2 présente la méthodologie suivie au cours de cette thèse, y compris le schéma expérimental, les méthodes de caractérisation et les protocoles électrochimiques. Une introduction détaillée sur diverses techniques de caractérisation physico-chimique et électrochimique et les paramètres expérimentaux correspondants sont également donnés dans ce chapitre.

Les chapitres 3 à 5 font état des trois articles publiés durant cette thèse.

Le chapitre 6 et 7 résument les résultats et propose des orientations de recherche futures pour ce projet.

Chapitre 3 : Article 1: Résultats des nanotiges de Titane synthétisées sur une feuille de Titane

Le TiO_2, en raison de son coût abordable, de sa disponibilité commerciale, de son caractère non toxique et de sa résistance élevée à la corrosion et aux environnements acides, émerge comme un candidat prometteur en tant que support catalytique alternatif au carbone dans les piles à combustible. Contrairement au carbone, souvent utilisé comme support pour les électrocatalyseurs à base de platine dans ces systèmes, le TiO_2 offre une stabilité accrue face à la corrosion et une meilleure durabilité. De plus, le TiO_2 présente une stabilité supérieure dans des environnements acides, alcalins et oxydants, ce qui en fait un matériau attractif pour des applications telles que les piles à combustible direct à l'éthanol (DEFC).

Les DEFC suscitent un intérêt croissant en raison de leur potentiel d'application dans les secteurs des transports et des dispositifs électroniques portables. L'éthanol, en tant que carburant vert, présente une densité d'énergie théorique élevée et peut être produit en grande quantité à partir de sources de déchets non conventionnelles, telles que les déchets alimentaires, agricoles et forestiers. Cela positionne les DEFC comme des sources d'énergie à faibles émissions de gaz à effet de serre, contribuant ainsi aux efforts en faveur de solutions énergétiques plus durables.

Les études sur l'utilisation du TiO_2 en tant que support catalytique pour l'oxydation de l'éthanol (ROE) sont limitées, mais présentent un intérêt croissant. Cette recherche vise à combler cette lacune en combinant la méthode hydrothermale avec le dépôt laser pulsé (PLD) pour créer des

catalyseurs tridimensionnels de platine sur des réseaux de nanotiges de TiO_2. La variation de la concentration de HCl pendant la synthèse du TiO_2 permet d'obtenir différentes morphologies de TiO_2, offrant ainsi une flexibilité dans la conception des structures catalytiques.

Les résultats montrent que les structures d'électrodes Pt/TiO_2/Ti, où le TiO_2 est composé d'un mélange de nanofils et de nanotiges, présentent une surface électroactive supérieure, une activité spécifique de surface accrue et une activité électrocatalytique considérablement améliorée dans la ROE par rapport à d'autres électrocatalyseurs, bien qu'ils aient la même charge de platine. Cette optimisation de la synthèse du TiO_2 via la méthode hydrothermale, combinée à la croissance du catalyseur de platine par ablation laser, ouvre des perspectives prometteuses pour le développement de structures d'électrodes efficaces dans le contexte des technologies DEFC.

Des feuilles de titane ont d'abord été nettoyées avec de l'acétone dans un bain à ultrasons pendant 20 minutes. Ensuite, ces feuilles de Ti ont été rincées abondamment à l'eau. Après séchage à l'air, les feuilles ont été attaquées chimiquement dans une solution de HCl à 18 % (15 mL) à 80 °C pendant 15 minutes pour éliminer la couche d'oxyde de titane. Après, les feuilles de Ti ont été chargées dans un autoclave en acier inoxydable doublé de Teflon de 23 mL (Parr Instrument) rempli de 10 mL de solution aqueuse d'HCl et maintenues à 180 °C pendant 10 heures pour compléter la réaction hydrothermale. Quatre concentrations d'HCl ont été considérées, à savoir 0,6, 0,6M200, 0,78 et 1,12 M. Pour simplifier, les échantillons sont étiquetés comme suit : Échantillon 0,6M, Échantillon 0,6M200 (200 indique la température de synthèse), Échantillon 0,78M et Échantillon 1,12M.

Par la suite, des films minces de Pt ont été déposés sur des feuilles de Ti et des substrats de TiO_2/Ti par dépôt pulsé au laser (PLD) en utilisant une cible pure de Pt (99,99 %, Kurt J. Lesker Co). Tous les films de Pt ont été déposés à température ambiante avec 50 000 impulsions laser sous 2 Torr de gaz He en utilisant un laser excimère KrF (λ = 248 nm), une largeur d'impulsion de 17 ns et une fréquence de répétition de 50 Hz. La fluence du laser a été fixée à 4 J/cm^2 et la distance cible-substrat a été réglée à 5 cm. Avant chaque dépôt, la chambre a été évacuée à l'aide d'une pompe turbo (4×10^{-5} Torr). Les cibles étaient continuellement tournées et déplacées pendant le dépôt afin d'obtenir une ablation uniforme. La charge en Pt dans tous les cas était de 0,120 mg/cm^2 (mesurée par activation neutronique, NAA).

La morphologie de surface des échantillons a été examinée au moyen d'un microscope électronique à balayage (MEB) (JEOL, JSM 6300 F) fonctionnant à une tension d'accélération de 10 kV. La structure cristalline de tous les échantillons a été déterminée par diffraction des rayons X (DRX) à l'aide d'un diffractomètre Bruker D8 Advance équipé d'une source Cu Kα (λ = 1,5406

A). Le courant du tube était de 40 mA avec une tension de tube de 40 kV. Tous les diffractogrammes ont été acquis en mode de balayage de diffraction à incidence rasante (GID) avec un faible angle incident de 3° et une taille d'étape angulaire 2θ de 0,04° avec un temps d'acquisition de 5 s par étape. Des mesures de spectroscopie photoélectronique à rayons X (XPS) ont été réalisées pour déterminer la composition chimique des éléments de surface sur les échantillons et leurs états d'oxydation. L'étude a été réalisée dans un spectromètre VG Escalab 220i-XL équipé d'une source Al Kα (1486,6 eV). L'anode a été exploitée à 10 kV et 20 mA, et l'énergie de passage de l'analyseur a été fixée à 20 eV. Les échantillons ont été analysés avec une taille de spot de 150 × 800 µm située approximativement au centre de l'échantillon. Tout d'abord, des spectres d'ensemble dans la plage de 0 à 1350 eV ont été acquis, suivis de spectres d'analyse multiplex à plus haute résolution (niveaux de coeur Ti 2p, Pt 4f, C1s et O 1s). L'analyse des éléments a été effectuée avec le logiciel CasaXPS (Casa Software Ltd.) en ajustant les spectres de niveaux de coeur après une élimination du fond de Shirley. Le pic du niveau de coeur C 1s à 284,6 eV, résultant de contaminants d'hydrocarbures à la surface, a été utilisé comme référence interne. Tous les spectres ont été recalibrés par rapport au pic du niveau de coeur C 1s de la contamination par le carbone adventice.

L'acide sulfurique (H_2SO_4, 96 %) et l'éthanol (pureté à 100 %) ont été achetés auprès d'Agros Organics et Commercial Alcohols inc., respectivement. Les réactifs ont été utilisés tels quels sans purification supplémentaire. La caractérisation électrocatalytique a été évaluée par voltammétrie cyclique (VC) ou voltammétrie linéaire (LSV) dans une solution de H_2SO_4 à 0,5 M et dans un mélange de solutions de C_2H_5OH à 1 M + H_2SO_4 à 0,5 M par une cellule électrochimique conventionnelle à trois compartiments avec une électrode de référence Ag/AgCl, 4 M de NaCl, une bobine de platine comme contre-électrode, et des échantillons Pt/Ti et Pt/TiO_2/Ti comme électrodes de travail. Tous les potentiels dans ce travail sont cités par rapport à Ag/AgCl. Avant chaque mesure électrochimique, l'électrolyte a été désaéré en faisant passer de l'argon à travers la solution pendant 30 minutes. Ensuite, la surface des électrodes de travail Pt/Ti et Pt/TiO_2/Ti a été nettoyée et activée électrochimiquement dans une solution de H_2SO_4 à 0,5 M par plusieurs cycles de potentiel dans la plage de -0,2 à 1,3 V avec une vitesse de balayage de 50 mV/s jusqu'à ce qu'un état stable soit atteint. L'état stable est atteint (lorsque le dernier VC est presque identique au précédent) après environ 15 cycles de VC. Les mesures d'EOR ont été effectuées dans une solution de C_2H_5OH à 1 M + H_2SO_4 à 0,5 M avec des plages de potentiel de 0 à 1,0 V par rapport à Ag/AgCl à une vitesse de balayage de 5 mV/s (état quasi-stationnaire). Toutes les mesures électrochimiques ont été effectuées à température ambiante et les données ont été acquises par un potentiostat-galvanostat contrôlé par ordinateur (Autolab, PGSTAT 20, GPES).

L'objectif principal de cet article est de combiner la technique hydrothermale et la méthode de dépôt pulsé au laser (PLD) pour fabriquer des catalyseurs Pt tridimensionnels sur des réseaux de nanotiges de TiO_2 pour une EOR efficace. Les réseaux de TiO_2 sont préparés via une méthode hydrothermale acide en une étape en utilisant une feuille de Ti comme substrat et source de Ti. La concentration de HCl est variée pour faire pousser différentes morphologies de TiO_2. Les structures de TiO_2 bien adhérentes au substrat de Ti sont ensuite uniformément décorées avec le même chargement de films de Pt en forme de chou-fleur cultivés via la méthode PLD pour construire des catalyseurs 3D originaux. Tous les échantillons sont caractérisés par diffraction des rayons X (DRX), microscopie électronique à balayage (MEB) et spectroscopie photoélectronique à rayons X (XPS). De plus, la surface électroactive des électrocatalyseurs est obtenue par voltammétrie cyclique (VC) dans une solution de H_2SO_4 0,5 M. Les propriétés électrocatalytiques des réseaux de TiO_2 pour le Pt envers l'EOR sont étudiées via la voltamétrie linéaire (LSV) à l'état quasi-stationnaire dans un électrolyte de H_2SO_4 0,5 M + C_2H_5OH 1 M. L'électrocatalyseur Pt/TiO_2/Ti dans lequel le TiO_2 est constitué d'un mélange de nanofils et de nanotiges présente une surface électroactive supérieure et une activité spécifique de surface et une activité électrocatalytique significativement supérieures dans l'EOR par rapport à d'autres électrocatalyseurs, bien qu'ils aient le même chargement de Pt. L'optimisation de la concentration de HCl pour la synthèse du TiO_2 via la méthode hydrothermale combinée avec l'ablation laser pour la croissance du catalyseur au platine s'est révélée produire des structures d'électrodes prometteuses pour les technologies DEFC.

Chapitre 4 : Article 2: Résultats des nanotiges de Titane synthétisées sur une grille de Titane

Il existe une demande croissante de dispositifs légers, efficaces, abordables, durables et sûrs pour le stockage et la conversion d'énergie, répondant aux besoins des appareils électroniques portables de haute performance. La recherche actuelle se concentre sur des dispositifs électroniques flexibles et portables tels que les écrans enroulables, les diodes électroluminescentes, les montres intelligentes, les capteurs de condition physique et les capteurs implantables. Ces dispositifs nécessitent des sources d'alimentation à faible puissance avec des électrodes, des séparateurs et des substrats flexibles. Différents types de sources d'énergie légères sont en cours de développement, notamment des batteries Li-ion, des supercondensateurs, des cellules solaires, des piles à combustible et des bio-piles à combustible.

Les électrodes traditionnelles utilisées dans les sources d'énergie électrochimiques (EPS) contiennent des matériaux actifs, des liants polymères et des améliorants de conductivité. Cependant, ces composants ajoutent du poids et sont inadaptés à la flexibilité. La possibilité d'éliminer ces additifs et de fabriquer des électrodes flexibles sans liant ni additif représenterait une avancée significative. Les grilles métalliques basées sur le titane en tant que collecteurs de courant flexibles suscitent un vif intérêt en raison de leur flexibilité, de leur conductivité et de leurs structures tridimensionnelles (3D). Le TiO_2 est également étudié comme support de catalyseur dans les piles à combustible en remplacement du carbone.

Ce travail présente la première synthèse de nanotiges de Pt–TiO_2 en forme de cônes de pin en 3D sur des électrodes en treillis de Ti. Les propriétés structurales sont étudiées par microscopie électronique, diffraction des rayons X et spectroscopie photoélectronique. Les propriétés de transfert d'électrons sont évaluées pour la réaction d'oxydation de l'éthanol (ROE). En utilisant une approche innovante de croissance des matériaux, cette recherche vise à créer des électrodes flexibles de haute performance pour les technologies de piles à combustible direct à l'éthanol (DEFC).

Des treillis de titane mesurant 1,5 cm x 2 cm et ayant une épaisseur de 0,5 mm ont été soumis à un processus de nettoyage comprenant un bain ultrasonique d'acétone pendant 20 minutes. Après rinçage et séchage à l'air, ces treillis ont été soumis à une attaque chimique dans une solution d'HCl (18 %) à une température de 80 °C pendant 15 minutes. Cette opération était cruciale pour éliminer la couche native de TiO_2. Par la suite, les treillis de Ti ont été placés dans un autoclave en acier inoxydable en Téflon contenant une solution aqueuse d'HCl à 0,6 M. La synthèse hydrothermale a été réalisée à une température de 180 °C et a duré 10 heures. Les détails précis des conditions de synthèse peuvent être référencés dans notre publication antérieure.

Les films de platine ont été déposés sur les treillis de Ti et de TiO_2/Ti à température ambiante par la méthode de dépôt par laser pulsé (PLD), en utilisant une cible de platine pure. Les paramètres optimaux du dépôt par PLD ont été décrits dans nos publications antérieures. La morphologie de surface des matériaux a été analysée par microscopie électronique à balayage (SEM), tandis que la structure cristalline a été étudiée par diffraction des rayons X (XRD) et la composition de surface a été examinée par spectroscopie photoélectronique à rayons X (XPS).

Les propriétés électrochimiques des matériaux ont été étudiées par voltammétrie linéaire (LSV) dans des solutions d'H_2SO_4 ou de C_2H_5OH + H_2SO_4. Une cellule à trois électrodes a été utilisée, comprenant une électrode de référence Ag/AgCl (4 M NaCl), une bobine de platine

comme électrode auxiliaire, et des électrodes de travail Pt/Ti mesh ou Pt/TiO_2 arrays/Ti mesh. Toutes les mesures électrochimiques ont été réalisées à température ambiante à l'aide d'un Autolab PGSTAT 20.

Les réseaux de TiO_2 ont été synthétisés avec succès directement sur le treillis de Ti, formant une structure en nanotiges et en barres verticales. Le dépôt de Pt par PLD a produit une structure tridimensionnelle en forme de cônes de pin. Malgré une quantité de Pt similaire, la structure Pt/TiO_2 a montré une activité catalytique pour la réaction d'oxydation de l'éthanol (ROE) 4,4 fois supérieure à celle du Pt non supporté. De plus, la durabilité a augmenté de 6,6 fois par rapport au treillis Pt/Ti. Ces résultats suggèrent que de telles électrodes 3D sont prometteuses pour les piles à combustible, ouvrant des perspectives dans le domaine de l'électrochimie avancée.

Chapitre 5: Article 3: Résultats des nanotiges de Titane synthétisées sur un substrat de papier carbone

En raison de sa structure poreuse, de sa conductivité électrique élevée et de sa stabilité mécanique, le papier de carbone (CP) reste le principal substrat macroporeux pour les piles à combustible et d'autres dispositifs électrochimiques. Cependant, les supports en carbone sont sujets à la corrosion, affectant les performances. Le dioxyde de titane (TiO_2) est étudié comme alternative stable au carbone, bien que sa faible conductivité électrique soit un inconvénient.

Dans ce travail, nous proposons une nouvelle approche pour faire pousser directement des nanotiges de TiO_2 sur un substrat CP sans utiliser de modèles ou de liants. Nous utilisons la méthode de dépôt par laser pulsé (PLD) pour synthétiser une couche de semence de Ti sur le CP, sur laquelle des nanotiges de TiO_2 sont cultivées par une technique hydrothermale. Les nanotiges de TiO_2 ainsi obtenues sont caractérisées par microscopie électronique à balayage (SEM), diffraction des rayons X (XRD) et spectroscopie photoélectronique à rayons X (XPS). Ensuite, des films de Pt sont déposés par PLD sur les nanotiges de TiO_2/CP.

Nous évaluons les propriétés physiques et électrocatalytiques du Pt/nanotiges de TiO_2/CP pour l'oxydation de l'éthanol (ROE), une réaction importante pour les piles à combustible à l'éthanol. Les performances de cette configuration hybride sont également évaluées comme anode dans une pile à combustible directe à l'éthanol (DEFC) microfluidique sans membrane.

Une couche de semence de Ti a été cultivée sur le substrat CP (papier de carbone non traité) par la technique PLD pour produire des nanotiges de TiO_2. La PLD sous vide a été utilisée avec

un laser excimère KrF, produisant également une fine couche de TiO_2 sur le CP. Avant chaque synthèse, la chambre PLD a été évacuée, et les échantillons ont subi un nettoyage et une attaque chimique, suivis d'une procédure hydrothermale. Des films de Pt lisses et poreux ont été cultivés par PLD à température ambiante. Les conditions de dépôt ont été ajustées pour obtenir une morphologie souhaitée. La charge de Pt a été évaluée par analyse d'activation neutronique. Des échantillons de référence avec du Pt poreux ont également été déposés sur CP et (TiO_2)UV/CP.

La morphologie a été évaluée par MEB, la structure cristalline par diffraction des rayons X, et les états de surface par XPS. Les performances électrochimiques ont été évaluées par CV, LSV, et chronoampérométrie dans des solutions d'acide sulfurique et d'éthanol. Toutes les mesures ont été effectuées à température ambiante. La performance des électrodes a été testée dans une pile à combustible microfluidique sans membrane, alimentée avec une solution d'éthanol et d'acide sulfurique.

Fondamentalement, nous avons développé une nouvelle méthodologie pour cultiver des matériaux hiérarchiques de nanotiges de TiO_2 dans le but d'améliorer l'activité électrocatalytique et la durabilité des catalyseurs. Les nanotiges de TiO_2 ont été cultivées par la méthode hydrothermale à partir d'une couche de semence de Ti précédemment déposée par PLD sur un substrat CP conducteur. Ensuite, des films minces de Pt ont été déposés sur les nanotiges de TiO_2 par PLD pour créer une électrode structurée hybride 3D Pt/TiO_2-NRs/CP. L'électroactivité et la durabilité de cette électrode vis-à-vis de l'ROE étaient nettement supérieures à celles de l'électrode Pt/CP, y compris l'électrode composite commerciale au Pt. La couche de catalyseur préparée Pt/TiO_2-NRs/CP sans Nafion (l'ionomère conducteur de protons) et le PTFE (le liant) peuvent également réduire le coût des assemblages membrane-électrode dans la technologie des piles à combustible. En raison de l'utilisation courante du substrat CP et du TiO_2 dans de nombreuses applications électrochimiques, cette structure hybride TiO_2-NRs/CP pourrait également trouver des applications potentielles dans les piles à combustible, les piles à combustible microbiennes, la photoélectrochimie, les supercondensateurs et les batteries lithium-ion, pour n'en citer que quelques-unes.

7 CONCLUSIONS

En conclusion, cette thèse présente une exploration approfondie de la synthèse et de l'optimisation des films de TiO_2 en tant que support catalytique pour le Pt, notamment dans

l'électro-oxydation de l'éthanol, en lien avec les technologies de piles à combustible directes à l'éthanol (DEFC). La méthode hydrothermale acide utilisée pour la croissance des réseaux de TiO_2 directement sur une feuille de titane se révèle rentable, respectueuse de l'environnement et sans besoin de modèle. En variant la concentration d'HCl pendant la synthèse, diverses morphologies de TiO_2 ont été obtenues, allant des nanotiges et nanofils à des cristaux plus grands. L'augmentation observée de la taille cristalline avec une concentration d'HCl plus élevée, confirmée par des analyses SEM, diffraction des rayons X (XRD) et spectroscopie photoélectronique des rayons X (XPS), indique la possibilité de régler les structures de TiO_2. La performance catalytique des structures Pt/TiO_2/Ti, en particulier celles préparées avec 0,6 M d'HCl, se distingue par une activité spécifique d'aire et des activités massiques actuelles significativement plus élevées pour l'électro-oxydation de l'éthanol. Ce résultat prometteur, dépassant les catalyseurs Pt non supportés, suggère des applications potentielles dans les DEFC. Une exploration ultérieure implique la synthèse réussie de réseaux de TiO_2 directement sur une maille de titane, révélant un mélange de nanotiges en forme de fleur et de structures barres alignées verticalement. Le dépôt du catalyseur Pt sur ces structures donne une structure unique en 3D en forme de cône de pin, comme confirmé par des analyses SEM, XRD et XPS. Cette structure présente une activité catalytique améliorée et une durabilité supérieure par rapport aux électrodes Pt/CP, démontrant le potentiel de réduction des coûts dans les assemblages d'électrodes à membrane. La thèse se conclut en mettant en avant la méthodologie développée pour la croissance de nanotiges de TiO_2 hiérarchiques, soulignant l'activité électrocatalytique et la durabilité supérieures obtenues dans l'électrode structurée en 3D Pt/TiO_2-NRs/CP. Les applications potentielles s'étendent au-delà des DEFC, incluant les piles à combustible, les piles à combustible microbiennes, la photoélectrochimie, les supercondensateurs et les batteries au lithium-ion. Les découvertes contribuent au domaine plus large de la catalyse et des applications électrochimiques, ouvrant la voie à d'autres avancées et innovations dans les technologies de conversion d'énergie.

TABLE OF CONTENTS

LIST OF FIGURES

LIST OF TABLES

LIST OF ABBREVIATIONS

AFCs	Alkaline Fuels Cells
BE	Binding Energy
CA	Chronoamperometry
CE	Counter Electrode
CL	Catalyst Layer
CP	Carbon Paper
CV	Cyclic Voltammetry
CVD	Chemical Vapor Deposition
DEFCs	Direct Ethanol Fuel Cells
DFT	Density Functional Theory
DL	Double Layer
DMFCs	Direct Methanol Fuel Cells
ECSA	Electrochemical Active Surface Area
EOR	Ethanol Oxidation Reaction
ESA	Electroactive Surface Area
FC	Fuel Cells
FTIR	Fourier Transform Infrared Spectroscopy

FWHM	Full Width at Half Maximum
KE	Kinetic Energy
LSV	Linear Sweep Voltammetry
MA	Mass Activity
MEA	Membrane Electrode Assembly
NAA	Neutron Activation Analysis
ORR	Oxygen Reduction Reaction
PEM	Proton Exchange Membrane
PLD	Pulsed Laser Deposition
RF	Roughness Factor
SEM	Scanning Electron Microscopy
SOFCs	Solid Oxide Fuels Cells
TEM	Transmission Electron Microscopy
WE	Working Electrode
XPS	X-ray Photoelectron Spectroscopy
XRD	X-Ray Diffraction

1 INTRODUCTION

1.1 General introduction

One of the most significant cornerstones of our contemporary way of life is energy. It is essential to our daily lives because it fuels our cars, cooks our food, keeps us warm, cools us off, lights our nights, and links us to people close and far. Our energy consumption is largely derived from the combustion of fossil fuels, which primarily refer to petroleum (also known as crude oil), coal, and natural gas. Fossil fuels, as is generally known, are regarded as non-renewable resources since they do not replenish themselves sufficiently within a time frame that is relevant to people. It is an undeniable fact that they will eventually run out because of their limited reserves and the world's growing energy needs, and it is only a matter of time. According to British Petroleum, the world's proven reserves of oil, natural gas, and coal are only enough to last, respectively, 50.7, 52.8, and 114 years at the current production rate [1]. Burning fossil fuels has resulted in a wide range of environmental issues, including global warming, air pollution, acid rain, and other issues, aside from worries about the depletion of fossil fuels. The effects of these environmental catastrophes, particularly the global warming brought on by excessive CO_2 emissions, are devastating and will ultimately have an impact on all life on Earth, including humans. Energy-related CO_2 emissions have been forecasted by the U.S. Energy Information Administration (EIA) for the years 2012 through 2040 [2]. According to the research, CO_2 emissions will increase from 32.2 billion tons in 2012 to 35.6 billion tones in 2020 and 43.2 billion tons in 2040. Developing nations with a high population density, like China and India, contribute significantly to the expansion as a result of their rapid rise in energy demand. Due to their rapid rates of economic and population expansion, developing nations will account for over 60% of the world's main energy consumption by 2040. Due to their rapidly increasing energy demand, high population emerging nations like China and India contribute significantly to the rise. Due to their rapid rates of economic and population expansion, developing nations will by 2040 consume around 60% of the world's main energy.

A dynamic change occurs in the energy supply as a result of the rising energy demand, the depletion of fossil fuels, and the accelerating deterioration of the environment. It is becoming more diverse, allowing us to lessen our over-reliance on conventional methods that are inefficient and polluting, particularly the burning of fossil fuels. Exploring commercially feasible, clean, and

renewable energy is acknowledged as a long-term solution in this situation, and their development is already under progress. Figure 1.1 [3] illustrates the figure from the EIA's energy forecast report that indicates renewable energy is the fastest-growing energy source in the world, expanding at an average rate of 2.6 percent annually. These sources include geothermal, hydropower, biomass (bioethanol), solar, wind, and others. Each of them demonstrates its particular advantages and limitations. For instance, while there are plenty of energy resources available for solar and wind power, these sources are sporadic and geographically limited.

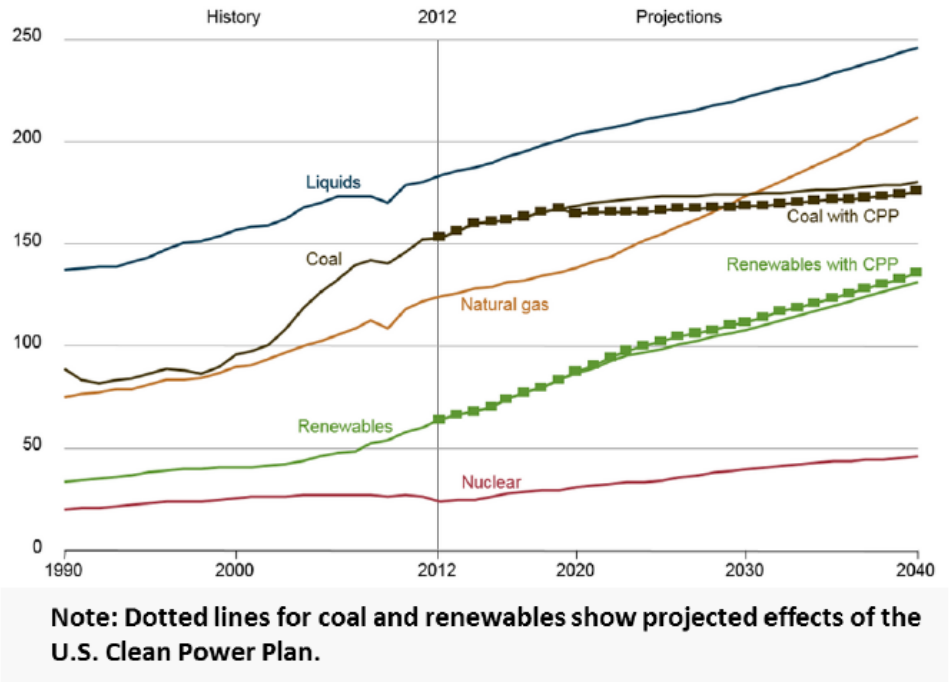

Figure 1.1 World energy consumption by energy sources, 1990-2040 (quadrillion Btu) [3].

Additionally, electrochemical energy sources, such as batteries, fuel cells (FCs), and electrochemical capacitors, seem potential as power sources for mobile, stationary, and automotive applications [4]. Due to their alluring qualities, including as fuel flexibility, high energy density, high efficiency, low to zero CO_2 emissions, and silent operation, FCs have attracted a lot of interest in recent decades. As scalable power plants, FCs have a variety of uses, including mobility, permanent prime/backup power, and portable electronics [5]. Fuel cell (FC) system revenue increased by almost $1 billion in 2014, reaching 2.2 billion in sales. The stationary distributed power that has been widely employed as the primary or backup power for residential and commercial operations remains the most profitable market for FCs as of 2014 approximately

10% of Fortune 500 firms presently employ fuel cells for stationary or motive power generation, according to the 2014 fuel cell technologies market report [6]. As of 2015, automakers like Honda, Hyundai, and Toyota began to provide fuel cell electric cars (FCEVs), which are now accessible to customers in various locations (the United States, Germany, France, the UK, South Korea, Canada), thanks in part to numerous governments' FC-support policies. The commercialization of FCEVs is expected to proceed more quickly as a result of the mass production of FCEVs and their rising use in the automotive industry. As for portable power application, micro-FCs from the size of thumbnail to handhold even to small-bread-box-scale are able to meet varying power requirements of various portable devices. To date, various businesses such as Intelligent energy UPP, MyFC, Brunton and Neah power systems, sell hydrogen cartridges and mini fuel cell units that can give you electricity on the move. Micro-FCs are anticipated to be the personal power source for the entire world in a disruptive long-term vision, freeing humans from dependence on electrical outlets and grids. Since the tiny fuel cell market is still in its infancy, we would need to witness both incremental and ground-breaking performance improvements to get to this point.

1.2 The background

What factors led to the aforementioned changes in FCs, and what are the biggest problems FCs are currently facing? First, we must comprehend the nature and operation of an FC.

1.2.1 What is a fuel cell?

A FC is a galvanic cell which, with the assist of catalysts, converts the chemical energy stored in a fuel directly into electrical energy through an electrochemical reaction between the fuel and an oxidant [5]. Taking the classic H_2/O_2 FCs as an example, in which H_2 gas is the fuel and O_2 gas serves as the oxidant. H_2/O_2 FCs overall reaction is similar to the straightforward combustion reaction of H_2, which is represented in equation 1.1.

$$Overall\ reaction\text{: } 2H_2 + O_2 \rightarrow 2H_2O + Energy\ (Heat\ or\ electricity) \qquad (1.1)$$

Exothermic reaction describes the combustion of hydrogen. H_2 in the atmosphere can be ignited to release energy in a chaotic explosion. H-H bonds and O-O bonds are specifically broken at the atomic level, whereas H-O bonds are produced when H_2 molecules and O_2 molecules collide. The energy difference between the initial and final states that is released via the aforementioned bonding reconfiguration processes can only be recovered as heat energy. Heat energy must first be transferred into mechanical energy, which must then be translated into electrical energy in order to create electricity. Because of the energy loss experienced during

each step and the heat engine's Carnot cycle restriction, the multi-steps (illustrated in Figure 1.2) have a significantly lower energy efficiency.

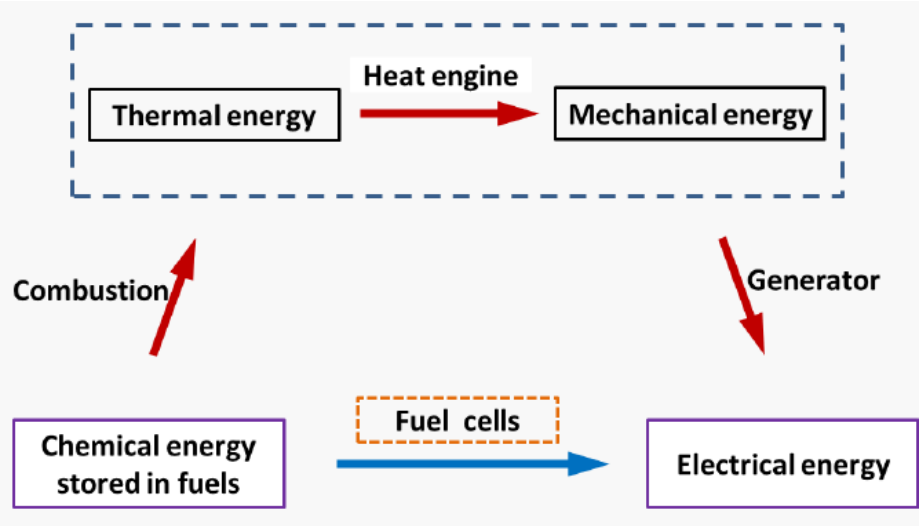

Figure 1.2 Graphical illustration of the difference in energy conversion between fuel cells and traditional combustion processes [7].

FCs, in contrast, provide a further method for utilizing electrons during the bonding reconfiguration processes between high-energy reactant and low-energy product, allowing for a more effective conversion of the chemical energy of the fuel into electricity. By using a membrane to keep two gases apart, FCs split the aforementioned overall reaction into two parts, requiring electron transport to finish the bonding reconfiguration occurring over a significantly prolonged length scale. In a nutshell, H_2 molecules lose electrons on one side (the anode), as shown in equation 1.2, to create protons that cross the membrane. As seen in equation 1.3, these protons form water on the opposite side (cathode) where they interact with O_2 molecules and gain electrons from the cathode.

$$Anode\ reaction: 2H_2 \rightarrow 4H^+ + 4e^- \quad (1.2)$$

$$Cathode\ reaction: O_2 + 4H^+ + 4e^- \rightarrow 2H_2O \quad (1.3)$$

In essence, both reactions on the two electrodes occur on catalyst surfaces, lowering the energy barrier of reactions and enhancing overall kinetics in the process. By utilizing the electrons as they move through an external circuit from the anode to the cathode, electricity can be generated. In FCs, the entire procedure does not include converting heat into mechanical energy, resulting in high conversion efficiency of up to 60%. When compared to the combustion reaction, this value is two to three times higher.

As demonstrated in the Ragone plot, FCs have a substantially higher energy capacity when compared to other electrochemical power sources (Figure 1.3). Because both FCs and batteries produce electricity through electrochemical reactions, they function similarly. However, when they produce electricity, which may be seen as the outer structures of factories that take fuels as raw materials and chunk out electricity as product, FCs are not consumed. In contrast to batteries, which require more time to recharge, they may continually and quickly produce power as long as fuel is continuously supplied.

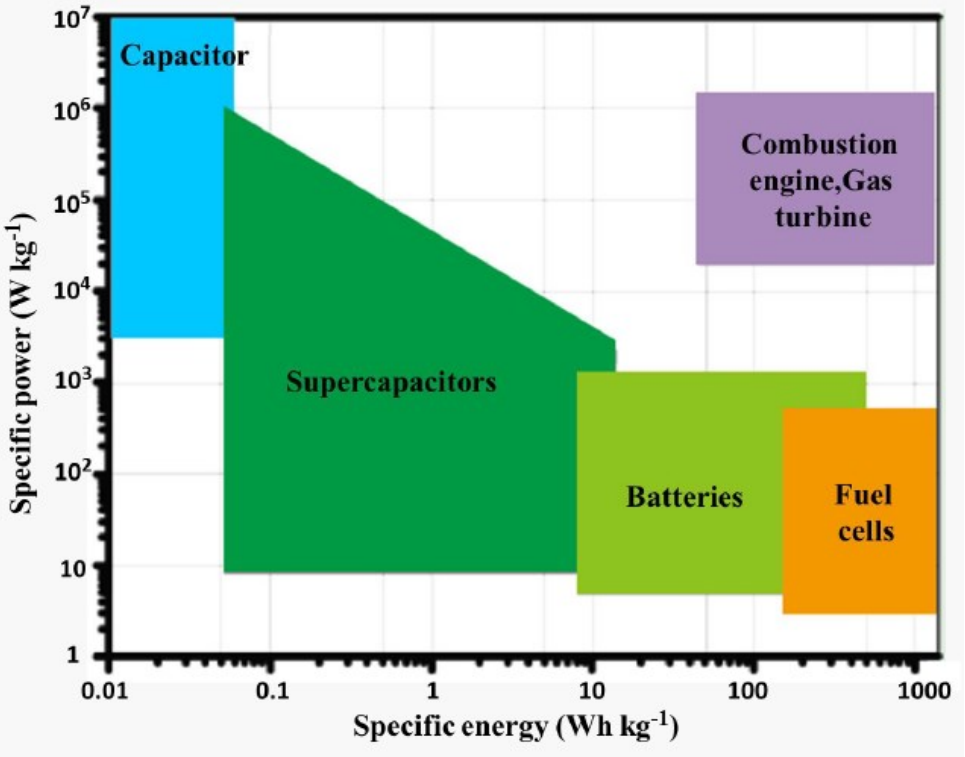

Figure 1.3 Ragone plot representing specific energy vs. specific power for traditional power source and electrochemical power sources [4].

1.2.2 Types of fuel cells

Many different FC kinds are currently being developed. The electrolyte used in individual cells is the most common way to categorize fuel cells, and there are five main types: solid oxide fuel cells (SOFCs), Polymer electrolyte membrane (PEMFC) fuel cells molten carbonate fuel cells (MCFCs), phosphoric acid fuel cells (PAFCs), and alkaline fuel cells (AFCs). The kind of electrochemical processes occurring in FCs, the kinds of catalysts that are suitable, the fuel needed, the operating temperature range, and other parameters are all influenced by the type of

electrolyte. Each form of FC's best-suited applications is determined by these qualities. Table 1.1 provides a quick synopsis of these five FCs.

PEMFCs are one of these five major groups of FCs, and because of their low operating temperature and quick start-up characteristics, they are seen to be one of the most promising power sources for portable and transportation applications [8]. The membrane electrode assembly (MEA), which comprises of two electrodes (anode and cathode) and a proton exchange membrane (such as Nafion ionomer) sandwiched in between, is a crucial component of PEMFCs. A fuel cell stack can be created by combining numerous MEAs to produce the needed electrical output. Fuels come in a variety of options, including gaseous H_2 or liquid H-rich organic compounds like methanol, ethanol, formic acid, and ethylene glycol, among others. Accordingly, PEMFCs can be further divided into H_2-PEMFCs [9], direct methanol FCs (DMFCs) [10, 11], direct ethanol FCs (DEFCs) [12], direct formic acid FCs (DFAFCs) [13], direct ethylene glycol FCs (DEGFCs) [14], and so forth based on the type of fuel utilized in the cell.

Table 1.1 The comparison of different types of FCs [8, 15].

Fuel cell type	Common Electrolyte	Operation temperature range (˚C)	Charge carrier	Electrode reactions	Applications
PEMFC	Solid polymer (Nafion)	50 – 100	H^+	Anode: $2H_2 \rightarrow 4\ H^+ + 4e^-$ Cathode: $O_2 + 4H^+ + 4e^- \rightarrow 2H_2O$	Backup power Portable power Transportation
SOFC	Yttria-stablized Zirconina (YSZ)	600 – 1000	O^{2-}	Anode: $H_2 + O^{2-} \rightarrow H_2O + 2e^-$ Cathode: $\frac{1}{2}O_2 + 2e^- \rightarrow O^{2-}$	Auxiliary power Electric utility Large distributed generation
MCFC	Molten salt consisting of a binary or ternary mixture of lithium, potassium and/or sodium carbonate	600 – 700	CO_3^{2-}	Anode: $H_2 + CO_3^{2-} \rightarrow H_2O + CO_2 + e^-$ Cathode: $\frac{1}{2}O_2 + CO_2 + 2e^- \rightarrow CO_3^{2-}$	Electric utility Large distributed generation
PAFC	Phosphoric acid soaked in a matrix	150 – 200	H^+	Anode: $2H_2 \rightarrow 4H^+ + 4e^-$ Cathode: $O_2 + 4H^+ + 4e^- \rightarrow 2H_2O$	Distributed generation
AFC	Aqueous solution of potassium hydroxide soaked in a matrix	60 – 90	OH^-	Anode: $2H_2 + 4OH^- \rightarrow 4H_2O + 4e^-$ Cathode: $O_2 + H_2O \rightarrow 4e^- + 4OH^-$	Military Space Backup power, transportation

1.2.3 Introduction of DEFCs

Due of ethanol's appealing qualities, DEFCs have gained a lot of interest in recent years [12, 16–18]. At normal room temperature and atmospheric pressure, ethanol is a liquid and, unlike hydrogen, is simple to handle, store, and move around. Ethanol is immediately oxidized rather than transformed into hydrogen gas in DEFCs. As can be seen in table 1.2, liquid fuels like ethanol have a much higher volumetric energy density than gaseous fuels such as H2, which makes the system more compact and offers a promising future as energy sources for portable electronic devices such as mobile phones, notebook computers, and portable power supplies. In addition, the use of liquid ethanol makes it possible to use existing gasoline infrastructure instead of spending significant costs to build hydrogen infrastructure.

Table 1.2 The Volumetric and gravimetric energy densities of different small organic fuels [19, 20]

Fuels	Volumetric energy density (kWh L^{-1})	Gravimetric energy density (kWh kg^{-1})
Hydrogen	0.18 (@1000 psi, 25 ^{0}C)	-
Methanol	4.82 (100 wt.%)	6.09
Ethanol	6.28 (100 wt.%)	8.00
Formic acid	1.75 (88 wt.%)	1.74 [21]
Ethylene Glycol	5.87 (100 wt.%)	5.3

Ethanol has many advantages over the most widely used liquid alcohol (methanol), including lower toxicity, a theoretically higher energy density, biocompatibility, and widespread availability from renewable biomasses like sugar cane, wheat, corn, straw, or even algae [22]. The world's first sustainable biofuels economy is found in Brazil, which is also regarded as a policy model for other nations and a leader in the bioethanol industry. Brazil produced 7093 million gallons of ethanol in 2015, ranking second in the world only to the United States [23]. Natural Resources Canada [24] reports that Canadian farmers cultivate millions of tons of crops annually that can be used to make bio-ethanol, a clean, renewable fuel, without harming the country's food supply. This makes Canada a country of renewable possibility. This enormous energy source equates to an annual supply of 436 million gallons of currently underutilized renewable fuels [23]. As a result, the development of DEFCs has a strong basis thanks to the bioethanol industry's explosive growth.

When it comes to how well ethanol performs in FCs, its oxidation kinetics at low temperatures are comparable to methanol's. However, ethanol has a lower permeability through

the Nafion membrane compared to methanol [18, 25]. As a result, ethanol exhibits a lower crossover rate (the speed at which ions or molecules pass through a membrane) than methanol and has a less significant impact on the efficiency of energy conversion.

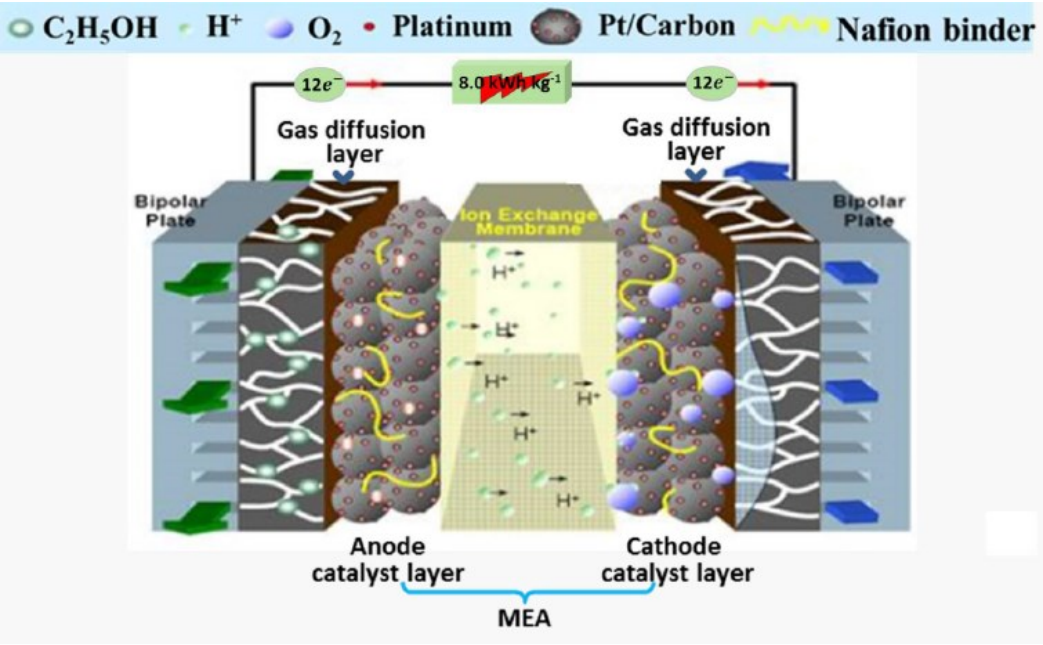

Figure 1. 4 Schematic diagram of a typical MEA in DEFCs [26].

The MEA with a sandwich-like shape is the key component of DEFCs, as it is with other PEM-based FCs [8]. A single MEA is made up of a proton-exchange membrane in contact with an anode and a cathode electrode on either side, as shown in Figure 1.4. The Nafion® membrane, manufactured by DuPont, is currently the most developed, commercially accessible, performance-durability membrane used for PEM-based FCs. This membrane is responsible for transferring protons generated from the anode to the cathode and spatially separating two electrodes. Catalysts are required for the anode and cathode electrodes in order for these reactions to take place faster (catalysts only accelerate reactions). The performance of the catalysts on the anode and cathode has a significant impact on the energy conversion efficiency of DEFCs. As of yet, Pt-based catalysts are thought to be the most effective and long-lasting catalysts for cathode and anode reactions, respectively.

The ethanol oxidation reaction (EOR) at the anode is a more intricate, multiple-electron mechanism than H_2 oxidation, as indicated in equation 1.4. The complete oxidation of ethanol results in the cleavage of C-H, C-O, and C-C bonds and produces 12 electrons, exceeding the 6 electrons in DMFCs and the 4 electrons in H_2-PEMFCs [27]. Gaseous O_2 is supplied to the

cathode of DEFCs in a similar manner as H_2-PEMFCs, and oxygen reduction reaction (ORR) takes place by mixing O_2 with the electrons and protons produced on the anode (equation 1.5) [22, 27]. The entire response of DEFCs is thus represented by equation 1.6, with the enthalpy change (ΔH^0), Gibbs free energy (ΔG^0), and equilibrium standard electromotive force (*emf*) of -1367.9 kJ mol^{-1}, -1326.7 kJ mol^{-1} and 1.145 V, respectively [22, 27].

$$Anode\ reaction: CH_3CH_2OH+3H_2O \rightarrow 2CO_2+12H^++12e^- \quad E^0=0.084\ V\ vs\ SHE \quad (1.4)$$

$$Cathode\ reaction: 3O_2 + 12H^++12e^- \rightarrow 6H_2O \quad E^0=1.229\ V\ vs\ SHE \quad (1.5)$$

$$Overall\ reaction: CH_3CH_2OH +3O_2 \rightarrow 2CO_2+3H_2O \quad E^0=1.145\ V\ vs\ SHE \quad (1.6)$$

Under reversible normal circumstances, the ratio between theoretical energy efficiency and the usable energy ΔG^0 and the total energy from the chemical reaction, ΔH^0, can be determined with equation 1.7.

$$\eta_{theo}= \frac{\Delta G^0}{\Delta H^0}\times 100\% = \frac{1326.7}{1367.9}\times 100\% = 97\% \quad (1.7)$$

However, the kinetics of ethanol oxidation are more challenging, resulting in a high overpotential and a poor current density despite the thermodynamic data of DEFCs being promising. Due to three principal potential losses, the cell voltage measured at a current density j during operation decreases below the equilibrium potential E^0 [28]. The definition of the real cell voltage E_{cell} is [28]:

$$E_{cell}= E^0-\Delta E_{acti}-\Delta E_{ohmic}-\Delta E_{conc} \quad (1.8)$$

where E_{acti} is the activation loss or activation overpotential caused by the need to move electrons and break/form chemical bonds in both EOR and ORR; E_{ohmic} is the ohmic loss primarily brought on by material and interface resistances; and E_{conc} is the concentration loss or concentration polarization brought on by the decrease in reactant concentration on both the anode and the cathode as they are consumed in reactions. Figure 1.5 is a typical DEFC polarization curve that highlights the potential losses mentioned previously. Due to the slow kinetic speeds of both EOR and ORR, activation loss is the primary source of the abrupt drop in potential that occurs at low current densities. More active catalysts are required on both electrodes in order to reduce activation losses. Pt-based catalysts have so far been widely used in DEFCs as catalysts for ORR and EOR [29]. Ohmic losses intensify as the current density increases to intermediate levels. Due to the mass transport limit of reactants that are accessible to the reactive sites in catalyst layers, as current intensity keeps rising, the cell voltage dramatically decreases.

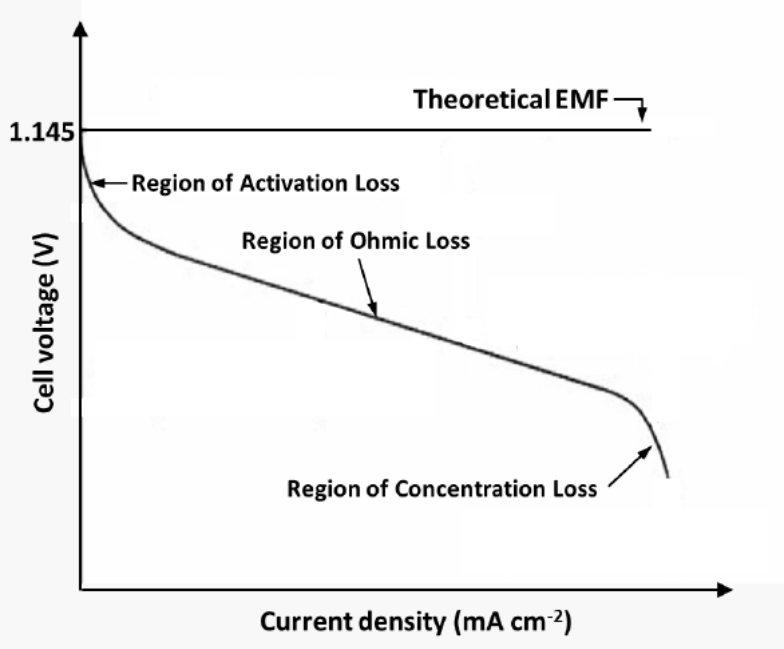

Figure 1.5 Schematic of an ideal polarization curve with the corresponding regions and overpotentials [28].

Therefore, the potential efficiency must be taken into consideration when calculating the overall efficiency of a DEFC. The potential efficiency is defined as follows:

$$\eta_{potential} = \frac{\text{Ecell}}{1.145} \times 100\% \qquad (1.9)$$

The actual energy efficiency of a DEFC is described as follows for the full oxidation reaction of ethanol to CO_2 under operational conditions:

$$\eta = \eta_{theo} \times \eta_{potential} = 97\% \times \frac{\text{Ecell}}{1.145} \times 100\% \qquad (1.10)$$

Given E_{cell} of a DEFC is 0.5 V, the energy efficiency is 42%.

However, there are still important difficulties that need to be resolved in addition to the aforementioned efficiency losses. For instance, the issue with the intricate EOR and ORR reaction processes that occur on the anode and cathode, respectively. On the anode, additional by-products including acetic acid and acetaldehyde are frequently produced by incomplete chemical pathways, resulting in a significant loss in energy efficiency, as opposed to complete oxidation to CO_2, which releases 12 electrons. H_2O_2 frequently forms on the cathode instead of H_2O, which further reduces energy efficiency. Another noteworthy issue is the ethanol crossover effect [17], albeit if less severe than methanol. Ethanol crosses through the polymer membrane to the

cathode, leading to the cathode having a mixed potential as both EOR and ORR taking place at the same electrode. As a result, the cathode potential gets lower, creating a further fall in the potential efficiency beside of the aforementioned three potential losses.

Therefore, the primary goals and working directions for the study and development of DEFCs become how to mitigate these efficiency losses. In a nutshell, it entails researching extremely effective, lasting catalysts for ORR and EOR as well as creating stable membranes with strong proton conductivity and low ethanol permeability. Pt-based catalysts have been created in the framework of the current work, primarily for the EOR in acid medium. However, it is also in our best interests to learn how this doctoral project's manufactured catalysts might be used in ORR.

1.3 Literature review

1.3.1 Introduction to anode catalysts for DEFCs

Catalysts have a big impact on how much DEFCs cost, perform, and last. Pt and Pt-based catalysts are the most often utilized and thoroughly researched anode and cathode catalysts for DEFCs operated in acidic medium [30-37] in terms of catalytic performance and durability. Due to the high cost and restricted supplies of Pt, lowering the loading of Pt in catalysts layer is of essential importance to overcome the cost barrier for the commercialization of DEFCs [37]. As a result, the most popular method for maximizing Pt use is to scatter nanostructured Pt catalysts on high-surface-area support materials like carbon black (for example, Vulcan XC-72) [38, 39]. To date, Vulcan XC-72 supported Pt is commonly employed as anode and cathode catalysts in DEFCs. Indeed, Vulcan XC-72 support considerably increases the catalytic activity of catalysts. While throughout long-term operation of FCs, it endures severe corrosion, producing the agglomeration, dissolution, and isolation of Pt nanoparticles, in turn considerably compromising the performance and durability of DEFCs [34, 40].

It is widely known that Pt as anode catalysts is particularly active towards C-H bonding cleavage and dissociative adsorption of ethanol, but it cannot accomplish the complete oxidation of ethanol to CO_2 releasing 12 electrons by effectively breaking C-O and C-C bonds at low temperatures. Through partial oxidation of ethanol (2-electron and 4-electron oxidation), unwanted by-products acetaldehyde (CH_3CHO) and acetic acid (CH_3COOH) are generated, respectively. The incomplete oxidation of ethanol not only lowers the energy efficiency due to fewer electrons exchanged relative to the complete oxidation reaction, but also gives rise to

acetate or (bi)sulfate that strongly adsorbs on the surface of catalysts and significantly affects the reactivity of the catalysts [41, 42]. In addition, Pt itself has little resistance to poisoning, since intermediate species such as CO_{ads} could be extensively adsorbed on its surface, poisoning the catalysts and thus leading to a sluggish reaction rate and potentially an irreversible deterioration of the catalytic performance [43].

To solve the foregoing issues in DEFCs, a considerable deal of work has been concentrated on researching multi-component catalysts in comparison to pure Pt, targeted to develop highly active, selective and durable catalysts. In recent years, various attempts have been made, such as mixing Pt with non-noble transition metals to generate binary/ternary catalysts, adding transition metal oxides to Pt to form nanocomposite catalysts. A complete literature review addressing the works on Pt-transition metal (Pt-M) and Pt-transition metal oxides catalysts is elaborated in the next section. According to the scope of this thesis, catalysts utilized in the acidic medium will be exclusively presented and addressed.

1.3.2 Ethanol oxidation on functional metal oxide–based catalysts

In addition to extensive studies on catalysts, much effort has been made to explore novel Pt-based catalyst by introducing diverse functional metal oxides (FMOs) such as CeO_2, SnO_2, MnO_2, TiO_2, WO_3, etc. As is well known, these FMOs are cheap and abundant compared with Pt, and thus the incorporation of high specific-surface-area FMOs could largely reduce the cost of catalysts. Furthermore, these FMOs also feature the following significant qualities qualifying for future uses in DEFCs:

1) High chemical and electrochemical stability under fuel cell operating conditions, reducing the agglomeration or coalescence of catalysts nanoparticles and thus increasing their durability.

2) The strong interaction of catalyst nanoparticles with oxide supports (metal-support interaction, SMSI) could immobilize catalysts nanoparticles on the surfaces of support materials, preventing from the growth and sintering of catalyst nanoparticles, and could also alter the electron distribution of catalysts enabling to diminish the CO poisoning effect [44].

3) Readily producing numerous hydroxyl (OH) groups on their surfaces, which might increase the catalytic performance on the basis of bifunctional mechanism [45].

It has been reported that FMOs in DEFCs function as support materials to boost the use of Pt, and/or as co-catalysts (promoter) to assist specific catalytic processes [39]. However, most

FMOs have a low electronic conductivity which might be increased by nano-structuring them or by mixing them with more conductive carbon materials to produce composites or by doping foreign elements. Nanostructured carbons, such as carbon nanotubes, graphene, mesoporous carbon, and others, are regarded as the main supports in composite materials. FMOs are considered as the secondary supports which are generally used to promote and modify the primary supports [9].

In the following portion, many FMOs are particularly chosen to be introduced in detail, including their structure, characteristics, emerging aspects pertinent to the DEFCs application, and the investigations conducted on various Pt-FMOs systems for ethanol oxidations and in this thesis our focus is on TiO_2.

1.3.2.1 TiO2–based catalysts

Titanium dioxide, also known as titanium (IV) oxide, is the naturally occurring oxide of titanium. Titanium dioxide occurs in nature in three main phases: rutile, anatase, and brookite, [46]. The unit cells of the three phases of TiO_2 are presented in Figure 1.6. Rutile phase is the most frequent natural form of TiO_2. Rutile has a body-centered tetragonal unit cell, with unit cell parameters a=b=4.584 Å, and c=2.953 Å. Six oxygen atoms form an octahedron around each titanium cation. The oxygen anions have a co-ordination number of 3 resulting in a trigonal planar co-ordination. Rutile also shows a screw axis when the octahedra are viewed sequentially [47]. Anatase crystallizes in the tetragonal system. The common pyramid of anatase, parallel to the faces of which there are perfect cleavages, has an angle over the polar edge of 82°9', the comparable angle of rutile being 56°52½' [48]. Brookite belongs to the orthorhombic dipyramid crystal class 2/m 2/m 2/m. The unit cell parameters are: a=5.4558 Å, b=9.1819 Å and c=5.1429 Å. The formula is TiO_2, with 8 formula units per unit cell (Z=8). The brookite structure is constructed up of distorted octahedra with a titanium ion at the center and oxygen ions at each of the six vertices. Each octahedron forms an orthorhombic shape when it shares three edges with neighboring octahedra [49]. The bandgaps of rutile and anatase TiO_2 are generally estimated to be 3.03 and 3.20 eV, respectively [50].

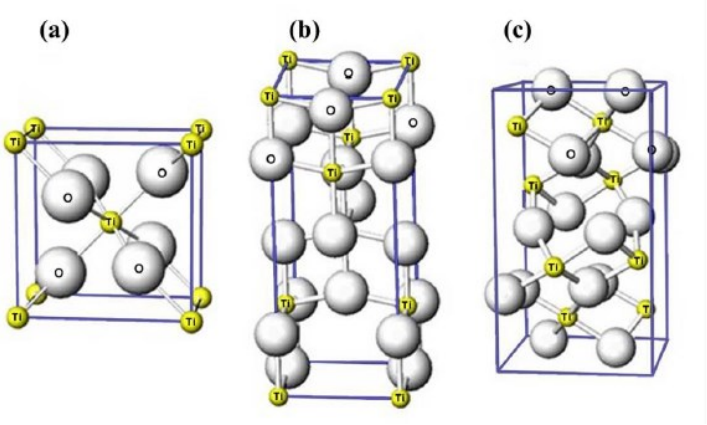

Figure 1.6 The crystal structure of TiO_2 in phase: a) Rutile, b) anatase, c) brookite.

For fuel cell application, nanostructured Ti oxides have been introduced to improve the performance either as membrane or as catalyst support or as catalyst itself. Pu et al. [51] review the numerous applications in each area. Under UV illumination, TiO_2 was shown to be an efficient photocatalysts for the degradation of organic pollutants present in different environments such as water or air, due to its strong redox activity [52]. Pt-TiO_2 electrodes were mostly discussed in the literature as photocatalysts for photo-electrochemical cells [46, 53]. Park et al. demonstrated a significantly increased MOR performance of Pt-TiO_2 nanostructure electrode under UV irradiation in comparison with that without UV illumination [54]. The authors attributed the remarkably enhanced performance under UV illumination to the photocatalysis of methanol oxidation by photo-generated holes in TiO_2. Hosseini demonstrated photocatalytic and UV-cleaning characteristics of Pt nanoparticle-decorated titania nanotubes (Pt-NPs/TNT) towards electrooxidation process of methanol [55]. Pt-NPs/TNT electrode was swept in 0.1 M H_2SO_4 +0.1M methanol aqueous solution for 250 cycles in the potential range of 0.0 -1.0V vs. SCE. Inevitably, the current density became decreased with rising cycle numbers, mostly due to the CO poisoning impact. After exposing the electrode to UV for 5 min, curiously, authors found that the cyclic voltammograms of Pt-NPs/TNT could revert to its original shape and magnitude, which was ascribed to the self-cleaning properties of TiO_2. Additionally, it was noted that the peak current density of MOR under UV illumination was almost 2.1 times greater than it was in the absence of UV irradiation. On the basis of the experiments and relevant literature, authors concluded that the electrooxidation of methanol on Pt-NPs and the photo electrooxidation of methanol on TiO_2 took place simultaneously under UV illumination and contributed to the enhanced peak current density in CV tests. Because TiO_2 is more durable than traditional carbon supports for ORR, it has also been suggested as a potential cathode [56–58]. Various

mechanisms have been discussed for the role of TiO_2 and the electrocatalytic activity of Pt-TiO_2 towards ORR. TiO_2 reduces Pt particle aggregation for cathodic electrodes and shields the Nafion membrane from peroxide radicals produced during ORR [58, 59].

On the other hand, some researches have reported that TiO_2 can boost the electrocatalytic activity of Pt towards methanol oxidation and ethanol oxidation in darkness by minimizing CO poisoning impact [60]. Kamat et al. observed that TiO_2 can increase the performance of the Pt–Ru catalyst for methanol oxidation without UV irradiation by minimizing CO poisoning effects [61]. Yu et al. synthesized composite anode catalyst (Pt/C+TiO_2) in a relatively easy manner by ultrasonically combining commercial Pt/C and TiO_2 nanoparticles, and influence of the size and the quantity of TiO_2 were examined [60]. Pt/C+TiO_2 electrocatalyst with 20 wt percent of TiO_2 particles (10 nm in diameter) demonstrated the greatest catalytic performance for ethanol oxidation which is substantially greater than the pristine Pt/C. The promoted catalytic performance of Pt/C+TiO_2 was ascribed to the presence of TiO_2 which could promote CO oxidative removal verified by CO stripping test, and the optimum content and size of TiO_2 which could guarantee an optimized TiO_2-Pt-C interfaces and good electronic conductivity for composite catalysts. The synergistic effect of Pt catalysts with sub micrometer-sized TiO_2 sphere support has been reported by Hua et al [62], which lowered the onset potential towards MOR and EOR compared with Pt supported by carbon black demonstrating enhanced reaction kinetics. By means of thermal decomposition of chloride precursors H_2PtCl_6 and $TiCl_3$ at high temperature, Hasa et al. prepared Pt-TiO_2 binary electrocatalysts with different Pt: TiO_2 molar ratios for EOR and MOR [63]. Pt (50 percent)-TiO_2 (50 percent) was found to be the optimal composition, which presented dramatically enhanced EOR and MOR activity than pure Pt. The formation of smaller Pt nanoparticles and their uniform dispersion were said to be encouraged by the addition of TiO_2, which was cited as the primary cause of the improved electrocatalytic performance of Pt-TiO_2 binary electrodes rather than the bifunctional effect.

1.3.3 Reaction mechanism of EOR

It is well known that the complete oxidation of ethanol leads to the breakdown of C-C bond and generates adsorbed CO species that are finally oxidized to CO_2. The whole process involves 12-electron transfer per ethanol molecule, giving rise to an energy density of 8.0 kWh kg^{-1}. However, under low temperatures, it was found that the breakdown of C-C bond is not easily accomplished on currently available Pt catalysts. Various intermediates (e.g. $CH_{x,ads}$, CO_{ads}, CH_3COH_{ads}) and products (e.g. CH_3CHO, CH_3COOH, CO_2 and methane) are formed through

numbers of parallel reactions, which largely lowers the exploitable energy density (8.0 kWh kg^{-1}) of ethanol. Therefore, a comprehensive understanding of the reaction mechanism for the oxidation of ethanol is valuable and critical for the designing of novel catalysts with high activity, selectivity, and stability.

In this context, numerous studies have been devoted to elucidating the reaction mechanism of ethanol oxidation by identifying the adsorbed intermediates and quantifying the reaction products and by-products [64, 65]. To achieve this, some traditional electrochemical methods, such as CV, CA and rotating disc electrodes (RDE) have been combined with other physicochemical techniques including *in situ* FTIR [66, 67], (on line) differential electrochemical mass spectrometry (DEMS) [66-68], high performance liquid chromatography (HPLC) [69], gas chromatography (GC) [70], *in situ* nuclear magnetic resonance spectroscopy (NMR) [71], and surface enhanced Raman spectroscopy (SERS) [72]. Furthermore, theoretical studies with DFT calculations have been conducted to provide a fundamental basis for the understanding of experimental observations and to give a further experimental guidance [73-76].

To date, it has been generally accepted that the major oxidation products during the EOR are CH_3CHO, CH_3COOH (acetic acid), and CO_2. The global mechanism of the ethanol electro-oxidation on Pt-based catalysts in acid medium can be simply represented as Figure 1.7, which is composed of several parallel reactions [64, 72]. The desired path leads to the formation of CO_2 exchanging 12 electrons during the entire process. It goes through the breakdown of C-C bond from ethanol or CH_3CHO, the generation of adsorbed intermediates $C1_{ads}$ which represent hydrocarbon fragments with one carbon atom (such as CO_{ads}, $CH_{x,ads}$ species), and finally the oxidation of $C1_{ads}$ intermediates to CO_2 with the aid of OH species [72]. However, it has been found that most of the ethanol molecules undergo partial oxidations on Pt electrodes, in which C-C bond is preserved forming CH_3CHO (or CH_3COOH) involving 2-electron (or 4-electron) exchange. Meanwhile, some CH_3CHO could re-adsorb on the surface of catalysts, and be further decomposed to form $C1_{ads}$ intermediates and eventually be oxidized to CO_2, or be directly oxidized to CH_3COOH which is found to be a dead-end product.

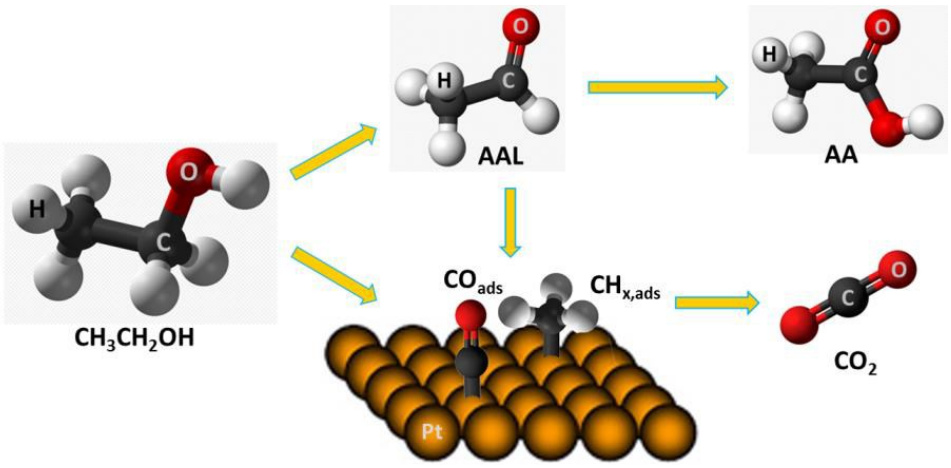

Figure 1.7 Schematic of the global reaction mechanism for the electro-oxidation of ethanol on Pt electrodes in acidic medium [64, 72].

The product yield of the EOR on Pt catalysts was found to be largely dependent on ethanol concentration [77, 78], electrode potential at which the reaction occurs. These studies allow us to improve our understanding on the reaction mechanism of EOR. Wang et al. investigated the effect of the ethanol concentration on product yields for carbon-supported Pt catalysts by combining on-line mass spectrometric analysis and electrochemical current measurements [78]. Under room temperature, it was found that ethanol oxidation to CH_3CHO was favored at high ethanol concentrations, whereas at low concentrations the formation of CH_3COOH prevailed. The yield of CO_2 was low at all concentrations ranged from 0.001 M to 0.5 M. By using FTIR, the results on polycrystalline Pt obtained by Camara et al., that are in accordance with that reported by Wang et al. [77]. At low ethanol concentrations (< 0.1 M), it was found that CH_3COOH was the main product, whereas CH_3CHO was not detected, and the yield of CO_2 was detected to be 6 times lower than that of CH_3COOH. When the ethanol concentration is above 0.1 M, the pathways generating CH_3COOH and CO_2 were significantly inhibited, probably owing to the limited availability of free sites for the H_2O adsorption, which is the O-donor in the formation reactions for CO_2 and CH_3COOH. When the concentration was increased over 0.2 M, the formation of CH_3CHO became dominant. Hitmi and coworkers found the same variation from CH_3COOH to CH_3CHO with the increase of ethanol concentration [70]. As for the electrode potential, Hitmi et al. have studied its effect on the production yield via chromatographic techniques (HPLC, GC) in 0.025 M ethanol + 0.1 M $HClO_4$ [70]. At potentials lower than 0.8 V vs. RHE, CH_3CHO was detected to be the dominant product. At potentials above 0.8 V where the dissociation of water was initiated to form oxygenated species, CH_3COOH became the major product.

1.3.4 Problematics of the electro-catalyst for EOR

Over the past decades, many advances have been made in increasing the performance of DEFCs [64]. Nevertheless, there are still some critical problems concerning the electro-catalysts to address, in particular difficulties from the development of anode catalysts, which are summarized as follows:

(i) The high cost of electro-catalysts. Platinum is scarce and expensive noble metal and the high loading of Pt in MEA is a critical obstacle limiting the commercialization of DEFCs [79];

(ii) Sluggish reaction kinetics at the anode;

(iii) The difficulties associated with ethanol complete oxidation to CO_2 and the C-C bond breaking. The partial oxidation of ethanol not only lowers the efficiency of entire fuel cell but also deteriorate the durability of catalysts due to the numerous poisoning intermediates;

(iv) The low durability of catalysts is another significant issue for the practical application of DEFCs. During long-term operation of DEFCs, electrochemical corrosion of support materials (e.g. Vulcan XC-72 and carbon nanotubes) leads to aggregation, dissolution, and isolation of catalysts, in turn resulting in the performance degradation of the entire DEFC [10].

1.3.5 The objectives of the thesis

As discussed in the problematics section, catalyst supports such as carbon-based materials used in fuel cell devices are expensive and prone to corrosion, which causes the detachment and/or aggregation of the catalyst. TiO_2 is cheap, non-toxic, exhibits a high mechanical resistance, very stable in acidic and oxidative environments. Our ultimate objective is to develop TiO_2 nanorods as an alternative catalyst support to conventional carbons in low-temperature DEFCs to improve catalyst dispersion and durability. Towards that aim, we will follow the subsequent sub-objectives:

1) Develop the acidic hydrothermal technique and optimize the processing parameters to synthesize on substrate TiO_2 nanorods using Ti foil and Ti mesh as substrates and a Ti source. Several synthesis parameters will be varied, including the concentration of HCl, time, temperature and solution volume.

2) Carbon paper (CP) constructed from a network of carbon fibers is still the principal product of the macroporous substrate for the gas diffusion layer (GDL) of proton exchange membrane fuel cells (PEMFCs). The second goal of this work is to synthesize TiO_2 nanorods on CP substrate without resorting to the use of templates or binders. We thus propose a new

approach that consists in first synthesizing via pulsed laser deposition (PLD) a Ti seed layer on CP. Above this Ti seed layer, hierarchically oriented TiO_2-nanorods are grown in one step via hydrothermal technique using the optimized processing parameters discovered in objective 1).

3) Optimize the pulsed laser deposition parameters to grow Pt nanoparticles (benchmark catalyst) onto TiO_2 nanorods/substrates (Ti foil, Ti mesh, carbon paper). The objective here is to fabricate hierarchical Pt/TiO_2 nanorods/substrate as advanced hybrid electrocatalysts. Thus, grown electrocatalysts will be subjected to ethanol electrooxidation reaction (OER) study in order to investigate the TiO_2-nanorods/substrate supporting properties on the electrocatalytic performance of Pt.

4) Fuel cell performance. The Pt supported TiO_2 nanorods structures that exhibit the best electrochemical performance towards EOR (objective 3) will be integrated in an air breathing micro direct ethanol fuel cells device to obtain current-voltage, power density and durability profiles. Finally, with the aim of comparing the competitiveness of our hybrid electrocatalysts, fuel cell performance comparison with the state-of-the-art composite Pt catalyst will be conducted.

REFERENCES

[1] BP. BP Statistical Review of World Energy 2016, London, BP, (2016) pp. 7 (oil), p. 21(gas), p. 31 (coal) http://www.bp.com/energyoutlook (Accessed November 7th, 2016).

[2] U.S. Department of Energy, U.S. Energy Information Administration (EIA), Independent Statistics & Analysis. International energy outlook 2016, Washington, DC, (2016) pp. 5 http://www.eia.gov/forecasts/ieo/ (Accessed November 7th, 2016).

[3] U.S. Department of Energy, U.S. Energy Information Administration (EIA), Independent Statistics & Analysis. International energy outlook 2016, Washington, DC, (2016) pp. 9 http://www.eia.gov/forecasts/ieo/ (Accessed November 7th, 2016).

[4] M. Winter, R.J. Brodd. Chem. Rev., 104 (2004) 4245-4270.

[5] G. Hoogers. Fuel cell technology handbook, CRC press, Boca Raton, FL, 2003.

[6] U.S. Department of Energy, Office of Energy Efficiency & Renewable Energy, Fuel Cell Technologies Office. Fuel Cell Technologies Market Report 2014, Washington, D.C, (2015) pp. 13 http://energy.gov/eere/fuelcells/market-analysis-reports (Accessed November 7th, 2016).

[7] S. Sun. DEVELOPMENT OF NOVEL NANOMATERIALS FOR HIGH-PERFORMANCE AND LOW-COST FUEL CELL APPLICATIONS PhD Dissertation in Mechanical and Materials Engineering (The University of Western Ontario, London, Ontario, Canada) (2011) 263 p.

[8] J. Zhang. PEM fuel cell electrocatalysts and catalyst layers: fundamentals and applications, Springer Science & Business Media, 2008.

[9] H.A. Gasteiger, S.S. Kocha, B. Sompalli, F.T. Wagner. Appl. Catal. B, 56 (2005) 9-35.

[10] S. Basri, S.K. Kamarudin, W.R.W. Daud, Z. Yaakub. Int. J. Hydrogen Energy, 35 (2010) 7957-7970.

[11] V. Neburchilov, J. Martin, H. Wang, J. Zhang. J. Power Sources, 169 (2007) 221-238.

[12] E. Antolini. J. Power Sources, 170 (2007) 1-12.

[13] X. Yu, P.G. Pickup. J. Power Sources, 182 (2008) 124-132.

[14] A. Serov, C. Kwak. Appl. Catal. B, 97 (2010) 1-12.

[15] A. Brouzgou, A. Podias, P. Tsiakaras. J. Appl. Electrochem., 43 (2013) 119-136.

[16] J. Friedl, U. Stimming. Electrochim. Acta, 101 (2013) 41-58.

[17] S. Song, P. Tsiakaras. Appl. Catal. B, 63 (2006) 187-193.

[18] M.Z.F. Kamarudin, S.K. Kamarudin, M.S. Masdar, W.R.W. Daud. Int. J. Hydrogen Energy, 38 (2013) 9438-9453.

[19] B. Pignataro. Ideas in Chemistry and Molecular Sciences: Advances in Nanotechnology, Materials and Devices, John Wiley & Sons, 2010.

[20] J. Zhang, H. Liu. Electrocatalysis of direct methanol fuel cells: from fundamentals to applications, John Wiley & Sons, 2009.

[21] C. Rice, S. Ha, R. Masel, A. Wieckowski. J. Power Sources, 115 (2003) 229-235.

[22] S. Badwal, S. Giddey, A. Kulkarni, J. Goel, S. Basu. Applied Energy, 145 (2015) 80-103.

[23] Renewable Fuels Association. World Fuel Ethanol Production. http://ethanolrfa.org/resources/industry/statistics/#1454098996479-8715d404-e546 (Accessed November 7th, 2016).

[24] Natural Resources Canada, Ethanol. http://www.nrcan.gc.ca/energy/alternative-fuels/fuel-facts/ethanol/3493 (Accessed November 7th, 2016).

[25] S. Song, W. Zhou, Z. Liang, R. Cai, G. Sun, Q. Xin, V. Stergiopoulos, P. Tsiakaras. Appl. Catal. B, 55 (2005) 65-72.

[26] C. Lamy, A. Lima, V. LeRhun, F. Delime, C. Coutanceau, J.M. Léger. J. Power Sources, 105 (2002) 283-296.

[27] C. Lamy, A. Lima, V. LeRhun, F. Delime, C. Coutanceau, J. Léger. J. Power Sources, 105 (2002) 283-296.

[28] C. Lamy, C. Coutanceau, J.M. Leger. Catalysis for sustainable energy production, (2009) 1-46.

[29] C. Lamy, E.M. Belgsir, J.M. Léger. J. Appl. Electrochem., 31 (2001) 799-809.

[30] E. Antolini. J. Power Sources, 170 (2007) 1-12.

[31] Y. Nie, L. Li, Z. Wei. Chem. Soc. Rev., 44 (2015) 2168-2201.

[32] A. Chen, P. Holt-Hindle. Chem. Rev., 110 (2010) 3767-3804.

[33] S. Song, P. Tsiakaras. Appl. Catal. B, 63 (2006) 187-193.

[34] M.Z.F. Kamarudin, S.K. Kamarudin, M.S. Masdar, W.R.W. Daud. Int. J. Hydrogen Energy, 38 (2013) 9438-9453.

[35] J. Friedl, U. Stimming. Electrochim. Acta, 101 (2013) 41-58.

[36] A. Brouzgou, A. Podias, P. Tsiakaras. J. Appl. Electrochem., 43 (2013) 119-136.

[37] A. Brouzgou, S.Q. Song, P. Tsiakaras. Appl. Catal. B, 127 (2012) 371-388.

[38] Y. Shao, J. Liu, Y. Wang, Y. Lin. J. Mater. Chem., 19 (2009) 46-59.

[39] Z. Zhang, J. Liu, J. Gu, L. Su, L. Cheng. Energy & Environmental Science, 7 (2014) 2535-2558.

[40] Y.-J. Wang, D.P. Wilkinson, J. Zhang. Chem. Rev., 111 (2011) 7625-7651.

[41] M.J. Prieto, G. Tremiliosi-Filho. Electrochem. Commun., 13 (2011) 527-529.

[42] F. Colmati, G. Tremiliosi-Filho, E.R. Gonzalez, A. Berna, E. Herrero, J.M. Feliu. Faraday Discuss., 140 (2009) 379-397.

[43] C. Lamy, A. Lima, V. LeRhun, F. Delime, C. Coutanceau, J. Léger. J. Power Sources, 105 (2002) 283-296.

[44] G.N. Vayssilov, Y. Lykhach, A. Migani, T. Staudt, G.P. Petrova, N. Tsud, T. Skála, A. Bruix, F. Illas, K.C. Prince, V.r. Matolı´n, K.M. Neyman, J. Libuda. Nat. Mater., 10 (2011) 310-315.

[45] S. Basri, S.K. Kamarudin, W.R.W. Daud, Z. Yaakub. Int. J. Hydrogen Energy, 35 (2010) 7957-7970.

[46] D. Reyes-Coronado, G. Rodríguez-Gattorno, M.E. Espinosa-Pesqueira, C. Cab, R.d. Coss, G. Oskam. Nanotechnology, 19 (2008) 145605.

[47] U. Diebold. Surf. Sci. Rep., 48 (2003) 53-229.

[48] D.A.H. Hanaor, C.C. Sorrell. J. Mater. Sci., 46 (2011) 855-874.

[49] L. Pauling, J.H. Sturdivant. Zeitschrift für Kristallographie-Crystalline Materials, 68 (1928) 239-256.

[50] D.O. Scanlon, C.W. Dunnill, J. Buckeridge, S.A. Shevlin, A.J. Logsdail, S.M. Woodley, C.R.A. Catlow, M.J. Powell, R.G. Palgrave, I.P. Parkin, G.W. Watson, T.W. Keal, P. Sherwood, A. Walsh, A.A. Sokol. Nat. Mater., 12 (2013) 798-801.

[51] P. Xiao, X. Guo, D.-J. Guo, H.-Q. Song, J. Sun, Z. Lv, Y. Liu, X.-P. Qiu, W.-T. Zhu, L.-Q. Chen, U. Stimming. Electrochim. Acta, 58 (2011) 541-550.

[52] T. Berger, D. Monllor-Satoca, M. Jankulovska, T. Lana-Villarreal, R. Gomez. ChemPhysChem, 13 (2012) 2824-2875.

[53] M.E. Kurtoglu, T. Longenbach, Y. Gogotsi. International Journal of Applied Glass Science, 2 (2011) 108-116.

[54] K.-W. Park, S.-B. Han, J.-M. Lee. Electrochem. Commun., 9 (2007) 1578-1581.

[55] M.G. Hosseini, M.M. Momeni. Electrochim. Acta, 70 (2012) 1-9.

[56] X. Liu, J. Chen, G. Liu, L. Zhang, H. Zhang, B. Yi. J. Power Sources, 195 (2010) 4098-4103.

[57] S. Siracusano, A. Stassi, E. Modica, V. Baglio, A.S. Aricò. Int. J. Hydrogen Energy, 38 (2013) 11600-11608.

[58] J. Shim, C.-R. Lee, H.-K. Lee, J.-S. Lee, E.J. Cairns. J. Power Sources, 102 (2001) 172-177.

[59] Y. Fu, Z. Wei, S. Chen, L. Li, Y. Feng, Y. Wang, X. Ma, M. Liao, P. Shen, S. Jiang. J. Power Sources, 189 (2009) 982-987.

[60] L. Yu, J. Xi. Electrochim. Acta, 67 (2012) 166-171.

[61] K. Drew, G. Girishkumar, K. Vinodgopal, P.V. Kamat. J. Phys. Chem. B, 109 (2005) 11851-11857.

[62] H. Hua, C. Hu, Z. Zhao, H. Liu, X. Xie, Y. Xi. Electrochim. Acta, 105 (2013) 130-136.

[63] B. Hasa, E. Kalamaras, E.I. Papaioannou, L. Sygellou, A. Katsaounis. Int. J. Hydrogen Energy, 38 (2013) 15395-15404.

[64] Y. Wang, S. Zou, W.-B. Cai. Catalysts, 5 (2015) 1507-1534.

[65] I. Kim, O.H. Han, S. Chae, Y. Paik, S.H. Kwon, K.S. Lee, Y.E. Sung, H. Kim. Angewandte Chemie International Edition, 50 (2011) 2270-2274.

[66] T. Iwasita, E. Pastor. Electrochim. Acta, 39 (1994) 531-537.

[67] Q. Wang, G.Q. Sun, L.H. Jiang, Q. Xin, S.G. Sun, Y.X. Jiang, S.P. Chen, Z. Jusys, R.J. Behm. Phys. Chem. Chem. Phys., 9 (2007) 2686-2696.

[68] H. Wang, Z. Jusys, R.J. Behm. J. Power Sources, 154 (2006) 351-359.

[69] S. Rousseau, C. Coutanceau, C. Lamy, J.-M. L´eger. J. Power Sources, 158 (2006) 18-24.

[70] H. Hitmi, E.M. Belgsir, J.M. Léger, C. Lamy, R.O. Lezna. Electrochim. Acta, 39 (1994) 407-415.

[71] L. Huang, E.G. Sorte, S.G. Sun, Y.Y.J. Tong. Chem. Commun., 51 (2015) 8086-8088.

[72] S.C.S. Lai, S.E.F. Kleyn, V. Rosca, M.T.M. Koper. J. Phys. Chem. C, 112 (2008) 19080-19087.

[73] F. Vigier, C. Coutanceau, A. Perrard, E. Belgsir, C. Lamy. J. Appl. Electrochem., 34 (2004) 439-446.

[74] L. Jiang, L. Colmenares, Z. Jusys, G.Q. Sun, R.J. Behm. Electrochim. Acta, 53 (2007) 377-389.

[75] R.M. Antoniassi, A. Oliveira Neto, M. Linardi, E.V. Spinacé. Int. J. Hydrogen Energy, 38 (2013) 12069-12077.

[76] A. Neto, M. Linardi, D. Anjos, G. Tremiliosi-Filho, E. Spinacé. J. Appl. Electrochem., 39 (2009) 1153-1156.

[77] A. Ferre-Vilaplana, C. Buso-Rogero, J.M. Feliu, E. Herrero. J. Phys. Chem. C, 120 (2016) 11590-11597.

[78] H. Wang, Z. Jusys, R.J. Behm. J. Phys. Chem. B, 108 (2004) 19413-19424.

[79] X. Teng. Materials and Processes for Energy: Communicating Current Research and Technological Developments, Formatex Research Center, (2013) 473-484.

2 EXPERIMENTAL METHODS

2.1 Synthesis of 1D TiO2 nanostructured materials

To create 1D TiO_2 nanostructures with a variety of morphologies, such as nanotubes, nanorods, nanowires, nanobelts, nanosheets, and nanofibers, numerous techniques have been devised. Six primary preparation techniques have been reported in the literature and will be briefly introduced in this section: hydrothermal, electrochemical anodization, vapor deposition, sol–gel, template-assisted, and electrospinning methods.

2.1.1 Hydrothermal method

The hydrothermal method is the most used method for the fabrication of 1D TiO_2 nanostructures. It is usually conducted in a stainless-steel vessel with high temperature and pressure. The hydrothermal method has attracted much attention due to its simple procedure and low production cost. Kasuga et al. reported the fabrication of TiO_2 based nanotubular materials by the hydrothermal method for the first time in 1998 [1,2]. In this process, amorphous TiO_2 powder was treated at high temperatures in a highly concentrated NaOH solution, and no sacrificial templates were needed. Since then, many investigations have been carried out on the synthesis of nanotubes, [3,4] nanorods, [5,6] nanowires, [7,8] nanobelts [9,10] and nanosheets [11,12] using the hydrothermal method, as shown in Figure 2.1. Obviously, the hydrothermal synthesis of 1D TiO_2 nanostructures is a well-established technique and near 100% conversion of the precursors to 1D TiO_2 nanostructured materials is achieved in one single process. The synthesis method can be divided into acid-hydrothermal and alkali-hydrothermal approaches according to the reactants used for the hydrothermal synthesis of 1D TiO_2 nanostructures [13]. In the former method, the reactants are usually titanium salts with hydrochloric acid.

The reaction normally leads to the formation of TiO_2 nanorods. The reactants in the latter method are generally TiO_2 nanoparticles using sodium hydroxide solution. Dissolution–recrystallization is always involved in this process and the products include nanotubes, nanowires, and nanobelts. These two methods have different reaction mechanisms, which produce different morphologies and crystalline phases of the product in the 1D nanostructures.

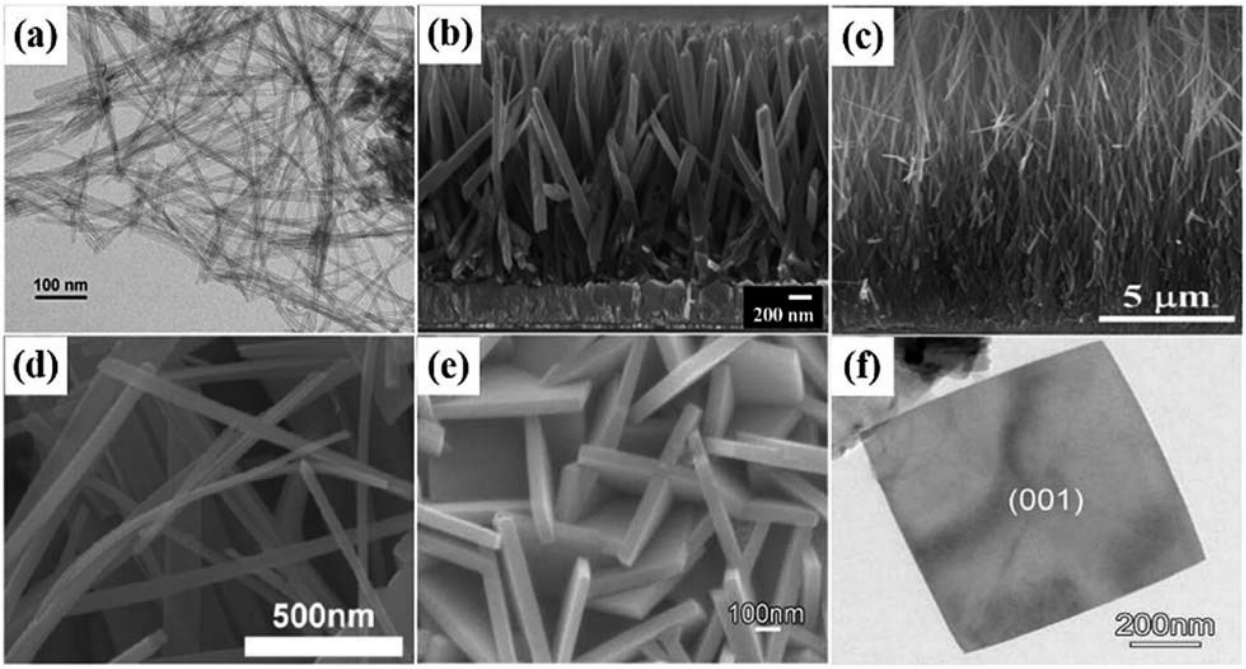

Figure 2.1 Different morphology types of 1D TiO_2 nanostructures synthesized by hydrothermal methods [4].

It is obvious that under particular hydrothermal conditions, TiO_2 in a variety of phases and morphologies can be converted to nanotubes. During the hydrothermal process, layer structured sodium titanate formed as an intermediate product on the surface of TiO_2 nanoparticles. Then, the Na^+ cations residing between the edge-shared TiO_6 octahedral layers can be replaced gradually by H_2O molecules. The size of intercalated H_2O molecules is larger than that of Na^+ ions, so the interlayer distance becomes enlarged, and the static interaction between neighboring TiO_6 octahedral sheets is weakened, causing the layered titanate particles to exfoliate to form nanosheets. To release the high surface tension, the nanosheets curl up from the edges to form TiO_2 nanotubes [14,15]. The dominant driving force for this curving process is still in discussion. Besides, hydrothermal conditions such as the type of precursor (TiO_2 nanoparticles or metal substrates), the type and concentration of the reaction solution, temperature, time, etc. have an important effect on the structures and morphologies of TiO_2. Morgan et al. investigated the effect of concentration of NaOH solution and temperature on nanostructure formation from Degussa P25 through alkaline hydrothermal treatment [81]. As shown in Figure 2.2, different morphologies and structures of TiO_2 can be transferred from each other by adjusting the hydrothermal conditions.

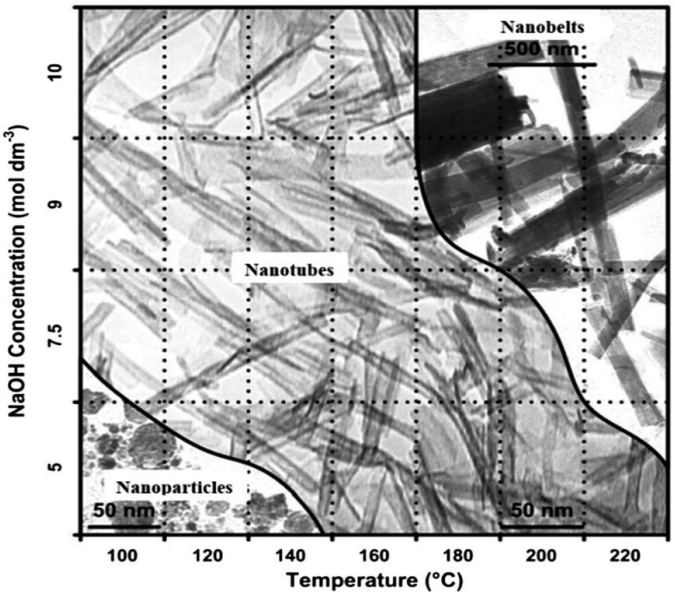

Figure 2.2 Morphological phase diagram of Degussa P25 evolution indicating regions of nanostructure formation after 20 h of hydrothermal treatment. Reproduced from [16].

Besides, Tanaka and Peng et al. investigated the effect of concentration of NaOH solution, temperature and reaction time on nanostructure formation by using a Ti substrate as a precursor through alkaline hydrothermal treatment [17,18]. Their results are consistent with the ones obtained by Morgan et al. There are some disadvantages in the conventional hydrothermal method. First, slow reaction kinetics result in long reaction time. Second, the short length of the nanotube's limits. their wide applications. Third, nanotubes are non-uniform on a large-scale. Various approaches, such as ultrasonication assisted, microwave-assisted, and rotation-assisted hydrothermal methods, have been explored to solve these problems. In particular, Tang et al. grew elongated titanate nanotubes with length up to tens of micrometers by a stirring hydrothermal method (Figure 2.3), [19,20] which has a major breakthrough on the development process of TiO_2 nanotubes. They obtained uniform nanotubes with a high aspect ratio by optimizing the stirring rate. This method has resulted in 1D TiO_2-based nanotubular materials for long-life and ultrafast rechargeable lithium-ion batteries.

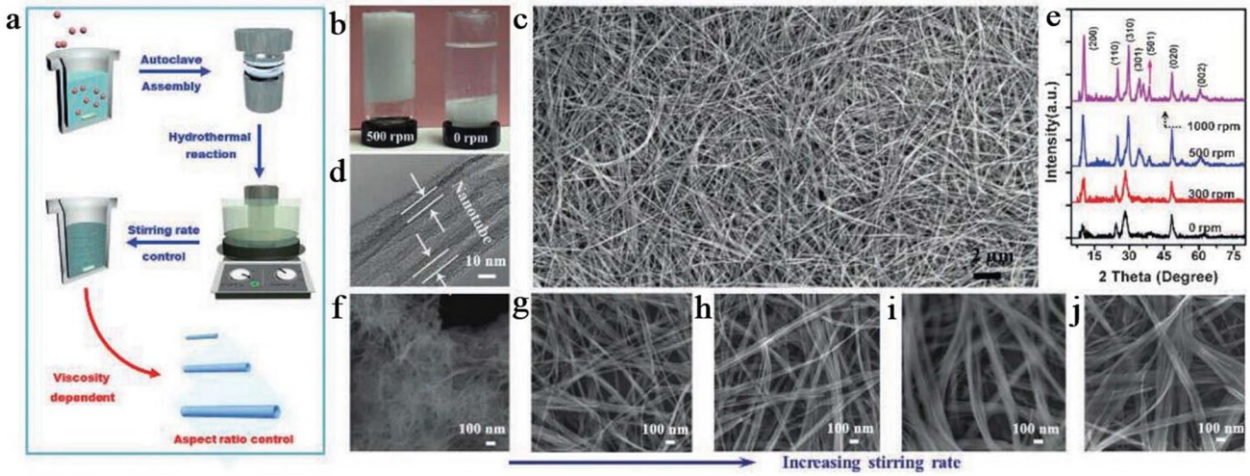

Figure 2.3 Fabrication and characterization of titanate nanotubes with different aspect ratios [19,20].

2.1.2 Solvothermal method

The solvothermal method is also a common synthesis approach used for the fabrication of 1D TiO_2 nanostructures [21–23]. It is similar to the hydrothermal method which is usually conducted in a stainless-steel vessel with high temperature and pressure. In addition, these two methods generally use TiO_2 nanoparticles, $TiCl_4$ or tetrabutyl titanate as the precursor. However, the solvothermal method is usually conducted in an organic solvent (ethanol, ethylene glycol, n-hexane, etc.), while the hydrothermal method usually reacts in water solutions [24,25]. Wang et al. synthesized a bundle of nanowires and open-ended TiO_2 nanotubes by the solvothermal method using ethanol and glycerol as solvents, respectively (Figure 2.4 a and b) [26]. The obtained 1D TiO_2 nanostructures were found to exhibit a favorable discharge performance as anode materials in the application of lithium-ion batteries. What's more, anatase-type nitrogen–fluorine (N–F) co-doped TiO_2 nanobelts were prepared by a facile one-step solvothermal method (Figure 2.4 c). And the composites showed much higher photocatalytic degradation activity than TiO_2 nanoparticles [27]. Besides, Zhao's group successfully fabricated vertically aligned TiO_2 nanorods by the solvothermal method for preparing photoanodes for dye-sensitized solar cells and discussed the effect of thermal treatment on their performances (Figure 2.4 d). It was found that the annealed TiO_2 nanorods showed increased power conversion due to improved crystallites [28]. Compared to the hydrothermal method, how to choose appropriate solvents is the key for the solvothermal method, which also limits its wide applications.

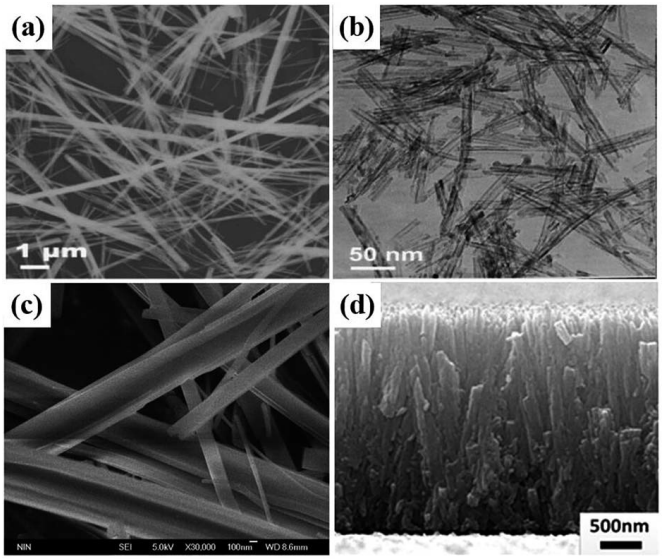

Figure 2.4 SEM images of various TiO_2 morphologies synthesized by the solvothermal method: (a) nanowires, (b) nanotubes, (c) nanobelts, and (d) nanorods [24].

2.1.3 Electrochemical anodization method

1D TiO_2 nanotube arrays (TiO_2 NTAs) can be synthesized by a facile electrochemical anodization method on a Ti metal substrate. Compared to other 1D TiO_2 nanostructured materials, TiO_2 NTAs are excellent photoanode materials that have been used for a long time because they are stable, non-toxic, environmentally friendly, inexpensive, recyclable and easily synthesized. The first report on anodized TiO_2 dates back to 1984, Assefpour-Dezfuly et al. produced porous TiO_2 by performing etching in alkaline peroxide first, followed by anodization in chromic acid [29]. As presented before, Zwilling and co-workers reported on the formation of nanoporous anodized titania in fluoride containing electrolyte in 1999, making a breakthrough of work undertaken on porous/tubular anodized Ti over the last two decades [95]. Since then, much effort has been made to optimize experimental parameters with different electrolytes in order to efficiently achieve high quality self-organized TNAs. Categorized into 5 generations (Figure 2.5), highly ordered anodic TiO_2 nanotube arrays with long nanotubes have been realized, and the development is still ongoing. In general, the type of electrolyte, pH, applied potential, time and temperature affect the morphology and structure of TiO_2 NTAs. Hydrofluoric acid-based water aqueous electrolytes are most widely used in titanium anodization to produce TiO_2 nanostructures. However, the length of nanotubes is only a few hundred nanometers. In F -based inorganic and organic neutral electrolytes, much longer and smoother nanotubes could be grown. The anodization voltage

influences the morphology of formed nanostructures, while the anodization time mainly affects the length of TiO_2 nanotubes. The temperature of the electrolyte affects the dissolution rate. As a result, TiO_2 NTAs are normally grown at 20–25 C (room temperature). Appropriate selection of anodization parameters for the TiO_2 NTA fabrication is key to the successful growth of high-quality nanotubes.

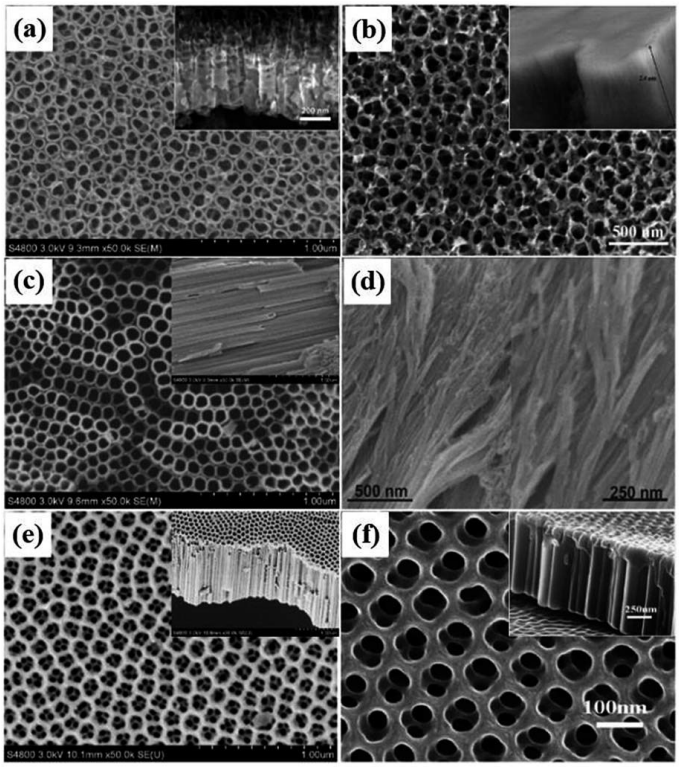

Figure 2.5 SEM images of the 1st generation in the HF electrolyte [30].

2.1.4 Chemical vapor deposition method

Chemical vapor deposition (CVD) has been developed to construct high-quality 1D TiO_2 nanostructures. 1D TiO_2 nanostructures formed on a silicon substrate coated with Ti or $TiCl_4$ in a sealed chamber at high temperature. Du et al. have grown uniform TiO_2 nanowires via the CVD method using $TiCl_4$ as the source reagent (Figure 2.6a) [31]. Chen and H_{oa} et al. successfully synthesized nanorods and nanobelts by the CVD method (Figure 2.6 b and c) [32,33]. However, stringent experimental conditions and high costs put a limit to their wide production.

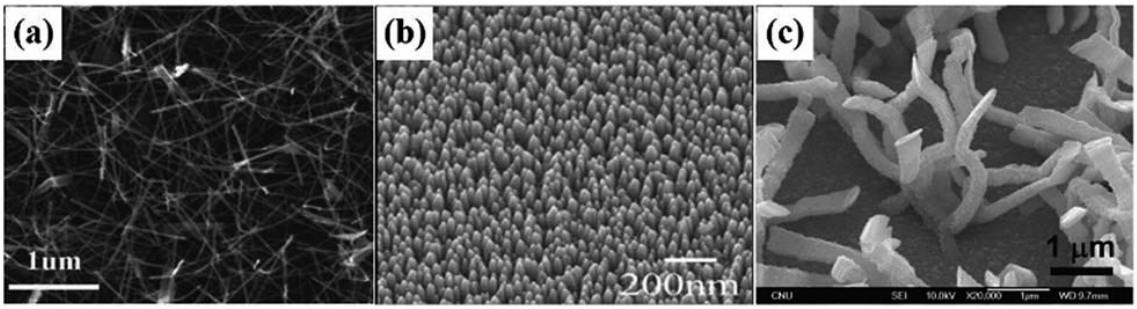

Figure 2.6 SEM images of nanowires (a), nanorods (b) and nanobelts (c) prepared by chemical vapor deposition. Reproduced from [31].

2.2 Synthesis methods

2.2.1 Pulsed laser deposition (PLD)

PLD, also called Laser Ablation Deposition (LAD), is a physical vapor deposition technique for producing thin films. Smith and Turner utilized this method for the first time in 1965 [34].

2.2.1.1 Single-beam PLD

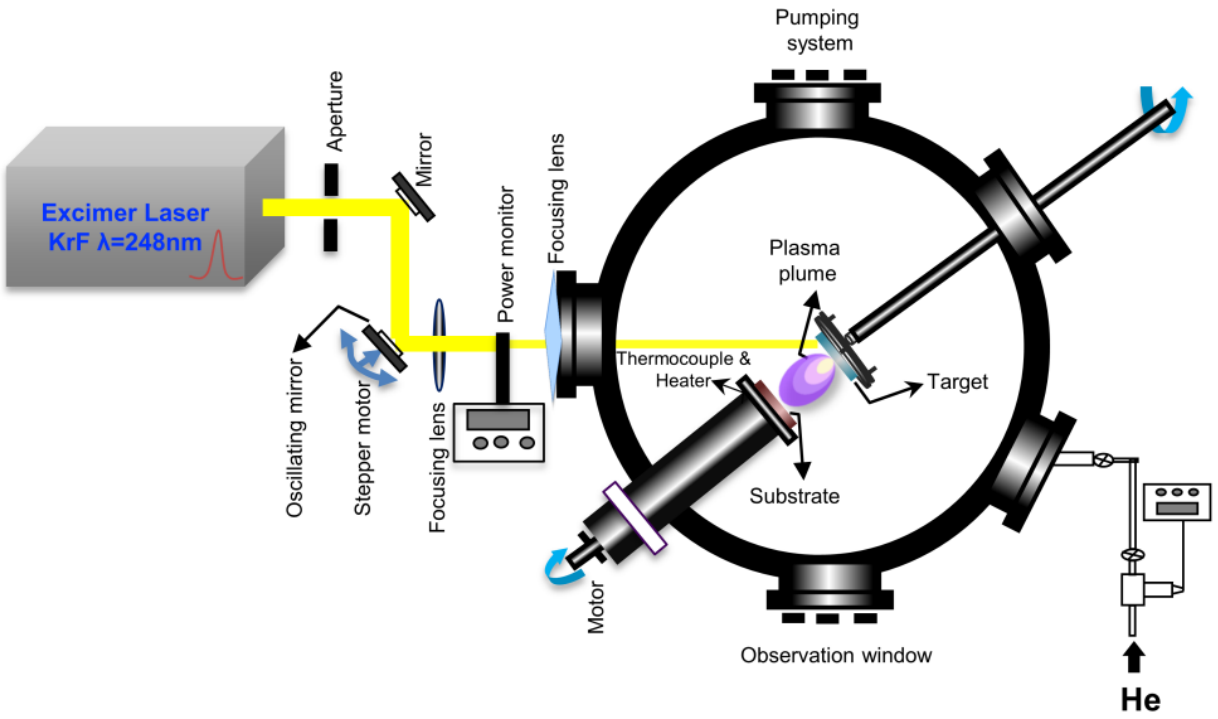

Figure 2.7 Schematic diagram of single beam PLD set-up.

In Figure 2.7, a solid or liquid surface (referred to as the "target") is illuminated by a high-power ultraviolet (UV) pulsed laser beamed via a quartz window and focused by a quartz lens. The material will be heated to its melting point locally at a specific power density and laser pulse duration, then it will quickly melt, evaporate, and eject a brilliant plasma plume from the target. The plume is then gathered on the substrate, where film begins to develop. You can vacuum the chamber or fill it with inert or reactive gas. Typically, the target rotates continuously to prevent being ablated at the same location repeatedly.

One of the adaptable and effective tools for creating high-quality thin films is PLD. Using PLD to grow thin film has a lot of benefits:

- Simple growth and setup procedures.
- Due to the flexibility of wavelength and power density, almost any type of material, including complex oxides, nitrides, carbides, and borides as well as polymer-metal composites, can be ablated.
- For the majority of ablated materials, the desired composition (stoichiometry) can be transferred congruently [35].
- The quantity of laser pulses may be accurately regulated to determine the film's thickness [36].
- It is possible to create multi-layer films with various compositions.
- Versatility. By manipulating the deposition conditions (chamber pressure, reactive or passive gases, target-substrate separation distance, number of pulses), as well as the laser beam parameters (wavelength, pulse duration fluence, and laser density), it is possible to create films with a variety of morphologies, structures, and functionalities [37].

Today, UV-emitting excimer lasers like KrF (248 nm), ArF (193 nm), and F_2 (157 nm) are widely utilized in PLD. Due to its shallow material penetration and ability to remove only atoms close to the surface, UV light is recommended. Longer wavelengths have the potential to penetrate further, resulting in eruptions and subsurface evaporation that may cause larger clusters to be expelled [38].

2.2.1.2 PLD mechanism

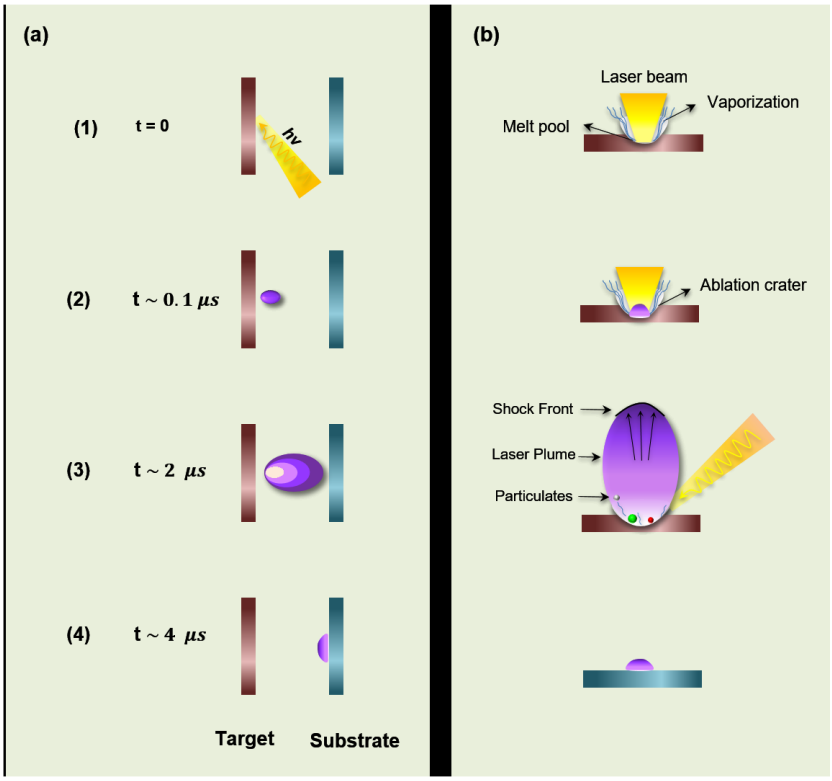

Figure 2.8 The four PLD stages (a) Time evaluation of PLD deposition processes (b) Corresponding physical phenomena of material removal and deposition

In contrast to the ease of system setup, the PLD principle is a tremendously complex physical phenomenon. The impact of the high-power pulsed radiation on a solid target involves all of the physical processes of laser-material interaction. In addition, it entails the production of the plasma plume from highly energetic species, the subsequent passage of the material that has been ablated through the plasma plume onto the heated substrate surface, and the final film-growth procedure. There are normally four PLD stages to the PLD process (Figure 2.8) [39].

Electromagnetic radiation, which may be visualized as an electric vector field and magnetic field, is what a laser beam is fundamentally (Figure 2.9).

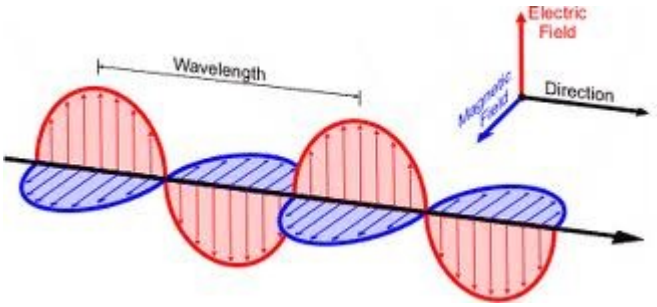

Figure 2.9 the electromagnetic radiation's electric and magnetic field vectors.

An electromagnetic wave's electronic field amplitude, E, can be calculated as follows:

$$\boldsymbol{E}=\sqrt{(2\Phi/cn\varepsilon_0)} \qquad \text{Eq. (2.1)}$$

where, Φ is the power density; ε_0, the permittivity of free space, c, the velocity of light; n, the refractive index. Normally, when power density of laser is greater than 2 × 108 W cm^{-2}, atomic excitation and ionization take place.

The incident laser causes the nuclei's lattice and electrons to vibrate as it hits the target. Some laser may be reflected, some refracted, some scattered or transmitted, and some may be absorbed during interaction. The excess energy of the electrons, such as the kinetic energy of the free electrons and the excitation energy of the bound electrons, is caused by the absorbed laser [40]. When free electrons oscillating in the laser beam's electromagnetic field clash with excited and ground-stated neutrals, some of their energy is transmitted to the lattice and heat is produced [41]. The heated surface is the objective. The substance begins to melt, boil, vaporize, and ionize when the temperature hits the melting threshold, creating a solid-liquid barrier at the surface.

The first incoming pulse initiates a large number of smaller clusters when the plume species impact the ground. These subcritical clusters have a tendency to split into mobile species that will form new clusters of various sizes when no vapor is present. With the exception that some of the mobile atoms will now reach already created clusters, the following pulse will start the identical process once more [42]. Between1× 10^{-3} to 1Å can be found in the deposition rate per laser pulse. The substrate experiences nucleation and film growth processes when the condensation rate is greater than the rate at which particles reach the substrate [43]. Typically, there is a considerable difference between the energy of the atoms and aggregates on the substrate surface and the energy of the arriving species. These energies are influenced by a number of key factors,

including the substrate characteristics, background gas pressure, and the target-to-substrate distance D_{ts} [44]:

• **Substrate,** including its composition, temperature, and translation and rotation

• **Background gas pressure**. When material is ejected into space at high speeds and energy, it can damage a surface by sputtering atoms from previously deposited layers or generate defects such dislocations, fissures, and holes [45]. The layers that are deposition are compact thin films at low pressure. Due to sputtering from the substrate, the deposition rate initially rises with an increase in gas pressure, reaches a maximum, and then declines once more.

• **Target-to-substrate distance D_{ts}**. When the plasma length is equal to the target-to-substrate separation distance, the optical position is attained, resulting in a uniform, homogeneous film with stoichiometric structure.

PLD produces thin films with substantially less uniform thickness than a thermal evaporation source with an equivalently small surface area, as seen by the cos and cos thickness distributions, respectively [43]. Typically, the deposition area is only a few square centimeters. It was discovered that adding an inert background gas (Ar) significantly reduced the flux of ions, lessening the internal stress of the films and preventing blistering. The creation of superior, uniform, blister-free thin films is the last step.

2.3 Characterizations of the structural properties of electrode materials

This section covers the many physical methods used to characterize the morphology and microstructure of the electrode materials created for this research. Scanning electron microscopy (SEM), X-ray diffraction (XRD), and X-ray photoelectron spectroscopy are the main techniques for characterizing materials (XPS). Additionally, Neutron Activation Analysis (NAA) was employed for measuring the mass loading (g cm^{-2}) of Pt on the deposits.

2.3.1 Scanning electron microscopy (SEM)

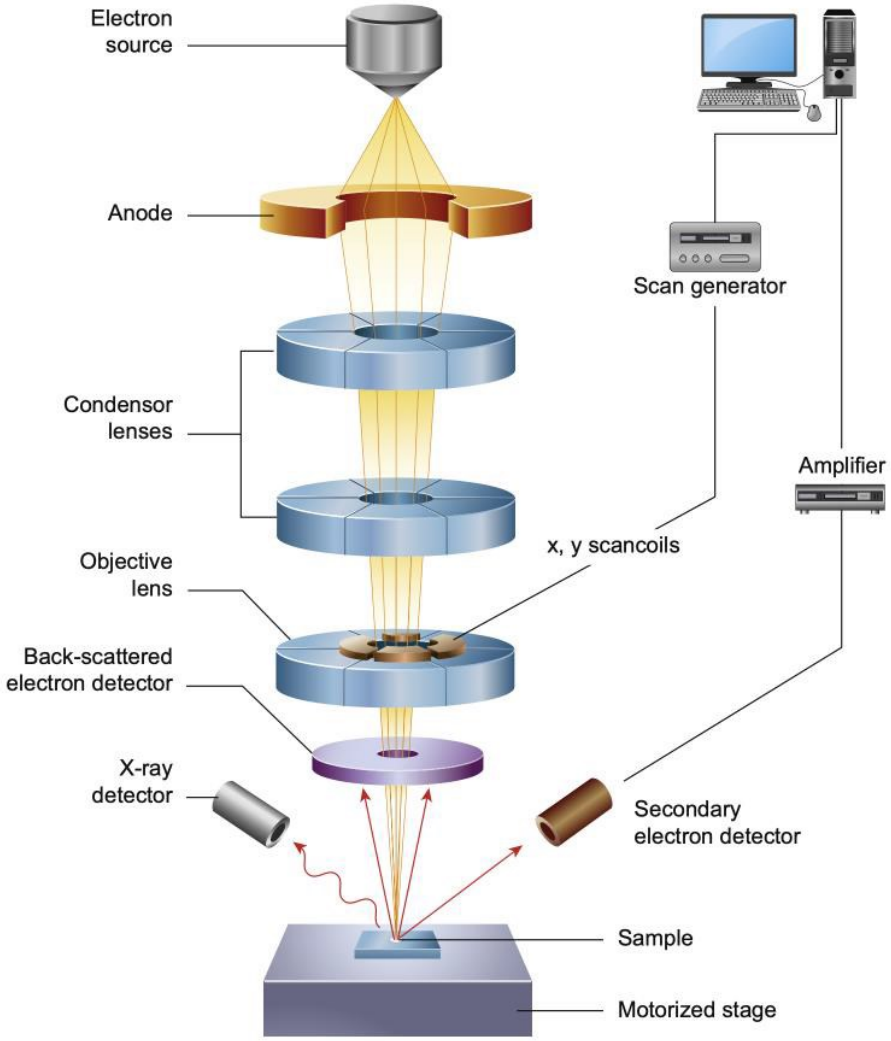

Figure 2.12 the SEM microscope's schematic representation of its essential parts [49].

For study of the specimen surface, scanning electron microscopy (SEM) has been a typical technique. With their high resolution, depth of field, and 3D quality, SEM images of surfaces provide a visual view of the topography and morphology of the bulk specimen as collected from several detectors.

The electron gun (electron source and accelerating anode), electromagnetic lenses to concentrate the electrons, a vacuum chamber holding the specimen stage, and a variety of detectors to gather the signals emitted by the specimen are the main elements of a SEM, as shown in Figure 2.12.

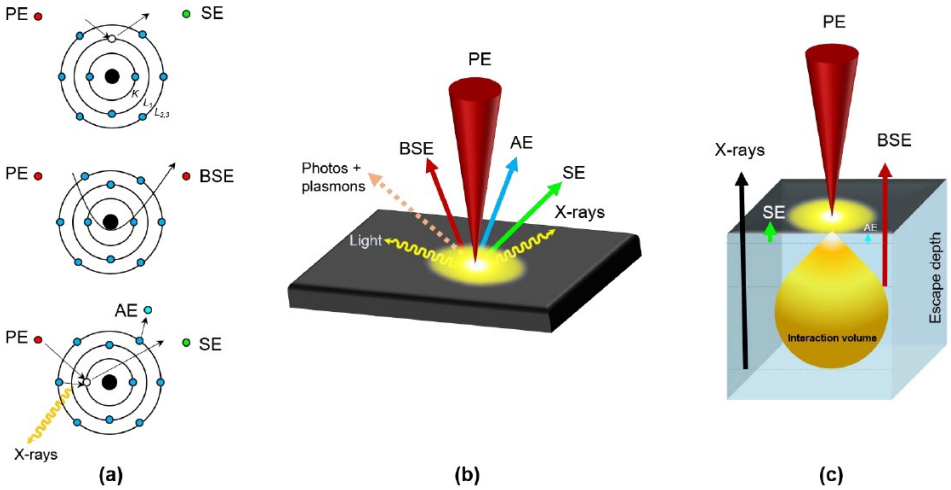

Figure 2.13 (a) the method through which the specimen's atom emits SE, BSE, AE, and X-rays. (b) Distinct signals produced by interactions between electron matter and bulk specimen. (c) The thickness of the thick specimen from which SE, BSE, and X-rays can escape is constrained by the samples' absorption of these radiations by inelastic scattering inside the interaction volume.

By burning a tungsten filament at the cathode and emitting an electron beam from an electron cannon above, the beam is accelerated downward and focused down onto the sample by a combination of condenser lenses, apertures, and an electromagnetic field (1-30kV). The interaction volume is the teardrop-shaped area of the specimen where the primary electron (PE) beam (2-10 KeV) interacts with the sample (3-20 cm in diameter), causing the electrons to repeatedly lose energy through random scattering and absorption (Figure 2.13c). Most SEM produce images using two types of electrons. Secondary electrons (SE) are produced as a result of the inelastic interaction between the electron beam and the sample, in which low energy electrons form distinctive patterns with the electrons that escaped from the surface sample's circling atoms. When a secondary electron leaves a vacancy in the core shell (K), an outer shell (L1) electron leaps into it, releasing energy in the form of distinctive X-rays that can be exploited in energy dispersive spectroscopy (EDS). Sometimes, extra energy can create a second outer shell (L2,3) in an excited state, which will cause the emission of Augur electrons (AE). Backscattered electrons (BSEs), which have an exceptionally high energy, pass close to atomic nuclei and are reflected back as a result of elastic interactions between the beam and the deeper region of the sample. The mechanism of the emission of SE, BSE, AE, and X-rays from the specimen's atom is summarized in Figure 2.13a. Different indications produced by electron matter interactions with the bulk material are shown in Figure 2.13b (Figure 2.13c).

AE is drawn to a secondary electron detector, while BSE and X-rays are also picked up by other sensors. An image of the actual object is scanned into a monitor and displayed row by row, dot by dot. Secondary electrons are primarily used for surface topography imaging; backscattered electrons for surface structure and average elemental information because BSEs are sensitive to atomic number Z; X-rays and Auger electrons for qualitative elemental composition with different thicknesses and sensitivity; and X-rays and gamma rays for quantitative elemental composition. The only color used for image processing is grayscale. SEM photos are usually black and white because of this.

2.3.2 X-Ray Diffraction (XRD)

A potent non-destructive method for characterizing crystalline materials is X-ray diffraction (XRD) (fingerprint). It offers details on the lattice characteristics and typical crystallite size.

Constructive interference between monochromatic X-rays and a crystalline sample is the foundation of X-ray diffraction. These X-rays are produced in a cathode ray tube by speeding electrons toward a target (at the anode) through a strong potential field, blasting the target material with electrons, and burning a tungsten filament in a vacuum to produce electrons. When electrons have enough energy to knock off the target material's inner shell electrons, the characteristic spectra $K_{\alpha 1}$, $K_{\alpha 2}$, $K_{\beta 1}$, $K_{\beta 2}$, $L_{\alpha 1}$, $L_{\alpha 2}$, $L_{\beta 1}$ and $L_{\beta 2}$ are created when the electrons from the outer shells leap into these gaps, as seen in Figures 2.14a and b. The only characteristic radiation typically employed in XRD is the greatest intensity K radiation; all other radiation is blocked out by filters or monochromators.

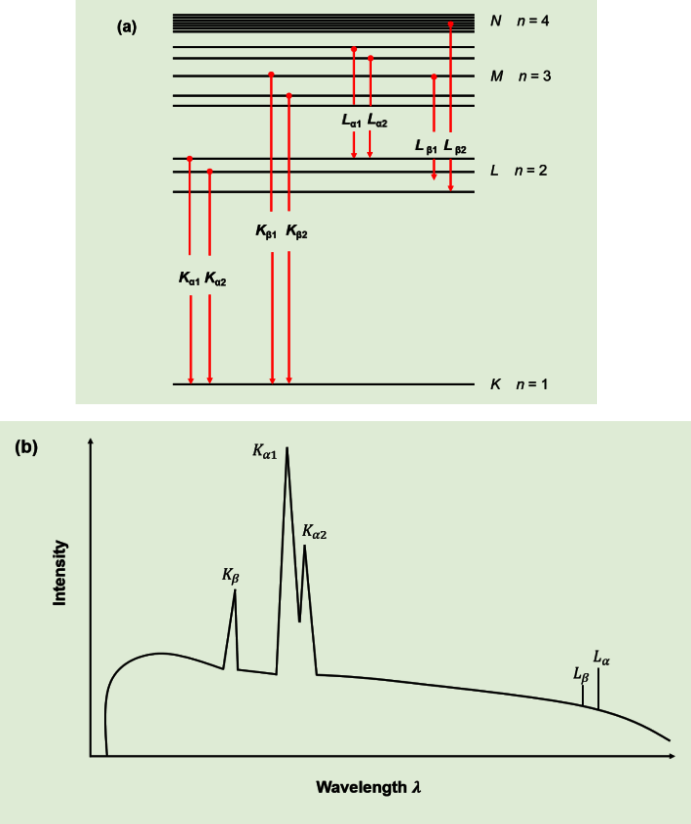

Figure 2.14 Atomic level transition for the copper atom in (a). (b) Diagram showing a typical X-ray emission spectrum from an X-ray tube.

The K radiation is then focused and collimated before being directed at the sample. Constructive interference happens when the incident X-rays hitting the sample conform to Bragg's law (Eq. (2.2)). The precise geometrical requirements for diffraction are shown in Figure 2.15.

$$n\lambda = 2d_{hkl}\, sin\theta \qquad \text{Eq. (2.2)}$$

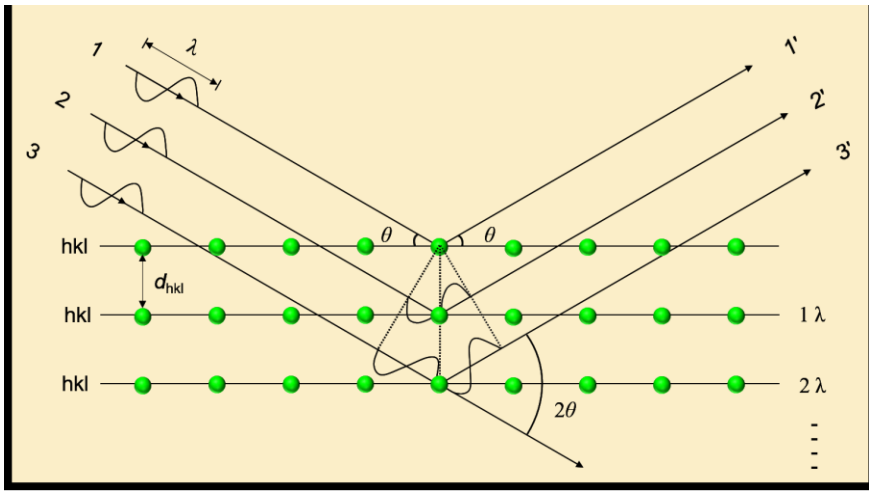

Figure 2.15 Geometrical condition for diffraction from lattice planes.

n is an integer known as the order of reflection, λ is the incident X-ray beam's wavelength, The Miller indices, h, k, and l, are also known as the distance between the crystallographic planes with (hkl) orientation of the crystalline lattice, and θ is the angle of the incident (scattering) ray to the crystal planes.

When the sample is scanned over a range of 2θ during acquisition, all potential lattice diffraction directions can be obtained.

Scherrer's equation was used to estimate the average crystallite size L:

$$L = \frac{K\lambda_{K\alpha}}{\beta \cos\theta_{max}} \qquad \text{Eq. (2.3)}$$

K is the shape factor, which is frequently assumed to be unity (0.89 as the normal value), and λ is the wavelength of the incident K-ray radiation. β is the peak's selected line's broadening at half its maximum intensity (FWHM) (in radians). θ is the Bragg angle.

XRD analysis for this thesis was carried out using a Bruker D8 Advance diffractometer. equipped with a Cu K_α source (λ= .15406 nm) operating at 40 kV and 40 mA. Each and every diffractogram was collected in the symmetric θ−2θ scan mode from 2θ=20°-90° with a low incident angle of 2° and a 2θ angular step size of 0.04° using a 4 s per step capture time. The software DIFFRAC.EVA V14 analyzed the diffraction peaks position (2θ) and the accompanying FWHM values.

2.3.3 X-ray photoelectron spectroscopy (XPS)

X-ray photoelectron spectroscopy (XPS), a quantitative method for determining the surface elemental composition, empirical formula, chemical state, and electronic state of the elements within a material is known as electron spectroscopy for chemical analysis (ESCA). XPS examination is extremely surface-sensitive; typically, it can probe any solid substrate down to a depth of about 10 nm. All elements can be properly analyzed with XPS, with the exception of hydrogen and helium. It is because H and He only have valence electrons, which has a very low photoelectron cross section, and XPS is not very sensitive to valence electrons. High vacuum is used to accomplish the XPS (P<10−7 mbar) or ultra-high vacuum (UHV, P<10−9 Pa) with the photon source of Mg K_α ($h\nu$=1253.6 eV) or Al K_α ($h\nu$=1486.6 eV). Figure 2.16 displays an example of a typical XPS setup.

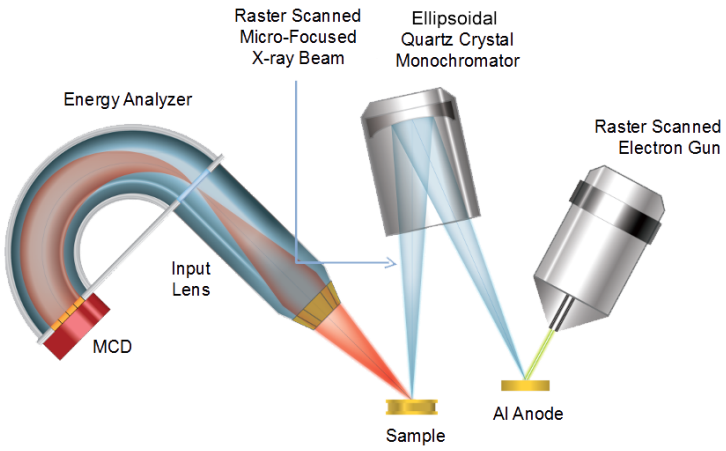

Figure 2.16 Typical XPS setup with photo source shown schematically.

In X-ray photoelectron spectroscopy (XPS), a sample is exposed to an X-ray beam in vacuum. The electrons are then collected and scattered to an energy analyzer, where their kinetic energies are determined, and to a detector, which counts the number of photoelectrons at various kinetic energies. The electrons are then ejected from the atom's core shell and escape from the surface to vacuum. Figure 2.17 shows a simplified diagram of this procedure. The term "photoelectron" refers to the released electron with a specific amount of kinetic energy E_K.

The electron binding energy to the nucleus relative to the Fermi level is given by:

$$\boldsymbol{E_B = h\nu - E_K - \Phi} \qquad \text{Eq. (2.4)}$$

In this expression, the energy of the utilized X-ray photons is denoted by $h\upsilon$. The work function PHI is the amount of energy needed to eject a photoelectron into space from the level of energy that is most occupied. The material and the spectrometer are key factors. The photoelectron's kinetic energy is known as E_K. An element is identified and its chemical bonding state in the material is estimated using the value of E_B and chemical shift (difference from elemental state).

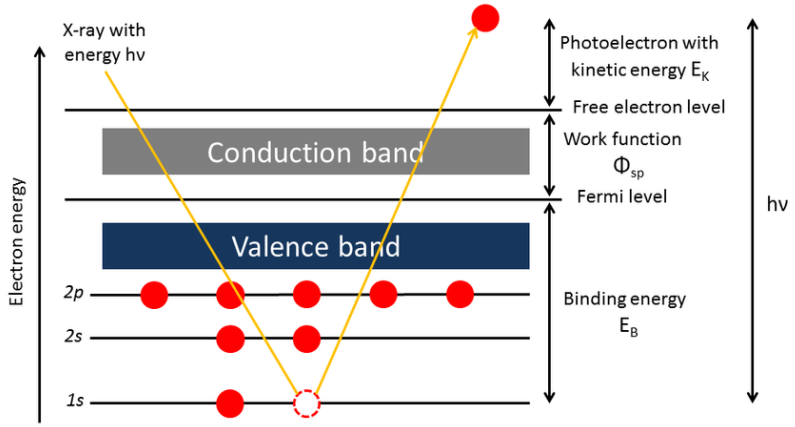

Figure 2.17 XPS's basic concept diagram.

XPS measurements were performed using an Al K source on a VG Escalab 220i-XL set (1486.6 eV). The anode was driven at 10 kV and 20 mA. The anode was driven at 10 kV and 20 mA. The analyzer's pass energy was set at 20 eV. The system's base pressure was 10^{-9} mbar. A spot size of 250 x 1000 m was used for analysis on all samples, about in the middle of the sample. Prior to obtaining higher resolution multiplex scan spectra (Pt_{4f}, Ti_{2p}, O_{1s}, and C_{1s} core levels) a survey spectrum with a range of 0 to 1300 eV was initially taken. With Casa XPS software version 2.3.12 (Casa Software Ltd.), the components were quantified by fitting the core level spectra following Shirley background reduction. Asymmetrically modified Gaussian/Lorentzian line shapes were employed to fit the metallic components, while symmetrical Gaussian/Lorentzian were utilized to suit the other components. For charge correction, the hydrocarbon contaminants at the surface that caused the C_{1s} core level peak at 284.6 eV was used as an internal reference binding energy.

2.4 Electrochemical characterizations

2.4.1 Three electrode assembly

A working electrode (WE), a counter electrode (CE), and a reference electrode make up the system (RE). In a three-electrode system, a WE is typically utilized in conjunction with a CE and a RE. At WE, there is an interest response. A Lugging capillary that is situated close to WE at a distance of 1 mm between them separates the RE from the analyte solution to reduce the ohmic drop (engendered by the electrolyte resistance). The potential difference between WE and RE is represented by the observed cell voltage E. To give a consistent potential over time or under changing temperature conditions, the RE should not be polarized. However, its position should not obstruct the mass movement of ions or molecules. The CE is made of an inert substance and is also referred to as the auxiliary electrode (e.g., Pt, Au, graphite, glassy carbon). Instead of taking part in the electrochemical reaction, it normally conducts electricity from the signal source into the solution, keeping the current at the proper level. The total surface area of the CE must be greater than that of the WE because the current flows between both, preventing the CE from acting as a limiting factor in the electrochemical process under study's kinetics. Figure 2.18 displays how this experiment was set up.

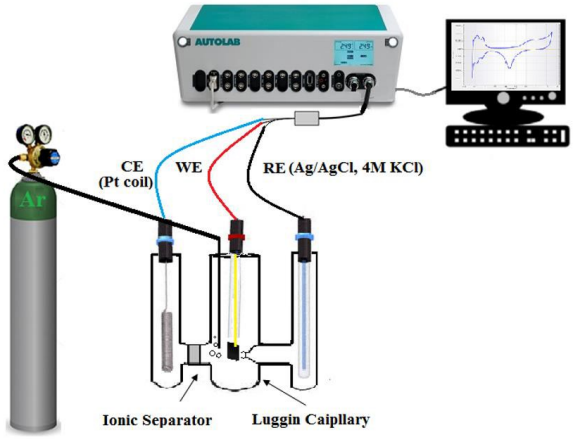

Figure 2.18 Diagram of the experimental setup.

2.4.2 Linear sweep voltammetry and cyclic voltammetry

The working electrode potential is scanned linearly as a function of time between two predetermined potentials (initial potential E_1 to the switching potential E_2) in cyclic voltammetry (CV), a potentiodynamic electrochemical measurement, as depicted in Figure 2.19a. The potential

range is often specified such that all anticipated reactions can happen. Contrarily, in aqueous electrolytes, the potential range should be within the electrode's water window because the potentials that trigger the evolution of hydrogen and oxygen should not be exceeded [50]. The scan rate $v = dE/dT$ is the potential variation's speed, and it is the most crucial CV parameter. A greater current is obtained because a faster scan rate will cause the diffusion layer's size to shrink. Additionally, by adjusting the scan rate, the kinetics of an electrochemical redox process can be determined. Typical values of v vary from 1 mV s^{-1} to 1000 mV s^{-1}.

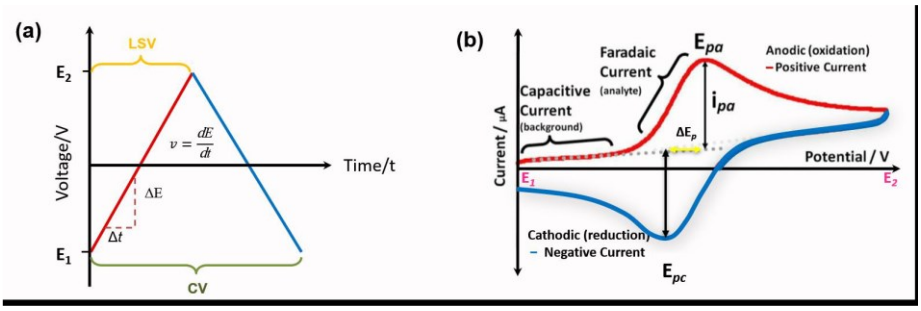

Figure 2.19 (a) Used voltage-time profiles for LSV and CV(b) Common CV traces.

Figure 2.19b illustrates a forward scan (red line, from E_1 to E_2), As the potential is applied, the current maintains a basic steady state. Electric-double layer capacitance created at the electrode's surface is what causes this initial current to flow. There is no electron transfer because this process is non-faradaic. The current in this capacitor i_c (also known as double layer or non-faradaic) can be expressed in writing as [51]:

$$|\boldsymbol{i_c}| = \boldsymbol{AC_d\, v} \qquad \text{Eq. (2.5)}$$

where A (cm^2) is the electrode region, C_d (F cm^{-2}) the double-layer capacitance and v (mV s^{-1}) the scan rate.

Electroactive species start to oxidize as soon as they approach the analyte's oxidation potential, and the anodic current begins to increase. The current known as faradaic current, which follows the power law, results from the transport of electrons between species and the electrode:

$$\boldsymbol{i = a v^b} \qquad \text{Eq. (2.6)}$$

where the values of a and b are movable. The Faradaic (diffusion-controlled) and non-Faradaic (capacitive) currents can be thought of as the total of the b value. Freely diffusing redox species are involved in the electrochemical reversible electron transfer process at 298 K, and the accompanying current i is proportional to $v^{1/2}$, on the basis of the Randles-Sevcik equation. The peak current i_p^{rev} will be [52]:

$$i_p^{rev} = \pm (2.69 \times 10^5)\, n^{3/2} ACD\, v^{1/2} \qquad \text{Eq. (2.7)}$$

where i_p^{rev} (A) is the peak current, the overall number of electron transfers is n, A (cm^2) is the electrode area, D ($cm^2\ s^{-1}$) is the oxidized analyte diffusion coefficient, C ($mol\ cm^{-3}$) is the analyte's bulk concentration, and ν ($mV\ s^{-1}$) is the scan rate.

The mass transfer of new analyte from the bulk solution to the electrode and a decrease in analyte concentration at the electrode surface are both results of the electrochemical reaction. With the increasing of potential, the mass transfer of new analyte to the electrode and achievement of its peak are the results of the reduced product of the analyte being completely consumed from the electrode surface. The peak happens when the Nernst equation describes the equilibrium between the analyte and its reduced product. The peak current i_{pa} and peak potential E_{pa} are shown in Figure 2.19b. As the voltage is increased, the analyte depletion zone expands and the diffusion layer widens. As the mass transfer to the electrode becomes slower, the current also becomes less. The direction of the scan is reversed when reaching the switching potential E_2, and the backward scan starts (Figure 2.19b, blue line, from E_2 to E_1). The reverse scan reduces the oxidized species. An identically shaped cathodic peak is seen, which indicates that the electrochemical process is reversible. One cycle of the cyclic voltammogram is represented by this entire cycle.

Through the peak current ratio i_{pa}/i_{pc} and peak potential separation, CV can also reveal information regarding kinetics and the reversibility of an electrochemical system ΔE_p. For a reversible chemical and electrochemical reaction, peak current ratio of it i_{pa}/i_{pc} is 1, and the ΔE_p is 59/n mV (2.3 RT/nF) at 298 K, where n represents how many electrons were moved during the process.

The foundation of CV is the linear sweep voltammetry principle (LSV). Unlike CV, LSV has a single sweep that ends inside a predetermined voltage range.

2.4.3 Chronoamperometry

Chronoamperometry (CA) is an electrochemical technique that involves stepping the square-wave potential of the working electrode and measuring the current that results from the faradaic processes that take place at the electrode as a function of time.

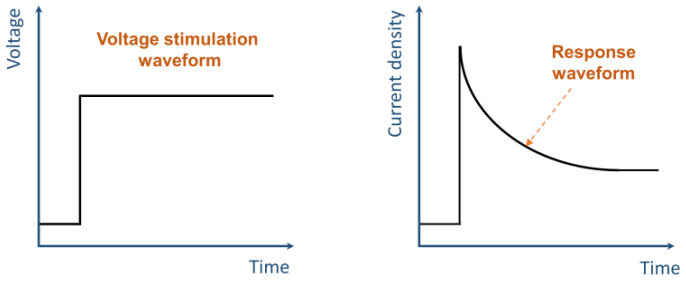

Figure 2.20 Waveform and response for CA.

A typical CA potential excitation waveform and the related current response are shown in Figure 2.20. In CA, a capacitive current i_c and a Faradaic i_F current contribute to the current response to the step potential, similar to CV. The double layer charging correlates to the capacitive current, which only occurs momentarily. The current of interest is the Faradaic current, which is brought on by the transport of electrons. The Cottrell equation was used after this current downturn [51].

$$i = nFAD^{0.5}C_b/\pi^{0.5}t^{0.5} \qquad \text{Eq. (2.8)}$$

where A (cm^2) is the electrode area, C_b (mol cm^{-3}) is the bulk concentration, t (s) is the time, n is the number of electrons exchanged in the half cell, F is the Faraday's Constant (96,485 C mol^{-1}), D (cm^2 s^{-1}) is the diffusion coefficient of the oxidized analyte.

The equation demonstrates that the Faradaic current is proportional to $1/t^{0.5}$. The response is suitable for semi-infinite linear diffusion, which implies there is no stirring of the solution, linear diffusion to the flat electrode, no additional reactions, and no ion migration (with a supporting electrolyte to ensure this) [43]. In general, the double layer capacity C_d and ohmic resistance R_Ω of the electrolyte cause the response current to decline exponentially with time more or less quickly.

Chronoamperometry is used to assess the durability of electrocatalyst during an electrochemical reaction (in this case ethanol oxidation). A good electrocatalyst should maintain a high steady state current density in order to be considered efficient and stable.

2.4.4 Experimental Procedures

In this study, all electrochemical tests are conducted in a three-electrode cell equipped with an EcoChemie Autolab potentiostat/galvanostat (PGSTAT) at room temperature. The catalysts produced by PLD were used as WE, a Pt coil as CE, and an Ag/AgCl (4 M KCl) catalyst as RE.

The electrocatalytic activities towards EOR are examined in the deaerated solutions of 1 M C_2H_5OH + 0.5 M H_2SO_4.

2.4.4.1 Cyclic Voltammetry on polycrystalline Pt

Figure 2.21 shows a typical CV profile of a polycrystalline Pt electrode in an electrolyte of sulfuric acid at a specific scanning rate $\nu = dE/dt$. The three unique potential zones are the hydrogen region (H-region), the double layer (DL) region, and the oxide region (O-region).

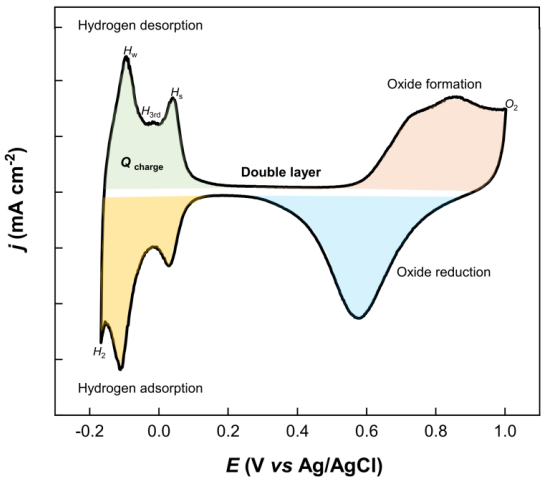

Figure 2.21 CV of polycrystalline Pt electrode in 0.5 M H_2SO_4 solution at scan rate of 50 mVs^{-1}.

1) H-region

The hydrogen underpotential deposition reaction occurs in the potential region from -0.17 to 0.2 V (vs Ag/AgCl) during the positive-going sweep (H_{upd}).

$$\boldsymbol{Pt{-}H_{ads} \leftrightarrow Pt{+}H^{+}{+}e^{-}} \qquad \text{Eq. (2.9)}$$

As is evident from Figure 2.21, it clearly displays three distinct peaks (H_w, H_s *and* H_{3rd}) in H_{upd}. Peak H_w is due to the weakly bound hydrogen on the planes of Pt (110) and (111) [56–57], While peak H_s, which lies between the H_w and H_s, is attributed to the Pt (100) plane for the tightly bound hydrogen [56], peak H_{3rd} is attributed to UPD H_2 [57]. There are clearly defined peaks in the region of underpotential hydrogen adsorption in the reverse, negative-going sweep.

$$\boldsymbol{Pt{+}H^{+}{+}e^{-} \leftrightarrow Pt{-}H_{ads}} \qquad \text{Eq. (2.10)}$$

The hydrogen evolution reaction (HER) takes place when the negative-going sweep is below 0.17 V:

$$2H^{+}+2e^{-}\rightleftharpoons H_2\ (g) \qquad \text{Eq. (2.11)}$$

Hydrogen desorption H_{des} and adsorption H_{ads} have similar peak positions indicating a reversible electrochemical reaction.

2) DL region

Without a Faradaic reaction, the double layer (DL) goes through charging and discharging processes. If present, solution impurities, surface contamination, traces of O_2, and heavy metal desorption may appear in the DL region [49].

3) O-region

The region where OH_{ads}, chemisorbed oxygen, subsurface oxygen, preliminary Pt oxide structures, and surface-oxide phases coexist, is between 0.5 and 1.0 V. The electrode potential and total surface covering have a significant impact on their existence [59].

$$Pt+H_2O\leftrightarrow Pt^{\delta+}\ O^{\delta-}+2\ H_{aq}^{+}+2\ e^{-} \qquad \text{Eq. (2.12)}$$

$$Pt^{\delta+}-\ O^{\delta-}\longrightarrow Pt^{2+}-\ O^{2-} \qquad \text{Eq. (2.13)}$$

The oxygen evolution reaction (OER) takes place when the positive-going potential is higher than 1 V:

$$2H_2O\leftrightarrow O_2\ (g)+4e^{-}+4H^{+} \qquad \text{Eq. (2.14)}$$

The peak of Pt oxide reduction is located in the reversal, between 1 V and 0.5 V in the negative-going sweep.

$$PtO_{ads}+2H^{+}+2e^{-}\rightarrow Pt+H_2O \qquad \text{Eq. (2.15)}$$

The asymmetric peaks of Pt oxide formation (O_{form}) and oxidation reduction (O_{red}), which are seen in Figure 2.21, show that this process is irreversible.

2.4.4.2 Electrochemical active surface area (ESA) estimation

The real electrochemically active surface area (ESA) of Pt electrodes is often calculated by integrating the charge in the hydrogen adsorption region of the voltammograms Q_H (Fig. 2.21), corrected for the double-layer current by back extrapolation of the current from the double layer region, using a conversion factor of 210 μC cm^{-2} for the removal of a monolayer of adsorbed

hydrogen. The ESA is a key parameter of fuel cell electrodes. The measurement of the ESA permits comparing the specific catalytic activity of different electrocatalysts and investigating the catalyst utilization and degradation when used in different conditions and electrode architectures.

The roughness factor (RF) provides further useful information about the electroactivity, particularly the effect of surface morphology that controls or provides greater electrocatalytic activity, i.e., the higher is the surface roughness, the greater is the electrocatalytic activity.

The roughness factor (RF) is defined by the ratio of the ESA to the geometric area (A_g).

$$RF = ESA / A_g \qquad \text{Eq. (2.16)}$$

2.4.4.3 Ethanol oxidation reaction (EOR)

To assess a catalyst's catalytic activity, there are two crucial factors to consider: (1) the onset potential of ethanol oxidation E_{onset}. This is the potential at which an anodic current starts to flow. The interactions between CO_{ad} and OH_{ad}, which affect E_{onset}, are connected to thermodynamic reactions [61]. (2) The forward anodic peak current density (j_{pa}). A greater j_{pa} indicates a higher rate of ethanol oxidation. The value of j_{pa} is related to the kinetic parameters of the electrocatalytic processes and electronic transfer rate [62]. During ethanol oxidation, the forward anodic peak corresponds to the oxidation of initially chemisorbed species (acetaldehyde, acetic acid and CO) resulting from ethanol adsorption. On the other hand, the backward oxidation peak is related to the removal of residual carbonaceous species, which are not completely removed or oxidized during the forward scan, rather than caused by freshly chemisorbed species [63]. A good catalyst for ethanol oxidation reaction is the one which demonstrates a lower onset potential and a higher peak current at a relatively low potential.

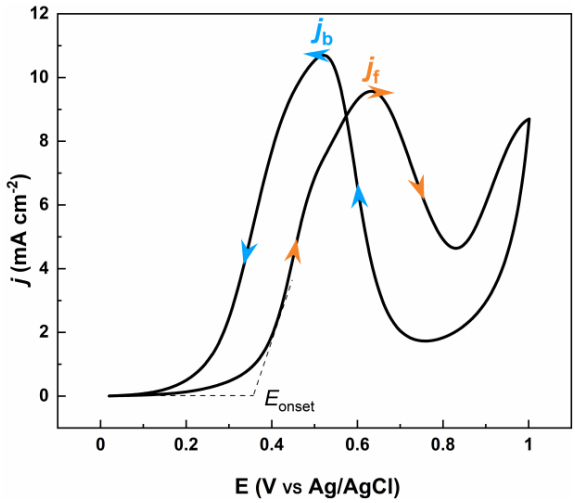

Figure 2.22 CV of Pt/CP electrode in 0.5 M H_2SO_4 + 1 M C_2H_5OH solution at scan rate of 5 mVs^{-1}.

A typical CV profile of ethanol oxidation on a Pt electrode in H_2SO_4 solution is shown in Figure 2.22. As seen in the diagram, the extremely low current density values in the $H_{des/ads}$ region (E<0.2 V) are likely a result of the ethanol adsorption or CO poisoning intermediates on the catalyst surface, which prevent hydrogen adsorption and obstruct other surface reactions [64]. The EOR current density jf begins to increase at E>0.2 V and reaches its maximum value at 0.63 V as a result of the production of Pt-OH, which makes it easier for CO poisoning species to migrate. The current density then decreases, which can be attributed to the conflict between the ethanol's adsorption and the water molecules' activation to create Pt-O species. The reaction is still restrained during the backward scan until the Pt-O electro-reduction at 0.53 V, and then j_b increases suddenly due to the liberation of active metallic Pt sites for ethanol adsorption [63].

2.4.4.4 Electrocatalyst durability and stability

Particularly in the practical application, a catalyst's strength and stability are crucial for the fuel cell. According to theory, chronoamperometric measurements can be used to determine the kinetic information for the ethanol oxidation. In a mixed solution of 0.5 M H_2SO_4 and 1 M C_2H_5OH, the chronoamperometry was performed at room temperature by stepping the potential from open circuit potential (OCP) to 0.6 V for 1 hour. In our work, 0.6 V was chosen because it was close to the electrocatalysts' forward peak potential for ethanol oxidation (Figure 2.22). Typical chronoamperograms exhibited by our catalyst is shown in Figure 2.23.

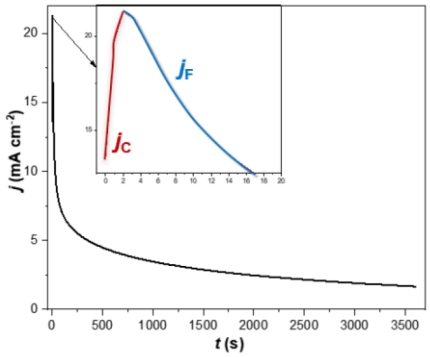

Figure 2.23 CA profile of Pt/CP electrode in 0.5 M H_2SO_4 + 1 M C_2H_5OH solution at 0.6 V for 1 h.

The double layer charging action caused the transient current density (j_c) to increase dramatically in the first 10 s, as seen in Figure 2.23. The poison from the buildup of intermediate species, including CO_{ads} and CHO_{ads} species during the EOR, led the current density (j_F) to drop dramatically and degrade over time. Within 3600 seconds, the current density reached a quasi-stable state.

References

[1] 66 T. Kasuga, M. Hiramatsu, A. Hoson, T. Sekino and K. Niihara, Langmuir, 1998, 14, 3160–3163.

[2] T. Kasuga, M. Hiramatsu, A. Hoson, T. Sekino and K. Niihara, Adv. Mater., 1999, 11, 1307–1311.

[3] G. Armstrong, A. R. Armstrong, J. Canales and P. G. Bruce, Chem. Commun., 2005, 2454–2456.

[4] D. V. Bavykin, V. N. Parmon, A. A. Lapkin and F. C. Walsh, J. Mater. Chem., 2004, 14, 3370–3377.

[5] R. L. Dong, S. J. Jiang, Z. Li, Z. Y. Chen, H. P. Zhang and C. C. Jin, Mater. Lett., 2015, 152, 151–154.

[6] B. Liu and E. S. Aydil, J. Am. Chem. Soc., 2009, 131, 3985–3990.

[7] Y. B. Xie, C. Xia, H. X. Du and W. Wang, J. Power Sources, 2015, 286, 561–570.

[8] J. Y. Liao, B. X. Lei, H. Y. Chen, D. B. Kuang and C. Y. Su, Energy Environ. Sci., 2012, 5, 5750–5757.

[9] D. Sarkar and K. K. Chattopadhyay, ACS Appl. Mater. Interfaces, 2014, 6, 10044–10059.

[10] M. C. Li, Y. J. Jiang, R. Q. Ding, D. D. Song, H. Yu and Z. Chen, J. Electron. Mater., 2013, 42, 1290–1296.

[11] F. R. Wang, G. Q. Zhang, Z. Zhao, H. Q. Tan, W. X. Yu, X. M. Zhang and Z. C. Sun, RSC Adv., 2015, 5, 9861–9864.

[12] S. L. Feng, J. Y. Yang, H. Zhu, M. Liu, J. S. Zhang, J. Wu and J. Y. Wan, J. Am. Ceram. Soc., 2011, 94, 310–315.

[13] J. Tian, Z. H. Zhao, A. Kumar, R. I. Boughton and H. Liu, Chem. Soc. Rev., 2014, 43, 6920–6937.

[14] S. H. Lim, J. Z. Luo, Z. Y. Zhong, W. Ji and J. Y. Lin, Inorg. Chem., 2005, 44, 4124–4126.

[15] A. Nakahira, T. Kubo and C. Numako, Inorg. Chem., 2010, 49, 5845–5852.

[16] D. L. Morgan, H. Y. Zhu, R. L. Frost and E. R. Waclawik, Chem. Mater., 2008, 20, 3800–3802.

[17] X. S. Peng and A. C. Chen, Adv. Funct. Mater., 2006, 16, 1355–1362.

[18] S. I. Tanaka, N. Hirose and T. Tanaki, J. Electrochem. Soc., 2005, 152, C789–C794.

[19] Y. X. Tang, Y. Y. Zhang, J. Y. Deng, D. P. Qi, W. R. Leow, J. Q. Wei, S. Y. Yin, Z. L. Dong, R. Yazami, Z. Chen and X. D. Chen, Angew. Chem., Int. Ed., 2014, 53, 13488–13492.

[20] Y. X. Tang, Y. Y. Zhang, J. Y. Deng, J. Q. Wei, T. L. Hon, B. K. Chandran, Z. L. Dong, Z. Chen and X. D. Chen, Adv. Mater., 2014, 26, 6111–6118.

[21] Q. Y. Jia, W. X. Que and J. Zhang, Phys. Status Solidi A, 2011, 208, 2313–2316.

[22] C. T. Nam, J. L. Falconer, L. M. Du and W. D. Yang, Mater. Res. Bull., 2014, 51

[23] P. F. Wang, Y. H. Ao, C. Wang, J. Hou and J. Qian, Mater. Lett., 2013, 101, 41–43.

[24] N. T. Q. Hoa and D. N. Huyen, J. Mater. Sci., 2013, 24, 793–798.

[25] Y. J. Chen, G. H. Tian, Z. Y. Ren, C. G. Tian, K. Pan, W. Zhou and H. G. Fu, Eur. J. Inorg. Chem., 2011, 5, 754–760.

[26] Q. Wang, Z. H. Wen and J. H. Li, Inorg. Chem., 2006, 45,6944–6949.

[27] Z. L. He, W. X. Que, J. Chen, X. T. Yin, Y. C. He and J. B. Ren, ACS Appl. Mater. Interfaces, 2012, 4, 6816–6826.

[28] J. Y. Zhao, J. X. Yao, Y. Z. Zhang, M. N. Guli and L. Xiao, J. Power Sources, 2014, 255, 16–23.

[29] M. Assefpour-Dezfuly, C. Vlachos and E. H. Andrews, J. Mater. Sci., 1984, 19, 3626–3639.

[30] V. Zwilling, E. Darque-Ceretti, A. Boutry-Forveille, D. David, M. Y. Perrin and M. Aucouturier, Surf. Interface Anal., 1999, 27, 629–637.

[31] J. Du, X. Gu, H. Z. Guo, J. Liu, Q. Wu and J. G. Zou, J. Cryst. Growth, 2015, 427

[32] C. A. Chen, Y. M. Chen, A. Korotcov, Y. S. Huang, D. S. Tsai and K. K. Tiong, Nanotechnology, 2008, 19, 075611.

[33] N. T. Q. Hoa and E. T. Kim, Electrochem. Solid-State Lett., 2008, 11, K1–K3.

[34] H.M. Smith, A. Turner, Appl. Opt., 4 (1965) 147-148.

[35] C.W. Schneider, T. Lippert, Springer, 2010, pp. 89-112.

[36] C. Popescu, G. Dorcioman, A.C. Popescu, Laser ablation applied for synthesis of thin films: insights into laser deposition methods, Applications of Laser Ablation: Thin Film Deposition, Nanomaterial Synthesis and Surface Modification, (2016) 1.

[37] E. Papadopoulou, V. Zorba, A. Pagkozidis, M. Barberoglou, E. Stratakis, C. Fotakis, Thin Solid Films, 518 (2009) 1267-1270.

[38] A.A. Tseng, World Scientific, 2008.

[39] R. Eason, John Wiley & Sons, 2007.

[40] M. Datta, L. Romankiw, D. Vigliotti, R. Von Gutfeld, Appl. Phys. Lett., 51 (1987) 2040-2042.

[41] M. von AUmen, in, Springer-Verlag, Berlin, 1987.

[42] V. Nazabal, P. Němec, in: Springer Handbook of Glass, Springer, 2019, pp. 1293-1332.

[43] I. Weaver, C. Lewis, J. Appl. Phys., 79 (1996) 7216-7222.

[44] D. Marla, U.V. Bhandarkar, S.S. Joshi, J. Appl. Phys., 109 (2011) 2.

[45] E. Morintale, C. Constantinescu, M. Dinescu, Physics AUC, 20 (2010) 43-56.

[46] J. Yang, Z. Zhang, X. Men, X. Xu, X. Zhu, Langmuir, 26 (2010) 10198-10202.

[47] A. Gorbunoff, in: Photon Processing in Microelectronics and Photonics V, International Society for Optics and Photonics, 2006, pp. 61060U.

[48] A. Gorbunov, W. Pompe, A. Sewing, S. Gaponov, Appl. Surf. Sci., 96 (1996) 649-655.

[49] A. Gorbunoff, John Wiley & Sons, Inc. (2007) 131-160.

[50] B. Inkson, Elsevier, 2016, pp. 17-43.

[51] J. Bard, L.R. Faulkner, Fundamentals and applications, Electrochemical Methods, 2 (2001) 580-632.

[52] K. Scott Elsevier, 2016, pp. 29-66.

[53] J. Flórez-Montaño, G. García, O. Guillén-Villafuerte, J.L. Rodríguez, G.A. Planes, E. Pastor, Electrochim. Acta, 209 (2016) 121-131.

[54] T. Housmans, J. Feliu, M. Koper, J. Electroanal. Chem., 572 (2004) 79-91.

[55] B. Loo, T. Furtak Electrochim. Acta, 25 (1980) 505-508.

[56] K. Kinoshita, P. Stonehart, Electrochim. Acta, 20 (1975) 101-107.

[57] T. Frelink, W. Visscher, J. Van Veen, Electrochim. Acta, 40 (1995) 545-549.

[58] V. Climent, J.M. Feliu, J. Solid State Electrochem., 15 (2011) 1297.

[59] M. Alsabet, M. Grden, G. Jerkiewicz, J. Electroanal. Chem., 589 (2006) 120-127.

[60] M. Łukaszewski, M. Soszko, A. Czerwiński, Int. J. Electrochem. Sci, 11 (2016) 4442 4469.

[61] M. De Souza, R. Gomes, A. De Bortoli, Int. J. Hydrogen Energy, 43 (2018) 13475-13488.

[62] M.A.R. Queiroz, J. Ribeiro, Catalysts, 9 (2019) 277.

[63] Z. Liu, L. Hong, J. Appl. Electrochem., 37 (2007) 505-510.

[64] J. Asgardi, J.C. Calderón, F. Alcaide, A. Querejeta, L. Calvillo, M.J. Lázaro, G. García, E. Pastor, Appl. Catal. B, 168 (2015) 33-41.

3 THE 1ST ARTICLE

Three-dimensional Pt catalyst on TiO_2 structures: Synthesis, characterization, and optimal morphology for efficient ethanol electro-oxidation in acidic medium

Catalyseur Pt tridimensionnel sur structures TiO_2: Synthèse, caractérisation et morphologie optimale pour une électro-oxydation de l'éthanol en milieu acide

Authors:

Naser Mohammadi, Chahrazed Benabid, HaixiaWang, Juan Carlos Abrego-Martinez, Youling Wang, Mohamed Mohamedi

Énergie, Matériaux et Télécommunications (EMT), Institut National de la Recherche Scientifique (INRS), 1650 Boulevard Lionel Boulet, Varennes, Quebec, J3X 1S2, Canada

Title of the journal or book:

SN Electrochemical Science Advances

SN Electrochem Sci Adv. 2020;e2000020.

DOI: 10.1002/elsa.202000020

Contribution:

I combined the hydrothermal and pulsed laser deposition methods, several three-dimensional Pt catalysts on TiO_2 structures are prepared and studied for the electro-oxidation of ethanol in acidic medium. I conducted the characterization and ethanol oxidation experiments, analyzed the data and interpreted the results. I contributed in the writing with the help of my supervisor.

Abstract

By combining the hydrothermal and pulsed laser deposition methods, several three-dimensional Pt catalysts on TiO_2 structures are prepared and used for the electro-oxidation of

ethanol in acidic medium. SEM reveals that TiO_2 prepared with 0.6 M of HCl consist of a mixture of nanowires and nanorods. For higher HCl concentrations, the TiO_2 are either in the form of vertically aligned bars

or large branched crystals in the form of flowers-like. Despite having the same loading of Pt, among the 3D Pt/TiO_2/Ti structures, only those with TiO_2 prepared with 0.6M of HCl shows a higher area specific activity and current mass activities exceptionally superior of about >50 times than those of unsupported Pt/Ti catalyst toward ethanol oxidation reaction, which suggests a promising application in ethanol fuel cells.

KEYWORDS

ethanol electro-oxidation, hydrothermal synthesis, platinum, pulsed laser deposition, titanates

Résumé:

En combinant les méthodes de dépôt hydrothermique et laser pulsé, plusieurs catalyseurs de Pt tridimensionnels sur des structures de TiO_2 sont préparés et utilisés pour l'électro-oxydation de l'éthanol en milieu acide. MEB révèle que le TiO_2 préparé avec 0,6 M de HCl est constitué d'un mélange de nanofils et de nanotiges. Pour des concentrations plus élevées en HCl, le TiO_2 se présente soit sous la forme de barres alignées verticalement ou de gros cristaux ramifiés en forme de fleurs. Malgré le même chargement de Pt, parmi les structures 3D Pt/TiO_2/Ti, seules celles avec du TiO_2 préparé avec 0,6 M de HCl montrent une activité spécifique de zone plus élevée et des activités de masse actuelles exceptionnellement supérieures d'environ > 50 fois à celles de Pt/non supporté. Catalyseur Ti vers la réaction d'oxydation de l'éthanol, ce qui suggère une application prometteuse dans les piles à combustible à l'éthanol.

Mots clés: Électro-oxydation de l'éthanol, synthèse hydrothermale, platine, dépôt laser pulsé, titanates

3.1 Introduction

TiO_2 is cheap, commercially available, nontoxic, and possesses a high mechanical and corrosion resistance. Since its discovery for electrochemical photocatalysis of water at a semiconductor electrode [1,2], TiO_2 received a lot of interest and was extensively employed in numerous technologies such as photocatalytic degradation of pollutants [3], water splitting [4,5], photocathode for the photoelectrochemical hydrogen evolution from water [6], solar cells, supercapacitors, lithium-ion batteries, biomedical devices [7], and implants for bone tissue

engineering [8]. In fuel cell systems, carbon materials are usually employed as the supports for platinum or platinum alloy- based electrocatalysts because it has high-surface area and good electronic conductivity [9]. Besides being expensive, carbon is prone to corrosion, which during its erosion induces the detachment and/or aggregation of the noble metal nanoparticles catalyst. This yield to the deterioration of both catalytic activity and durability; alternative carbon supports that have high durability are therefore needed for practical fuel cell operation [10,11]. Since TiO_2 is also more stable in acidic, alkaline, and oxidative environments it is thus being studied as an alternative catalyst support to activated carbon or carbon nanostructures in low-temperature fuel cells such as H_2/O_2 [12,14], direct methanol fuel cells (DMFC) [15,18], and in microbial fuel cells [19,20]. The studies in DMFCs reported that electrode in which TiO_2 acts as a support to Pt displays highly catalytic activity and CO tolerance for methanol oxidation reaction, which was attributed to synergistic effect between Pt nanoparticles and the TiO_2 support.

The direct ethanol fuel cells (DEFCs) are being paid more attention due to their potential applications in transportation and portable electronic devices [21]. The reasons behind this interest are linked to the fact that ethanol possess a high theoretical energy density (8.0 kW h kg^{-1}) and as a green fuel, it can be easily made in large quantities from non-conventional waste sources like food, agricultural, and wood wastes [21]. This could drive DEFCs favorable low greenhouse gas emission power sources. Reported studies on TiO_2 as catalytic support toward the ethanol oxidation reaction (EOR) are scarce and to the best of our knowledge, only three short communications were reported on that subject [22,24]. Earlier, Song et al prepared TiO_2 nanotubes (TNT) powder using sol-gel method [22]. The TiO_2 nanotubes powder was mixed with 83.4% Pt/C and Nafion solution to make a composite electrode. The authors found that the TNT can greatly enhance the catalytic activity of Pt for ethanol oxidation and increase the utilization rate of platinum. Later on, the same group investigated the role of the structural water contained in the TNTs and concluded that TNTs could promote Pt/C catalyzing ethanol oxidation due to that existing structural water [23]. Thereafter, Xiaoshan He and Chenguo Hu reported the synthesis of Pt nanoparticles on TiO_2 nanorod arrays grown directly on a Ti foil via a hydrothermal method [24]. The authors found that Pt/TiO_2/Ti electrocatalyst displays high catalytic activity for the EOR in both acidic and alkaline media as a result of synergistic effect of Pt nanoparticles and the TiO_2 support. The main objective of this paper is to combine the hydrothermal technique and the pulsed laser deposition (PLD) method to build three-dimensional Pt catalysts on TiO_2 nanorod arrays for effective EOR. TiO_2 arrays are prepared via a one-step acidic hydrothermal method using Ti foil as substrate and a Ti source. The concentration of HCl is varied to grow different morphologies of TiO_2. TiO_2 structures that were well adhered to the Ti substrate are further uniformly decorated

with the same loading of Pt cauliflower-like films grown via the PLD method building original 3D catalysts. All the samples are characterized by X-ray diffraction (XRD), scanning electron microscopy (SEM), and X-ray photoelectron spectroscopy (XPS). In addition, the electroactive surface area of the electrocatalysts is obtained through cyclic voltammetry (CV) in 0.5M H_2SO_4 solution. The electrocatalytic supporting properties of the TiO_2 arrays for Pt towards the EOR are studied via linear scan voltammetry (LSV) at quasi steady state in 0.5 M H_2SO_4 + 1 M C_2H_5OH electrolyte. The Pt/TiO_2/Ti electrocatalyst in which TiO_2 is made of a mixture of nanowires and nanorods exhibits a higher electroactive surface area and area specific activity and significantly superior electrocatalytic activity in EOR compared with other electrocatalysts, though they have the same loading of Pt. Optimization of HCl concentration for TiO_2 synthesis via the hydrothermal method combined with laser ablation for platinum catalyst growth is shown to produce promising electrode structures for DEFC technologies.

3.2 EXPERIMENTAL SECTION

3.2.1 TiO2/Ti Synthesis

Titanium foils were first cleaned with acetone in an ultrasonic bath for 20 min. Then, the foils were rinsed with a large amount of water. After drying in air, the foils were chemically etched in 18 wt% HCl (15 mL) solution at 80◦C for 15 min to remove the titanium oxide layer. Next the Ti foils were loaded into a 23 mL Teflon-lined stainless-steel autoclave (Parr Instrument) filled with 10 mL HCl

aqueous solution and kept at 180◦C for 10 h to complete the hydrothermal reaction. Four concentrations of HCl were considered, namely, 0.6, 0.6M200, 0.78, and 1.12 M.

To simplify, the samples are labeled Sample 0.6M, Sample 0.6M200 (200 indicates the temperature of synthesis), Sample 0.78M, and Sample 1.12M.

3.2.2 Pt/TiO2/Ti synthesis

Thin films of Pt were grown onto Ti foil and TiO_2/Ti substrates by PLD using pure Pt target (99.99%, Kurt J. Lesker Co). All Pt films were grown at room temperature with 50 000 laser pulses under 2 Torr of He gas using KrF excimer laser (λ = 248 nm), pulse width = 17 ns, and repetition

rate = 50 Hz. The laser fluence was fixed to 4 J/cm^2 and the target-substrate distance was set to 5 cm. Prior to each deposition, the chamber was evacuated using a turbo pump (4×10^{-5} Torr). The targets were continuously rotated and translated during the deposition in order to obtain a uniform ablation. The Pt loading in all cases was 0.120 mg/cm^2 (measured by neutron activation

analysis, NAA). More information on the working principle of the PLD can be found elsewhere [25–26].

3.2.3 Structural and morphological characterization

The surface morphology of the samples was examined by means of a SEM (JEOL, JSM 6300 F apparatus) operated at an accelerating voltage of 10 kV. The crystalline structure of all samples was determined by XRD using Bruker D8 Advance diffractometer equipped with a Cu Kα source

(λ = 1.5406 A). The tube current was 40 mA with a tube voltage of 40 kV. All diffractograms were acquired in the Grazing Incidence Diffraction (GID) scan mode with a low incident angle of 3◦ and a 2θ angular step size of 0.04◦ with an acquisition time of 5 s per step. XPS measurements were

performed in order to determine the chemical composition of the surface elements on the samples and their oxidation states. The study was carried out in a VG Escalab 220i-XL equipped with an Al Kα source (1486.6 eV). The anode was operated at 10 kV and 20 mA and the pass energy of the analyzer was fixed at 20 eV. The samples were analyzed with a spot size of 150 × 800 μm located approximately in the center of the sample. First, survey spectra in the 0–1350 eV range were acquired, followed by higher resolution multiplex scan spectra (Ti 2p, Pt 4f, C1 s, and O 1s core levels). The analysis of the elements was carried out with CasaXPS software (Casa Software Ltd.) by fitting the core level spectra after a Shirley background removal. The C 1s core level peak at 284.6 eV, resulting from hydrocarbon contaminants at the surface, was used as an internal reference. All spectra have been recalibrated with respect to the C 1s core level peak of adventitious carbon contamination.

3.2.4 Electrochemical experiments

Sulfuric acid (H_2SO_4, 96 %) and ethanol (100% purity) were purchased from Agros Organics and Commercial Alcohols inc., respectively. The reactants were used as received without further purification. The electrocatalytic characterization was evaluated by cyclic voltammetry (CV) or linear scan voltammetry (LSV) in 0.5 M H_2SO_4 and in a mixture of 1 M C_2H_5OH + 0.5 M H_2SO_4 solutions by a conventional three compartment electrochemical cell with an Ag/AgCl, 4 M NaCl reference electrode, a platinum coil as a counter electrode, and Pt/Ti and Pt/TiO_2/Ti samples as working electrodes. All potentials in this work are quoted versus Ag/AgCl. Prior to each electrochemical measurements, the electrolyte was deaerated by bubbling argon through the

solution for 30 min. Then the surface of the Pt/Ti and Pt/TiO_2/Ti working electrodes was cleaned and activated electrochemically in 0.5 M H_2SO_4 by several potential cycling within −0.2 to 1.3 V range with 50 mV/s until a steady state is reached. The steady state is attained (when the last CV is almost identical to the previous one) after about 15 CV cycles. EOR measurements were conducted in 1 M C_2H_5OH + 0.5 M H_2SO_4 with potential ranges from0 to 1.0 V versus Ag/AgCl at the scan rate of 5 mV/s (quasi-steady state). All electrochemical measurements were done at room temperature and data were acquired by a computer-controlled potentiostatgalvanostat (Autolab, PGSTAT 20, GPES).

3.3 RESULTS AND DISCUSSION

3.3.1 Structure and morphology characterization of TiO2

The corresponding formations of the TiO_2 samples prepared at different HCl concentrations are shown in Figure 1. The surface morphology of the Ti foil is reported in Figure S1 for reference. We investigated a series of hydrothermal conditions such as the concentration of HCl, temperature and time on the influence on the morphology of TiO_2. Only the most successful and reproducible syntheses are presented and discussed here. Synthesis with a concentration of 1.12 M HCl and a solution volume of 10 mL did not produce TiO_2 anchored on the substrate. The resulting product was mainly TiO_2 powder (Figure S2). Only for this concentration of 1.12 M HCl, we reduced the volume of HCl by 5 mL and obtained TiO_2 well adhered to the Ti substrate. Figure 1 shows the SEM images of Sample 0.6M, Sample 0.6M200, Sample 0.78M, and Sample 1.12M. As seen from these images, the deposits are a mixture of nanowires and nanorods at the Sample 0.6M (Figure 1a) and Sample 0.6M200 (Figure 1b). As for Sample 0.78M, there is the appearance of a large number of vertically aligned bar-shaped TiO_2 and a decrease in density of nanowires and nanorods (Figure 1c). When the concentration of HCl increased to 1.12 M, the deposit obtained was mainly composed of large crystals of TiO_2 arranged in the form of flowers-like (Figure 1d and with increasing magnification in Figure S3). Obviously, high concentrations of HCl of 0.78 M and 1.12 M do not bring beneficial effects for forming high density of nanosized TiO_2.

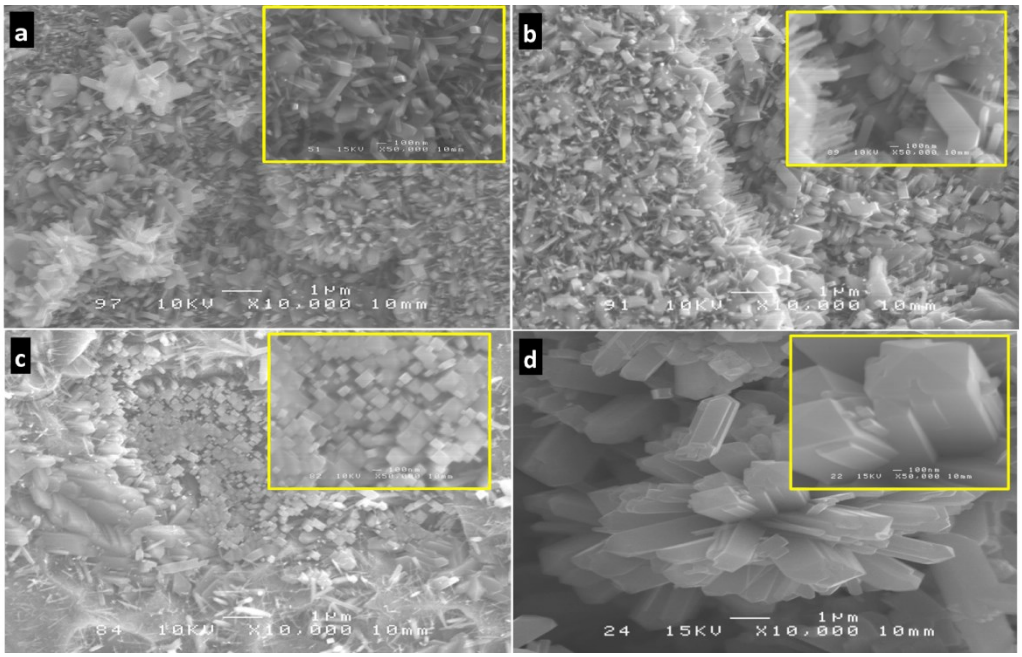

Figure 1. SEM micrographs of hydrothermal-synthesized TiO_2 films onto Ti foil substrate. (a) Sample 0.6M; (b) Sample 0.6M200; (c) Sample 0.78M and (d) Sample 1.12M.

The crystalline structures of the TiO_2/Ti samples are shown in Figure 2. XRD patterns of the Ti foil are also reported for referencing. Crystalline features of the TiO_2/Ti are evident in all XRD profiles. The as identified peaks correspond to rutile TiO_2 (JCPDS 21-1276). Since in all the XRD patterns, the most intensive peak is the TiO_2 (111), it was used to estimate the average crystallite size (L) by the Debye-Scherrer equation: $L=0.89\ \lambda/\ \beta\ cos\ \theta$, where λ is the wavelength of 1.5406 Å, β is the full-width at half-maximum (FWHM) and θ is the Bragg angle in radians. The average crystallite size was found to increase with the increase of HCl concentration used during the hydrothermal synthesis, namely 34.3 nm for Sample 0.6M and Sample 0.6M200, 41.5 and 48 nm for Sample 0.78M and Sample 1.12M, respectively.

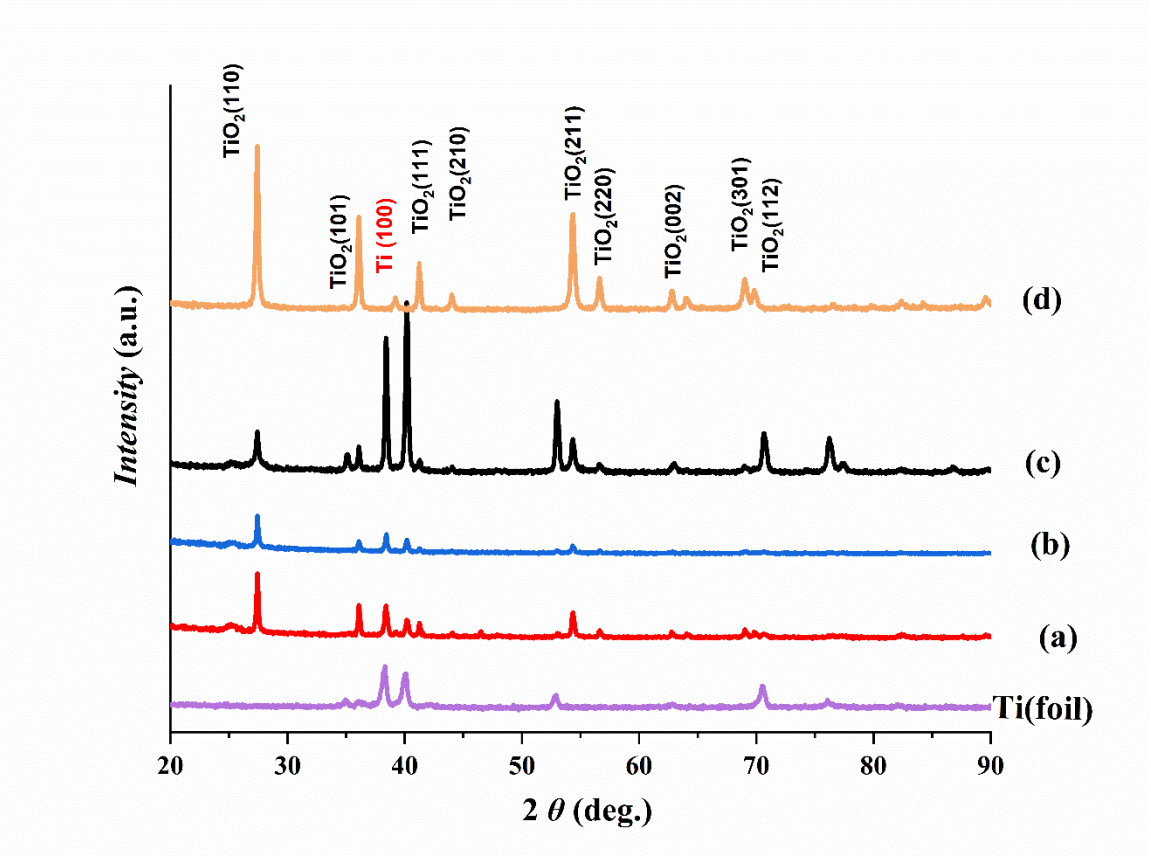

Figure 2. XRD analysis of (a) Sample 0.6M; (b) Sample 0.6M200; (c) Sample 0.78M; (d) Sample 1.12M and Ti (foil).

X-ray photoelectron spectroscopy (XPS) was employed to examine the surface of the TiO_2 component. The XPS survey spectra revealed that the surface samples consisted of Ti, O, and C (Figure S4). The carbon contamination is practically impossible to circumvent. Luckily, it is usually restricted to the film-air interface. Figure 3 displays the high-resolution XPS Ti 2p and O 1s core levels obtained at all the TiO_2 samples and Table 1 summarizes the relevant features of these spectra. The position of the Ti 2p doublet Ti $2p_{1/2}$ and Ti $2p_{3/2}$ and the binding energy separation (ΔBE) of 5.60~5.64 eV between them indicated that in all cases, Ti was in fully oxidized state of Ti^{4+} at the surface [27-29]. Oxygen O 1s lines are asymmetrical in all synthesized samples, which indicates that oxygen occurs in two different chemical states at least. The O 1s spectrum (Figure 3, right plots) could be satisfactorily resolved into two contributions. The first contribution within binding energies of 529.5~530 eV is ascribed to lattice oxygen and the second contribution within 531~532 eV is attributed to non-lattice oxygen [30]. The lattice oxygen corresponds to oxygen that occupies the normal lattice sites in the TiO_2 structure. The non-lattice oxygen has been

interpreted differently [31]. The oxygen state of higher *BE* is often supposed to be the oxygen in the surface state is causing the high-energy component of the asymmetrical O 1s line. High-energy component has been assigned to oxygen bonded to Ti^{+3} ($O–Ti^{3+}$). Others have argued that it is due to the presence of hydroxyl species (OH) that are easily formed at the surface of oxide films.

If we consider the relative areas corresponding to the main O 1s component (associated mainly to Ti^{4+}-O bonds) and the relative area corresponding to the main Ti 2p contribution, we find that the corresponding [O]/[Ti] atomic ratio 2.7 and 2.4 for Sample 06M and Sample 06M200, respectively. These values are close, within the error of the experimental determination to the expected stoichiometric ratio of 2.0. On the other hand, for Sample 0.78M and Sample 1.12M, the [O]/[Ti] atomic ratio was of 4.2 and 3.5, respectively. Meng et al. have attributed the presence of the non-lattice O component to the porosity, owing to the fact that it is related to the moisture that accumulates principally in the pores or empty columns of the material [32]. Using the ratio of $O_{II}/(O_I+O_{II})$ as a measure of the porosity it may be concluded that Sample 0.78M and Sample 1.12M with the largest deviation from stoichiometry are more porous than the stoichiometric films (see Table 1).

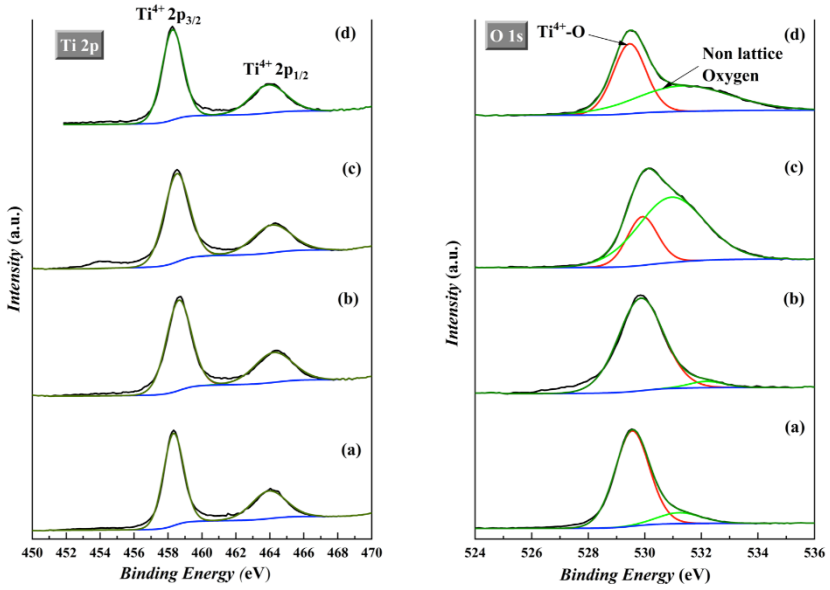

Figure 3. High-resolution XPS spectra of Ti 2p core level (left) and O 1s core level (right). (a) Sample 0.6M; (b) Sample 0.6M200; (c) Sample 0.78M and (d) Sample 1.12M.

TABLE 1 XPS parameters of the Ti/TiO_2 samples

Sample	Ti $2p_{3/2}$ (eV)	Ti $2p_{1/2}$ (eV)	O1 s (eV)	O 1s (eV)	[O]/[Ti]	$O_{II}/(O_I+O_{II})$[a]
Sample 0.6M	458.32	463.95	529.55	531.22	2.7	0.13
Sample 0.6M200	458.64	464.23	529.86	532.10	2.4	0.05
Sample 0.78M	458.52	464.14	529.92	532.18	4.2	0.25
Sample 1.12M	458.27	463.91	529.46	531.56	3.5	0.48

[a] O_I corresponds to the oxygen lattice, whereas O_{II} relates to the non-lattice oxygen.

3.3.2 Structure and morphology characterization of Pt/TiO2

TiO_2 samples, Pt films were grown by PLD onto each TiO_2 sample in addition to on Ti foil as a benchmark electrode. Figure S5 presents the SEM images of Pt grown on Ti substrate, which reveal that Pt film is dense and displays a smooth surface with several cracks. On the other hand, the surface morphology of the Pt films grown on the TiO_2 samples is completely different (Figure 4). The Pt particles perfectly mould the different shapes (nanowires, nanorods or the large crystals) of the underlying TiO_2.

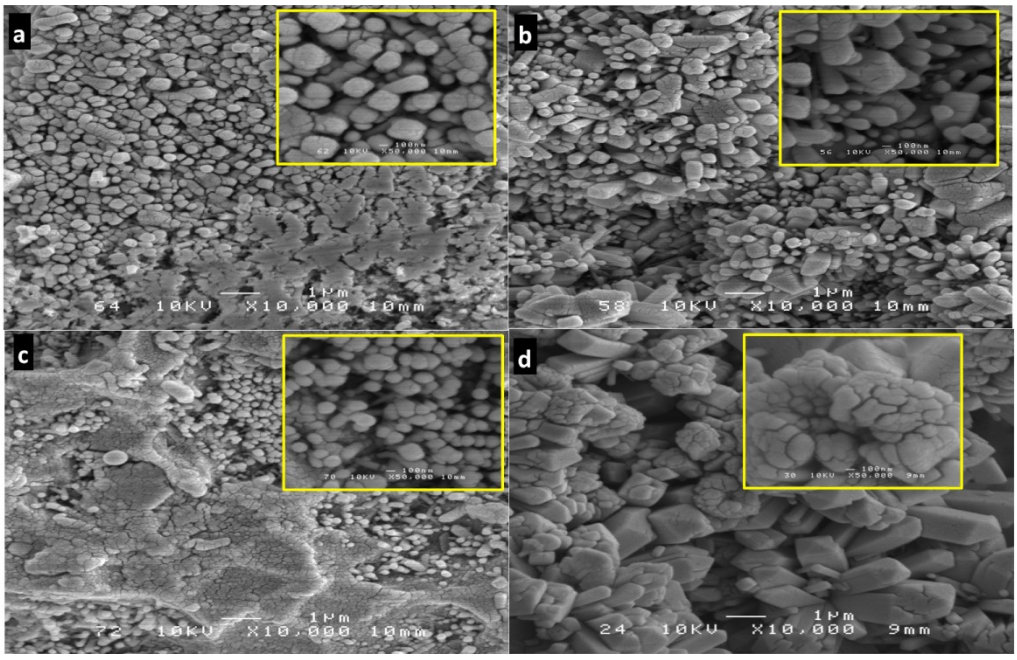

Figure 4. SEM micrographs of PLD-grown Pt films onto TiO_2 films. (a) Pt/Sample 0.6M; (b) Pt/Sample 0.6M200; (c) Pt/Sample 0.78M and (d) Pt/Sample 1.12M.

The XRD patterns shows diffraction peaks of Pt, which could be indexed respectively to (111), (200), and (220) planes of a (JCPDS PDF No. 04-0802), face centred cubic (fcc) structure (Figure 5). The most intensive reflection (111) of Pt particles was employed to estimate the average crystallite size and the lattice constant by Debye-Scherrer equation and Bragg's law,

respectively. The average crystallite size of Pt deposited onto the different TiO_2 samples has not notably changed. At Sample 0.6M, Sample 0.6M200, Sample 0.78M and Sample 1.12M, the crystallite size was found to be 8, 10, 9.3 and 9.7 nm, respectively. The lattice parameter was estimated to be near to 0.3920~0.3924 nm, which close to the bulk value of 0.3924 nm. The extracted values of the crystallite size and lattice parameter show that the morphology of the beneath TiO_2 does not significantly affect the crystalline structure of the above Pt films.

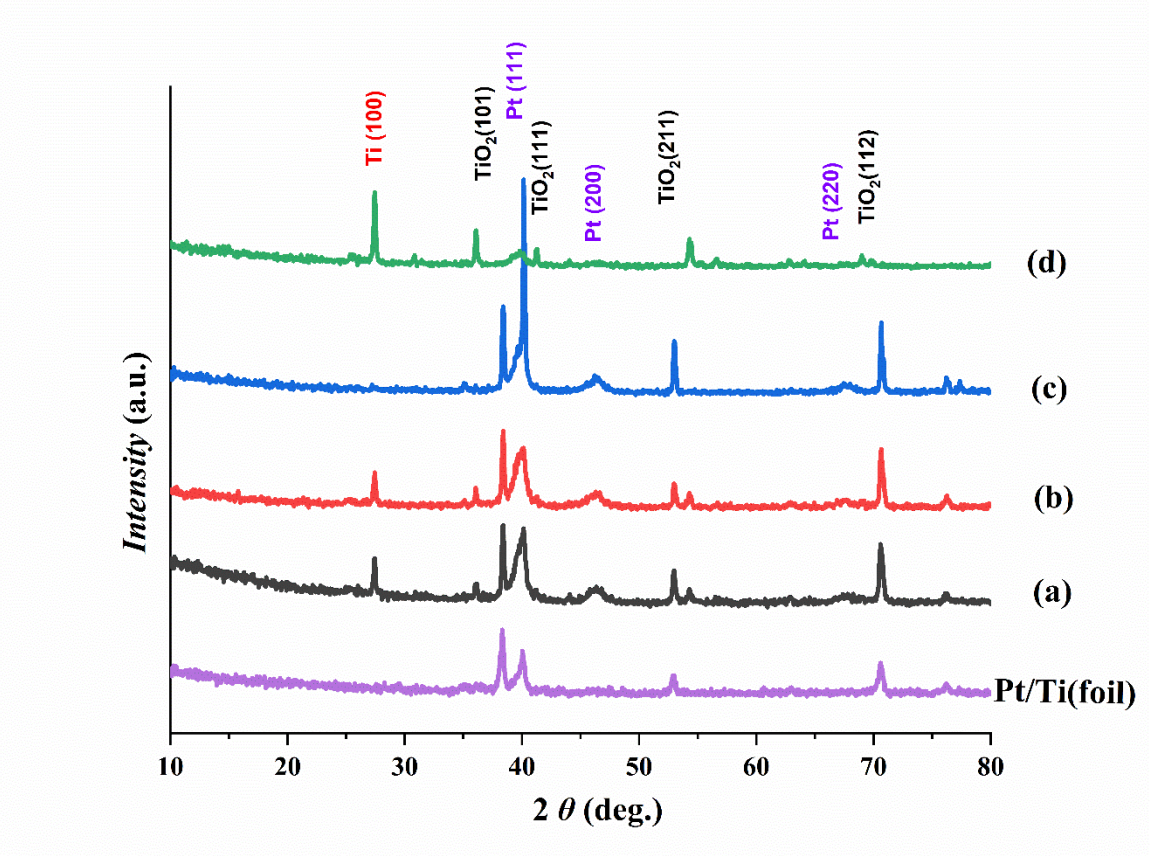

Figure 5. XRD analysis of (a) Pt/Sample 0.6M; (b) Pt/Sample 0.6M200; (c) Pt/Sample 0.78M; (d) Pt/Sample 1.12M and Pt/Ti (foil).

The XPS survey spectra typically showed the presence of weak bands of carbon and oxygen but strong bands of Pt at the surface of the Pt/TiO_2/Ti samples (Figure S6). The presence of oxygen at the surface occurred as a result of post-exposure in air. The metallic components of the Pt 4f region were fitted using a Gaussian/Lorentzian asymmetrically modified line shape and the results are shown in Figure 6. The Pt 4f spectrum exhibits a doublet containing a low energy band (Pt $4f_{7/2}$) and a high energy band (Pt $4f_{5/2}$) at 71.65 and 74.95 eV, respectively. The 3.3 eV

binding energy difference between the Pt $4f_{7/2}$ and Pt $4f_{5/2}$ confirms that Pt being present in a metallic state [33].

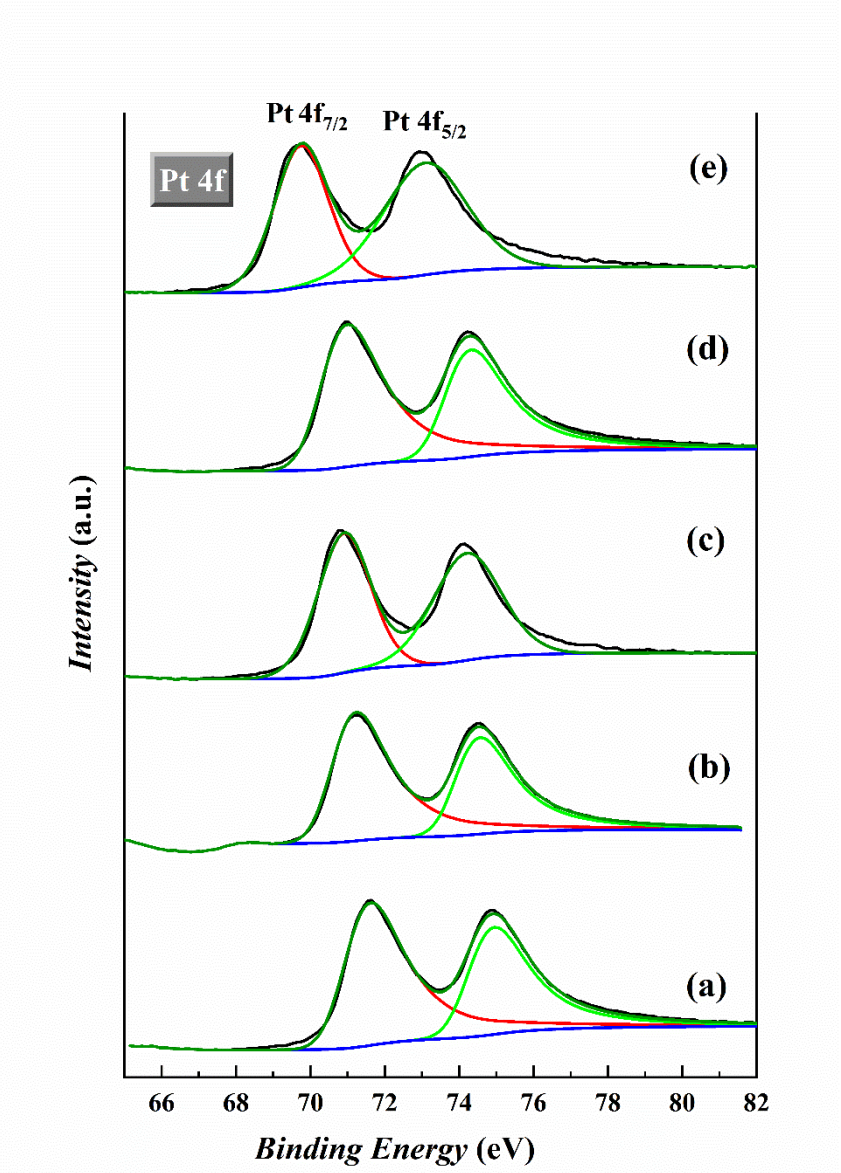

Figure 6. High-resolution XPS spectra of Pt 4f core. (a) Pt/Sample 0.6M; (b) Pt/Sample 0.6M200; (c) Pt/Sample 0.78M; (d) Pt/Sample 1.12M and (e) Pt/Ti (foil).

3.3.3 Electrochemical characterization

Figure 7 compares CVs with potential scan rate of 50 mV s^{-1} at the Pt/TiO_2/Ti electrodes in 0.5 M H_2SO_4 deaerated solution. The benchmark electrode made of PLD-grown Pt on Ti foil is also reported in the figure. It has to be recapped that all electrodes shown in Figure 7 contained similar amount of Pt. At the Sample 0.6M, Sample 0.6M200 and Sample 0.78M catalysts, the CVs

comprise the well-known hydrogen adsorption (H_{ads}) and desorption (H_{des}) peaks in the potential region of ca. -0.2 to 0.1 V vs. Ag/AgCl [34-36]. The H_{ads}/H_{des} peaks are distinctively sharper, which clearly indicates the higher number of the exposed Pt surfaces [37]. The Pt oxide formation starts at within 0.50~0.6 V range whereas its equivalent reduction peak potential takes place between 0.50 and 0.55 V vs. Ag/AgCl. On the other hand, the H_{ads}/H_{des} and PtOx features are barely seen at Pt/Ti foil and Sample 1.12M catalysts. Despite the similar loading of Pt, the current density resolution was markedly affected by the morphology of the underneath substrate TiO_2 and Ti.

The extent of the effect of the TiO_2 films on the electroactivity of Pt can basically be characterized as the electroactive surface area (*ESA*), which is estimated by integrating the charge in the hydrogen adsorption region (Q_H) of the voltammograms corrected for the double-layer current, using a conversion factor Q_{ref} of 210 $\mu C\ cm^{-2}$ [38]. Accordingly, the *ESA* of Pt/Sample 0.6M, Pt/Sample 0.6M200, Pt/Sample 0.78M and Pt/Sample 1.12M was estimated to be 7.3, 3.87, 3.48 and 1.9 cm^2 higher than 1.43 cm^2 of bare Pt/Ti catalyst. The electrochemical activity of the $Pt/TiO_2/Ti$ catalysts can be further evaluated with the area specific activity (*ASA*) (normalized by the Pt catalyst loading to generate mass activity) as follows: $ASA = Q_H/(Q_{ref} \times m_{Pt} \times A_g)$, where m_{Pt} and A_g represent the Pt loading and the geometric electrode area, respectively. It should be noted that the *ESA* specifies an inherent electrocatalytic value of a catalyst, while *ASA* is an important parameter regarding the practical application, in other words, the economic value of the catalyst, which principally is the activity normalized to cost. Accordingly, *ASA* was found to be 37.2, 21.6, 7.2 and 8 $m^2\ g^{-1}$ larger than the 5 $m^2\ g^{-1}$ of bare Pt/Ti. These results can be explained by estimating the roughness factor *RF* (ESA/A_g), which was found around 45.6, 25.6, 8.7 and 9.5 versus 5.6 of bare Pt/Ti. The estimated *ESA*, *ASA* and *RF* showed that the performance of the $Pt/TiO_2/Ti$ electrodes is far superior to that of bare Pt/Ti, clearly demonstrating the beneficial catalytic support of TiO_2 to Pt. This being observed, we note however that despite a similar Pt loading the four the $Pt/TiO_2/Ti$ electrodes exhibited different electroactivities. These variances demonstrate that the effective utilization of Pt is strongly affected by the morphology of the underlying TiO_2. Thus, it can be suggested that TiO_2 films made of mixture of nanowires and nanorods (Figure 1a and 1b) offer a more effective utilization of Pt nanoparticles. The increasing diameter of the nanorods becoming bars or large crystals (Figure 1c and 1d) resulted in a significant reduction in the specific surface area, which explains their lower electroactivity.

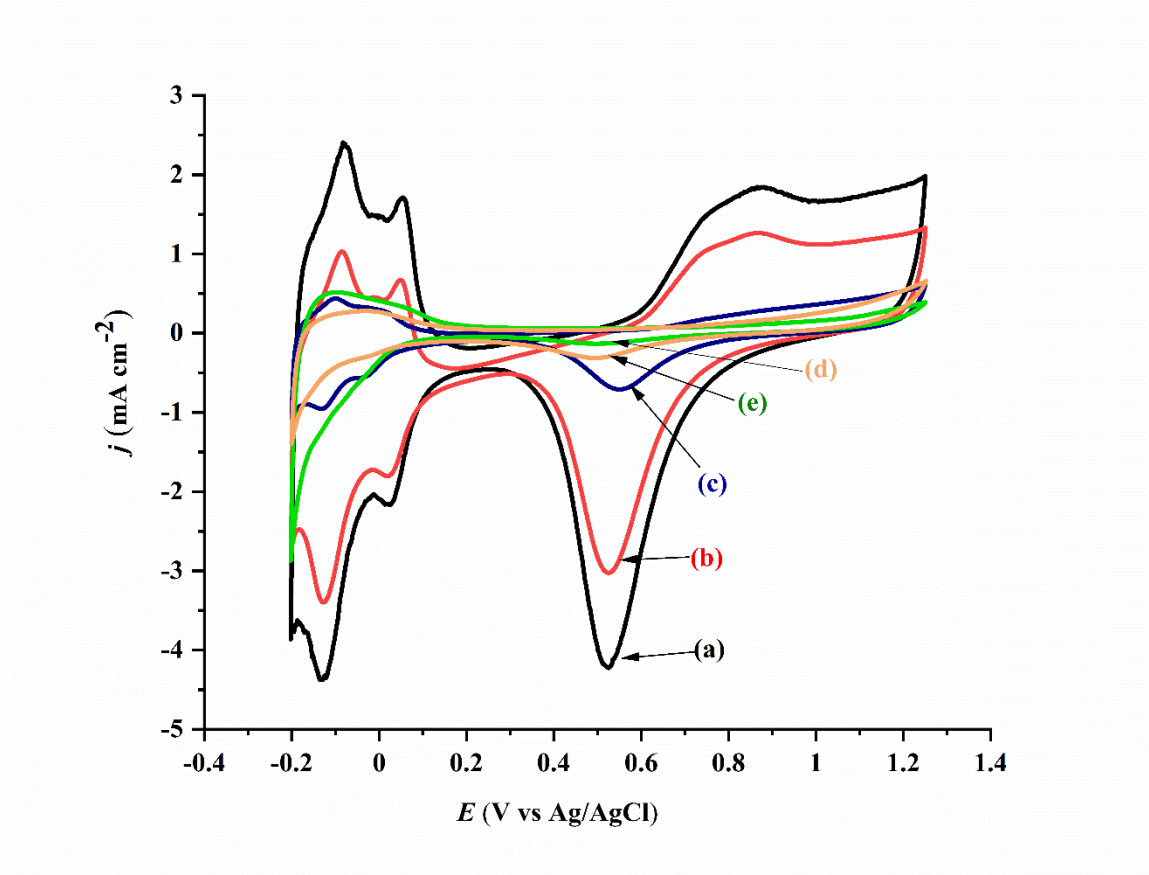

Figure 7. Cyclic voltammetry in 0.5 M H_2SO_4-argon purged solution with a potential scan rate of 50 mV s^{-1}. (a) Pt/Sample 0.6M; (b) Pt/Sample 0.6M200; (c) Pt/Sample 0.78M; (d) Pt/Sample 1.12M and (e) Pt/Ti (foil).

Subsequently, the electrocatalytic catalytic supporting capacity of the as-grown TiO_2 to Pt was investigated towards electrooxidation of ethanol. Figure 8a shows LSVs recorded in 0.5 M H_2SO_4+1 M C_2H_5OH solution with slow scan rate of 5 mV s^{-1} (quasi-steady state). The LSVs at all the electrodes displayed characteristic EOR waves in agreement with the literature [39-40]. Table 2 resumes the onset potential, E_{onset}, j@ 0.45V, peak current density j_p, and specific mass activity *SMA* (j_p/m_{Pt}) values extracted from LSVs of Figure 8. E_{onset} is a parameter that furnishes information related to the kinetic of an electrochemical reaction and is described here as the potential at which the oxidation current of ethanol initiates. j@ 0.45V is an arbitrary criterion close to the expected operating voltage of DEFCs devices and permits to compare the evolution of the EOR activity between various catalysts. Thus, from Table 2, it can be seen that only Pt/Sample 0.6M, Pt/Sample 0.6M200 catalysts oxidize ethanol at potentials significantly lower (by 100 mV) than that delivered by Pt/Ti catalyst. These observations demonstrate that Sample 0.6M and Sample 0.6M200 promoted faster kinetics of the EOR at Pt catalyst. The same catalysts exhibited

current densities and mass activities exceptionally higher of about more than 50 times than those of Pt/Ti catalyst, whereas Sample 1.12M delivered weak activity towards EOR (Figure 8b and Table 2) almost similar to bare Pt/Ti.

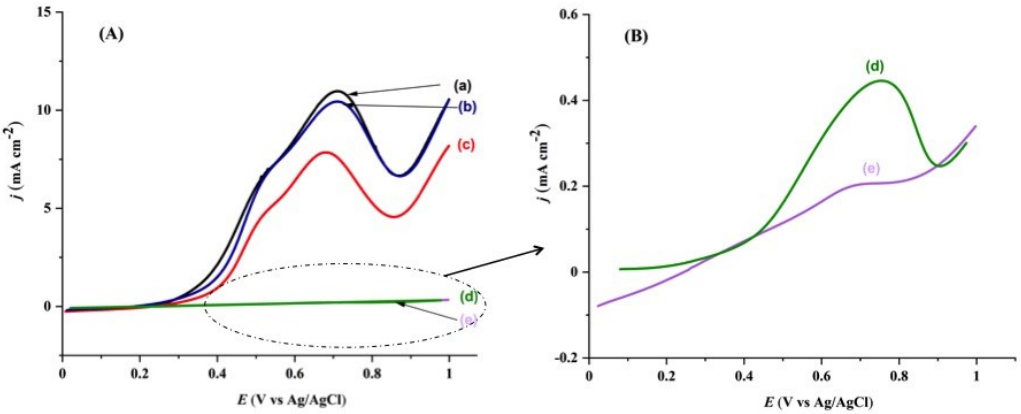

Figure 8. Linear scan voltammetry in 0.5 M H_2SO_4+ 1 M C_2H_5OH solution with a potential scan rate of 5 mV s^{-1}. (A): (a) Pt/Sample 0.6M; (b) Pt/Sample 0.6M200; (c) Pt/Sample 0.78M; (d) Pt/Sample 1.12M and (e) Pt/Ti (foil). (B) Zoom in of (d) and (e) LSV curves.

Table 2. Electrochemical EOR activity

Catalyst	E_{onset} (V)	j@0.45V (mA cm^{-2})	j_p (mA cm^{-2})	*SMA* (mA mg^{-1}_{Pt})
Pt/Ti	0.4	0.09	0.20	1.70
Pt/Sample 0.6M	0.3	4.00	10.7	89.0
Pt/Sample 0.6M200	0.3	3.27	11.1	92.8
Pt/Sample 0.78M	0.4	2.20	7.85	67.4
Pt/Sample 1.12M	0.4	0.10	0.20	1.70

It is therefore clear that TiO_2 films consisting of a mixture of nanorods and nanowires have greatly improved the electrocatalytic performance of platinum. These films are therefore an excellent catalyst support not only for Pt but may also be for Pt-alloys being investigated for oxygen reduction reaction, methanol or ethanol electrooxidation reaction in fuel cells technology or as photocathode for the photoelectrochemical hydrogen evolution from water.

As to the mechanism responsible for the effect of HCl concentration on the morphology of the TiO_2, it is likely that when the concentration of HCl is low, the Ti foil dissolves relatively slowly. The Ti^{3+} produced by the dissolution of Ti foil gradually increases with the augmentation of HCl concentration [41]. As a result, the crystalline phase content of TiO_2 also increases and aggregates to form nanorods (Figure 1c and 1d). In order to obtain a clear picture of the mechanism involving the growth of rutile TiO_2 nanorods with different aspect ratios, it will require further consideration of other synthesis parameters such as temperature, reaction time, volume of the solution and titanium foil thickness.

3.4 Conclusion

The prime objectives of this paper is to synthesize and optimize the morphology of TiO_2 films and evaluate their catalytic supporting properties towards Pt (as a benchmark catalyst) for ethanol electrooxidation, a reaction relevant to DEFC technologies. Thus, TiO_2 arrays are grown directly on the Ti foil via a hydrothermal acidic method, which is cost-effective, environmentally benign and does not require the use of templates. The concentration of HCl during synthesis is varied so as to obtain various morphologies of TiO_2. SEM observations reveal that TiO_2 prepared with 0.6 M of HCl are made of a mixture of nanorods and nanowires. Increasing the HCl concentration lead to a significant decrease in the density of the nanowires and nanorods and instead large bars or crystals are grown. XRD analysis identifies all as-grown products as rutile TiO_2. The average crystalline size is found to increase with the increase of HCl concentration. XPS analysis shows that Ti was in fully oxidized state of Ti^{4+} at the surface. However, at samples prepared with concentration of HCl higher than 0.6 M, the surface atomic [O]/[Ti] ratio is found to deviate from the stoichiometric value of TiO_2. This is ascribed to the porosity of the materials that allows moisture to accumulate in the pores or between the voids of the vertically aligned bars or the branched ones.

Despite having the same loading of Pt, among the four 3D Pt/TiO_2/Ti structures, only those with TiO_2 prepared with 0.6 M of HCl show a higher area specific activity and current mass activities towards EOR exceptionally higher of about more than 50 times than those of unsupported Pt catalyst, suggesting a promising application in DEFCs.

Acknowledgements

This work financially supported by the Natural Sciences Engineering Research Council of Canada (NSERC) and the Centre Québécois sur les Matériaux Fonctionnels (CQMF). Y. Wang

and H. Wang are grateful to China Scholarship Council for a PhD scholarship. J.C. Abrego-Martínez is grateful to UNESCO-MATECSS Excellence PhD Scholarship Program.

References

[1] A. Fujishima, K. Honda, Nature 1972, 238, 37-38.

[2] K. Hashimoto, H. Irie, A. Fujishima, Jpn. J. Appl. Phys. 2005, 44, 8269-8285.

[3] L. Razzaboni, M. Altomare, M. Pedeferri, M. V. Diamanti, and P. Schmuki, ChemElectroChem 2020, 7, 2859–2863.

[4] Y. Kageshima, T. Fujita, F. Takagi, T. Minegishi, K. Teshima, K. Domen, Y. Amao, H. Nishikiori, ChemElectroChem 2019, 6, 4859-4866.

[5] R. Vadakkekara, R. Illathvalappil, S.Kurungot, ChemElectroChem, 2018, 5, 4000-4007.

[6] W. Kong, X. Zhang, B. Chang, Y. Guo, Y. Li, S. Zhang, B. Yang, ChemElectroChem 2020, 7, 792-799.

[7] M. Ge, C. Cao, J. Huang, S. Li, Z. Chen, Ke-Qin Zhang, S. S. Al-Deyab and Yuekun Lai, J. Mater. Chem. A 2016, 4, 6772-6801.

[8] T. K Ahn, D. H Lee, T. S Kim, G. chol Jang, S. J. Choi, J. B. Oh, G. Ye S. Lee, Adv Exp Med Biol. 2018, 1077, 355-368.

[9] S. Sharma, B. G. Pollet, J. Power Sources 2012, 208, 96-119.

[10] Y. Shao, G. Yin, Z. Wang, Y. Gao, J. Power Sources 2007, 167, 235-242.

[11] X. Yu, S. Ye, J. Power Sources 2007, 172, 145-154.

[12] S. Jiang, B. Yi, C. Zhang, S. Liu, H. Yu, Z. Shao, J. Power Sources 2015, 276, 80-88.

[13] D. -S. Kim, E. F. Abo Zeid, Y.-T. Kim, Electrochimica Acta 2010, 55, 3628-3633.

[14] S. Tominaka, A. Ishihara, T. Nagai, and Ken-ichiro Ota, ACS Omega 2017, 2, 5209-5214.

[15] M. Abdullah, S. K. Kamarudin and L. K. Shyuan, Nanoscale Res Lett 2016, 11, 553.

[16] K. Drew, G. Girishkumar, K. Vinodgopal, P.V. Kamat, J. Phys. Chem. B 2005, 109, 11851-11857.

[17] E. Antolini, Appl. Catal. B: Environ. 2018, 237, 491-503.

[18] X. Wu; W. Zhuang; L. Lu; L. Li; J. Zhu; L. Mu; W. Li; Y. Zhu; X. Lu, Appl. Surf. Sci. 2017, 426, 890-896.

[19] S. Ait Ali Yahia, L. Hamadou, M. J. Salar-García, A. Kadri, V. M. Ortiz-Martínez, F. J. Hernández-Fernández, A. Pérez de los Rios, N. Benbrahim, Appl. Surf. Sci. 2016, 387, 1037–1045.

[20] T. Yin, Z. Lin, L. Su, C. Yuan, and D. Fu, ACS Appl. Mater. Interfaces 2015, 7, 400-408.

[21] S. Ramachandran and U. Stimming, Energy Environ. Sci. 2015, 8, 3313-3324.

[22] H. Song, X. Qiu, X. Li, F. Li, W. Zhu, L. Chen, J. Power Sources 2007, 170, 50-54.

[23] H. Song, X. Qiu, D. Guo, F. Li, J. Power Sources 2008, 178, 97-102.

[24] X. He, C. Hu, J. Power Sources 2011, 196, 3119–3123.

[25] M. N. Ashfold, F. Claeyssens, G. M. Fuge, S. J. Henley, Chem. Soc. Rev. 2004, 33, 23-31.

[26] R. Eason, Pulsed laser deposition of thin films: applications-led growth of functional materials. John Wiley & Sons, New Jersey, 2007.

[27] B. Erdem, R. A. Hunsicker, G. W. Simmons, E. D. Sudol, V. L. Dimonie, M. S. El-Aasser, Langmuir 2001, 17, 2664-2669.

[28] J. F. Marco, A. Cuesta, M. Gracia, J. R. Gancedo, P. Panjan, D. Hanzel, Thin Solid Films 2005, 492, 158-165.

[29] R. Sanjinés, H. Tang, H. Berger, F. Gozzo, G. Margaritondo, and F. Lévy, J. Appl. Phys. 1994, 75, 2945-2951.

[30] B. Bharti, S. Kumar, Heung-No Lee and R. Kumar, Sci. Rep. 2016, 6, 32355.

[31] X. Pan, M.-Q. Yang, X. Fu, N. Zhang and Y.-J. Xu, Nanoscale 2013,5, 3601-3614.

[32] Li-Jian Meng, C. P. Moreira de Sá, and M. P. dos Santos, Thin Solid Films 1994, 239, 117-122.

[33] C. D. Wagner, W. M. Riggs, L. E. Davis, J. F. Moulder, G. E. Muilenberg, Handbook of X-ray Photoelectronic Spectroscopy, Perkin-Elmer Corp, Eden Prairie, Minnesota, 1979.

[34] G. Jerkiewicz, Electrocatalysis 2010, 1, 179-199.

[35] K. Kinoshita, D. R. Ferrier, P. Stonehart, Electrochim. Acta 1978, 23, 45-54.

[36] T. J. Schmidt, H. A. Gasteiger, G. D. Stäb, P. M. Urban, D. M. Kolb, R. J. Behm, J. Electrochem. Soc. 1998, 145, 2354-2358.

[37] Q.-S. Chen, F. J. Vidal-Iglesias, J. Solla-Gullon, S.-G. Sun, J. M. Feliu, Chem. Sci. 2012, 3, 136-147.

[38] A. Pozio, M. De Francesco, A. Cemmi, F. Cardellini, L. Giorgi, J. Power Sources 2002, 105, 13-19.

[39] H. Wang, Z. Jusys, R.J. Behm, J. Power Sources 2006, 154, 351-359.

[40] T. Iwasita, E. Pastor, Electrochim. Acta 1994, 39, 531-537.

[41] W. Guo, C. Xu, X. Wang, S. Wang, C. Pan, C. Lin and Z. Lin Wang, J. Am. Chem. Soc. 2012, 134, 4437-4441.

Supplementary material

Three-dimensional Pt catalyst on TiO_2 Structures: Synthesis, Characterization and Optimal Morphology for Efficient Ethanol Electrooxidation in Acidic Medium

Naser Mohammadi, Chahrazed Benabid, Haixia Wang, Juan Carlos Abrego-Martinez, Youling Wang and Mohamed Mohamedi

Énergie, Matériaux et Télécommunications (EMT), Institut National de la Recherche Scientifique (INRS), 1650 Boulevard Lionel Boulet, Varennes, Quebec, J3X 1S2, Canada

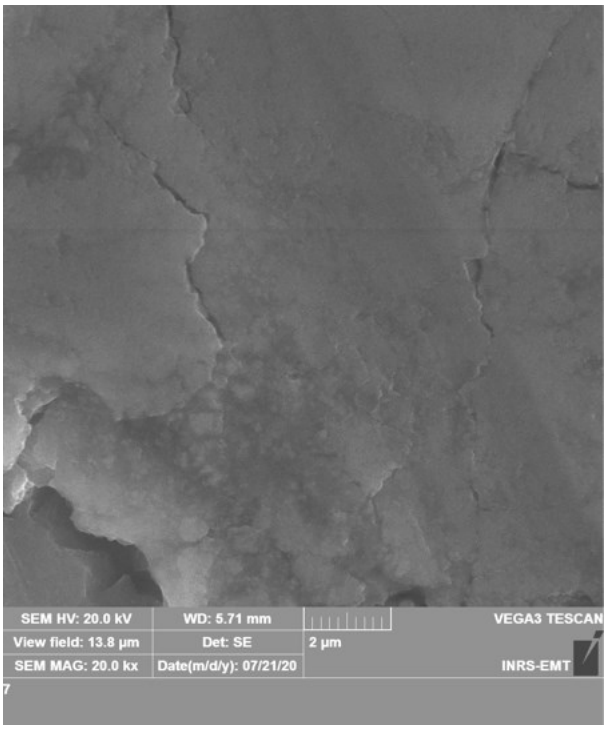

Figure S1. SEM image of the Ti foil. The image was taken with a Vega 3 Tescan electron microscope.

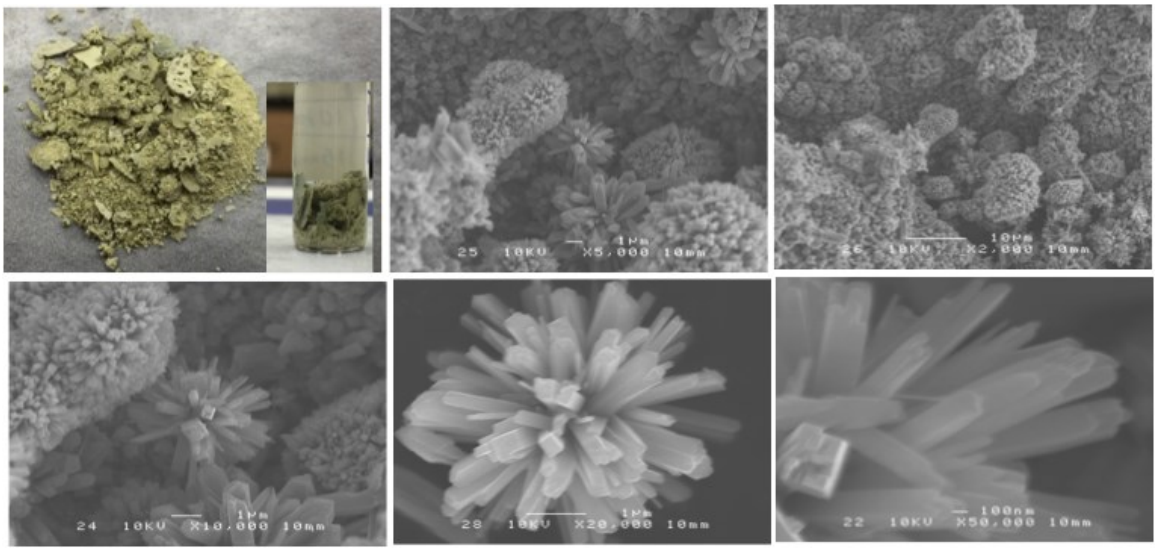

Figure S2. Picture and SEM images with increasing amplification of the TiO_2 powder using a concentration of 1.12 M HCl and 10 mL of the reaction solution.

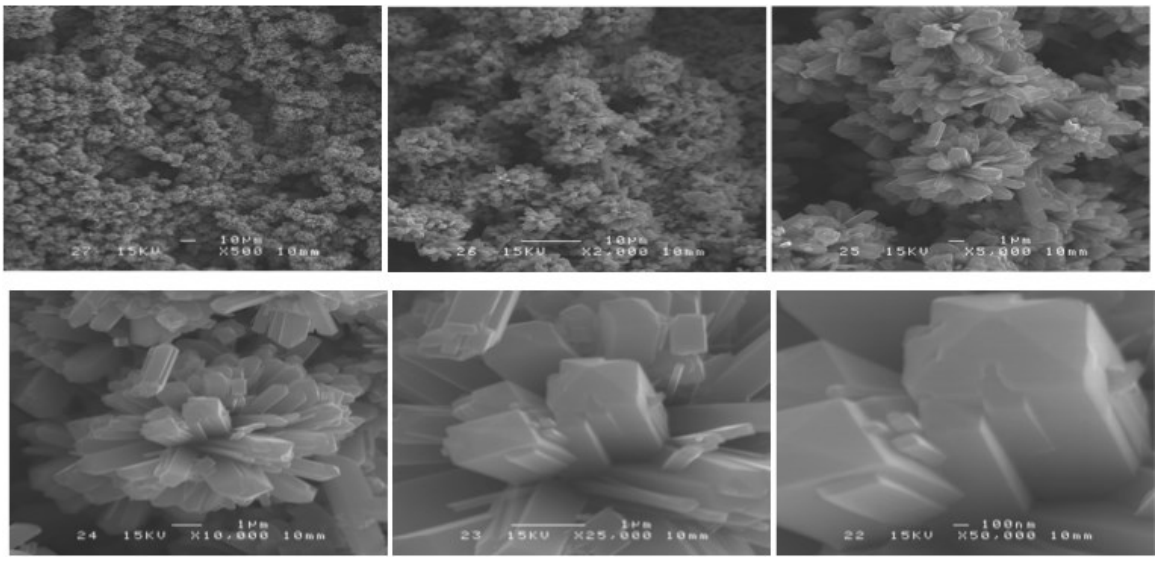

Figure S3. Picture and SEM images with increasing amplification of the TiO_2 using a concentration of 1.12 M HCl and 5 mL of the solution.

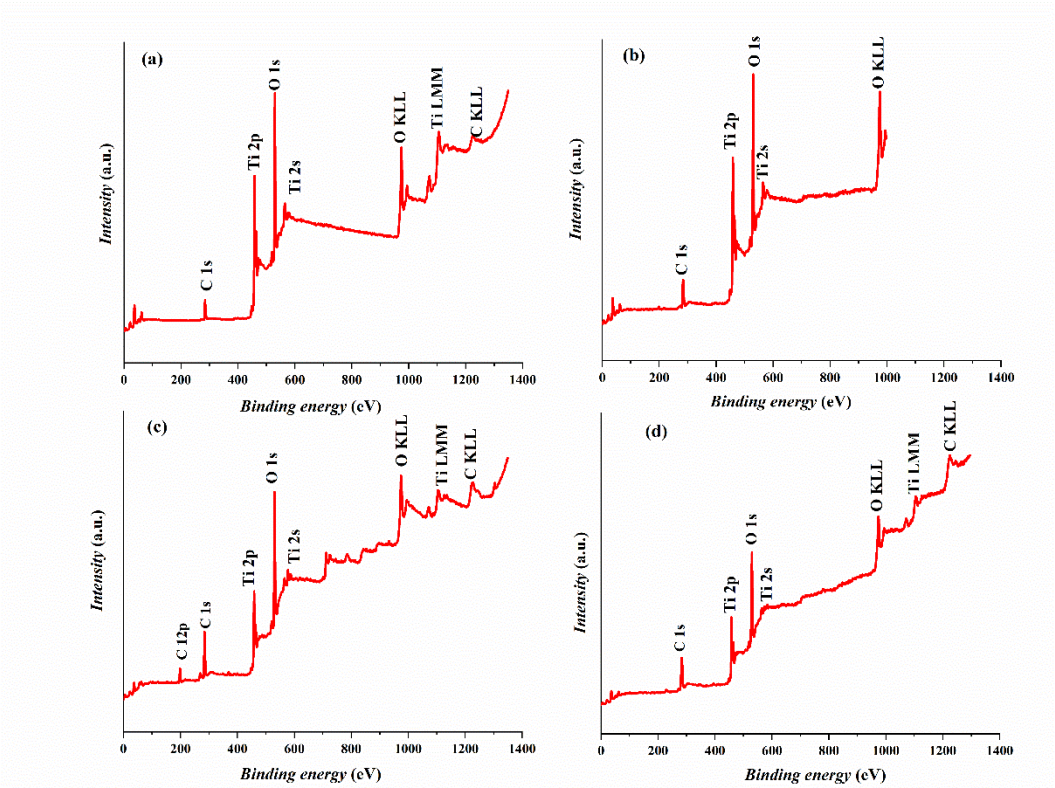

Figure S4. XPS survey scans of (a) Sample 0.6M, (b) Sample 0.6M200, (c) Sample 0.78M and (d) Sample 1.12M.

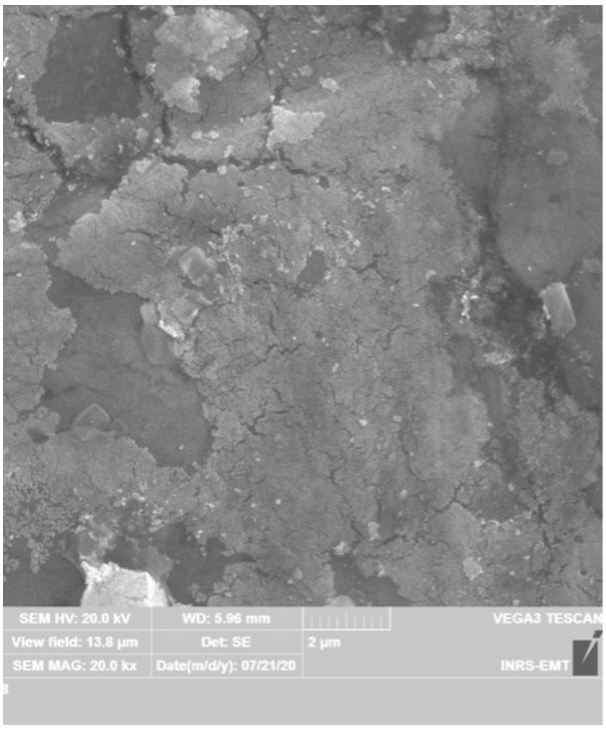

Figure S5. SEM image of Pt/Ti (foil) catalyst. The image was taken with a Vega 3 Tescan electron microscope.

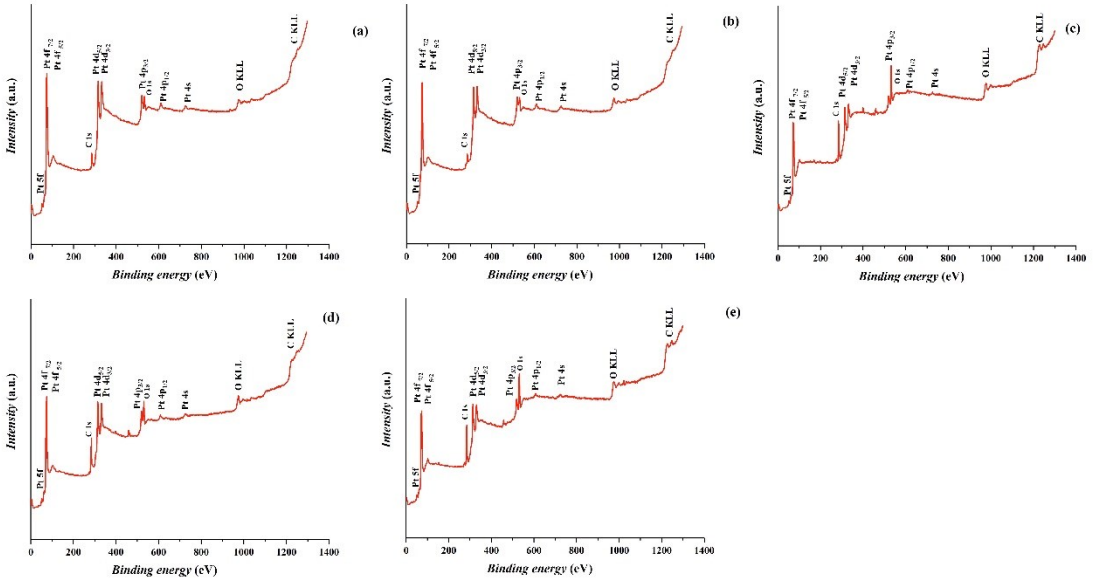

Figure S6. XPS survey scans of (a) Pt/Sample 0.6M, (b) Pt/Sample 0.6M200, (c) Pt/Sample 0.78M, (d) Pt/Sample 1.12M and (e) Pt/Ti foil.

4 THE 2ND ARTICLE

Three-Dimensional Pinecones-like Binder-Free Pt–TiO_2 Nanorods on Ti mesh Structures: Synthesis, Characterization and Electroactivity towards Ethanol Oxidation

Nanobâtonnets de Pt–TiO_2 sans liant tridimensionnels de type pomme de pin sur des structures en maille de Ti: synthèse, caractérisation et électroactivité vis-à-vis de l'oxydation de l'éthanol

Authors:

Naser Mohammadi, Juan Carlos Abrego-Martinez, and Mohamed Mohamedi

Énergie, Matériaux et Télécommunications (EMT), Institut National de la Recherche Scientifique (INRS), 1650 Boulevard Lionel Boulet, Varennes, Quebec, J3X 1P7, Canada

Title of the journal or book:

MOLECULES

Molecules 2022, 27, 1921

DOI: 10.3390/molecules27061921

Contribution :

I combined the hydrothermal and pulsed laser deposition methods and synthesized (3-D) pinecones-shaped Pt/TiO_2/Ti mesh structures. I conducted the structural characterizations and ethanol oxidation experiments, analyzed the data and interpreted the results. I contributed in the writing with the help of the co-authors.

Abstract

We report here the synthesis of binderless and template-less three-dimensional (3-D) pinecones-shaped Pt/TiO_2/Ti mesh structure. The TiO_2 hydrothermally synthesized onto Ti mesh is composed of a mixture of flowers-like nanorods and vertically aligned bar-shaped structures,

whereas, Pt film grown by pulsed laser deposition displays a smooth surface. XRD analyses reveal an average crystallite size of 41.4 nm and 68.5 nm of the TiO_2 nanorods and Pt, respectively. In H_2SO_4 solution, the Pt oxide formation at the Pt/TiO_2/Ti mesh electrode is 180 mV negative than that at the Pt/Ti mesh electrode, indicating that TiO_2 provides oxygeneous species at lower potentials, which will facilitate the removal of CO-like intermediates and accelerate ethanol oxidation reaction (EOR). Indeed, the Pt/TiO_2/Ti mesh catalyst exhibits current activity of 1.19 mA towards EOR remarkably superior by 4.4 times than Pt/Ti mesh electrode (0.27 mA). Moreover, the presence of TiO_2 as support to Pt delivers a steady-state current of 2.1 mA, which an increment in durability of 6.6 times compared to Pt/Ti mesh (0.32 mA). Pt is chosen here as a benchmark catalyst and we believe that with catalysts that perform better than Pt, such 3-D pinecones structures can be useful for a variety of catalytic or photoelectrochemical reactions.

Keywords: titanium dioxide; titanium mesh; platinum; hydrothermal method; pulsed laser deposition; ethanol electrooxidation

Résumé

Nous rapportons ici la synthèse d'une structure de maille Pt/TiO_2/Ti en forme de pomme de pin tridimensionnelle (3-D) sans liant et sans gabarit. Le TiO_2 synthétisé de manière hydrothermique sur le maillage de Ti est composé d'un mélange de nanotiges en forme de fleurs et de structures en forme de barre alignées verticalement, tandis que le film de Pt développé par dépôt laser pulsé affiche une surface lisse. Les analyses XRD révèlent une taille moyenne de cristallite de 41,4 nm et 68,5 nm des nanotiges de TiO_2 et de Pt, respectivement. Dans la solution H_2SO_4, la formation d'oxyde de Pt au niveau de l'électrode à mailles Pt/TiO_2/Ti est négative de 180 mV par rapport à celle de l'électrode à mailles Pt/Ti, ce qui indique que TiO_2 fournit des espèces oxygénées à des potentiels inférieurs, ce qui facilitera l'élimination des composés de type CO. intermédiaires et accélérer la réaction d'oxydation de l'éthanol (EOR). En effet, le catalyseur à mailles Pt/TiO_2/Ti présente une activité de courant de 1,19 mA vers EOR remarquablement supérieure de 4,4 fois à l'électrode à mailles Pt/Ti (0,27 mA). De plus, la présence de TiO_2 comme support au Pt délivre un courant en régime permanent de 2,1 mA, soit une augmentation de la durabilité de 6,6 fois par rapport au maillage Pt/Ti (0,32 mA). Le Pt est choisi ici comme catalyseur de référence et nous pensons qu'avec des catalyseurs plus performants que le Pt, de telles structures de pommes de pin 3D peuvent être utiles pour une variété de réactions catalytiques ou photoélectrochimiques.

Mots clés: Dioxyde de titane ; maille de titane; platine; méthode hydrothermale; dépôt laser pulsé; électrooxydation de l'éthanol.

4.1 Introduction

There is a growing need for lightweight, higher efficiency, cheap, durable and safe energy storage and conversion devices to meet special needs for next-generation high-performance portable electronic devices. Current research is focusing on flexible and wearable electronic devices such as roll-up display, light-emitting diodes, smart watches, fitness-tracking and implantable sensors that can monitor blood pressure and other health metrics [1]. Such devices are being developed rapidly and essentially require low power sources systems with flexible electrodes, separators and substrates to accomplish all-in-one flexible systems. Several types of lightweight power sources are being worldwide developed, including Li-ion batteries, supercapacitors, solar cells, fuel cells and biofuel cells [2-6].

Generally, traditional electrodes used in electrochemical power sources (EPSs) are composed of mixtures of active materials, polymeric binders and conductivity enhancers, like carbon black, graphite and carbon nanotubes, which are ink-coated over metal current collectors such as copper, aluminum or carbon paper. The additives, the metal collector elements are not only unsuitable for flexibility but add extra-weight to the EPS device. Hence, the ability to eliminate such additives and fabricate a binder and additive-free, flexible electrode would signify notable advancement for high-performance flexible EPSs. A flexible electrode could be either an electroactive material with inherent flexibility, or a composite catalyst layer built on a flexible substrate.

Metallic grids or meshes based on Ti as flexible current collectors are receiving a lot of attention due to their excellent flexibility, conductivity, and three-dimensional (3-D) structures that can host active materials. Few examples of using Ti mesh in electrochemical technology include fabrication of high performance Pt/Ti counter electrodes on Ti mesh for flexible large-area dye-sensitized solar cells [7], TiO_2 nanotubes on Ti mesh electrodes for improved photoelectrochemical reaction [8], TiO_2 nanotube arrays formed on Ti meshes for flexible dye-sensitized solar cells [9], TiO_2 nanotubes grown on Ti grid as anode for Li-ion microbatteries [10], MnO_2-modified TiN nanotube arrays on Ti mesh for flexible supercapacitors electrode [11], and electrochemical glucose sensor using ternary NiCoP nanosheet array deposited on a Ti mesh [12].

In addition to the fact that TiO_2 is not expensive to synthesize, non-toxic, possesses high mechanical and corrosion resistance, chemical stability in both alkaline, acidic, and oxidative environments; TiO_2 is investigated as a substitute catalyst support to carbon in fuel cells such as H_2/O_2 [13-15], direct methanol fuel cells (DMFC), [16-19] and microbial fuel cells [20-21].

In this work, we report for the first time the synthesis of original 3-D pinecones-like Pt–TiO_2 nanorods on Ti mesh electrodes. TiO_2 arrays are grown via hydrothermal technique on Ti mesh, whereas Pt film is grown by pulsed laser deposition (PLD) onto the TiO_2/Ti mesh. For comparison, Pt was also synthesized by PLD on bare Ti mesh. The structural properties of these materials are studied with scanning electron microscopy (SEM), X-ray diffraction (XRD) and X-ray photoelectron spectroscopy (XPS). The electron transfer properties of the Pt/TiO_2/Ti mesh are assessed for the ethanol oxidation reaction (EOR) with linear scan voltammetry (LSV). The EOR chosen is first and foremost important for the direct ethanol fuel cell (DEFC) technology and also because we have been actively studying the EOR for years. Pt is selected here as a model catalyst because of its well-known behavior towards EOR. Finally, the durability of the synthesized Pt/TiO_2/Ti mesh comparatively with Pt/Ti mesh is studied with long-term chronoamperometry (CA).

4.2 Results and Discussion

4.2.1 Materials characterization

The photograph and SEM images of the pristine Ti mesh are shown in Figure S1 (Supplementary Materials) for comparison. Figure 1 reports SEM micrographs at increasing magnifications of the TiO_2 grown by hydrothermal technique on Ti mesh. As can be seen from SEM the images, the Ti mesh was evenly coated with TiO_2. Higher magnifications show that the as prepared TiO_2 is composed of a mixture of flower-like nanorods and vertically aligned bar-shaped structures.

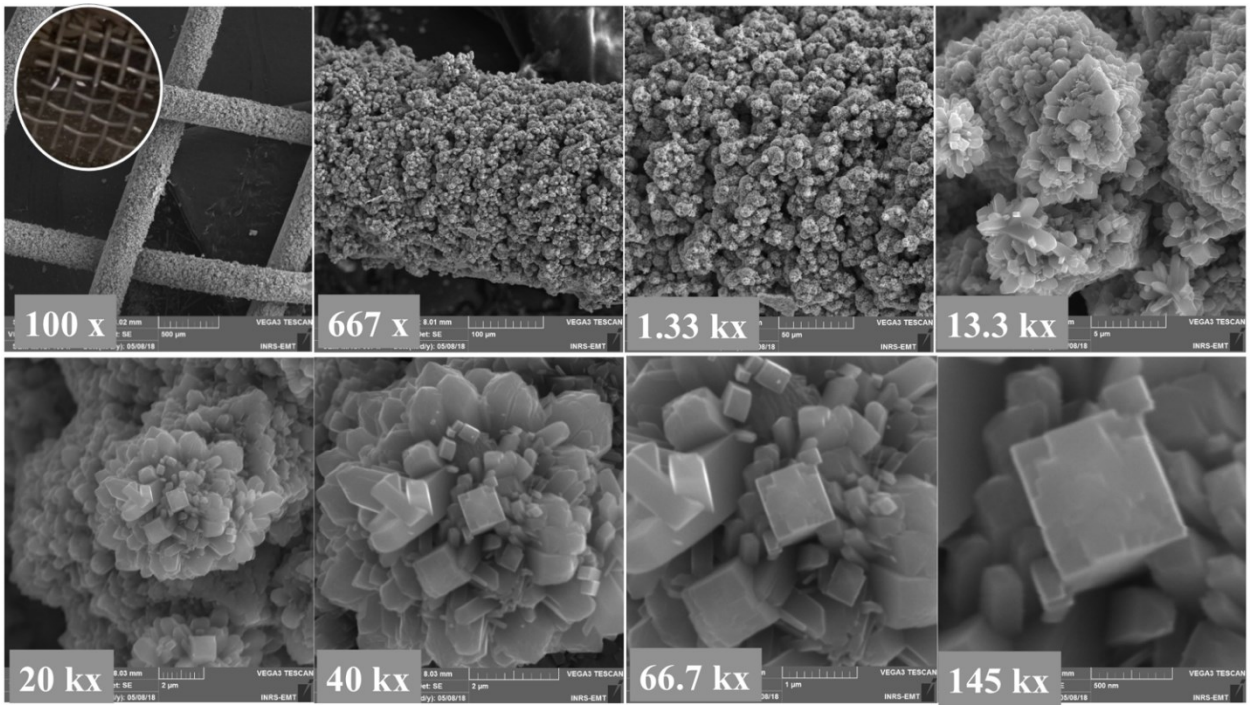

Figure 1. SEM images at different magnifications of hydrothermally-grown TiO_2 on Ti mesh. Inset at the top left figure represents a photograph of TiO_2/Ti mesh.

The XRD crystalline structure corresponding to the TiO_2/Ti mesh is reported in Figure 2. The peaks relate to rutile TiO_2 (JCPDS 21-1276). The highest peak TiO_2 (110) was employed to calculate the average crystallite size (L). This was done using the Debye-Scherrer equation: $L=0.89\ \lambda/\ \beta\ cos\ \theta$, with λ corresponding to the wavelength of 1.5406 Å, β to the full-width at half-maximum (FWHM), and θ is the Bragg angle. Accordingly, the average crystallite size of the TiO_2 nanorods was estimated to be 414 Å.

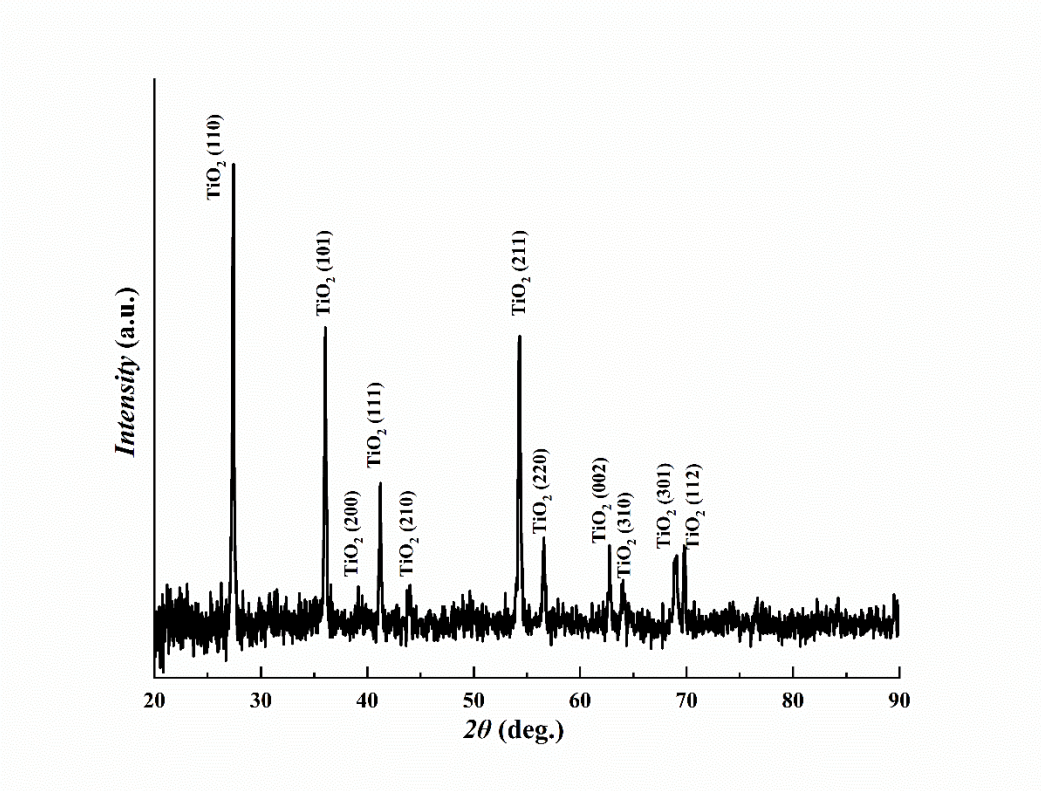

Figure 2. XRD analysis of TiO_2 grown onto Ti mesh via hydrothermal method.

Figure 3 shows the XPS spectra of the TiO_2/Ti mesh structure. The survey spectrum (Figure 3a) contains the most prominent lines of Ti 2p, O 1s and C 1s at standard positions. The carbon contamination is practically impossible to avoid. Fortunately, it is usually restricted to the film-air interface. Figure 3b and Figure 3c reveal respectively, the high-resolution XPS Ti 2p and O 1s peaks at the surface of TiO_2/Ti mesh. The positions of the Ti $2p_{1/2}$ and Ti $2p_{3/2}$ separated by 5.60 to 5.64 eV demonstrating by that Ti was as Ti^{4+} state at the surface [24-26]. The O 1s peak is asymmetrical, which signifies that oxygen appears in two different chemical states at least. The O 1s spectrum (Figure 3c) could be deconvoluted into two contributions that are OI and OII. The first contribution (OI) occurring within binding energies of 529.9~530 eV is ascribed the normal lattice sites occupied by oxygen in the TiO_2 structure. The second contribution (OII) appearing at 531~532 eV is ascribed to non-lattice oxygen [27]. This high binding energy component has been assigned to oxygen bonded to Ti^{+3} ($O–Ti^{3+}$) or to hydroxyl species that are simply created at the surface of oxide films [28]. By considering the relative areas related to the main O 1s component (linked principally to Ti^{4+}-O bonds) and the relative area of the main Ti 2p contribution, we obtain an [O]/[Ti] ratio of 3.8. Meng et al have studied the porosities of titanium oxide films prepared by

d.c. reactive magnetron sputtering at different oxygen partial and total pressures [29]. They have ascribed the presence of the non-lattice O component to porosity, as a result of the moisture that accrues mainly in the pores or void between the TiO_2 columns of the material, which might be responsible of the deviation from stoichiometry. The same authors have employed the ratio of $O_{II}/(O_I+O_{II})$ as a measure of the porosity. In our case, we found the $O_{II}/(O_I+O_{II})$ ratio equal to 0.44, which is slightly higher than 0.38 obtained by Meng et al for porous TiO_2 film that had a higher O-H bonding component. Therefore, it may be assumed that our synthesized TiO_2 arrays display porosity higher than the stoichiometric films.

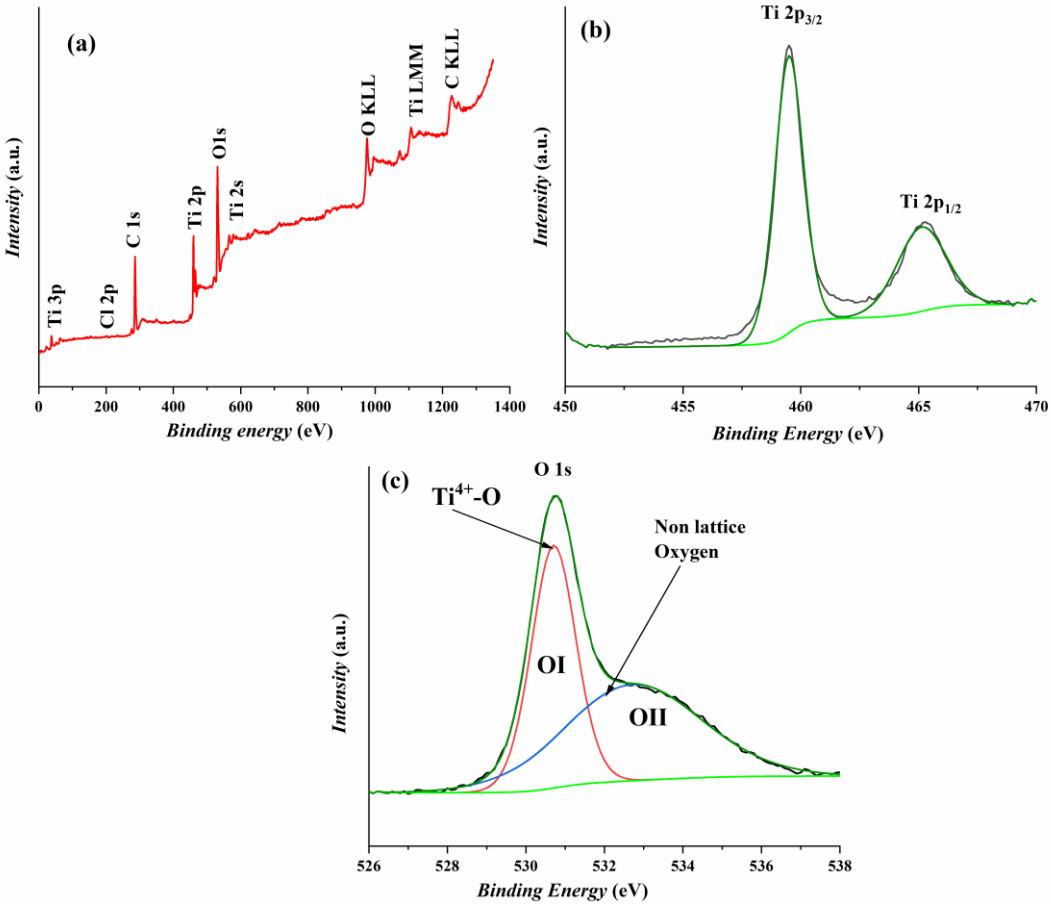

Figure 3. XPS analyses of TiO_2/Ti mesh. (a) Survey scan, (b) high-resolution XPS spectrum of Ti 2p core level, and (c) high-resolution XPS spectrum O 1s core level.

4.2.2 Characterization of Pt/TiO2/Ti mesh

SEM images of Pt/Ti mesh structure revealed that the surface morphology of the Pt film is very smooth (Figure 4). The XRD indexation (Figure 4, right side) of Pt peaks is in agreement with

respectively (111), (200), (220), (311) and (222) planes of a face centered cubic (fcc) structure (JCPDS PDF No. 04-0802). The most intensive diffraction peak Pt (111) is selected to calculate the lattice constant (*a*) and the average crystallite size of Pt by Bragg's law and Debye-Scherrer equation, respectively. The average crystallite size of Pt deposited Ti mesh was found to be 932 Å. On the other hand, the lattice constant was calculated to be close to 3.924 Å close to theoretical value of 3.923 Å.

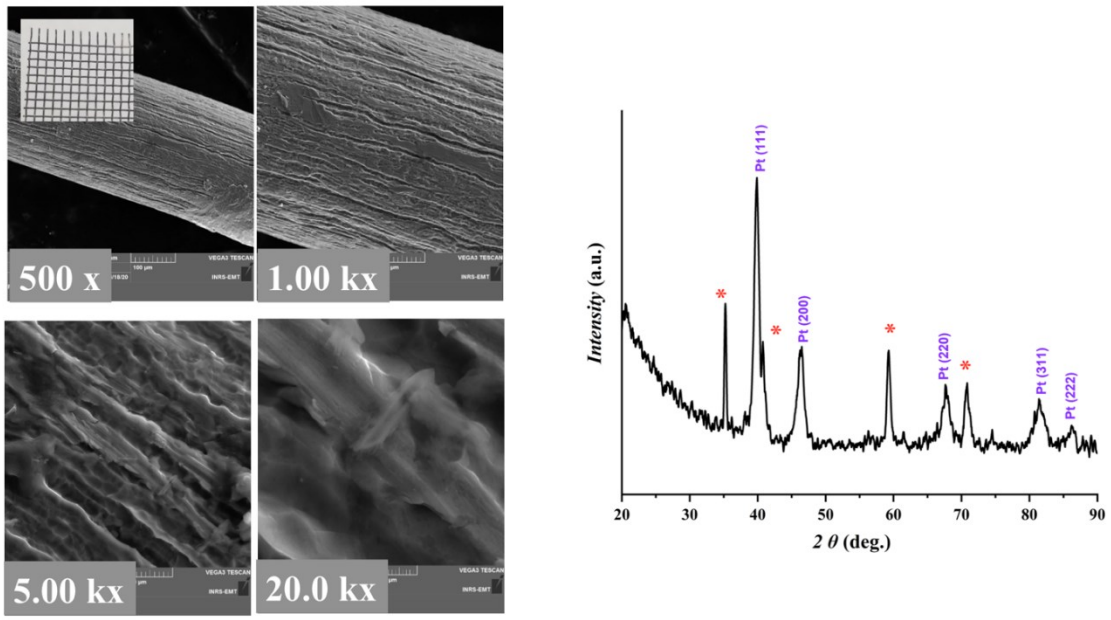

Figure 4. SEM micrographs at increasing magnifications of Pt grown by PLD onto Ti mesh. Inset at the top left figure represents a photograph of Pt/Ti mesh. Right side figure represents the XRD analysis of Pt/Ti mesh. (*) Corresponds to the TiO_2 substrate.

Instead, the morphology of Pt films deposited on the TiO_2 arrays is unlike from Pt synthesized on Ti mesh. Figure 5 at higher magnifications shows that the Pt/TiO_2 resembles to 3-D pinecones-shaped structure. The lattice parameter and the average crystallite size calculated from XRD of Figure 6 were found to be 3.885 Å and 685 Å, respectively. Table 1, resumes the various XRD characteristics of the Ti mesh, TiO_2/Ti mesh, Pt/Ti mesh and Pt/TiO_2/Ti mesh. From the table, it can be seen that the average crystallite size of Pt is smaller than that of Pt grown on Ti mesh, suggesting that TiO_2 enhanced the distribution quality of the Pt nanoparticles. It can also be observed that the lattice parameter of Pt synthesized on TiO_2 is lesser than that of Pt produced on Ti mesh. This might exhibit a size-induced lattice contraction in the as-prepared state with respect to bulk Pt. The interaction of oxides with metallic nanostructures has extensively been

investigated with particular emphasis on the effect of surface oxygen vacancies [30]. Oxygen vacancies at the metal support interface are recognized to induce charge transfer from the oxide to the metal easing the binding of the metal to the oxide. It has been reported that Pt is strongly adsorbed at oxygen vacancy sites in TiO_2 [31]. It has previously been discussed that lattice strain can dramatically affect electrochemical activity [32-34]. Hence it is anticipated that the support-induced lattice strain observed in Pt/TiO_2 could potentially enhance electrocatalytic activity, compared with Pt/Ti mesh.

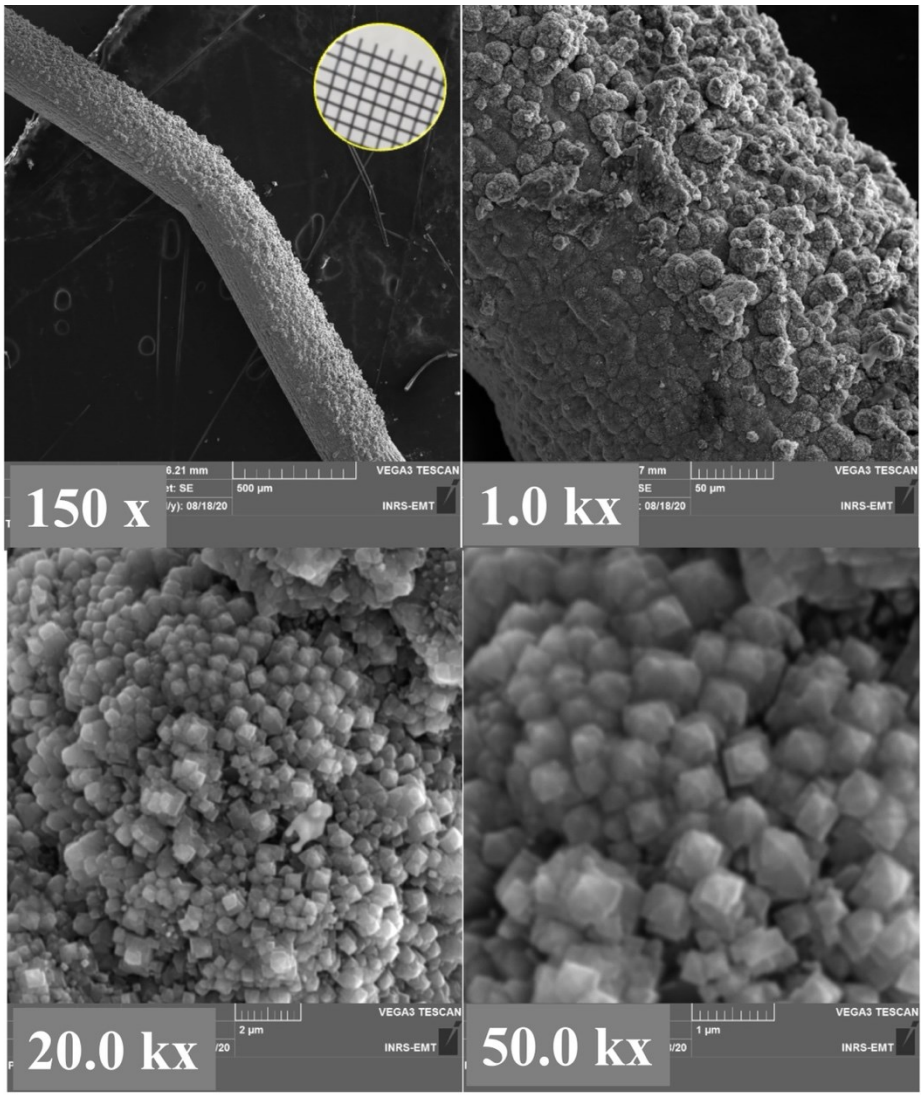

Figure 5. SEM micrographs at increasing magnifications of Pt grown by PLD onto TiO_2/Ti mesh structure. Inset at the top left figure represents a photograph of Pt/TiO_2/Ti mesh.

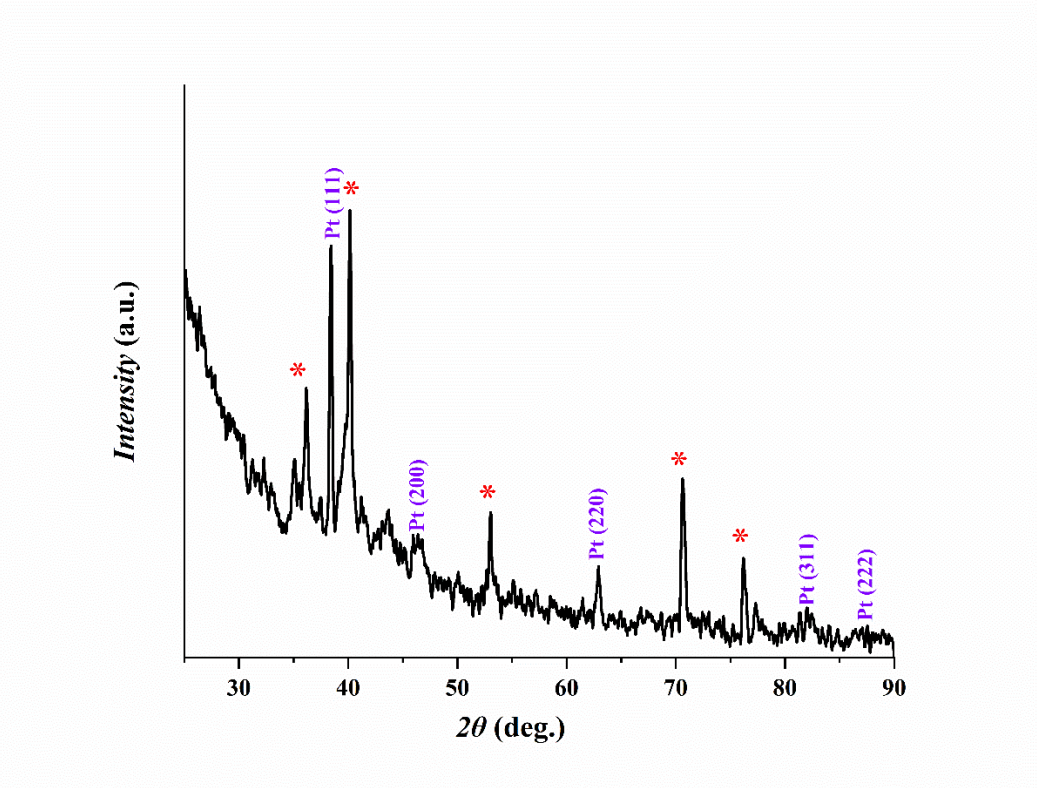

Figure 6. XRD analysis of Pt grown onto TiO_2/Ti mesh. (*) Corresponds to the TiO_2 substrate.

Table 1. XRD characteristics of the Ti mesh, TiO_2/Ti mesh, Pt/Ti mesh and Pt/TiO_2/Ti mesh.

	Ti mesh	**TiO_2/Ti mesh**	**Pt/Ti mesh**		**Pt/TiO_2**	
	Ti	Ti	Ti	Pt	Ti	Pt
Lattice constant (Å)	a=2.953 c=4.687	a=2.957 c=4.599	a=2.951 c=4.682	a=3.924	a=2.960 c=4.598	a=3.887
L (Å)	607.1	581.7	551.8	932.3	414.6	685.5

The XPS survey spectrum of the Pt/TiO_2 material shown in Figure S2 (Supplementary Materials) reveals that the surface exclusively consists of Pt, O and C elements. No Ti metal is detected indicating that the Pt film homogenously coats the underneath TiO_2 nanorods. Figure 7a and Figure 7b report the high-resolution Pt 4f core-level spectrum at the Pt/Ti mesh and Pt/TiO_2/Ti

mesh, respectively. The spectra show that Pt exists in the form of at least three oxidation states. The spectra were indeed were adequately deconvoluted into three overlapping curves assigned to Pt^0, Pt^{2+} and Pt^{4+} species. Table 2 resumes the binding energy (*BE*) and relative amount of these three species assessed from the relative area of the integrated peak intensities. The peaks position of Pt^0, Pt^{2+} and Pt^{4+} are in agreement with the values found in the literature [35-36]. The shift toward higher *BE* values compared to literature values (71.0 eV) is ascribed to the metal−support interaction and to small Pt nanoparticle sizes [37-38]. This positive shift may also imply metal−support interactions between TiO_2 and Pt as observed with XRD analyses. This interaction can change the electronic properties of Pt by increasing the Pt *d*-vacancy via electronic donation to Lewis acid centers such as Ti^{x+} at the Pt/TiO_2 interface [39-41].

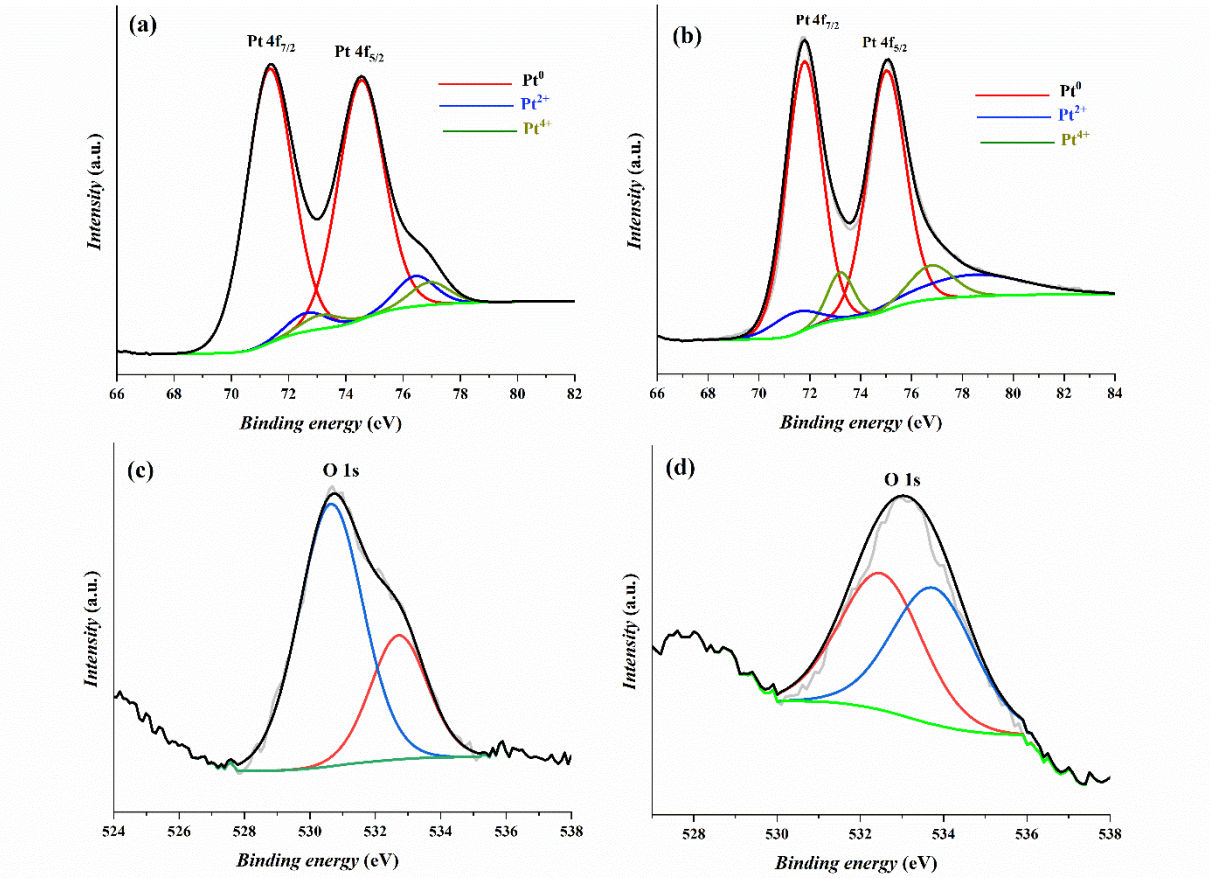

Figure 7. High-resolution XPS spectra of Pt 4f core level and O 1s core level. (a) and (c) Pt/Ti mesh. (b) and (d) Pt/TiO_2/Ti mesh.

From Table 2, it can be noted that in the Pt/Ti mesh, Pt^0 is widely distributed on the surface with 87.7 at% followed by slight relative concentrations (<7 at%) of Pt^{2+} and Pt^{4+}. It has to be noted

that for Pt deposition onto the Ti mesh, the former has not been etched on purpose in order to better assess the effect of TiO_2 morphology (layer vs nanorods) on the electrochemical performance. Hence, the oxygen is due to the native TiO_2 layer present on the surface of the mesh. As to Pt/TiO_2 sample, the concentration of Pt^0 decreased while those of Pt^{2+} and Pt^{4+} increased at the Pt-TiO_2. From Table 2, compared to Pt/Ti mesh, it is further noticed that in Pt/TiO_2/Ti mesh, the position of Pt^0 shifted by 0.45 eV toward higher *BE*s while that of Pt^{2+} moved by 1.26 eV toward lower *BE*s. These shifts can be explained by different sizes of Pt particles and different degrees of interaction with the TiO_2 support, signifying a strong interaction between the TiO_2 nanorods and the above Pt film. Other researchers have observed Pt/TiO_2 composites exhibiting ionized platinum, which was also ascribed to the strong interaction between Pt and TiO_2 support [39-40, 42]. This behavior can be assumed to the presence of oxygen vacancies at the TiO_2 support interface. The Pt^{4+} (PtO_2) is the result of Pt cations replacing those of Ti in the TiO_2 lattice, and the Pt atoms at the surface create Pt^{2+} species. The O 1s core level peaks for the Pt/Ti mesh and Pt/TiO_2/Ti mesh materials are shown in Figure 2c and Figure 2d, respectively. A simple visual inspection of the O1s peak shows that it is wide and asymmetrical (Figure 7c and 7d). Therefore, the peak could be well deconvoluted in two peaks and the resulting parameters are too reported in Table 2. In this case, the OI element is ascribed to the bulk lattice oxygen, whereas the OII component is attributed to the surface lattice oxygen [43].

Table 2. XPS fitting parameters from the core-level spectra of Pt 4f and O 1s.

Sample	Pt^0		Pt^{2+}		Pt^{4+}			O 1s	
	BE (eV)	at%	*BE* (eV)	at%	*BE* (eV)	at%	Pt^2/Pt^{4+}	O_I	O_{II}
Pt/Ti mesh	71.33	87.73	72.63	7.01	73.13	5.25	1.34	530.64 (70.5)	532.71 (29.5)
Pt/TiO_2	71.78	75.90	71.37	13.15	73.20	10.95	1.20	532.50 (50)	533.75 (50.0)

Numbers between brackets are species surface percentage.

4.2.3 Electrochemical characterization

Figure 8a recorded with 50 mV s^{-1} compares CVs of Pt/Ti mesh and Pt/TiO_2/Ti mesh electrodes in 0.5 M H_2SO_4 deaerated solution. It has to be reiterated that both electrodes contained similar amount of Pt (0.120 mg cm^{-2}). At the Pt/TiO_2/Ti mesh electrode, the CV contained the classical features of hydrogen atoms adsorption (H_{ads}) and hydrogen atoms desorption (H_{des}) peaks from -0.2 to 0.1 V [44-46]. On the other hand, the H_{ads}/H_{des} features were ill-defined at the Pt/Ti mesh electrode. In addition, the current of the H_{ads}/H_{des} peaks at the Pt/TiO_2/Ti mesh are distinctively greater than those delivered by the Pt/Ti mesh, which clearly indicates the greater surface area at the former electrode [47]. This also means that Pt/TiO_2 has larger surface area than Pt/Ti mesh. The larger surface area signifies smaller particle size [48], confirming by that TiO_2 improved the dispersion and utilization of the Pt nanoparticles, which is in line with the XRD analyses (Table 1). The Pt oxide formation ($PtOx_f$) at the Pt/Ti mesh starts at 0.74 V whereas its equivalent reduction ($PtOx_r$) peak potential takes place at 0.56 V vs. Ag/AgCl. On the other hand, $PtOx_f$ and $PtOx_r$ were located at 0.44 V and 0.48 V, respectively at the Pt/TiO_2/Ti mesh. This implies that TiO_2 can provide oxygenated species at lower potentials, which will facilitate the removal of CO-like intermediates and accelerate EOR.

Subsequently, the effect of the TiO_2 arrays on the electrocatalytic behaviour of Pt was investigated towards electrooxidation of ethanol. Figure 8b shows comparative LSVs obtained in 0.5 M H_2SO_4+1 M C_2H_5OH solution at 5 mV s^{-1} (quasi-steady state) at Pt/Ti mesh and Pt/TiO_2/Ti mesh electrodes. Forward and backward CVs in the 0.5 M H_2SO_4+1 M C_2H_5OH solution are shown in Figure S3. The LSVs at both electrodes showed characteristic EOR waves in accordance with the literature [49-50]. The onset potential, E_{onset}, peak potential (E_p), I@ 0.50V, and peak current I_p values extracted from LSVs of Figure 8b are reported in Table 3. E_{onset} is a criterion that provides knowledge about the kinetic of an electrochemical reaction and is identified here as the value at which a current begins for the electrooxidation ethanol. I@ 0.50 V is an experimental condition near to the projected functioning potential of DEFCs devices and allows comparing the progress of the EOR catalytic activity amongst different electrocatalysts. Hence from Table 3, it can be observed that E_{onset} and E_p are not significantly different at both electrodes. However, Pt/TiO_2/Ti mesh demonstrated the best catalytic activity toward EOR in terms I_p of 1.85 mA that is remarkably 3.5 times superior than I_p delivered by Pt/Ti mesh. Further outstanding performance of the Pt/TiO_2/Ti mesh is obviously its value of I@0.5V, which is 4.4 times superior to Pt/Ti mesh.

Chronoamperometric (CA) experiments were performed to examine the electrodes durability. Figure 8c shows the current-time (*I*-*t*) curves of Pt/Ti mesh and Pt/TiO_2/Ti mesh for EOR at 0.6 V upon 3600 s testing. It can be seen that in both CA profiles, the current increased abruptly, then decreased and ultimately attained a quasi-steady-state behavior. In Figure 8c, one can observe that the current decay for the EOR on the Pt/TiO_2/Ti mesh catalyst is significantly slower than that on the bare Pt/Ti catalyst. The first current increase is due to the double-layer charging effect, whereas the initial decay was caused by the rapid increase of the surface coverage by intermediate species, such as adsorbed CO during EOR [51]. After 3600 s, the quasi steady-state current density (I_{ss}) at the Pt/TiO_2/Ti mesh was 6.6 times greater than that of Pt/Ti mesh (Table 3).

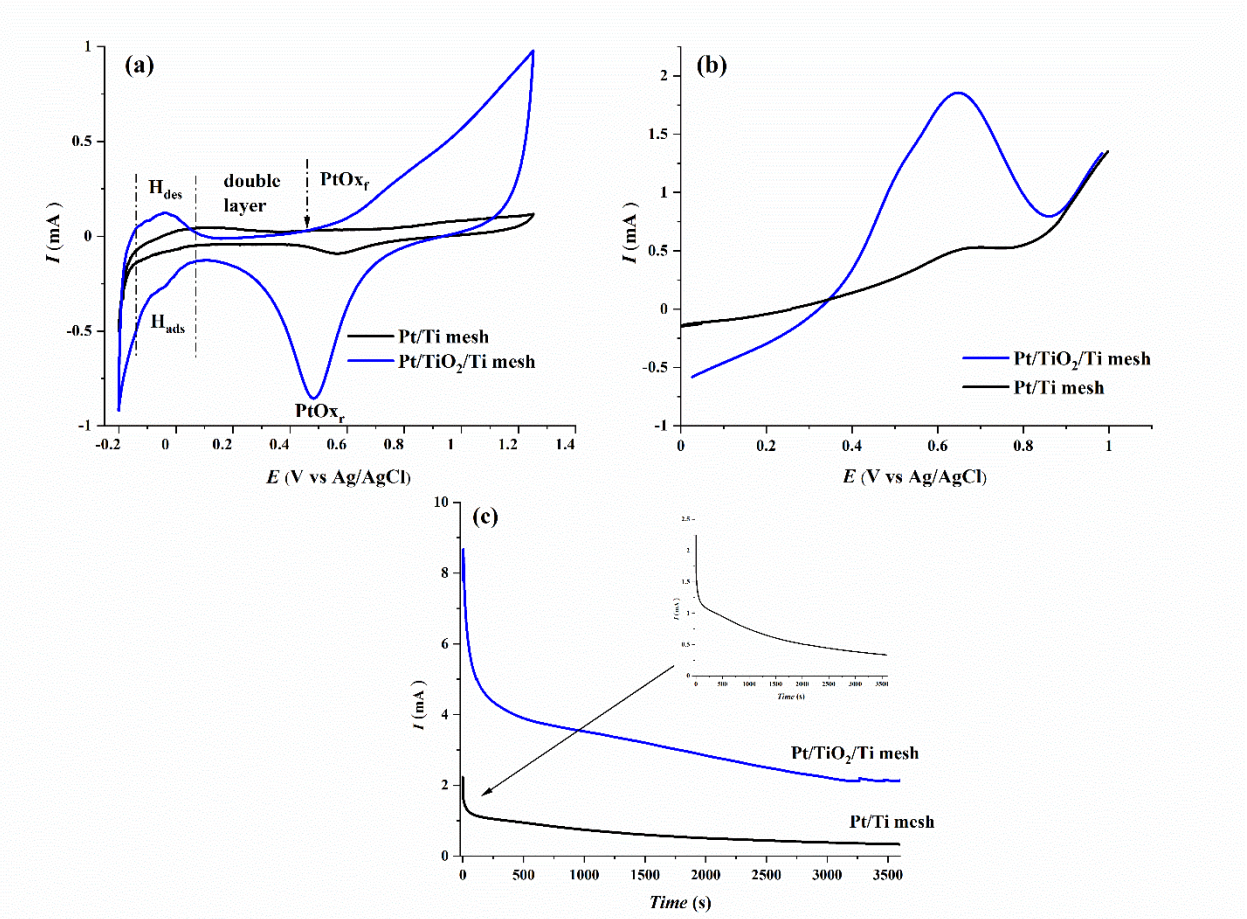

Figure 8. Electrochemical studies (a) Cyclic voltammetry in 0.5 M H_2SO_4-argon purged solution with a potential scan rate of 50 mV s^{-1}. (b) Linear scan voltammetry in 0.5 M H_2SO_4+ 1 M C_2H_5OH solution with a potential scan rate of 5 mV s^{-1}. (c) Chronoamperometry in 0.5 M H_2SO_4+ 1 M C_2H_5OH solution.

Table 3. Comparative main electrochemical performance parameters.

	EOR				Durability
	E_{onset} (V)	E_p (V)	I_p (mA)	$I@0.5\ V$ (mA)	I_{ss} (mA)
Pt/Ti mesh	0.26	0.67	0.53	0.27	0.32
Pt/TiO_2/Ti mesh	0.30	0.65	1.85	1.19	2.1

In summary, it is clear that incorporating TiO_2 flower-like nanorods and vertically aligned bar-shaped structures as a supporting material considerably increased the electrochemical activity of the Pt catalyst. Therefore, it can be suggested that the Pt/TiO_2 /CP catalyst offers a higher Pt utilization than the unsupported Pt/Ti mesh catalyst.

4.3 Materials and Methods

4.3.1 Growth of TiO2 arrays onto Ti mesh

Titanium meshes of 1.5 cm x 2 cm with 0.5 mm thickness were placed in an ultrasonic bath containing acetone and washed 20 minutes. After rinsing with water, drying in air, the titanium meshes were subjected to chemical etching in a solution containing 15 mL of HCl (18 wt %) solution, The chemical etching was conducted at a temperature of 80 °C and duration of 15 min. This operation is necessary to remove the native TiO_2 layer. Afterwards, the Ti meshes were placed inside a Teflon stainless steel autoclave (23 mL, Parr Instrument) containing 10 mL of 0.6 M of HCl aqueous solution. The hydrothermal synthesis was conducted at 180 °C and lasted 10 hours. The synthesis conditions effects on the microstructure of the obtained materials can be found in our previous publication [54].

4.3.2 Growth of Pt onto Ti mesh and TiO2 arrays

Platinum films were deposited onto Ti mesh and TiO_2/Ti mesh substrates at room temperature by PLD method employing pure Pt target (99.99%, Kurt J. Lesker Co). Details on the operating principle of the PLD are reported elsewhere [22-23]. The deposition conditions were: 50 kp laser pulses, 2 Torr of helium, KrF excimer laser (λ=248 nm), pulse width of 17 ns, repetition rate of 50 Hz, 4 Joules per cm^2 as the laser fluence, and 5 cm as the distance between the substrate (Ti or TiO_2) and the Pt target. Prior every deposition of Pt, evacuation of the PLD chamber was done at 4×10^{-5} Torr by a turbo pump. The amount of the deposited Pt assessed with neutron activation analysis was 120 $\mu g\ cm^{-2}$. The PLD deposition parameters were optimal and reported in our previous publications [52-53].

4.3.3 Materials Characterization

An SEM (TESCAN, LYRA3) operated at 20 kV was used to analyze the surface morphology of the synthesized materials. The crystalline structure of all samples was determined by XRD using Bruker D8 Advance diffractometer equipped with a Cu Kα source (λ=1.5406 Å). The tube current was 40 mA with a tube voltage of 40 kV. Diffractograms were acquired with an acquisition time of 5 s per step in the Grazing Incidence Diffraction (GID) scan mode using an incident angle of 3° and a 2θ angular of 0.04° step size. XPS analysis was conducted to examine the concentration of the elements and their valence states at the surface of the samples with a VG Escalab 220i-XL outfitted with an Al Kα source (1486.6 eV). 10 kV, 20 mA and pass energy of the analyzer 20 eV were the conditions that operated the anode. Survey spectra were first recorded from 0 to1350 eV. Afterwards, higher resolution multiplex scans (Ti 2p, Pt 4f, C1 s and O 1s core levels) were acquired. CasaXPS software (Casa Software Ltd.) was employed to analyze and quantify the elements by fitting the core level spectra once a Shirley background exclusion. The metallic components of the Pt 4f and Ti 2p regions were fitted using a Gaussian/Lorentzian asymmetrically modified line shape, and a Gaussian/Lorentzian line shape was used to fit the other components. The C 1s core level located at 284.6 eV, stemming from hydrocarbon impurities present at the surface of the samples, was employed as an internal reference. All XPS spectra have been readjusted with regard to the C 1s core level of accidental carbon impurity.

4.3.4 Electrochemical Experiments

Ethanol (100% purity) and Sulfuric acid (H_2SO_4, 96 %) were acquired from Commercial Alcohols inc. and Agros Organics, respectively. The reactants were used as received. The

electrochemical properties were studied by voltammetry or LSV. The electrolytic solution was either 0.5 M H_2SO_4 or 1 M C_2H_5OH + 0.5 M H_2SO_4. The 3-electrode cell contained an Ag/AgCl (4 M NaCl) acted as a reference electrode, a platinum coil as an auxiliary electrode, and Pt/Ti mesh or Pt/TiO_2 arrays/Ti mesh working electrodes. In this paper, the potentials are reported against Ag/AgCl. Before commencing each electrochemical experiment, argon was bubbled through the electrolytic solution for 30 min to remove dissolved oxygen. Then the surface of the Pt/Ti mesh and Pt/TiO_2/Ti mesh were subjected to electrochemical cleaning and activation in 0.5 M H_2SO_4 by multicycling voltammetry from -0.2 V to 1.3 V at 50 mV s^{-1} potential scan rate until a steady state voltammogram is reached. EOR experiments were performed with LSV using a mixture of 1 M C_2H_5OH and 0.5 M H_2SO_4 within 0 V to 1.0 V at 5 mV s^{-1}. It has to be mentioned the Ti meshes in all cases had the same geometric size. Electrochemical measurements were conducted at ambient temperature using an Autolab, PGSTAT 20.

4.4 Conclusions

TiO_2 arrays were successfully synthesized directly on the Ti mesh by a hydrothermal method in acidic medium. SEM observations revealed that as prepared TiO_2 is constituted of a mixture of flower-like nanorods and vertically aligned bar-shaped structures corresponding to rutile phase, as identified by XRD. By means of XPS, the [O]/[Ti] atomic ratio was found to 3.8. This deviation from stoichiometry is ascribed to porosity that permits moisture to accrue between the voids of the perpendicularly arranged TiO_2 bars or within the arranged flowers-like TiO_2 nanorods.

Afterwards, Pt catalyst as a benchmark catalyst was deposited by PLD onto such synthesized TiO_2 structures in order to assess their catalytic supporting properties. SEM imaging revealed an interesting 3-D pinecones-shaped Pt/TiO_2 structure. XRD analysis showed that the crystallite size of Pt in Pt/TiO_2 is smaller than that in Pt/Ti mesh, which demonstrates that the TiO_2 support enhances the dispersion quality of Pt nanoparticles. Furthermore, XPS analysis confirmed the strong interaction between Pt and the TiO_2 support, which induces ionized platinum (Pt^{2+} and Pt^{4+}).

Notwithstanding having similar amount of Pt, the three-dimensional pinecones-shaped Pt/TiO_2 structure exhibited current catalytic activity towards EOR remarkably superior by 4.4 times than unsupported Pt. Moreover, the presence TiO_2 as support enables 6.6 times increased current durability relative to Pt/Ti mesh. As mentioned in this work, Pt is chosen here as a model catalyst and we believe that with catalysts that perform better than platinum, such 3-D mesh architectured

electrodes are promising not only for fuel cells in general but can be useful for a variety of catalytic or photoelectrochemical reactions for other catalysts.

Funding: This research was funded by the Natural Sciences Engineering Research Council of Canada (NSERC), Discovery grant and The Centre Québécois sur les Matériaux Fonctionnels (CQMF). J. C. Abrego-Martínez is grateful to UNESCO-MATECSS Excellence PhD Scholarship Program.

References

[1] Gu, Y.; Zhang, T.; Chen, H.; Wang, F.; Pu, Y.; Gao, C.; and Li, S. Mini Review on Flexible and Wearable Electronics for Monitoring Human Health Information. Nanoscale Res. Lett. 2019, 14, 263.

[2] Zhao, Y.; Guo, J. Development of flexible Li-ion batteries for flexible electronics. InfoMat. 2020, 2, 866–878.

[3] Kim, D.W.; Jung, S.M.; and Jung, H.Y. A super-thermostable, flexible supercapacitor for ultralight and high performance devices. J. Mater. Chem. A 2020, 8, 532-542.

[4] Ning, F.; He, X.; Shen, Y.; Jin, H.; Li, Q.; Li, D.; Li, S.; Zhan, Y.; Du, Y.; Jiang, J.; Yang, H.; and Zhou, X. Flexible and Lightweight Fuel Cell with High Specific Power Density. ACS Nano 2017, 11, 5982–5991.

[5] Hashemi, S.A.; Ramakrishna, S.; and Aberle, A.G. Recent progress in flexible–wearable solar cells for self-powered electronic devices. Energy Environ. Sci. 2020, 13, 685-74.

[6] Kwon, C.H.; Ko, Y.; Shin, D.; Kwon, M.; Park, J.; Bae, W.K.; Lee, W.S.; and Cho, J. High-power hybrid biofuel cells using layer-by-layer assembled glucose oxidase-coated metallic cotton fibers. Nat. Commun. 2018, 9, 4479

[7] Yaoming, X.; Jihuai, W.; Gentian, Y.; Jianming, L.; Miaoliang, H.; Leqing, F.; and Zhang, L. Fabrication of high performance Pt/Ti counter electrodes on Ti mesh for flexible large-area dye-sensitized solar cells. Electrochim. Acta 2011, 58, 621-627.

[8] Kim, H.; Khamwannah, J.; Choi, C.; Shi, Y.; and Jin, S. Hydrothermally grown TiO_2 nanotubes on multi-layered Ti mesh electrodes for enhanced photoelectrochemical reaction. MRS Communications 2013, 3, 235-240.

[9] Luo, D.; Liu, B.; Fujishima, A.; and Nakata, K. TiO_2 Nanotube Arrays Formed on Ti Meshes with Periodically Arranged Holes for Flexible Dye-Sensitized Solar Cells. ACS Appl. Nano Mater. 2019, 2, 3943-3950.
[10] Sugiawati, VA.; Vacandio, F.; Galeyeva, G.; Kurbatov, A.P.; and Djenizian, T. Enhanced Electrochemical Performance of Electropolymerized Self-Organized TiO_2 Nanotubes Fabricated by Anodization of Ti Grid. Front. Phys. 2019, 7, 179.
[11] Chen, C.; and Yang, X. MnO_2 modified TiN nanotube arrays on Ti mesh for flexible supercapacitors electrode. RSC Adv. 2017, 7, 56440-56446.
[12] Wang, Z.; Cao, X.; Liu, D.; Hao, S.; Du, G.; Asiric, A.M.; and Sun, X. Ternary NiCoP nanosheet array on a Ti mesh: a high-performance electrochemical sensor for glucose detection. Chem. Commun. 2016, 52, 14438-14441.
[13] Jiang, S.; Yi, B.; Zhang, C.; Liu, S.; Yu, H.; Shao, Z. Vertically aligned carbon-coated titanium dioxide nanorod arrays on carbon paper with low platinum for proton exchange membrane fuel cells. J. Power Sources 2015, 276, 80-88.
[14] Kim, D.S.; Abo Zeid, E.F.; Kim, Y.T. Additive treatment effect of TiO_2 as supports for Pt-based electrocatalysts on oxygen reduction reaction activity. Electrochim. Acta 2010, 55, 3628-3633.
[15] Tominaka, S.; Ishihara, A.; Nagai, T.; and Ota, K. Noncrystalline Titanium Oxide Catalysts for Electrochemical Oxygen Reduction Reactions. ACS Omega 2017, 2, 5209-5214.
[16] Abdullah, M.; Kamarudin, S.K.; and Shyuan, L.K. TiO_2 Nanotube-Carbon (TNT-C) as Support for Pt-based Catalyst for High Methanol Oxidation Reaction in Direct Methanol Fuel Cell. Nanoscale Res. Lett. 2016, 11, 553.
[17] Drew, K.; Girishkumar, G.; Vinodgopal, K.; Kamat, P.V. Boosting Fuel Cell Performance with a Semiconductor Photocatalyst: TiO_2/Pt−Ru Hybrid Catalyst for Methanol Oxidation. J. Phys. Chem. B 2005, 109, 11851-11857.
[18] Antolini, E. Photo-assisted methanol oxidation on Pt-TiO_2 catalysts for direct methanol fuel cells: A short review. Appl. Catal. B: Environ. 2018, 237, 491-503.
[19] Wu, X.; Zhuang, W.; Lu, L.; Li, L.; Zhu, J.; Mu, L.; Li, W.; Zhu, Y.; Lu, X. Excellent performance of Pt-C/TiO_2 for methanol oxidation: Contribution of mesopores and partially coated carbon. Appl. Surf. Sci. 2017, 426, 890-896.
[20] Ait Ali Yahia, S.; Hamadou, L.; Salar-García, M.J.; Kadri, A.; Ortiz-Martínez, V.M.; Hernández-Fernández, F.J.; Pérez de los Rios, A.; Benbrahim, N. TiO_2 nanotubes as

alternative cathode in microbial fuel cells: Effect of annealing treatment on its performance. Appl. Surf. Sci. 2016, 387, 1037–1045.
[21] Yin, T.; Lin, Z.; Su, L.; Yuan, C.; and Fu, D. Preparation of Vertically Oriented TiO_2 Nanosheets Modified Carbon Paper Electrode and Its Enhancement to the Performance of MFCs. ACS Appl. Mater. Interfaces 2015, 7, 400-408.
[22] Ashfold, M.N.; Claeyssens, F.; Fuge, G.M.; Henley, S.J. Pulsed laser ablation and deposition of thin films. Chem. Soc. Rev. 2004, 33, 23-31.
[23] Eason, R. Pulsed laser deposition of thin films: applications-led growth of functional materials. John Wiley & Sons, New Jersey, USA, 2007.
[24] Erdem, B.; Hunsicker, R.A.; Simmons, G.W.; Sudol, E.D.; Dimonie, V.L.; El-Aasser, M.S. XPS and FTIR Surface Characterization of TiO_2 Particles Used in Polymer Encapsulation. Langmuir 2001, 17, 2664-2669.
[25] Marco, J.F.; Cuesta, A.; Gracia, M.; Gancedo, J.R.; Panjan, P.; Hanzel, D. Influence of a deposited TiO_2 thin layer on the corrosion behaviour of TiN-based coatings on iron. Thin Solid Films 2005, 492, 158-165.
[26] Sanjinés, R.; Tang, H.; Berger, H.; Gozzo, F.; Margaritondo, G.; and Lévy, F. Electronic structure of anatase TiO_2 oxide. J. Appl. Phys. 1994, 75, 2945-2951.
[27] Bharti B.; Kumar S.; Lee, H.N.; and Kumar, R. Formation of oxygen vacancies and Ti^{3+} state in TiO_2 thin film and enhanced optical properties by air plasma treatment. Sci. Rep. 2016, 6, 32355.
[28] Pan, X.; Yang, M.Q.; Fu, X.; Zhang, N.; and Xu, Y.J. Defective TiO_2 with oxygen vacancies: synthesis, properties and photocatalytic applications. Nanoscale 2013, 5, 3601-3614.
[29] Meng, L.J.; Moreira de Sá, C.P.; and dos Santos, M.P. Study of porosity of titanium oxide films by X-ray photoelectron spectroscopy and IR transmittance. Thin Solid Films 1994, 239, 117-122.
[30] Pacchioni, G. Electronic interactions and charge transfers of metal atoms and clusters on oxide surfaces. Phys. Chem. Chem. Phys. 2013, 15, 1737-1757.
[31] Strasser, P.; al. Lattice-strain control of the activity in dealloyed core–shell fuel cell catalysts. Nature Chem. 2010, 2, 454-460.
[32] Kitchin, J.R.; Nørskov, J.K.; Barteau, M.A.; and Chen, J.G. Role of strain and ligand effects in the modification of the electronic and chemical properties of bimetallic surfaces. Phys. Rev. Lett. 2004, 93, 156801.

[33] Wang, J.X.; et al. Oxygen reduction on well-defined core− shell nanocatalysts: particle size, facet, and Pt shell thickness effects. J. Am. Chem. Soc. 2009, 131, 17298–17302.
[34] Datye, A.; Kalakkad, D.; Yao, M.; and Smith, D.J. Comparison of metal-support interactions in Pt/TiO_2 and Pt/CeO_2. J. Catalysis 1995, 155, 148–153.
[35] Bera, P.; Priolkar, K.R.; Gayen, A.; Sarode, P.R.; Hegde, M.S.; Emura, S.; et al. Ionic dispersion of Pt over CeO_2 by the combustion method: structural investigation by XRD, TEM, XPS, and EXAFS. Chem. Mater. 2003, 15, 2049-60.
[36] Tang, X.; Zhang, B.; Li, Y.; Xu, Y.; Xin, Q.; Shen, W. The role of Sn in $Pt\text{-}Sn/CeO_2$ catalysts for the complete oxidation of ethanol. J. Mol. Catal. A Chem. 2005, 235, 122-129.
[37] Dablemont, C.; Lang, P.; Mangeney, C.; Piquemal, J.Y.; Petkov, V.; Herbst, F.; Viau, G. FTIR and XPS Study of Pt Nanoparticle Functionalization and Interaction with Alumina. Langmuir 2008, 24, 5832−5841.
[38] Kobayashi, H.; Teranishi, M.; Negishi, R.; Naya, S.; Tada, H. Reaction Mechanism of the Multiple-Electron Oxygen Reduction Reaction on the Surfaces of Gold and Platinum Nanoparticles Loaded on Titanium(IV) Oxide. J. Phys. Chem. Lett. 2016, 7, 5002−5007.
[39] Bedolla-Valdez, Z.I.; Verde-Gómez, Y.; Valenzuela-Muñiz, A.M.; Gochi-Ponce, Y.; Oropeza-Guzmán, M.T.; Berhault, G.; Alonso-Núñez, G. Sonochemical Synthesis and Characterization of Pt/CNT, Pt/TiO_2, and $Pt/CNT/TiO_2$ Electrocatalysts for Methanol Electro-Oxidation. Electrochim. Acta 2015, 186, 76−84.
[40] Xia, B.Y.; Wang, B.; Wu, H.B.; Liu, Z.; Wang, X.; Lou, X.W. Sandwich-Structured TiO_2−Pt−graphene Ternary Hybrid Electrocatalysts with High Efficiency and Stability. J. Mater. Chem. 2012, 22, 16499-16505.
[41] Qin, Y.H.; Li, Y.; Lv, R.L.; Wang, T.L.; Wang, W.G.; Wang, C.W. Enhanced Methanol Oxidation Activity and Stability of Pt Particles Anchored on Carbon-Doped TiO_2 Nanocoating Support. J. Power Sources 2015, 278, 639−644.
[42] Esfandiar, A.; Ghasemi, S.; Irajizad, A.; Akhavan, O.; Gholami, M. The decoration of TiO_2/reduced graphene oxide by Pd and Pt nanoparticles for hydrogen gas sensing. Int. J. Hydrogen Energy 2012, 37, 15423-32.
[43] Szuber, J.; Czempik, G.; Larciprete, R.; Koziej, D.; and Adamowicz, B. XPS study of the L-CVD deposited SnO_2 thin films exposed to oxygen and hydrogen. Thin Solid Films 2001, 391, 198-203.
[44] Jerkiewicz, G. Electrochemical Hydrogen Adsorption and Absorption. Part 1: Under-potential Deposition of Hydrogen. Electrocatalysis 2010, 1, 179-199.

[45] Kinoshita, K.; Ferrier, D.R.; Stonehart, P. Effect of electrolyte environment and Pt crystallite size on hydrogen adsorption—V. Electrochim. Acta 1978, 23, 45-54.
[46] Schmidt, T.J.; Gasteiger, H.A.; Stäb, G.D.; Urban, P.M.; Kolb, D.M.; Behm, R.J. Characterization of High-Surface-Area Electrocatalysts Using a Rotating Disk Electrode Configuration. J. Electrochem. Soc. 1998, 145, 2354-2358.
[47] Chen, Q.S.; Vidal-Iglesias, F.J.; Solla-Gullon, J.; Sun, S.G.; Feliu, J.M. Role of surface defect sites: from Pt model surfaces to shape-controlled nanoparticles. Chem. Sci. 2012, 3, 136-147.
[48] Kuriganova, A.; Faddeev, N.; Gorshenkov, M.; Kuznetsov, D.; Leontyev, I.; Smirnova, N. A Comparison of “Bottom-Up” and “Top-Down” Approaches to the Synthesis of Pt/C Electrocatalysts. Processes 2020, 8, 947.
[49] Wang, H.; Jusys, Z.; Behm, R.J. Ethanol electro-oxidation on carbon-supported Pt, PtRu and Pt_3Sn catalysts: A quantitative DEMS study. J. Power Sources 2006, 154, 351-359.
[50] Iwasita, T.; Pastor, E. A dems and FTir spectroscopic investigation of adsorbed ethanol on polycrystalline platinum. Electrochim. Acta 1994, 39, 531-537.
[51] Antolini, E. Platinum-based ternary catalysts for low temperature fuel cells: Part II. Electrochemical properties. Appl. Catal. B 2007, 74, 337–350.
[52] Hamoudi, Z.; El Khakani, M.A.; and Mohamedi, M. Binderless Nanothin Catalyst Layers for Next Generation of Micro-Fuel Cells: Concept, Fabrication, Results and Prospective. J. Electrochem. Soc. 2012, 159, B331-B339.
[53] Wang, Y.; Tabet-Aoul, A.; and Mohamedi, M. Room Temperature Synthesis of Mixed Platinum and Tin Oxide Nanocomposite Catalyst with Enhanced Mass Activity and Durability for Ethanol Electrooxidation in an Acidic Medium. J. Electrochem. Soc. 2016, 163, F1272-F1278.

Supplementary Materials

Three-Dimensional Pinecones-like Binder-Free Pt–TiO_2 Nanorods on Ti mesh Structures: Synthesis, Characterization and Electroactivity towards Ethanol Oxidation

Naser Mohammadi, Juan Carlos Abrego-Martinez and Mohamed Mohamedi

Énergie, Matériaux et Télécommunications (EMT), Institut National de la Recherche Scientifique (INRS), 1650 Boulevard Lionel Boulet, Varennes, Québec, J3X 1P7, Canada.

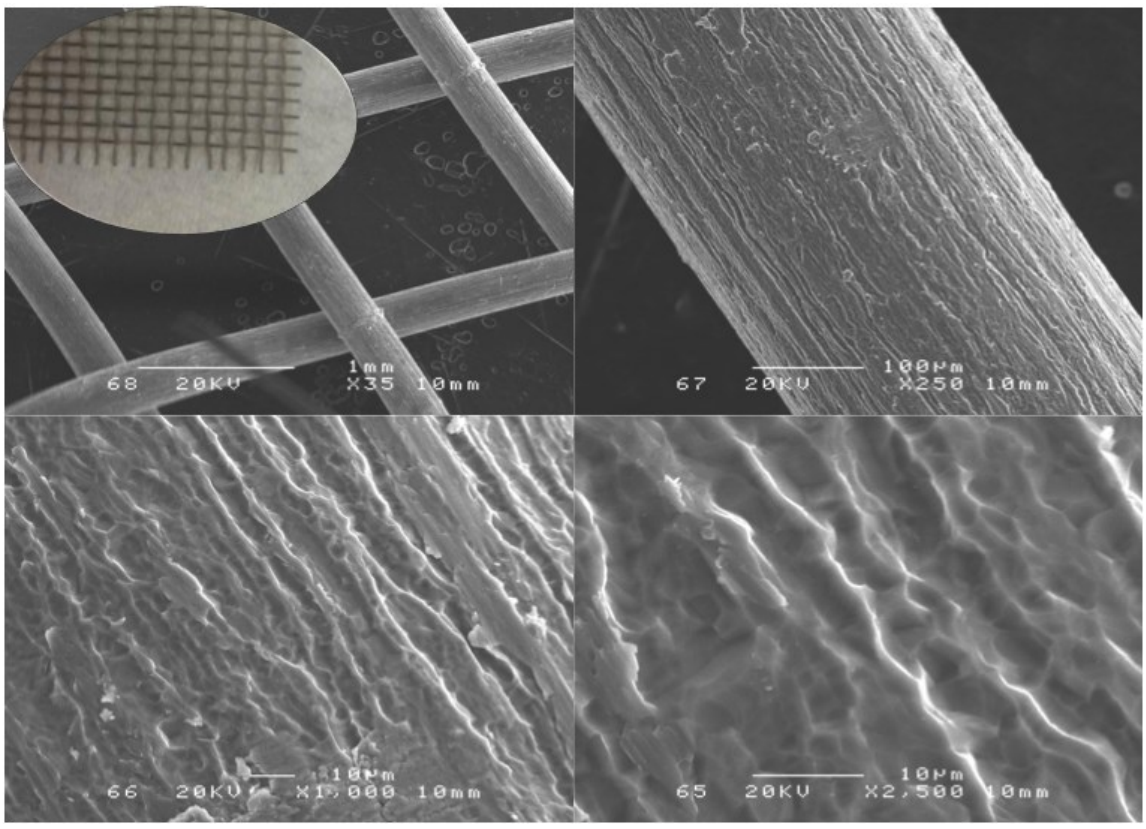

Figure S1. SEM micrographs at increasing magnifications of pristine Ti mesh. Inset at the top left figure represents a photograph of the Ti mesh.

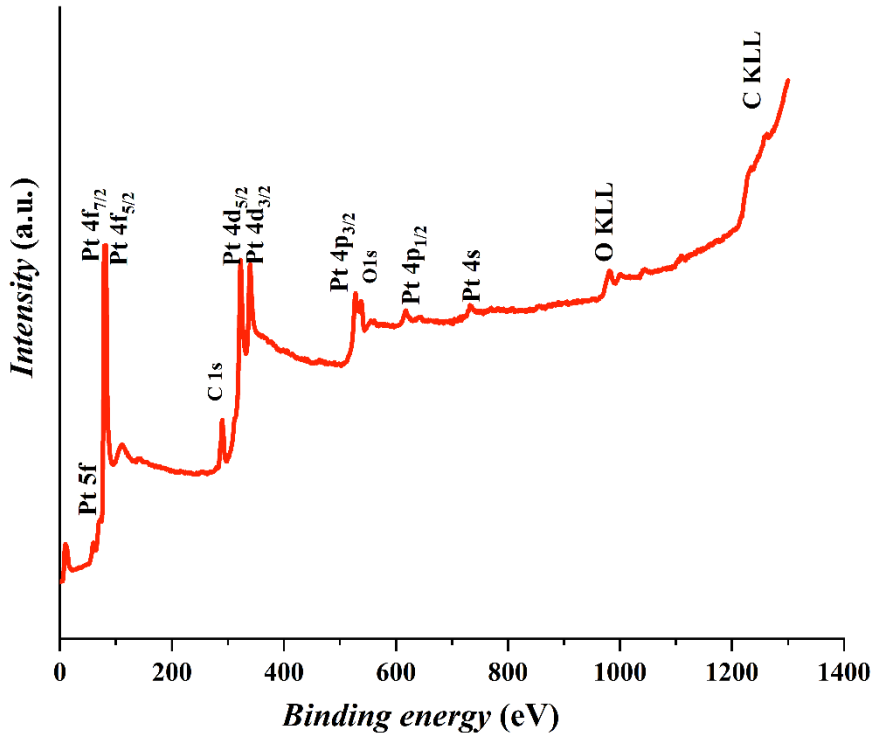

Figure S2. XPS survey scan of Pt film grown onto TiO_2 nanorods.

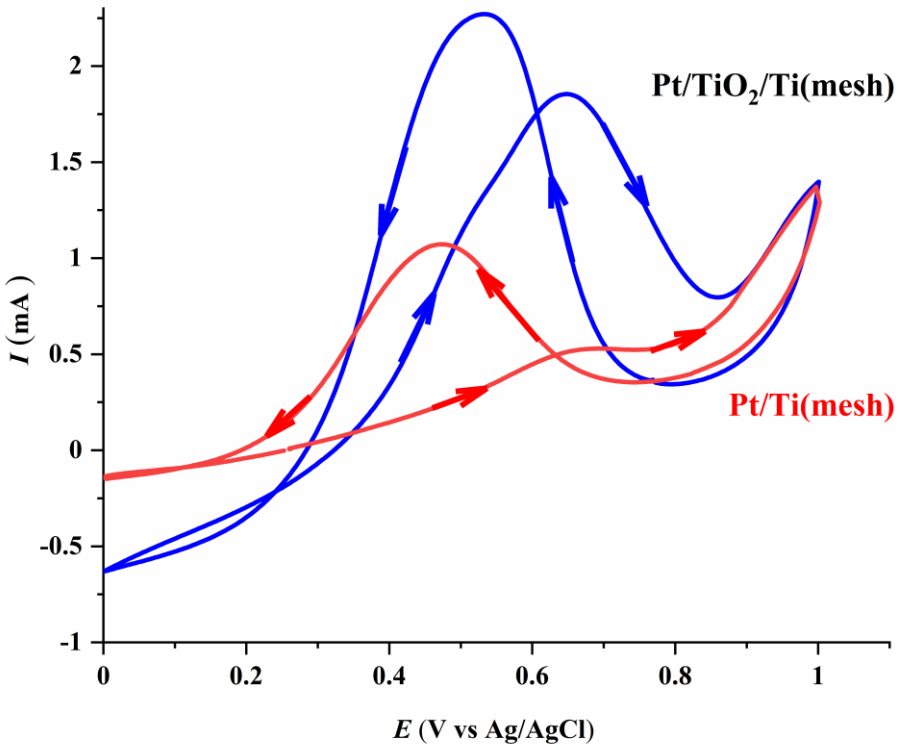

Figure S3. Cyclic voltammetry in 0.5 M H_2SO_4+ 1 M C_2H_5OH solution with a potential scan rate of 5 mV s^{-1}.

5 THE 3RD ARTICLE

Hierarchical TiO_2 nanorods grown on carbon paper via the combination of pulsed laser deposited Ti seed layer and hydrothermal technique as advanced hybrid electrocatalyst support

Nanotiges de TiO_2 hiérarchiques cultivées sur du papier carbone via la combinaison d'une couche de germe de Ti déposée par laser pulsé et d'une technique hydrothermique en tant que support d'électrocatalyseur hybride avancé

Authors:

Naser Mohammadi, Alonso Moreno Zuria, and Mohamed Mohamedi

Institut National de la Recherche Scientifique (INRS), Énergie, Matériaux et Télécommunications, 1650 Boulevard Lionel Boulet, Varennes, Québec, Canada J3X 1P7.

Title of the journal or book:

Hybrid Advances

Hybrid Advances 2 (2023) 100021

DOI: https://doi.org/10.1016/j.hybadv.2023.100021

Contribution:

I synthesized all the samples and I conducted all the electrochemical measurements and various physicochemical characterizations (XRD, SEM, and XPS). I analyzed the data and interpreted the results. Dr. Alonso Moreno Zuria designed and fabricated the microfluidic fuel cell. I participated in the writing with the help of the co-authors.

Abstract

This work presents the hydrothermal synthesis of hierarchical TiO_2 nanorods (NRs) grown for the first time from a pulsed laser deposited Ti seed layer on carbon paper (CP) substrate without the use of templates or binders. XRD reveals that TiO_2-NRs crystallize in rutile phase.

The as-prepared TiO_2-NRs greatly enhances the electroactivity and stability of Pt towards ethanol oxidation reaction. Durability studies with chronoamperometry show the specific mass activity of the Pt/TiO_2-NRs/CP catalyst is 47.92 mA mg^{-1} that is 7 times superior to that of the Pt commercial (6.72 mA mg^{-1}). The Pt/TiO_2-NRs/CP as anode in a membraneless microfluidic ethanol fuel cell delivers a maximum current density of 56.4 mA cm^{-2} and 5.1 mW cm^{-2} and a durability similar to commercial Pt anode of which the Pt loading is 16.7 higher than the Pt/TiO_2-NRs/CP catalyst. This performance can be credited to the 3-D open porous interface built of hierarchical TiO_2-NRs, which offers favorable electrolyte accessibility, better stability and straight pathways for the movement of electrons towards the electrode. Finally, the free-standing nature, the low platinum loading and the high stability make the TiO_2-NRs/CP a promising catalyst support for fuel cell technologies.

KEYWORDS

Titanium seed layer; carbon paper-coated titanium dioxide nanorods; self-supported hybrid structure; platinum electrocatalyst; ethanol electrooxidation; membrane less microfluidic fuel cell

Résumé:

Ce travail présente la synthèse hydrothermale de nanotiges de TiO_2 hiérarchiques (NR) cultivées pour la première fois à partir d'une couche de germe de Ti déposée par laser pulsé sur un substrat de papier carbone (CP) sans l'utilisation de modèles ou de liants. La DRX révèle que les TiO_2-NR cristallisent en phase rutile. Les TiO_2-NR tels que préparés améliorent considérablement l'électroactivité et la stabilité du Pt vis-à-vis de la réaction d'oxydation de l'éthanol. Des études de durabilité avec chronoampérométrie montrent que l'activité massique spécifique du catalyseur Pt/TiO_2-NRs/CP est de 47,92 mA mg^{-1} soit 7 fois supérieure à celle du Pt commercial (6,72 mA mg^{-1}). Le Pt/TiO_2-NRs/CP comme anode dans une pile à combustible à éthanol microfluidique sans membrane délivre une densité de courant maximale de 56,4 mA cm^{-2} et 5,1 mW cm^{-2} et une durabilité similaire à l'anode Pt commerciale dont la charge Pt est 16,7 plus élevée que le catalyseur Pt/TiO_2-NRs/CP. Cette performance peut être attribuée à l'interface poreuse ouverte 3D construite en TiO_2-NR hiérarchiques, qui offre une accessibilité favorable à l'électrolyte, une meilleure stabilité et des voies droites pour le mouvement des électrons vers l'électrode. Enfin, la nature autonome, la faible charge en platine et la grande stabilité font du TiO_2-NRs/CP un support de catalyseur prometteur pour les technologies des piles à combustible.

Mots clés: Couche de germe de titane; des nanobâtonnets de dioxyde de titane recouverts de papier carbone ; structure hybride autoportante ; électrocatalyseur au platine; électrooxydation de l'éthanol; pile à combustible sans membrane microfluidique

5.1 Introduction

Owing to its open porous structure, high electrical conductivity and high mechanical stability, carbon paper (CP) constructed from a network of carbon fibers is still the principal product of the macroporous substrate for the gas diffusion layer (GDL) of proton exchange membrane fuel cells (PEMFCs) [1-2]. CP is also employed as the substrate for other electroactive materials in a variety of electrochemical technologies, including rechargeable batteries [3], supercapacitors [4], enzymatic biofuel cells [5], microbial fuel cells [6] and photoelectrochemical cells [7]. These electroactive materials usually in powder form are mixed a binder and carbon materials for conductivity enhancement purposes and the mixture is then deposited on the CP substrate via several routes. The carbon materials are either activated carbons, carbon nanotubes, carbon nanofibers, or graphene [8]. Despite their unique electrical and structural properties, high surface area, such carbon supports are prone to corrosion in the oxidizing conditions like those in PEMFCs, which impairs the performance through the loss of catalyst connectivity, failure of the electrode pore structure, loss of hydrophobicity character, and an augmentation of the catalyst particle size [9].

Titanium dioxide (TiO_2) on the other hand is extremely stable and resistant to aggressive and corrosive environments and is investigated as substitute to carbon [10-18]. Of the setbacks of TiO_2 is its low electrical conductivity, especially compared to carbon materials. One way to increase the conductivity of TiO_2 is to synthesize it in the form of arrays of nanorods (NRs). Indeed such 1-D TiO_2 nanostructures would offer direct pathways for fast electron transfer [19]. It has been shown that the electron lifetime of TiO_2-NRs was superior than that of TiO_2 nanotubes by about 10^4 times [20]. In addition, NRs are more attractive since their size, shape and crystallographic orientation can be more simply adjusted to vertical orientations [21].

Several methods have been developed to prepare 1-D TiO_2 nanostructures on various substrates including hydrothermal, solvothermal, electrochemical anodization, chemical vapor deposition, template-assisted method, sol–gel and electrospinning [22]. Growing TiO_2-NRs directly on CP substrates has proven quite intricate and therefore only a few researchers have succeeded in this challenge. Towards PEMFCs application, Jiang et al synthesized aligned TiO_2 on CP substrate following two chemical steps using first a 0.05 M- 0.2 M $TiCl_4$ aqueous solution

to obtain TiO_2 seeds. Then, the as-prepared CP coated with TiO_2 seeds was placed in a stirred mixture of 0.05 mL-1.1 mL TBT (tetrabutyl titanate), 37 mL of concentrated HCl and 37 mL of deionized water and the whole was inserted into a 100 mL autoclave [23]. Then, the hydrothermal synthesis was conducted at 150 ^oC to obtain TiO_2-NRs, which were further annealed in air at 550 ^oC for 1 hour. For dye-sensitized solar cells, Guo et al used a complex process and synthesized rectangular bunched TiO_2-NR arrays on carbon fibers from titanium by a “dissolve and grow” method [24].

The prime goal of this work is to synthesize TiO_2 nanorods on CP substrate without resorting to the use of templates or binders. The second objective is to investigate the supporting properties of the TiO_2 nanorods towards Pt catalyst. We thus propose a new approach that successfully grows TiO_2-NRs directly on CP substrate. This consists in first synthesizing via pulsed laser deposition (PLD) a Ti seed layer on CP. Above this Ti seed layer, hierarchically oriented TiO_2-NRs are grown in one step via hydrothermal technique (Scheme 1). Such as grown TiO_2-NRs are characterized by scanning electron microscopy (SEM), X-ray diffraction (XRD) and X-ray photoelectron spectroscopy (XPS). Afterwards, both smooth and porous Pt films are PLD-deposited on the TiO_2-NRs/CP (Scheme 1). As a comparison catalytic support material, a smooth TiO_2 thin film was further fabricated by PLD onto CP. The physical and electrocatalytic characteristics of the prepared Pt/TiO_2-NRs/CP are investigated towards ethanol oxidation reaction (EOR), an important reaction for direct ethanol fuel cells (DEFCs). Because of its well-studied and known behaviour for EOR, Pt is selected here as a benchmark catalyst for basic studies. Finally, we evaluate the performance of the hybrid Pt/TiO_2-NRs/CP as anode in a mixed-reactant microfluidic membrane less DEFC.

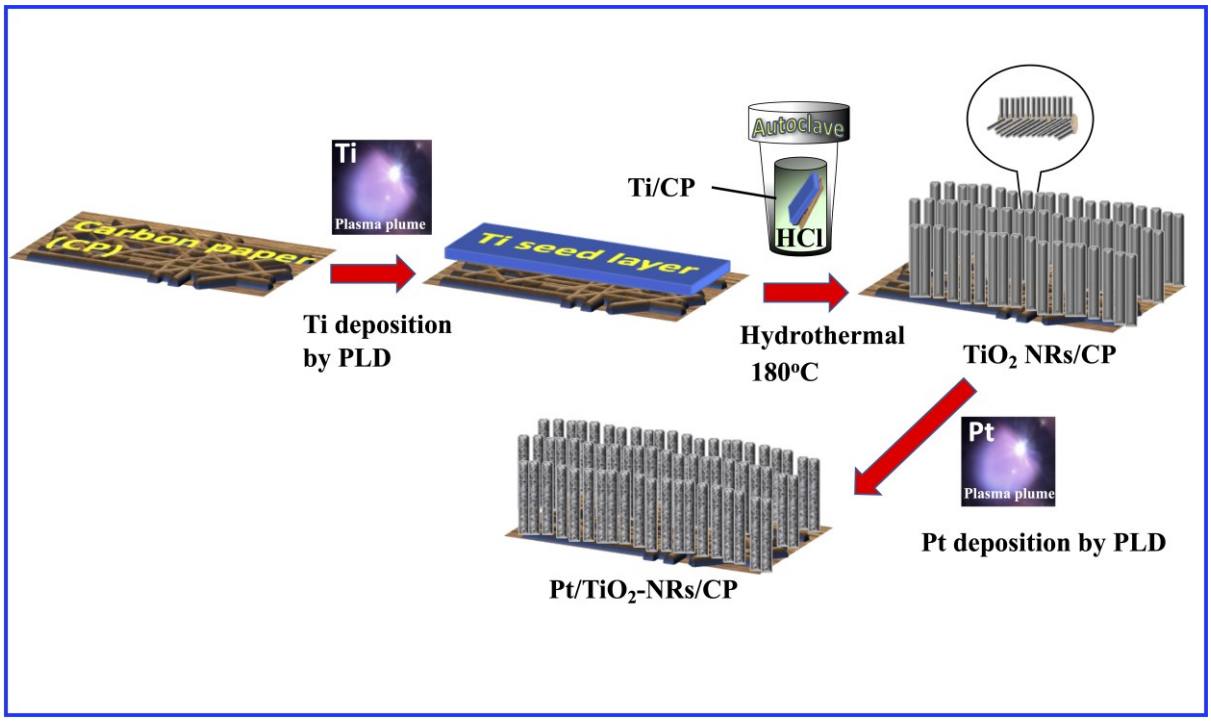

Scheme 1. Illustration of the production of Pt/TiO_2-NRs on CP substrate.

5.2 Materials and methods

5.2.1 Synthesis

5.2.1.1 Synthesis of Ti seed layer on carbon paper substrate via PLD.

To produce TiO_2 nanorods, a seed layer of Ti was grown on CP (Untreated Toray Carbon Paper, from Electrochem) substrate by PLD technique under vacuum (UV). All the deposition procedures were performed at room temperature using 300000 laser pulses, KrF excimer laser (λ=248 nm), a pulse width of 17 ns, a repetition rate of 50 Hz, and 4 Joules per cm^2 as the laser fluence. As a benchmark TiO_2 thin film was also deposited with 30000 laser pulses under vacuum by PLD onto CP substrate and labelled here as $(TiO_2)_{UV}$. The distance between the CP substrate and the Ti or TiO_2 targets (99.99%, Kurt J. Lesker Co) was 5 cm. Preceding every synthesis of Ti or TiO_2 films, the PLD chamber was evacuated at a pressure of 4×10^{-5} Torr by a turbo pump. Information on the functioning principle of the PLD can be found elsewhere [25-27].

5.2.1.2 Synthesis of TiO2 nanorods

The optimized growth conditions of TiO_2-NRs on Ti foil are reported in our previous publication [28]. Similarly, in the present work, the Ti seed layer/CP substrates were put in an ultrasonic bath filled with acetone and cleaned for 20 minutes. Afterward, the samples were washed with deionized water, dried in air and subjected to chemical etching at a temperature of 80 °C and for 15 minutes in a solution of 15 mL of HCl (18 wt %). This etching process is compulsory to remove the spontaneously formed native titanium dioxide due to exposition of Ti to air or water. Subsequently, the Ti/CP substrates were inserted in a Teflon 23 mL stainless steel autoclave (Parr Instrument) filled with of 0.6 M of HCl aqueous solution (10 mL) and the hydrothermal procedure was started at 180 °C for 10 hours.

5.2.1.3 Synthesis of Pt onto TiO2-NRs/CP

Smooth and porous Pt films were grown at room temperature by PLD. The smooth morphology was deposited under vacuum and labelled here Pt_{UV}, whereas the porous Pt film was fabricated under 2 Torr of Helium in the deposition chamber. All other deposition parameters were 50000 laser pulses, KrF excimer laser (λ=248 nm), pulse width of 17 ns, repetition rate of 50 Hz, and 4 Joules per cm^2 as the laser fluence. The distance between the TiO_2-NRs/CP substrates and the Pt target (99.99%, Kurt J. Lesker Co) was also 5 cm. The PLD chamber was evacuated at a pressure of 4×10^{-5} Torr before Pt deposition. As a benchmark samples, porous Pt was also deposited onto CP and $(TiO_2)_{UV}$/CP substrates. The Pt loading assessed by neutron activation analysis (NAA) was 0.120 mg cm^{-2} for all the catalysts. Further details regarding the working principle and application of NAA can be found elsewhere [29].

5.2.2 Materials Characterization

The surface morphology of the fabricated materials was assessed with an SEM (TESCAN, LYRA3) functioned at 20 kV. The crystalline structure of the samples was studied with XRD (Bruker D8 Advance diffractometer) with a Cu Kα source (λ=1.5406 Å). Diffractograms were recorded with an acquisition time of 5 seconds/step in the GID (Grazing Incidence Diffraction) scan mode (incident angle= 3°, 2θ angular of 0.04° step size). XPS was performed to estimate the concentration and the valence states of the chemical elements. This was done using a VG Escalab 220i-XL equipped with an Al Kα source (1486.6 eV). Survey spectra were first recorded from 0 to 1350 eV, followed by higher resolution scan of the core levels of elements of interest

that were C1 s, Ti 2p, O 1s and Pt 4f. CasaXPS (Casa Software Ltd.) was utilized to fit the core level spectra to a Shirley background exclusion. All spectra have been readjusted with regard to the C 1s core level (284.6 eV) of accidental carbon impurity.

5.2.3 Electrochemical measurements

Sulfuric acid (H_2SO_4, 96 %) and Ethanol (100% purity) were purchased from Agros Organics and Commercial Alcohols inc., respectively. The reactants were utilized with no additional purification. The electrochemical behaviours of the samples were assessed by cyclic voltammetry (CV) in 0.5 M H_2SO_4 for the estimation of the electroactive surface area (*ESA*). Linear scan voltammetry (LSV) and chronoamperometry were employed in 1 M C_2H_5OH + 0.5 M H_2SO_4 for the study of electroactivity and durability towards the EOR, respectively. The electrochemical cell housed an Ag/AgCl (4 M KCl) reference electrode, a platinum coil as a counter-electrode, and the prepared samples as the working electrodes. Before starting any electrochemical experiment, pure argon was bubbled through the electrolyte for 30 minutes to eliminate dissolved oxygen. Subsequently, all the electrodes were exposed to electrochemical cleaning and activation in 0.5 M H_2SO_4 through several CVs within -0.2 V to 1.3 V potential range at 50 mV s^{-1} potential scan rate until a steady state voltammogram is attained. All electrochemical measurements were done at ambient temperature using an Autolab, PGSTAT 20.

5.2.4 Evaluation in a □fluidic membraneless DEFC

The membraneless μfluidic fuel cell used in this work is described in details elsewhere [30]. In-brief, the system is V-shape air-breathing μfluidic fuel cell consisting of flow-through porous electrodes (0.02 cm^2 active area) positioned in a microchannel built of a 200 mm thick RTV silicone rubber, inserted between two PMMA plates machined with computer numerical control (CNC). Pt/CP, Pt/$(TiO_2)_{UV}$/CP, Pt_{UV}/TiO_2-NRs/CP, Pt/TiO_2-NRs/CP and commercial Pt Black ($2mg_{Pt}$ cm^{-2}) were all examined as anodes, whereas commercial Pt Black ($2mg_{Pt}$ cm^{-2}) acted as cathode in all tests. The fuel cell was then fed with a single solution containing 1 M C_2H_5OH + 0.5 M H_2SO_4. All performance measurements were conducted at room temperature, and the data were acquired with a Scribner Fuel Cell Test System (890CL load system), controlled with Fuel cell Test Software version 3.8.

5.3 Results and Discussion

Figure 1A shows the cross-sectional view SEM images at different magnifications of the Ti seed layer grown by PLD onto CP substrate. The images reveal that the Ti layer is dense, with a slightly rough surface and perfectly coating the carbon fibers of the CP substrate. The morphology of TiO_2 grown by hydrothermal from the Ti seed layer is shown in Fig. 1B. As it can be observed, the CP substrate was homogeneously covered with a dense and thick TiO_2 film (Fig. 1Ba-b). At higher magnifications (Fig. 1Bc-d), the SEM images show that the dense layer is comprised of vertically oriented nanorods with gaps on the top less than 1 um. This 3-D open porous structure is expected to be favorable for electrolyte accessibility. It has to be mentioned that we have varied the number of laser pulses during PLD to obtain several thicknesses of Ti seed layer and it is only with a 650 nm thickness that high density of TiO_2-NRs could be produced. This in agreement with the literature, where it was shown that both the morphology and adhesion of TiO_2 nanotubes produced from anodized Ti strongly depended on the effect of Ti foil thickness [30-31]. The morphology of the Pt film deposited under vacuum (Pt_{UV}) on the TiO_2-NRs reported in Fig. 1C shows that the film is compact and practically non-porous. For referencing, the morphology of Pt_{UV} film deposited onto bare CP substrate is shown by SEM images in Fig. S1. Instead, Pt film grown with 2 Torr of He on TiO_2 NRs is porous and made of aggregated Pt nanoparticles (Fig. 1D). Similar porous Pt deposited under similar conditions on bare CP and on smooth TiO_2 film can be seen in Fig. S2 and Fig. S3, respectively.

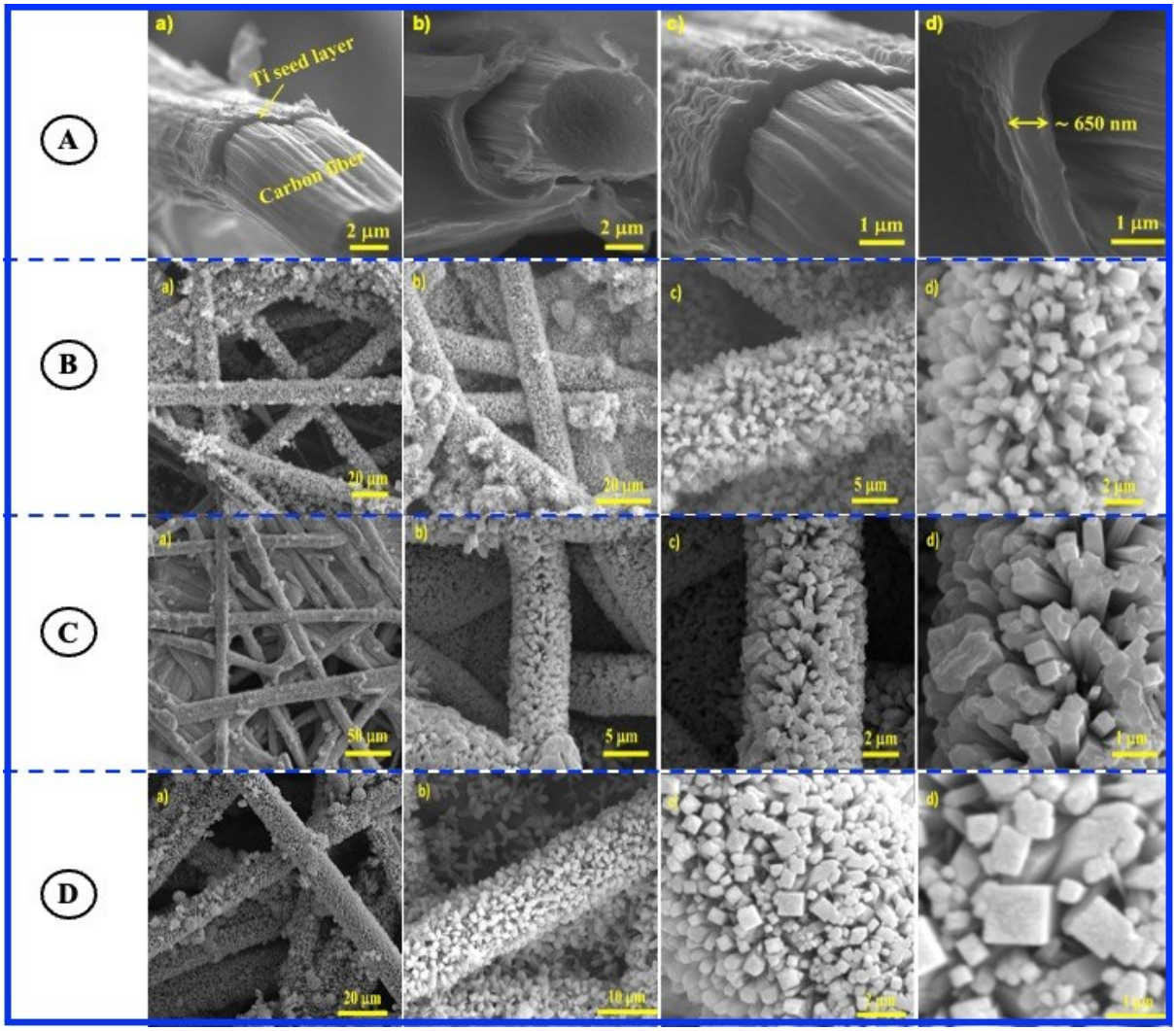

Figure. 1. SEM analysis of: A: Ti seed layer grown by PLD onto CP substrate. B: TiO_2-NRs/CP, C: Pt_{UV}/TiO_2-NRs/CP, and D: Pt/TiO_2-NRs. a), b), c) and d) represent different magnifications.

To examine the crystal structure of the above TiO_2-NRs, XRD spectrum was obtained and is shown in Fig. 2a. A part from the carbon peak (indicated by an asterisk) arising from CP substrate, the remaining peaks can be indexed to rutile TiO_2 (according to JCPDS 021-1276). Using the (110) peak, the average crystallite size (L) was estimated by the Debye-Scherrer equation: $L=0.89\ \lambda/\ \beta\ cos\ \theta$, where λ corresponds to the wavelength (1.5406 Å), β to the FWHM, and θ is the Bragg angle. Therefore, the mean crystallite size was found equal to 42.2 nm. The XPS survey spectrum corresponding to the TiO_2-NRs/CP structure revealed the most prominent lines of Ti, O and C (Fig. 2b). Figure 2c and Fig. 2d show respectively, the XPS core-levels spectra Ti 2p and O 1s P. The Ti $2p_{1/2}$ and Ti $2p_{3/2}$ were positioned at binding energy (*BE*) of 464.71 eV

and 458.96 eV, respectively. The *BE* separation of 5.75 eV indicates that Ti was as Ti^{4+} state [32-35]. The O 1s peak is non-symmetrical implying the presence of oxygen at least in two distinctive chemical states (Fig. 2d). The spectral region of oxygen O 1s could be satisfactorily fitted with two peaks. The peak appearing 530.14 eV is attributed the normal lattice sites occupied by oxygen in the TiO_2 structure. The peak occurring at 531.73 eV is due to non-lattice oxygen [35]. Taking into consideration the relative area associated to the principal O 1s element (related to Ti^{4+}-O) and that of the main Ti 2p contribution, a O/Ti ratio of 2.36 is obtained. The same result was observed TiO_2 thin film synthesized by PLD under vacuum, which showed a O/Ti ratio of 2.31 (Fig. S4).

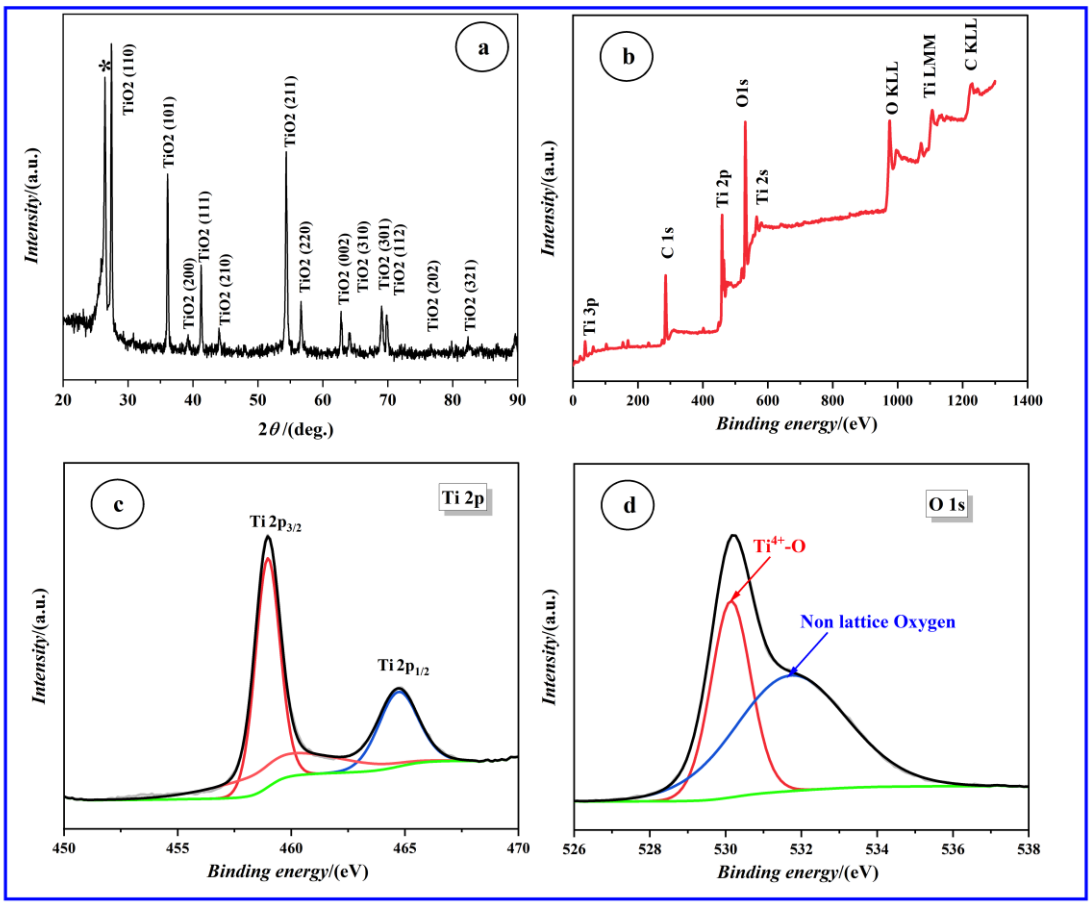

Figure. 2. Analyses of TiO_2-NRs/CP by: (a) XRD patterns; (b) XPS survey spectra; (c) Ti 2p core level, and (d) O 1s core level. (*) in Fig. 2a corresponds to carbon.

XRD analysis of CP/Pt are reported in our previous publication [36]. The diffraction patterns showed peaks of Pt(111), Pt(200), Pt(220), and Pt(311) and peaks of the CP substrate. On the other hand, the XRD of the $Pt/(TiO_2)_{UV}$/CP, Pt_{UV}/TiO_2-NRs/CP and Pt/TiO_2-NRs/CP samples (not shown) revealed dominant peaks of the TiO_2 and weak reflections of Pt. Such low intensities could

not be used to estimate the average crystallite size of Pt. It can though imply that the samples contain platinum whose particle size is very small as also observed with XRD analysis of Pt/TiO_2 by Stadnichenko et al [37]. However, the existence of Pt was verified by XPS survey scan of the Pt/CP, Pt/$(TiO_2)_{UV}$/CP, Pt_{UV}/TiO_2-NRs/CP and Pt/TiO_2-NRs/CP are reported in Fig. S5. At the former catalyst, the survey scan showed the presence of Pt, C and O elements at its surface. Instead, at Pt/$(TiO_2)_{UV}$/CP, Pt_{UV}/TiO_2-NRs/CP and Pt/TiO_2-NRs/CP, Ti element is further detected but its concentration was very small (< 3 at%). The Pt 4f spectrum of Pt/CP shows a doublet at *BE*s of 71.61 eV (Pt $4f_{7/2}$) and at 74.88 eV (Pt $4f_{5/2}$) (Fig. 3a). The 3.27 eV difference between the Pt $4f_{7/2}$ and Pt $4f_{5/2}$ confirms that Pt is in metallic state [38]. No additional valence states of Pt were found and adequate fitting of each core level peak was achieved with a single component with an asymmetric profile. On the other hand, at the surface of Pt/$(TiO_2)_{UV}$/CP, Pt_{UV}/TiO_2-NRs/CP and Pt/TiO_2-NRs/CP, the Pt 4f core-level spectrum reveals that Pt exists in three oxidation states (Fig. 3b,c,d) ascribed to Pt^0, Pt^{2+}, and Pt^{4+}. The peaks location of Pt^{2+}, and Pt^{4+} reported in Table I are in concordance with the literature [39-40]. In addition, the BE (Pt $4f_{5/2}$) shifted to lower values for Pt/$(TiO_2)_{UV}$/CP, Pt_{UV}/TiO_2-NRs/CP and Pt/TiO_2-NRs/CP samples. According to literature, a negative shift of the Pt 4f doublet relative to the value of typical for the bulk Pt metal points to the presence of smaller particles sizes in these samples [37, 41-42].

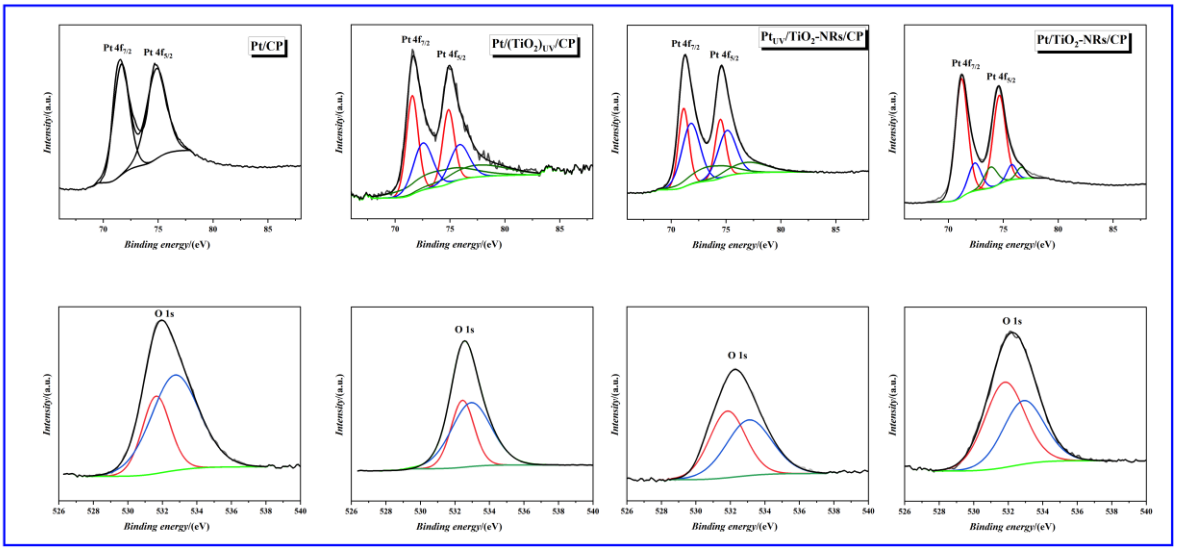

Figure. 3. XPS core-levels of Pt 4f (top figures) and O 1s (bottom figures) of the Pt deposited by PLD onto CP, $(TiO_2)_{UV}$, and TiO_2-NRs

Table I. XPS parameters extracted from Fig. 3.

Sample	Pt^0		Pt^{2+}		Pt^{4+}		Pt^{2+}/Pt^{4+}
	BE (eV)	at%	BE (eV)	at%	BE (eV)	at%	
Pt/CP	71.61	44.60					
	74.88	55.40					
Pt/$(TiO_2)_{UV}$/CP	71.56	22.03	72.53	17.38	73.91	17.76	0.98
	74.86	16.50	75.86	13.02	77.47	13.30	
Pt_{UV}/TiO_2-NRs/CP	71.14	18.78	71.79	25.47	73.58	12.94	1.97
	74.48	14.06	75.09	19.07	76.79	9.69	
Pt/TiO_2-NRs/CP	71.19	42.63	72.41	10.18	73.87	7.63	1.33
	74.63	31.93	75.83	4.36	76.76	3.27	

The electrocatalytic performance was first investigated with CVs conducted between -0.2 and 1.3 V in 0.5 M H_2SO_4 argon purged solution at a scan rate of 50 mV s^{-1}. The CVs (Fig. 4a) show similar features for the four catalysts, namely the typical hydrogen adsorption/desorption peaks between -0.2 and 0.1 V and oxide formation/reduction peaks between 0.7 V and 0.3 V [43-45]. Afterwards, the electrochemically active area (*ESA*) was estimated by integrating the charge in the hydrogen adsorption region (Q_H) of the CVs corrected for the current related to the double-layer, by means of a conversion factor Q_{ref} of 210 μC cm^{-2} [46]. Hence, the *ESA* of Pt/CP, Pt/$(TiO_2)_{UV}$/CP, Pt_{UV}/TiO_2-NRs/CP and Pt/TiO_2-NRs/CP was estimated to be 3.65, 4.02, 6.43 and 14.22 cm^2, respectively. It is clear that incorporating TiO_2-NRs as a supporting material considerably increased the *ESA* and by that enhancing the electrochemical activity of the Pt catalyst. Indeed, the peaks characteristics of hydrogen adsorption/desorption became better resolved with their corresponding current density increasing as well, which demonstrates the better utilization of Pt catalyst when supported by TiO_2-NRs. To further explain the differences in the *ESA* values and by that the intrinsic activity of the catalysts, the roughness factor *RF* was calculated by using the ratio *ESA*/geometric area of the electrode. Hence, *RF* values obtained for Pt/CP, Pt/$(TiO_2)_{UV}$/CP, Pt_{UV}/TiO_2-NRs/CP and Pt/TiO_2-NRs/CP were respectively, 3.1, 5.0, 12.8

and 22.2. Thus, a similar trend to that of *ESA* is observed with the *RF* results, i.e., electrode structure containing TiO_2-NRs displayed the highest *RF* values. The most efficient catalyst being Pt/TiO_2-NRs/CP whose *RF* is about 7 times higher than that of unsupported Pt/CP catalyst, which can be attributed to the porous structure of CP/TiO_2-NRs support and the interaction between Pt nanoparticles and TiO_2-NRs surface. On the other hand, to generate mass activity, the area specific activity *ASA* ($m^2\ g^{-1}$) = $Q_H/(Q_{ref}$ x m_{Pt} x $A_g)$ was calculated, with respectively m_{Pt} and A_g representing the Pt loading (0.120 mg cm^{-2}) and the geometric electrode area. As estimated, *ASA* of Pt/$(TiO_2)_{UV}$/CP, Pt_{UV}/TiO_2-NRs/CP and Pt/TiO_2-NRs/CP was 2.60, 4.18, 10.71 and 18.51 $m^2\ g^{-1}$, respectively. Thus, despite the same loading of Pt, the *ASA* of Pt/TiO_2-NRs/CP is 7 times higher than the unsupported Pt/CP catalyst. The conclusion of these studies indicates that TiO_2-NRs offers a higher Pt utilization.

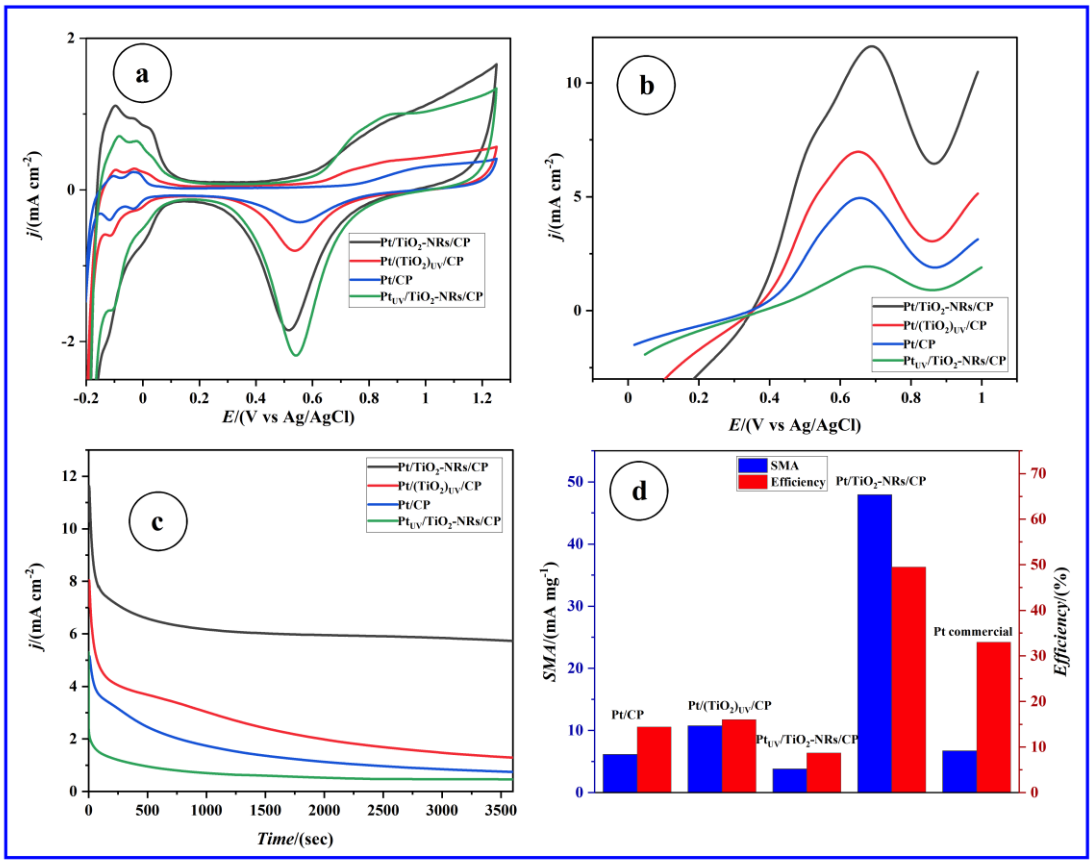

Figure. 4. Electrochemical studies (a) CVs in argon purged 0.5 M H_2SO_4 electrolyte with a potential scan rate of 50 mV s^{-1}. (b) LSVs in 0.5 M H_2SO_4+ 1 M C_2H_5OH solution with 5 mV s^{-1}. (c) Chronoamperograms in 0.5 M H_2SO_4+ 1 M C_2H_5OH solution. (d) *SMA* and efficiency (j_{3600}/j_0) extracted from Figure 5c.

To confirm the beneficial effect of the TiO_2-NRs towards a reaction of interest, the electrocatalytic performance in the EOR was investigated. Fig. 4b shows LSVs recorded in 0.5 M H_2SO_4+1 M C_2H_5OH electrolyte at slow scan rate of 5 mV s^{-1} at the four catalysts. The LSVs exhibited EOR profiles are similar to those reported in the literature [47-48]. The onset potential (E_{onset}) for the EOR at a given current density value, in this case 1 mA cm^{-2} was the more negative at Pt/TiO_2-NRs/CP catalyst (Table II). Another way to compare the electroactivity between the catalyst is to set an arbitrary criterion whose value would be near to the projected functioning voltage of DEFCs systems. Therefore, a current density at 0.6 V (*j*@0.6V) was selected to relate the performance towards the EOR between the various catalysts and the results are reported in Table II altogether with the peak current density (j_p) and the specific mass activity, *SMA* (j_p/Pt loading). It can be observed that both j@0.6V, j_p and *SMA* delivered by Pt/TiO_2-NRs/CP catalyst were more than 2 times superior to those exhibited by the unsupported Pt/CP catalyst. Although, the Pt_{UV}/TiO_2-NRs/CP contained TiO_2-NRs, it exhibited the lowest *j*@0.6V and *SMA*. This can be easily explained by the fact that Pt (deposited under vacuum) in this structure has a smooth and closed structure, which does not favor a high permeation (or accessibility) of the electrolyte to the contrary to Pt/CP, Pt/$(TiO_2)_{UV}$/CP, and Pt/TiO_2-NRs/CP catalysts in which Pt is of porous structure. In light of these results, it can be concluded that the Pt/TiO_2-NRs/CP catalyst provided kinetics of EOR much faster than the unsupported Pt/CP catalyst.

Ethanol dissociation at Pt surface results in the formation of intermediate products such as CH_x and CO. Particularly, the CO strongly adsorbs and poison the surface of Pt preventing further dissociation of ethanol, ultimately leading to a rapid drop in the electrocatalytic performance towards the EOR [48]. Therefore, the stability of the catalysts was studied with chronoamperometry in 0.5 M H_2SO_4 and 1.0 M C_2H_5OH solution at 0.6 V for 1 hour. As can be seen from Fig. 4c, the Pt/TiO_2-NRs/CP catalyst exhibited initial (j_0) and final steady-state current densities (j_{3600}) far superior to those of the other Pt-based catalyst. The current density of the EOR at all the catalysts declined in the earliest seconds, which is often ascribed to the formation of poisonous intermediates such as carbon monoxide (CO) during EOR [48].

Nevertheless, the current decay is far less significant at the Pt/TiO_2-NRs/CP catalyst, demonstrating high tolerance to CO poisoning. After a durability test of 1 hour, the Pt/TiO_2-NRs/CP catalyst exhibited a stable current density of 5.75 mA cm^{-2} almost 8 times greater than that of unsupported Pt/CP catalyst (0.74 mA cm^{-2}). As it can be noticed, here too the Pt_{UV}/TiO_2-NRs/CP showed the worst stability behavior in agreement with the CV findings. The durability

results further confirm that the Pt/TiO_2-NRs/CP catalyst had the utmost electrocatalytic activity and stability in the EOR.

Next, in order to situate the stability of the Pt/TiO_2-NRs/CP catalyst compared to commercial Pt; we have recorded chronoamperograms at 2 mg cm^{-2} Pt Black-Carbon Cloth commercial electrode used in fuel cell systems (purchased from Fuel Cell Store, USA) (Fig. S6). As expected, due to its high content of Pt, the commercial composite electrodes delivered high j_0 as compared to our binder-free catalysts. Nevertheless, and despite this high value of j_0, the current decay observed at the commercial catalyst was abrupt indicating bad durability. Indeed, Fig. 4d shows that the SMA (j_{3600}/Pt loading) of the Pt/TiO_2-NRs/CP catalyst is of 47.92 mA mg^{-1} that is 7 times superior to that of the Pt commercial (6.72 mA mg^{-1}). Furthermore, the efficiency estimated as j_{3600}/j_0 revealed that the commercial Pt retained only 33 % of its initial j_0, whereas the Pt/TiO_2-NRs/CP catalyst preserved almost 50% (Fig. 4d). Pt/TiO_2-NRs/CP displaying the greatest durability can be due to the innate stability of its 3-D structure, which enabled the adequate wetting of the electrolytic solution and charge transfer in the acidic-ethanol environment. Future work will include chronoamperometric tests for extended periods (few days), which are necessary to compare the durability, post-mortem morphological and structural characterizations of carbon and TiO_2 supported Pt catalysts.

Table II. Electrochemical EOR activity data extracted from Fig. 4b.

Catalyst	E_{onset}@1 mA cm^{-2} (V)	*j*@0.6V (mA cm^{-2})	*jp* (mA cm^{-2})	*SMA* (mA mg^{-1}_{Pt})
Pt/CP	0.45	4.47	4.95	41.25
Pt/$(TiO_2)_{UV}$/CP	0.42	6.52	6.97	58.08
Pt_{UV}/TiO_2-NRs/CP	0.56	1.54	1.94	16.17
Pt/TiO_2-NRs/CP	0.39	9.9	11.61	96.75

The enhanced electrocatalytic activity towards EOR of Pt/TiO_2-NRs/CP compared to the benchmark Pt/CP electrocatalyst can be supposed to be due to a few different phenomena. First, the deposition of Pt nanoparticles on the surface of the highly ordered TiO_2-NRs arrays revealing an extensive 3-D structure with high surface area/geometrical surface area ratio provides high catalytic activity both by *ESA* and roughness factor. Therefore, TiO_2-NRs offer better dispersion and utilization of Pt nanoparticles. Second and towards EOR, the E_{onset} (Table II) at Pt/TiO_2-NRs/CP is 60 mV lower than that at the Pt/CP catalyst. This indicates that the integrated TiO_2-

NRs promotes the oxidation of CO at low potentials. Indeed, TiO_2 is known be able to have a large surface density of hydroxyl groups [49], depending on its crystal structure and morphology. Therefore, TiO_2-NRs would be providing more OH species at low potentials, which promotes the oxidative removal of strongly bounded intermediates (such as CO) at faster rates than with Pt/CP catalyst. This is further demonstrated by chronoamperometry (Fig. 4c), where the decay in the current density due CO poisoning is the least significant at the Pt/TiO_2-NRs/CP catalyst, revealing a higher tolerance to CO poisoning as compared to Pt/CP. Finally, the higher current densities towards EOR achieved by the Pt/TiO_2-NRs/CP catalyst can be ascribed to the smaller size of the Pt nanoparticles distributed on the TiO_2-NRs as deduced from the above XPS analysis.

Figure 5 illustrates the performances of the membraneless μDEFC, which was fed with 0.027 mL of 1 M C_2H_5OH in 0.5M H_2SO_4 at 17μL min^{-1} flow rate. Fig. 5a and Fig. 5b display the polarization voltage-current density and the power density-current density profiles, respectively. Figure 5c resumes the maximum current densities and maximum power densities extracted from Fig. 5a and Fig. 5b. With the Pt/TiO_2-NRs/CP anode (0.120 mg cm^{-2} of Pt loading), a maximum current density of 56.4 mA cm^{-2} was delivered. This value is very close to that of the commercial electrode (67 mA cm^{-2}) of which the Pt loading is 16.7 higher than the Pt/TiO_2-NRs/CP anode. The maximum power density delivered by Pt/CP was of 3.7 mW cm^{-2}, whereas 5.1 mW cm^{-2} was provided with the Pt/TiO_2-NRs/CP anode. This means that 38% more power was gained by including TiO_2-NRs in the anode catalyst. The maximum power density of the cell using Pt/TiO_2-NRs/CP anode was also very close to the 5.4 mW cm^{-2} of the cell using commercial Pt anode. Afterwards, the durability of the membraneless μDEFC device was studied by chronoamperometry conducted at 0.21 V for 200 min and the resulting *I-t* profile are displayed in Fig. 5d. These chronoamperograms were recorded in passive mode with one injection of 0.027 mL of 1 M C_2H_5OH in 0.5M H_2SO_4 electrolyte. It can be observed that the current augmented sharply, before decreasing and eventually attaining a quasi-steady-state performance. In Fig. 5d, one can notice that the current decline for the EOR on the Pt/TiO_2-NRs/CP is appreciably lengthier than those of other catalysts. It is therefore clear that TiO_2-NRs prepared here have prominently enhanced the electrocatalytic activity and durability of Pt catalyst. Such TiO_2-NRs can thus be very good supports for other CP/Pt-based catalysts being studied for EOR or methanol electrooxidation reaction in direct alcohol fuel cells.

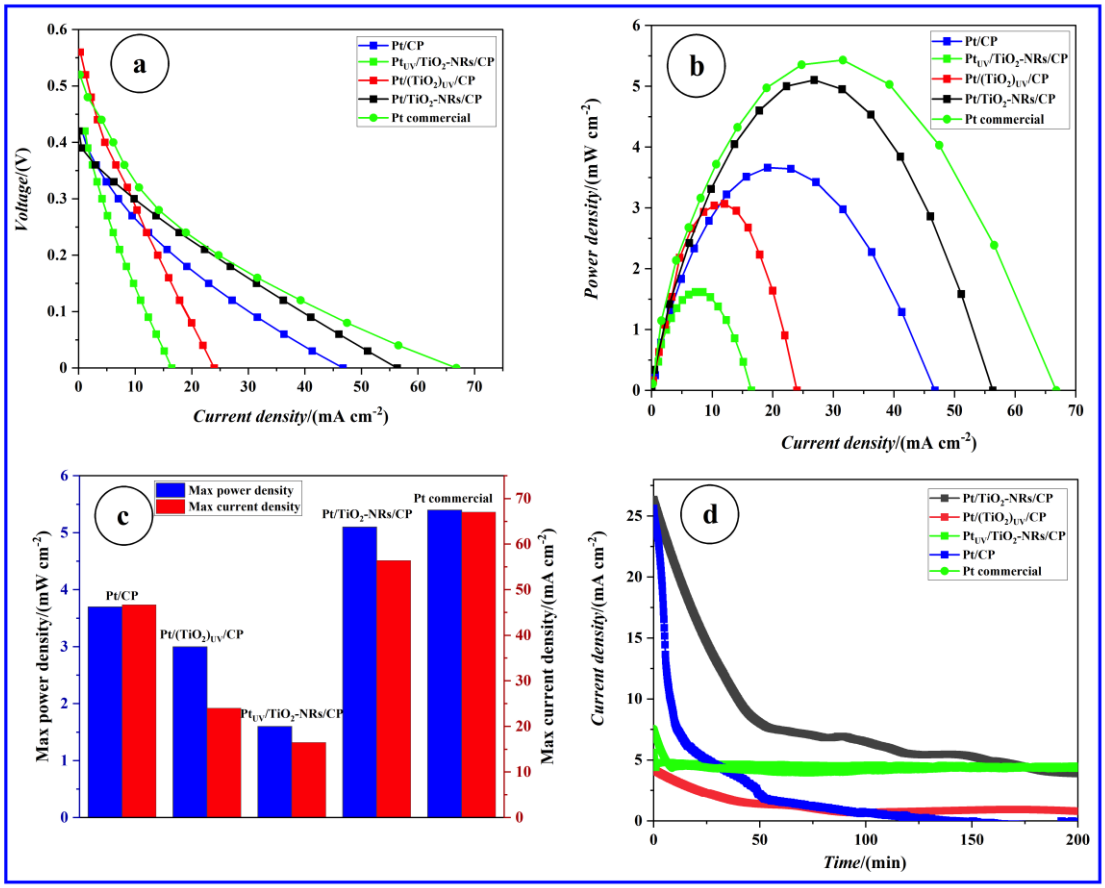

Figure. 5. Performance studies in air-breathing V-shape membraneless microfuel cell with 1 M C_2H_5OH in 0.5M H_2SO_4 electrolyte. (a) Polarization curves. (b) Power density curves. (c) Max power densities and maximum current densities. (d) Chronoamperometry.

5.4 Conclusions

Basically, we have developed a novel methodology for growing hierarchical TiO_2-NRs materials aimed at enhancing the electrocatalytic activity and durability of catalysts. The TiO_2 nanorods were grown by hydrothermal method from a Ti seed layer previously deposited by PLD a conductive CP substrate. Then, Pt thin films were deposited on the TiO_2-NRs with PLD to create a hybrid 3-D Pt/TiO_2-NRs/CP structured electrode. The electroactivity and durability of such electrode towards EOR was far superior to Pt/CP electrode including Pt commercial composite electrode. The Pt/TiO_2-NRs/CP prepared catalyst layer without Nafion (the proton-conducting ionomer) and the PTFE (the binder) can further reduce the cost of membrane electrode assemblies in fuel cell technology. Due to the common usage of CP substrate and TiO_2 in many electrochemical applications, this TiO_2-NRs/CP hybrid structure may also find potential

applications in fuel cells, microbial fuel cells, photoelectrochemistry, supercapacitors and lithium-ion batteries, to name few.

Acknowledgments

This work was financially supported by the Natural Sciences Engineering Research Council of Canada (NSERC), and the Centre Québécois sur les Matériaux Fonctionnels (CQMF). A. Moreno-Zuria is grateful to Consejo Nacional de Ciencia y Tecnología (CONACYT, Mexico) and Científicos Mexicanos en el Extranjero for a postdoctoral fellowship.

References

[1] O. Reza, S. Bahman, Review of gas diffusion layer for proton exchange membrane-based technologies with a focus on unitised regenerative fuel cells, Int. J. Hydrogen Energy 44 (2019) 3834-3860. https://doi.org/10.1016/j.ijhydene.2018.12.120.

[2] S. Park, J.-W. Lee, B.N. Popov, A review of gas diffusion layer in PEM fuel cells: Materials and designs, Int. J. Hydrogen Energy 37 (2012) 5850-5865. https://doi.org/10.1016/j.ijhydene.2011.12.148.

[3] K. Kretschmer, B. Sun, X. Xie, S. Chen and G. Wang, A free-standing LiFePO4–carbon paper hybrid cathode for flexible lithium-ion batteries, Green Chem. 18 (2016) 2691-2698. https://doi.org/10.1039/C5GC02602D.

[4] L. Yuan, X. Xiao, T. Ding, J. Zhong, X. Zhang, Y. Shen, B. Hu, Y. Huang, J. Zhou, Z. L. Wang, Paper-based supercapacitors for self-powered nanosystems, Angew. Chem. Int. Ed. 51 (2012) 4934-4938. DOI: 10.1002/anie.201109142.

[5] M. Fischback, K. Y. Kwon, I. Lee, S. J. Shin, H.G. Park, B. C. Kim, Y. Kwon, H. T. Jung, J. Kim, S. Ha, Enzyme precipitate coatings of glucose oxidase onto carbon paper for biofuel cell applications, Biotechnol. Bioeng. 109 (2012) 318-324. https://doi.org/10.1002/bit.23317.

[6] J. M. Sonawane, D. Pant, P. C. Ghosh, and S. B. Adeloju, Fabrication of a Carbon Paper/Polyaniline-Copper Hybrid and Its Utilization as an Air Cathode for Microbial Fuel Cells, ACS Appl. Energy Mater. 2 (2019)1891-1902. https://doi.org/10.1021/acsaem.8b02017.

[7] X. Zhang, X. Lu, Y. Shen, J. Han, L. Yuan, Li Gong, Z. Xu, X. Bai, M. Wei, Y. Tong, Y. Gao, J. Chen, J. Zhou and Z. L. Wang, Three-dimensional WO_3nanostructures on carbon paper: photoelectrochemical property and visible light driven photocatalysis, Chem. Commun. 47 (2011) 5804-5806. https://doi.org/10.1039/C1CC10389J.

[8] S. Shahgaldi, J. Hamelin, Improved carbon nanostructures as a novel catalyst support in the cathode side of PEMFC: a critical review, Carbon 94 (2015) 705-728. https://doi.org/10.1016/j.carbon.2015.07.055.

[9] N. Macauley, D. D. Papadias, J. Fairweather, D. Spernjak, D. Langlois, R. Ahluwalia, K. L. More, R. Mukundan, R. L. Borup, Carbon corrosion in PEM fuel cells and the development of accelerated stress tests, J. Electrochem. Soc. 165 (2018) F3148-F3160. [DOI: 10.1149/2.0061806jes.

[10] S. Jiang, B. Yi, C. Zhang, S. Liu, H. Yu, Z. Shao, Vertically aligned carbon-coated titanium dioxide nanorod arrays on carbon paper with low platinum for proton exchange membrane fuel cells, J. Power Sources, 276 (2015) 80-88. https://doi.org/10.1016/j.jpowsour.2014.11.093.

[11] D.-S. Kim, E. F. Abo Zeid, Y.-T. Kim, Additive treatment effect of TiO_2 as supports for Pt-based electrocatalysts on oxygen reduction reaction activity, Electrochim. Acta 55 (2010) 3628-3633. https://doi.org/10.1016/j.electacta.2010.01.055.

[12] S. Tominaka, A. Ishihara, T. Nagai, and Ken-ichiro Ota, Noncrystalline Titanium Oxide Catalysts for Electrochemical Oxygen Reduction Reactions, ACS Omega 2 (2017) 5209-5214 (2017). https://doi.org/10.1021/acsomega.7b00811.

[13] M. Abdullah, S. K. Kamarudin and L. K. Shyuan, TiO_2 Nanotube-Carbon (TNT-C) as Support for Pt-based Catalyst for High Methanol Oxidation Reaction in Direct Methanol Fuel Cell, Nanoscale Res. Lett. 11 (2016) 553. https://doi.org/10.1186/s11671-016-1587-2.

[14] K. Drew, G. Girishkumar, K. Vinodgopal, P. V. Kamat, Boosting Fuel Cell Performance with a Semiconductor Photocatalyst: TiO_2/Pt−Ru Hybrid Catalyst for Methanol Oxidation, J. Phys. Chem. B 109 (2005) 11851-11857. https://doi.org/10.1021/jp051073d.

[15] E. Antolini, Photo-assisted methanol oxidation on Pt-TiO_2 catalysts for direct methanol fuel cells: A short review, Appl. Catal. B: Environ. 237 (2018) 491-503. https://doi.org/10.1016/j.apcatb.2018.06.029.

[16] X. Wu, W. Zhuang, L. Lu, L. Li, J. Zhu, L. Mu, W. Li, Y. Zhu, X. Lu, Excellent performance of Pt-C/TiO_2 for methanol oxidation: Contribution of mesopores and partially coated carbon, Appl. Surf. Sci. 426 (2017) 890-896. https://doi.org/10.1016/j.apsusc.2017.07.219.

[17] S. Ait Ali Yahia, L. Hamadou, M. J. Salar-García, A. Kadri, V. M. Ortiz-Martínez, F. J. Hernández-Fernández, A. Pérez de los Rios, N. Benbrahim, TiO_2 nanotubes as alternative cathode in microbial fuel cells: Effect of annealing treatment on its performance, Appl. Surf. Sci. 387 (2016) 1037-1045. https://doi.org/10.1016/j.apsusc.2016.07.018.

[18] T. Yin, Z. Lin, L. Su, C. Yuan, and D. Fu, Preparation of Vertically Oriented TiO_2 Nanosheets Modified Carbon Paper Electrode and Its Enhancement to the Performance of MFCs, ACS Appl. Mater. Interfaces 7 (2015) 400-408. https://doi.org/10.1021/am506360x.

[19] H. Kmentova, S. Kment, L. Wang, S. Pausova, T. Vaclavu, R. Kuzel, H. Han, Z. Hubicka, M. Zlamal, J. Olejnicek, M. Cada, J. Krysa, R. Zboril, Photoelectrochemical and structural properties of TiO_2 nanotubes and nanorods grown on FTO substrate: Comparative study between electrochemical anodization and hydrothermal method used for the nanostructures fabrication, Catal. Today 287 (2017) 130-136. https://doi.org/10.1016/j.cattod.2016.10.022.

[20] J. Jitputti, Y. Suzuki, S. Yoshikawa, Synthesis of TiO_2 nanowires and their photocatalytic activity for hydrogen evolution, Catal. Commun. 9 (2008) 1265-1271. https://doi.org/10.1016/j.catcom.2007.11.016.

[21] A. Prathan, J. Sanglao, T. Wang, C. Bhoomanee, P. Ruankham, A. Gardchareon, D. Wongratanaphisan, Controlled Structure and Growth Mechanism behind Hydrothermal Growth of TiO_2 Nanorods, Sci. Rep. 10 (2020) 8065. https://doi.org/10.1038/s41598-020-64510-6.

[22] M. Ge, C. Cao, J. Huang, S. Li, Z. Chen, K.-Q. Zhang, S. S. Al-Deyab and Y. Lai, A review of one-dimensional TiO_2 nanostructured materials for environmental and energy applications J. Mater. Chem. A 4 (2016) 6772-6801. https://doi.org/10.1039/C5TA09323F.

[23] S. Jiang, B. Yi, C. Zhang, S. Liu, H. Yu, Z. Shao, Vertically aligned carbon-coated titanium dioxide nanorod arrays on carbon paper with low platinum for proton exchange membrane fuel cells, J. Power Sources 276 (2015) 80-88. https://doi.org/10.1016/j.jpowsour.2014.11.093.

[24] W. Guo, C. Xu, X. Wang, S. Wang, C. Pan, C. Lin, and Z. Lin Wang, Rectangular Bunched Rutile TiO_2 Nanorod Arrays Grown on Carbon Fiber for Dye-Sensitized Solar Cells, J. Am. Chem. Soc. 134 (2012) 4437-4441. https://doi.org/10.1021/ja2120585.

[25] M. N. Ashfold, F. Claeyssens, G. M. Fuge, S. J. Henley, Pulsed laser ablation and deposition of thin films, Chem. Soc. Rev. 33 (2004) 23-31. https://doi.org/10.1039/B207644F.

[26] R. Eason, in Pulsed laser deposition of thin films: applications-led growth of functional materials, John Wiley & Sons, New Jersey, 2007.

[27] J. Theerthagiri, K. Karuppasamy, S. J. Lee, J. Theerthagiri, K. Karuppasamy, Seung Jun Lee, R. Shwetharani, Hyun-Seok Kim, S. K. Khadheer Pasha, M. Ashokkumar & Myong Yong Cho, Fundamentals and comprehensive insights on pulsed laser synthesis of advanced materials for diverse photo- and electrocatalytic applications, Light. Sci. Appl. 11 (2022) 250. https://doi.org/10.1038/s41377-022-00904-7.

[28] N. Mohammadi, C. Benabid, H. Wang, J. C. Abrego-Martinez, Y. Wang, M. Mohamedi, Three-dimensional Pt catalyst on TiO_2 structures: Synthesis, characterization, and optimal morphology for efficient ethanol electro-oxidation in acidic medium, Electrochem. Sci. Adv. 1 (2021) e2000020. https://doi.org/10.1002/elsa.202000020.

[29] L. A. Hamidatou, Overview of Neutron Activation Analysis. In (Ed.), Advanced Technologies and Applications of Neutron Activation Analysis. IntechOpen, 2019. https://doi.org/10.5772/intechopen.85461.

[30] A. Moreno Zuria, J. C. Abrego-Martinez, S. Sun, M. Mohamedi, Prospects of membraneless mixed-reactant microfluidic fuel cells: Evolution through numerical simulation, Renew. Sustain. Energy Rev. 134(2020) 110045. https://doi.org/10.1016/j.rser.2020.110045.

[30] Ž. Marinko, L. Suhadolnik, B. Šetina Batič, V. S. Šelih, B. Majaron, J. Kovač, M. Čeh, Toward a Flexible and Efficient TiO_2 Photocatalyst Immobilized on a Titanium Foil, ACS Omega 6 (2021) 23233-23242. https://doi.org/10.1021/acsomega.1c02862.

[31] R. S. Hyam and D. Choi, Effects of titanium foil thickness on TiO_2nanostructures synthesized by anodization, RSC Adv. 3 (2013) 7057. https://doi.org/10.1039/C3RA40581H.

[32] B. Erdem, R. A. Hunsicker, G. W. Simmons, E. D. Sudol, V. L. Dimonie, M. S. El-Aasser, XPS and FTIR Surface Characterization of TiO_2 Particles Used in Polymer Encapsulation, Langmuir, 17 (2001) 2664-2669. https://doi.org/10.1021/la0015213.

[33] J. F. Marco, A. Cuesta, M. Gracia, J. R. Gancedo, P. Panjan, D. Hanzel, Influence of a deposited TiO_2 thin layer on the corrosion behaviour of TiN-based coatings on iron, Thin Solid Films, 492 (2005) 158-165. https://doi.org/10.1016/j.tsf.2005.07.038.

[34] R. Sanjinés, H. Tang, H. Berger, F. Gozzo, G. Margaritondo, and F. Lévy, Electronic structure of anatase TiO_2 oxide, J. Appl. Phys. 75 (1994) 2945-2951. https://doi.org/10.1063/1.356190.

[35] K. Siuzdak, M. Sawczak, M. Klein, G. Nowaczyk, S. Jurga, A. Cenian, Preparation of platinum modified titanium dioxide nanoparticles with the use of laser ablation in water, Phys. Chem. Chem. Phys. 16 (2014) 15199-15206. https://doi.org/10.1039/C4CP01923G.

[36] J. C. Abrego-Martínez, Y. Wang, J. Ledesma-Garcia, F. M. Cuevas-Muñiz, L. G. Arriaga, M. Mohamedi, A pulsed laser synthesis of nanostructured bi-layer platinum-silver catalyst for methanol-tolerant oxygen reduction reaction, Int. J. Hydrogen Energy 42 (2017) 28056-28062. https://doi.org/10.1016/j.ijhydene.2017.02.165.

[37] A. Stadnichenko, D. Svintsitskiy, L. Kibis, E. Fedorova, O. Stonkus, E. Slavinskaya, I. Lapin, E. Fakhrutdinova, V. Svetlichnyi, A. Romanenko, D. Doronkin, V. Marchuk, J.-D. Grunwaldt, A. Boronin, Influence of Titania Synthesized by Pulsed Laser Ablation on the State of Platinum during Ammonia Oxidation, Appl. Sci., 10 (2020) 4699. https://doi.org/10.3390/app10144699.

[38] C. D. Wagner, W. M. Riggs, L. E. Davis, J. F. Moulder, in Handbook of X-ray Photoelectronic Spectroscopy, Perkin-Elmer Corp, Eden Prairie, Minnesota, 1979.

[39] P. Bera, K. R. Priolkar, A. Gayen, P. R. Sarode, M. S. Hegde, S. Emura, R. Kumashiro, V. Jayaram, and G. N. Subbanna, Ionic Dispersion of Pt over CeO_2 by the Combustion Method: Structural Investigation by XRD, TEM, XPS, and EXAFS, Chem. Mater. 15 (2003) 2049-2060. https://doi.org/10.1021/cm0204775.

[40] X. Tang, B. Zhang, Y. Li, Y. Xu, Q. Xin, W. Shen, The role of Sn in Pt–Sn/CeO_2 catalysts for the complete oxidation of ethanol, J. Mol. Catal. A Chem. 235 (2005) 122-129. https://doi.org/10.1016/j.molcata.2005.03.018.

[41] M. K. Bahl, S. C. Tsai, Y. W. Chung, Auger and photoemission investigations of the platinum-$SrTiO_3$ (100) interface: Relaxation and chemical-shift effects, Phys. Rev. B 21 (1980) 1344-1348. https://doi.org/10.1103/PhysRevB.21.1344.

[42] B. A. Sexton, A. E. Hughes, K. Foger, XPS investigation of strong metal-support interactions on Group IIIa–Va oxides, J. Catal. 77 (1982) 85-93. https://doi.org/10.1016/0021-9517(82)90149-X.

[43] K. Kinoshita, D. R. Ferrier, P. Stonehart, Effect of electrolyte environment and Pt crystallite size on hydrogen adsorption—V, Electrochim. Acta 23 (1978) 45-54. https://doi.org/10.1016/0013-4686(78)87032-7.

[44] G. Jerkiewicz, Electrochemical Hydrogen Adsorption and Absorption. Part 1: Under-potential Deposition of Hydrogen, Electrocatalysis, 1 (2010) 179-199. https://doi.org/10.1007/s12678-010-0022-1.

[45] T. J. Schmidt, H. A. Gasteiger, G. D. Stäb, P. M. Urban, D. M. Kolb, R. J. Behm, Characterization of High-Surface-Area Electrocatalysts Using a Rotating Disk Electrode Configuration, J. Electrochem. Soc. 145 (1998) 2354-2358. https://doi.org/10.1149/1.1838642.

[46] A. Pozio, M. De Francesco, A. Cemmi, F. Cardellini, L. Giorgi, Comparison of high surface Pt/C catalysts by cyclic voltammetry, J. Power Sources 105 (2002) 13-19. https://doi.org/10.1016/S0378-7753(01)00921-1.

[47] H. Wang, Z. Jusys, R. J. Behm, Ethanol electro-oxidation on carbon-supported Pt, PtRu and Pt_3Sn catalysts: A quantitative DEMS study, J. Power Sources 154 (2006) 351-359. https://doi.org/10.1016/j.jpowsour.2005.10.034.

[48] S. C. Zignani, V. Baglio, E. R. Gonzalez, A. S. Aricò, Durability of a PtSn Ethanol Oxidation Electrocatalyst, ChemElectroChem 1 (2014) 1403-1406. https://doi.org/10.1002/celc.201400014.

[49] C. Y. Wu, K. J. Tu, J. P. Deng, Y. S. Lo, C. H. Wu, Markedly Enhanced Surface Hydroxyl Groups of TiO_2 Nanoparticles with Superior Water-Dispersibility for Photocatalysis. Materials (Basel) 10 (2017) 566. doi:10.3390/ma10050566.

Supplementary material

Hierarchical TiO_2 nanorods grown on carbon paper via the combination of pulsed laser deposited Ti seed layer and hydrothermal technique as advanced hybrid electrocatalyst support

Naser Mohammadi, Alonso Moreno Zuria, and Mohamed Mohamedi

Énergie, Matériaux et Télécommunications, Institut National de la Recherche Scientifique (INRS), 1650 Boulevard Lionel Boulet, Varennes, Québec, Canada J3X 1P7.

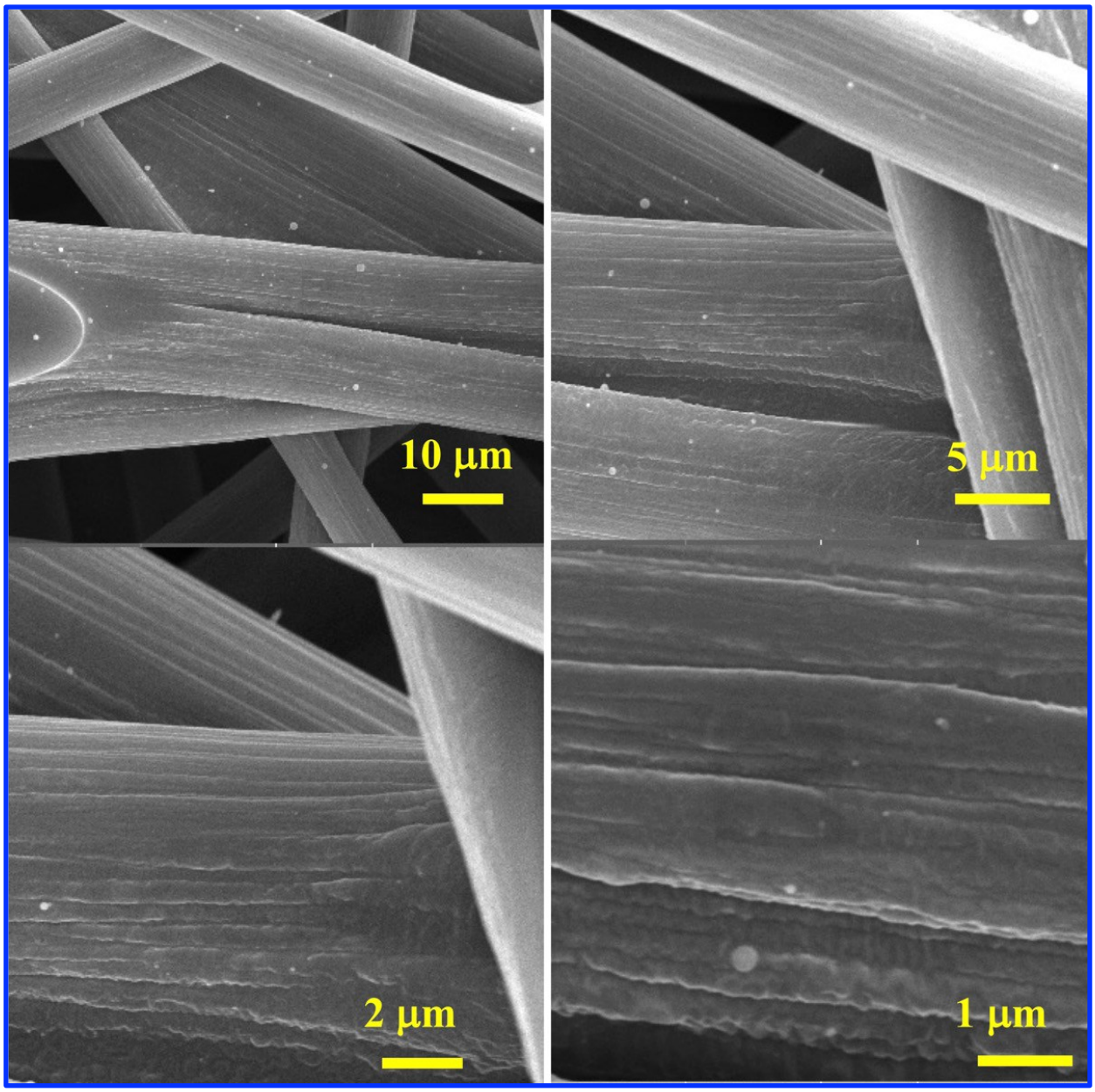

Figure S1. Pt_{UV}/CP. SEM analysis of a Pt smooth thin film grown layer grown by PLD under vacuum onto CP substrate.

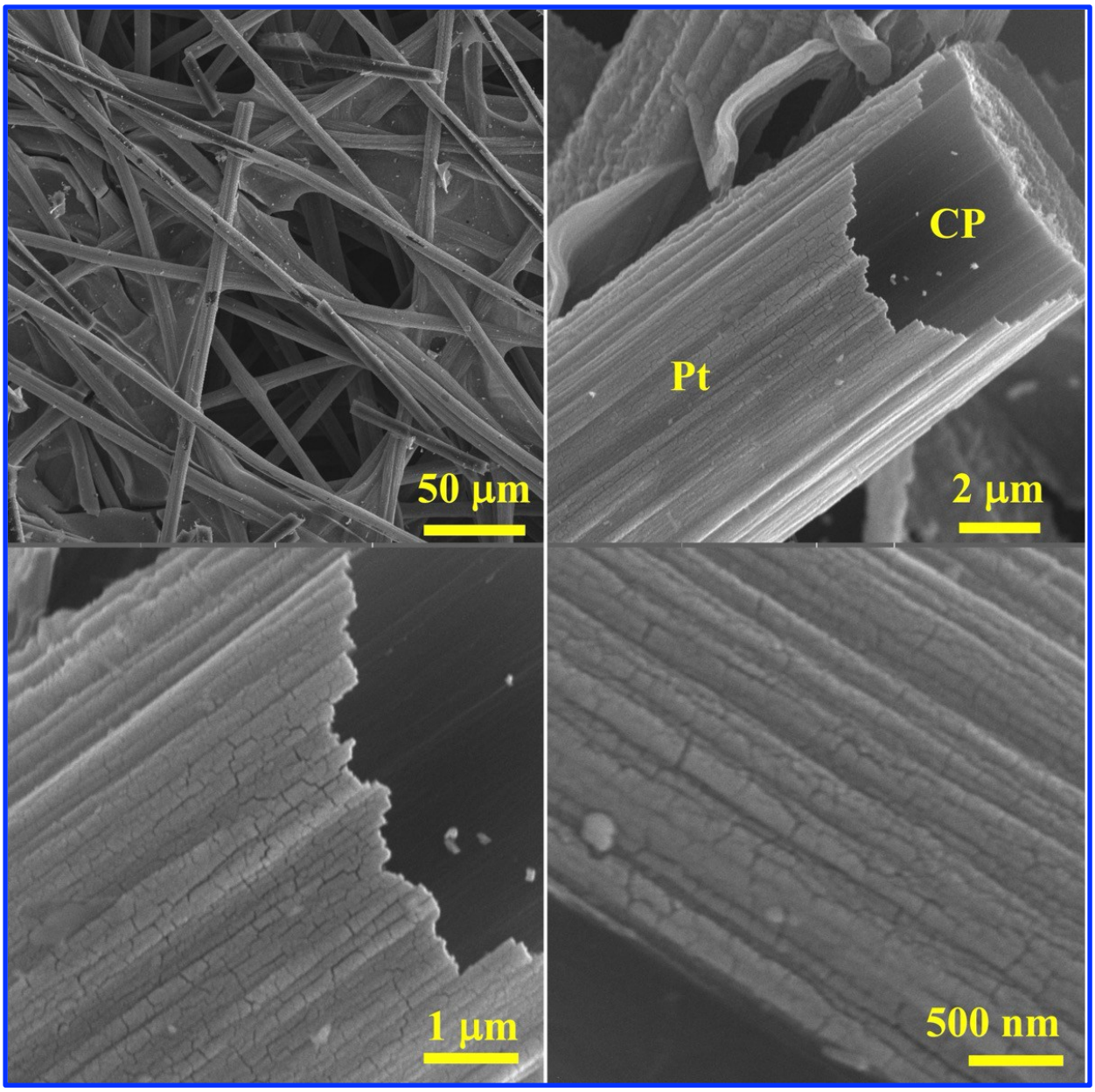

Figure S2. Pt/CP. SEM analysis of a Pt porous film grown layer grown by PLD under 2 Torr of Helium onto CP substrate.

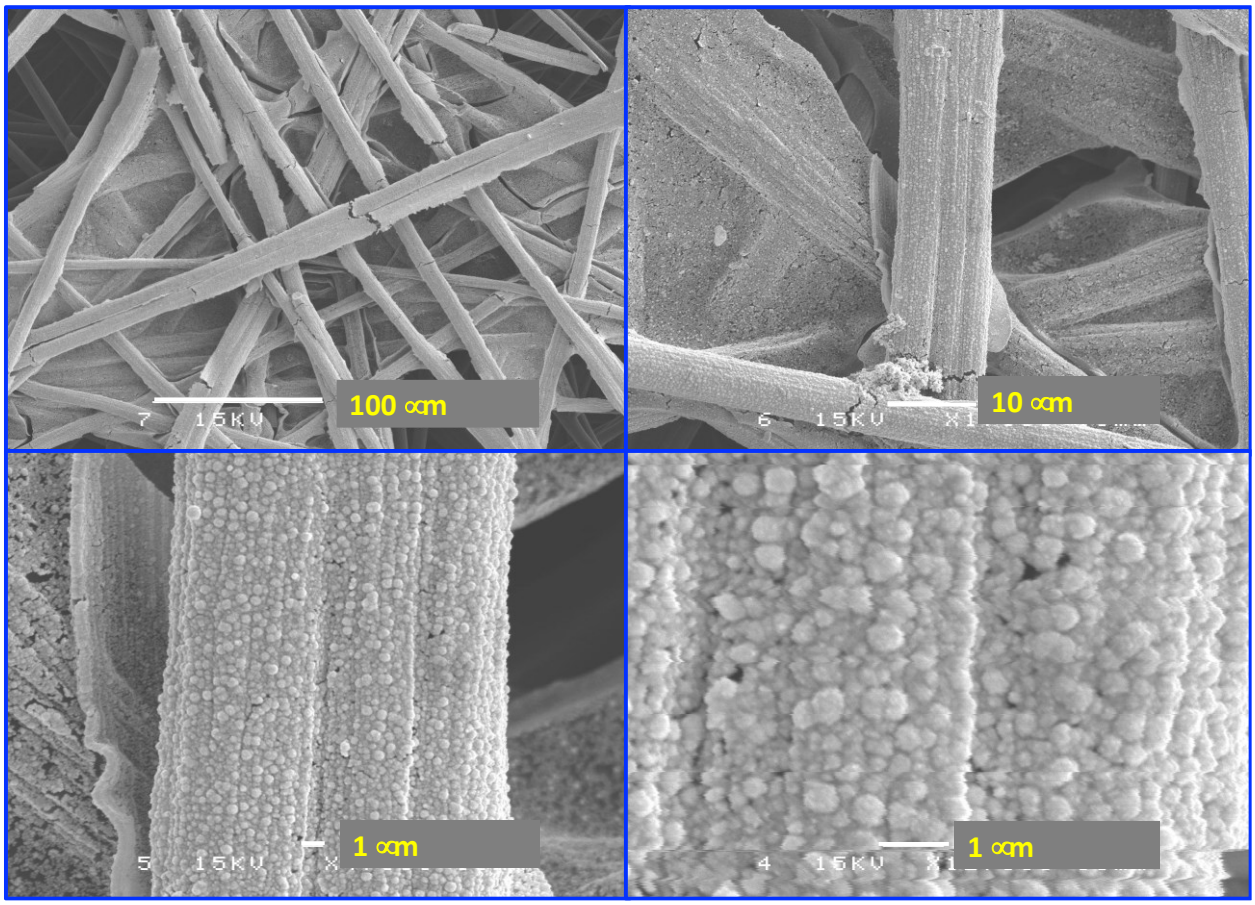

Figure S3. Pt/$(TiO_2)_{UV}$/CP. SEM analysis of a Pt porous film grown layer grown by PLD under 2 Torr of Helium onto smooth TiO_2 film/CP substrate.

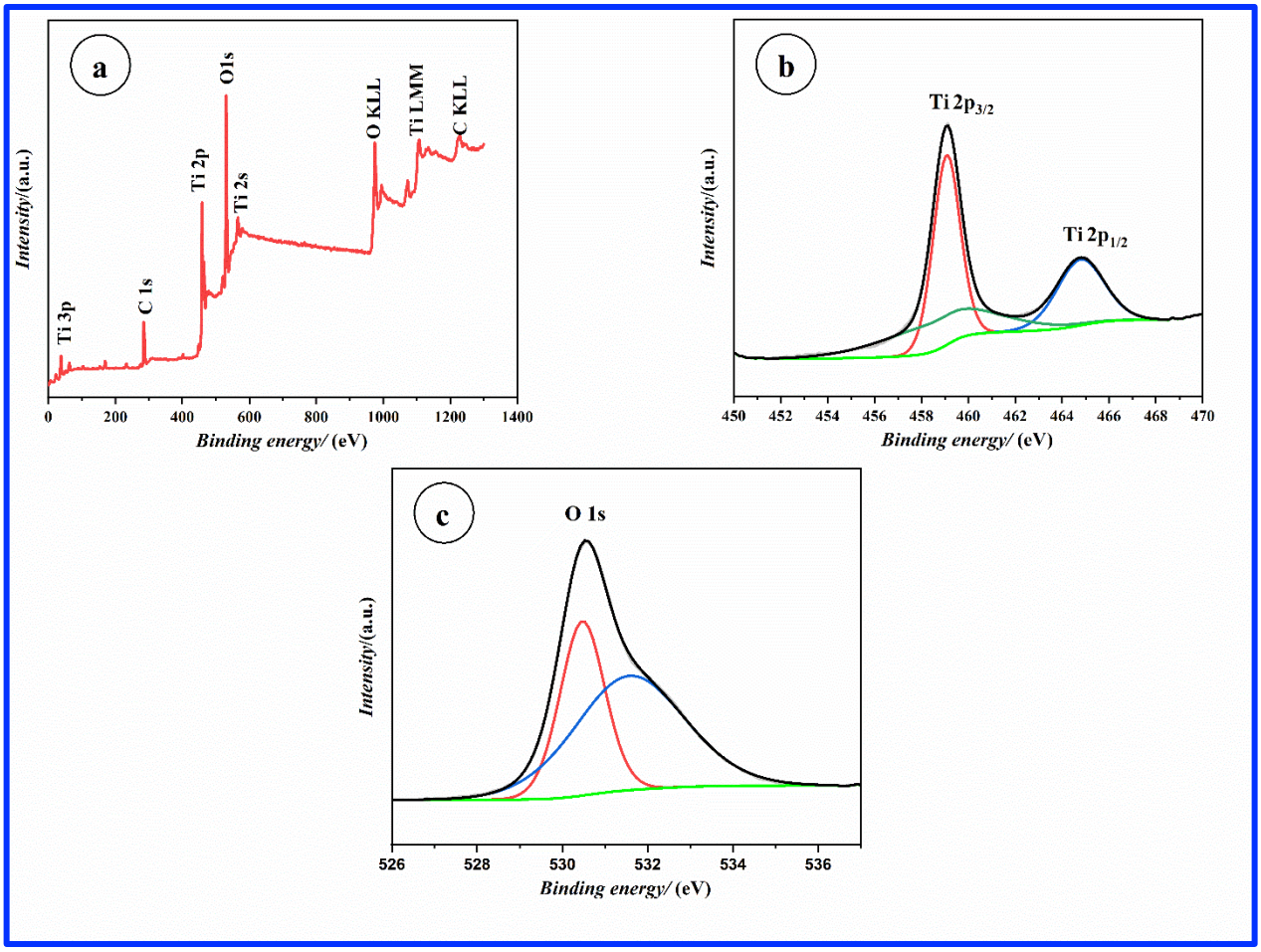

Figure S4. XPS analysis of a TiO_2 smooth film grown by PLD under vacuum onto CP substrate: (a) survey scan; (b) Ti 2p core level, and (c) O 1s core level.

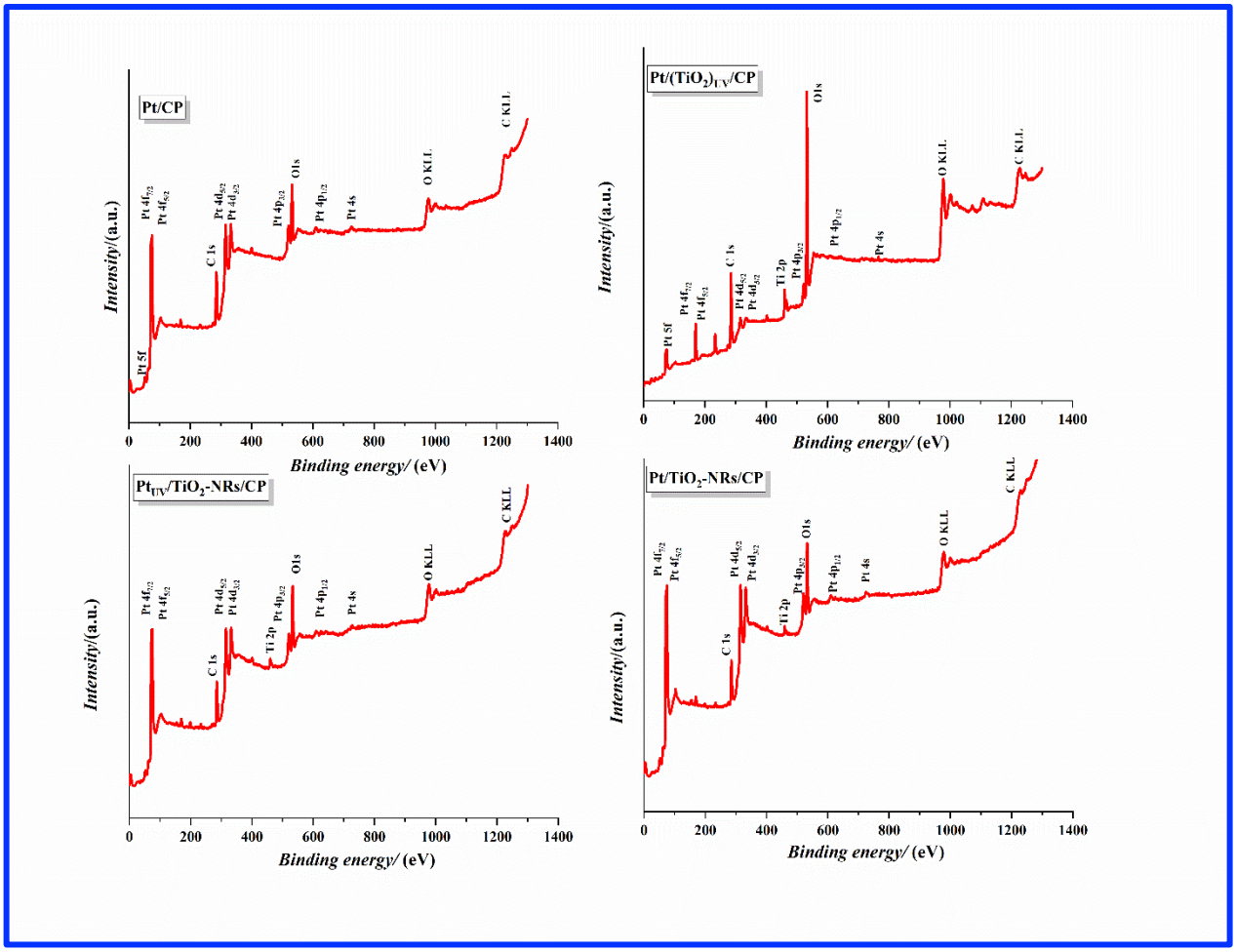

Figure S5. XPS survey scans. The samples are identified by the inserted legend.

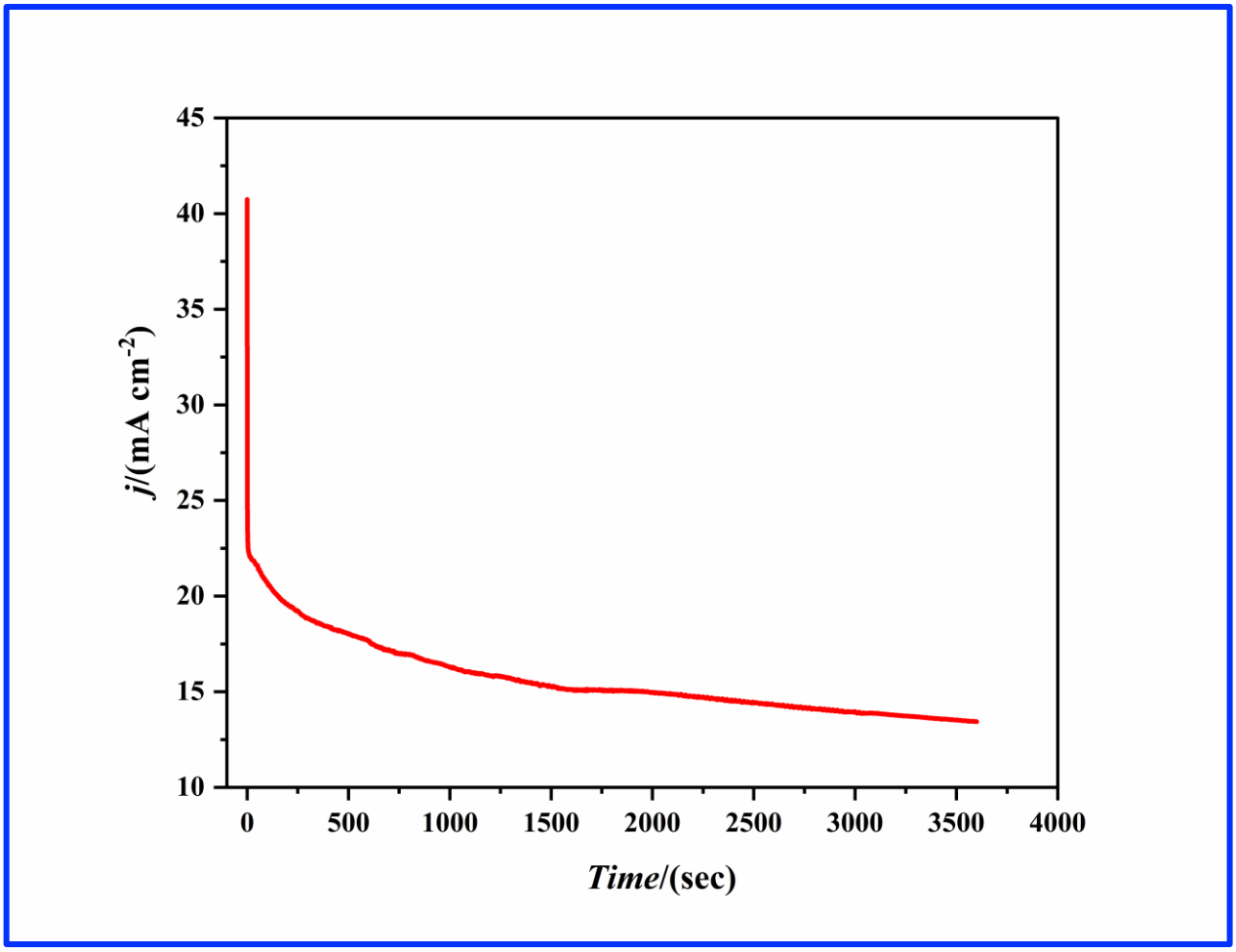

Figure S6. Durability of a Pt commercial electrode study by chronoamperometry in 0.5 M H_2SO_4+ 1 M C_2H_5OH solution.

6 CONCLUSION

In conclusion, this thesis presents a comprehensive exploration of synthesizing and optimizing TiO_2 films for use in catalytic support towards Pt, specifically in ethanol electrooxidation relevant to Direct Ethanol Fuel Cell (DEFC) technologies. The hydrothermal acidic method employed for TiO_2 array growth directly on Ti foil proves to be cost-effective, environmentally friendly, and template-free. By varying the concentration of HCl during synthesis, diverse TiO_2 morphologies were achieved, ranging from nanorods and nanowires to larger crystals. The observed increase in crystalline size with higher HCl concentration, as confirmed by SEM, XRD, and XPS analyses, indicates the tunability of TiO_2 structures.

The catalytic performance of Pt/TiO_2/Ti structures, particularly those prepared with 0.6 M HCl, stands out with significantly higher area-specific activity and current mass activities for ethanol electrooxidation. This promising outcome, surpassing unsupported Pt catalysts, suggests potential applications in DEFCs.

Further exploration involves the successful synthesis of TiO_2 arrays directly on Ti mesh, revealing a mixture of flower-like nanorods and vertically aligned bar-shaped structures. The Pt catalyst deposition onto these structures results in a unique 3D pinecone-shaped Pt/TiO_2 structure, as confirmed by SEM, XRD, and XPS analyses. This structure exhibits enhanced catalytic activity and durability compared to Pt/CP electrodes, showcasing the potential for flexible energy systems including fuel cells, batteries and supercapacitors.

The thesis concludes by highlighting a novel methodology for growing hierarchical TiO_2-NRs by hydrothermal method from a Ti seed layer previously deposited by PLD a conductive CP substrate. Pt thin films deposited on the TiO_2-NRs with PLD led to the creation of hybrid 3-D Pt/TiO_2-NRs/CP structured electrodes. The electroactivity and durability of such electrode towards EOR was far superior to Pt/CP electrode including Pt commercial composite electrode. The Pt/TiO_2-NRs/CP prepared catalyst layer without Nafion (the proton-conducting ionomer) and the PTFE (the binder) can further reduce the cost of membrane electrode assemblies in fuel cell technology. Due to the common usage of CP substrate and TiO_2 in many electrochemical applications, this novel TiO_2-NRs/CP hybrid structure is promising for several applications in fuel

cells, microbial fuel cells, photoelectrochemistry, supercapacitors and lithium-ion batteries, to name few.

7 PERSPECTIVES

We recall that the ultimate objective is to develop on substrate TiO_2 nanorods as an alternative catalyst support to conventional carbons in low-temperature DEFCs to improve catalyst dispersion and durability. Pt was chosen as a benchmark catalyst due to the fact that its electrochemical behavior towards the oxidation of ethanol is very well known. Having achieved this goal, there is however still room to further improve the electrocatalytic activity materials as well as their DEFC performances. Perspectives in few aspects are shown as follows:

1) Onto TiO_2 nanorods, grow catalysts which have demonstrated in our laboratory and in the literature electrochemical performances towards the EOR superior to that of platinum. Among these catalysts we can cite Pt-Sn and Pt-Rh alloys or composites based on metal oxides such as Pt-SnO_2, MnO_2-Pt, CeO_2-Pt or ternaries catalysts based such as Pt-Sn and Rh.

2) As reported in this thesis, TiO_2 is a highly investigated material for various electrochemical applications. The on substrate grown TiO_2 nanorods developed in this thesis would therefore be interesting to be considered for electrochemical energy technologies such as Li-ion batteries, supercapacitors and microbial fuel cells, to name few.

3) From a scientific point of view, it would be interesting to investigate and compare the electrocatalytic supporting properties of different morphologies of the TiO_2: 0D (nanoparticles, or quantum dots), 1D (nanorods), 2D (films) and 3D (bulk powders or bundles of nanorods). Results of such study may pave the way towards an optimal TiO_2 morphology with higher performance and durability.

8 APPENDIX

Publications

1. Naser Mohammadi, Alonso Moreno Zuria, and Mohamed Mohamedi.

Hierarchical TiO_2 nanorods grown on carbon paper via the combination of pulsed laser deposited Ti seed layer and hydrothermal technique. Hybrid Advances 2023, 100021.

2. **Mohammadi, N**.; Abrego-Martinez, J.C.; Mohamedi, M. Three-Dimensional Pinecone-like Binder-Free Pt–TiO_2 Nanorods on Ti Mesh Structures: Synthesis, Characterization and Electroactivity towards Ethanol Oxidation. Molecules 2022, 27, 1921.

3. Mohammadi Naser, Benabid C, Wang H, Abrego-Martinez JC, Wang Y, Mohamedi M. Three-dimensional Pt catalyst on TiO_2 structures: Synthesis, characterization and optimal morphology for efficient ethanol electro-oxidation in acidic medium. Electrochem Sci Adv. 2021; 1, e2000020.

4. X Zheng, **N Mohammadi**, A Moreno Zuria, M Mohamedi, Advanced Zinc–Air Batteries with Free-Standing Hierarchical Nanostructures of the Air Cathode for Portable Applications, ACS Applied Materials & Interfaces, 2021, 13, 61374-61385

Conferences

1. **Naser Mohammadi**, Haixia Wang, Juan Carlos Abrego Martinez and Mohamed Mohamedi, Preparation of vertically oriented carbon-coated Titanium dioxide nanorods as alternative catalyst support to carbon for fuel cells applications, BOSTON FALL MEETING AND EXHEBIT November 25 – 30, 2018 Boston, Massachusetts

2. Naser Mohammadi, Juan Carlos Abrego Martinez, Haixia Wang, Sun Shuhui and Mohamed Mohamedi, Synthesis, characterization and catalyst support properties of titanium dioxide nanorods grown on various substrates, THE 2ND INTERNATIONAL CONFERENCE ON ADVANCED MATERIALS AND PROCESSES FOR ENVIRONMENT, ENERGY AND HEALTH.

3. **Naser Mohammadi**, Juan Carlos Abrego Martinez, Haixia Wang, Sun Shuhui and Mohamed Mohamedi, Titanium dioxide nanoroads as alternative catalyst support to carbon for fuel cells

applications, INTERNATIONAL CONFERENCE OF ENERGY, MATERIALS AND PHOTONICS 8 – 11 JULY 2018 MONTREAL.

4. Xiaoying Zheng, Alonso Moreno Zuria, Juan Carlos Abrego Martinez, Naser Mohammadi and Mohamed Mohamedi, The Crystallinity Effect of Manganese Dioxide for Durability of Rechargeable Zn-Air Battery, 2020 ECS meeting, Meet. Abstr. MA2020-01 43.

5. **Naser Mohammadi**, Youling Wang, Haixia Wang, Juan Carlos Abrego Martinez and Mohamed Mohamed “Hydrothermal Growth of Titanium Dioxide Nanowires on Titanium foil with Platinum coated for PEM fuel cells”. CQMF / QCAM Centre Culturel, Sherbrooke 23 et 24 October 2017.